# On the Importance of Feedback in the Stream-Fed High Redshift Universe


Taysun Kimm
Christ Church College
University of Oxford

A thesis submitted for the degree of
*Doctor of Philosophy*

Trinity 2012

*To father and mother, and my wife Jiyeon*

# Declaration

I declare that no part of this thesis has been accepted, or is currently being submitted, for any degree or diploma or certificate or any other qualification in this University or elsewhere. This thesis is the result of my own work unless otherwise stated.

All the research was carried out in collaboration with my supervisor, Julien Devriendt, with Adrianne Slyz.

Chapter 3 has been published in The Monthly Notices of the Royal Astronomical Society: Kimm, T., Slyz, A., Devriendt, J. E. G., Pichon, C., 'Are cold flows detectable with metal absorption lines?', 413: L51-L55, 2011

Chapter 4 is to be submitted to the Astrophysical Journal: Kimm, T., Devriendt, J. E. G., Slyz, A., Pichon, C., Kassin, S. A., Dubois, Y., The angular momentum of baryons and dark matter halos revisited, to be submitted to ApJ, 2012

Chapter 6 has been published in The Monthly Notices of the Royal Astronomical Society: Kimm, T., Kaviraj, S., Devriendt, J. E. G., Cohen, S., Windhorst, R., Dubois, Y., Slyz, A., Hathi, N., Ryan, R. Jr., O'Connell, R., Dopita, M., Silk, J., 'Constraining stellar assembly and AGN feedback at the peak epoch of star formation', 425: L96-L100, 2012

# On the importance of feedback in stream-fed high redshift universe

Taysun Kimm
Christ Church College

Submitted for the Degree of Doctor of Philosophy

Trinity Term 2012

## Abstract

Cosmological hydrodynamic simulations have shown that galaxies are fed by dense, cold gas streams at high redshift. However, the presence of such gas has never been observationally confirmed. Using the HORIZON-MARENOSTRUM simulation, I examined whether cold flows are detectable with low-ionisation metal absorption lines, such as C II $\lambda$1334. It is concluded that due to their low metallicity and density, it is extremely difficult to prove/disprove the presence of cold flows using the metal absorption lines. Revisiting the acquisition of angular momentum in disc galaxies using high resolution simulations, I found that at the time of accretion, gas and dark matter do carry a similar amount of specific angular momentum which is systematically and significantly higher (at minimum by a factor of 2) than that of the dark matter halo as a whole. Whereas cold streams directly deposit this large amount of angular momentum within a sphere of radius $r \sim 0.1R_{\rm vir}$, dark matter particles easily pass through the central region, depositing their angular momentum over a much more spatially extended region. As a result, in our simulations neither the total specific angular momentum of the baryons nor its radial profile ever follows that of the virialised dark matter halo, contrary to what is typically assumed in the standard theory of disc galaxy formation. In order to better understand the formation of disc galaxies and the missing baryon problem in a $\Lambda$CDM universe, continuous, collective galactic winds are implemented. It is demonstrated that stellar feedback processes are able to suppress star formation by $\sim 30\%$ at $z = 3$, compared to that from the run without feedback sources, but it still produces an unrealistic central peak in the rotation curve. Although inclusion of hypernovae further suppresses star formation, it is unable to quench the formation of low-angular momentum stars enough to remove the peaked rotation curves at high redshift. Finally, feedback from active galactic nuclei turns out to be effective at suppressing star formation in massive galaxies at $1 < z < 2$, reproducing their observed number densities in the redshift range. However, further suppression of residual star formation is required to form quiescent galaxies at $z = 2$.

# Acknowlegements

First and foremost, I am deeply indebted to my supervisors, Dr. Julien Devriendt and Dr. Adrianne Slyz, for their patient guidance, encouragement and many motivating discussions. I have been very lucky to have supervisors who cared so much about my work, and I hope to continue collaborating with them in the future. In particular I would like to thank my colleagues, Dr. Yohan Dubois for teaching me how to use the RAMSES code, and Professor Christophe Pichon for many stimulating discussions on the acquision of angular momentum in disc galaxies. Special thanks also to Professor Sukyoung Yi for the encouragement and useful discussions during my DPhil study.

I must express my gratitude to my co-authors, Dr. Susan Kassin and members of the WFC3 ERS team, who allowed me to use their observational data. These data played an important role in understanding the properties of simulated galaxies as described in Chapter 4 and 6. I would like to offer special thanks to Dr. Sugata Kaviraj and Professor Joseph Silk for fruitful discussions and the financial support during my visit to Institut d'Astrophysique de Paris. I would also like to thank my friends Sam Geen and Amy McQuillan for the proofreading of this thesis.

I would like to thank the Oxford University Press for a generous Clarendon scholarship over the three years of my doctoral studies, without which this thesis would not been possible. I also gratefully acknowledge the financial support from Christ Church College and the Royal Astronomical Society, which allowed me to attend international conferences.

Last but not the least, I wish to thank my family for all their love and moral support: my parents Ok-Im and Young-Suk, sister Min-Jung, brother-in-laws Eun-Whan and Seong-Yeon, and parents-in-law Kyung-Hee and Byung-Chun, and my wife Jiyeon. No words can express how much I love and appreciate you. Thank you.

# Contents

# List of Figures

# Chapter 1

# Introduction

Understanding the formation of galaxies is a long-standing issue. Three decades ago, galaxies were thought to form in a simple monolithic collapse of a self-gravitating spherical cloud. Based on the observation that low metallicity stars have high eccentricities and low angular momenta, Eggen et al. (1962); Larson (1974) suggested that old, metal-poor halo stars form from initially free-falling gas in $\sim$ 100 Myr, whilst gas enriched by the halo star formation later settles into the disc and form a metal-rich population. However, Searle & Zinn (1978) noted a large metallicity spread in the halo globular clusters, and proposed a different picture in which the outer halo of the Milky Way is formed by the accretion of protogalactic, individual gas fragments. A more complete picture of galaxy formation theory was presented by White & Rees (1978), who considered the growth of galaxies in a hierarchical, dark matter-dominated universe. Based on the analytic theory of structure formation developed by Press & Schechter (1974), the authors came up with a picture in which gas first collapses into dark matter haloes, settles into the centre through atomic radiative cooling, and forms stars. Since then, many attempts have been made to further refine the hierarchical paradigm by comparing predictions from the theory and a large set of observations (e.g. Kauffmann et al., 1993; Katz et al., 1996; Devriendt et al., 1999; Somerville et al., 2008; Joung et al., 2009; Kimm et al., 2009; Oser et al., 2012).

An important prediction from the hierarchical picture is that the most massive structure forms last (Press & Schechter, 1974). This appears to be in stark contrast with the observations suggesting that the most massive galaxy forms first (e.g. Cowie et al., 1996; Juneau et al., 2005; Thomas et al., 2005). Using a galaxy sample at $0.8 < z < 2$ from the Gemini Deep Deep Survey, Juneau et al. (2005) found that less massive galaxies are more actively star forming, and that the star formation rate density declines with decreasing redshift for a given stellar mass. High [$\alpha$/Fe] abundances observed in massive galaxies also

require a short, strong burst of star formation in the high redshift universe, whereas less massive galaxies seem to have more extended star formation histories (Thomas et al., 1999).

In order to reconcile the anti-hierarchical features, galaxy formation theory necessitates some process that can effectively regulate star formation in massive galaxies. Inclusion of supernova explosions is not satisfactory, because gas blown away in a massive halo is prone to re-collapse and accumulate at its centre as the ejection of gas scales as $V_c^{-2}$ (Dekel & Silk, 1986). As a result, early theoretical models with supernova feedback predict too many massive galaxies (Kauffmann et al., 1999; Benson et al., 2003). This over-cooling problem has also been a puzzling issue in galaxy clusters, where observed X-ray flux is significantly weaker than theoretical predictions, in which hot halo gas suffers from radiative losses in the absence of an energy source and forms massive cooling flows in the cluster core (Fabian, 1994). A solution to the cooling catastrophe was found by Binney & Tabor (1995); Ciotti & Ostriker (1997), who argued that energy from a central massive black hole could offset the cooling flow. Silk & Rees (1998); King (2003) also put forward the idea that liberation of an Eddington-limited energy from the central engine self-regulates the growth of black hole and stars in the spheroid, resulting in the tight correlation between galaxy internal properties and the black hole mass (e.g. Magorrian et al., 1998; Gebhardt et al., 2000; Ferrarese & Merritt, 2000). X-ray cavities detected in cool-core clusters (Boehringer et al., 1993; McNamara et al., 2005; Fabian et al., 2006) are likely to reflect the feedback from active galactic nuclei in action. Motivated by these results, several studies tested the connection between supermassive black holes and star formation using semi-analytic models or numerical simulations, and reached a conclusion that feedback from active galactic nuclei can provide a plausible explanation for the anti-hierarchical features by quenching star formation at low redshift (e.g. Bower et al., 2006; Croton et al., 2006; Sijacki et al., 2007).

Meanwhile, Persic & Salucci (1992) claimed that a sizeable fraction of the baryons is missing in the local Universe. By convolving the luminosity function and mass-to-light ratios derived in the literature, they found that the total stellar mass can only account for less than 10% of the total baryons predicted by the $\Lambda$CDM cosmology. The contribution from hot gas to all baryons in clusters turned out to be even smaller than that from stars. Given that massive haloes are rare, the missing baryon problem indicates that it is the less massive haloes that are baryon-deficient. Indeed, on cluster scales ($M_{500} \geq 10^{14}\,h^{-1}$) hot gas alone appears to account for 90% of the total baryons in $r_{500}$, the radius within which the average density is 500 times the critical density of the Universe (e.g. Lin et al., 2003). The baryon deficiency in less massive haloes is not unexpected in the sense that the aforementioned supernova feedback can in

principle blow gas away more easily in smaller haloes (Dekel & Silk, 1986). For example, some semi-analytic models were successful at matching the low-end luminosity function by assuming that 20% – 60% of energy from supernova explosions is directly used to blow gas out/away (Benson et al., 2003; Khochfar et al., 2007). However, the question is how effective the explosion could be in reality, given that a large fraction of supernova energy is bound to be radiated away in the dense shell accumulated behind a shock (Thornton et al., 1998).

On smaller scales, there has also been some discrepancy between theory and observation. Whereas dark matter-only simulations predict that a halo with $\sim 10^{12} M_{\odot}$ should possess $\sim 300$ small haloes with $V_{\rm c} \gtrsim 20\,{\rm km\ s^{-1}}$ (Moore et al., 1999; Klypin et al., 1999), only about 60 satellites are observed in the local group (e.g. Simon & Geha, 2007). Using several semi-analytic models, Macciò et al. (2010) demonstrated that the interplay between reionisation by cosmic UV background radiation and supernova feedback may solve the missing satellite problem, matching the luminosity function in the range $-2 \leq M_V \leq -17$. Although recent high-resolution cosmological simulations could not confirm these results (Wadepuhl & Springel, 2011; Geen et al., 2012), the key to success in reproducing the observed luminosity function of the satellites again appears to lie in effective feedback processes.

Feedback is now central to understanding the formation of galaxies in the hierarchical paradigm. However, it should be emphasised that the basic framework of structure formation remains very similar to what it was three decades ago. The growth of the dark matter halo or acquisition of angular momentum can still be understood in the context of density perturbations growing in an expanding universe, as laid out by ΛCDM cosmology. This linear perturbation theory gives much insight into how the bottom-up picture arises, allowing us to predict gross features of the evolution of the universe. In this chapter, we present the important basic framework of galaxy formation before discussing numerical techniques and results from cosmological hydrodynamic simulations. Feedback processes will be described and discussed in detail in Chapter 2 and 5.

## 1.1 Cosmology

In 1929, Edwin Hubble found a linear correlation between the distances to galaxies and their receding velocities (Hubble, 1929), which is evidence of an expanding universe (Lemaître, 1927). This suggested that the Universe was once smaller and hotter. The observation of the nearly perfect blackbody spectrum by the Cosmic Background Explorer (COBE) supported the theory that the early Universe was hot and opaque. The abundances of deuterium, helium, and lithium processed in the hot universe lend further

support to the hot Big Bang model.

According to the standard hot Big Bang model, the inflationary expansion of the Universe occurs at $10^{-36} < t < 10^{-32}\,s$, making the Universe homogeneous and flat. When the temperature of the Universe decreases to $T \sim 3 \times 10^{12}\,K$ ($t \sim 10^{-5}\,s$), hadrons, such as protons and neutrons, are created. At this point, neutrons and protons are in equilibrium through interactions with electrons, positrons, and neutrinos. As the particles decouple around $t \sim 1\,s$ when the temperature drops to $10^{10}\,K$, light elements (deuterium, helium, beryllium, and lithium) are synthesised until about 20 minutes after the Big Bang. From then on, the Universe expands adiabatically until 380 000 years when the temperature of the Universe becomes so low ($T \sim 3000\,K$) that photons can no longer photo-dissociate hydrogen atoms and begin moving around freely. This important epoch is called the recombination era ($z \sim 1100$).

The dynamics of the Universe can be described with the Friedmann equation, which is a solution of the Einstein's field equation of general relativity for the Friedmann-Lemaître-Robertson-Walker metric,

$$H^2(t) \equiv \left(\frac{\dot{a}}{a}\right)^2 = \frac{8\pi G}{3}\rho - \frac{k}{a^2} + \frac{\Lambda}{3}, \tag{1.1}$$

where $H(t)$ is the Hubble parameter, and the scale factor ($a$) represents the expansion of the Universe by mapping the comoving coordinate ($\mathbf{x}$) to the physical coordinate ($\mathbf{r}$) as $\mathbf{r}(t) = a(t)\mathbf{x}$. The first term in Equation 1.1 includes the contribution from the matter density ($\rho_m$) and the radiation density ($\rho_r$), which scales as $a^{-3}$ and $a^{-4}$, respectively. The exponent -3 comes from mass conservation during the expansion, while an additional factor is required for the radiation, because waves propagating in an expanding universe are stretched. The second term is associated with the geometry of the universe, with $k > 0$ meaning a closed space. Observations of the cosmic microwave background radiation (e.g. Dunkley et al., 2009) suggest that the Universe is geometrically flat ($k = 0$). The last term was originally introduced to prevent stars from falling into Earth, but it is now widely accepted as a term accounting for the existence of "dark energy", which acts as a repelling force, contrary to the gravitational attraction exerted by conventional energy sources. As the universe expands, waves emitted at $\lambda_{\rm em}$ are redshifted and observed at $\lambda_{\rm obs}$. This defines the redshift ($z$)

$$z \equiv \frac{\lambda_{\rm obs}}{\lambda_{\rm em}} - 1 = \frac{a_0}{a} - 1.$$

Equation 1.1 gives another interesting scale, called the critical density ($\rho_c$), by setting $k = 0$ and $\Lambda = 0$

$$\rho_c(t) = \frac{3H^2(t)}{8\pi G}.$$

Equation 1.1 can then be written as

$$H^2(t) = \left(\frac{\dot{a}}{a}\right)^2 = H_0^2 \left[\frac{\Omega_{\mathrm{m},0}}{a^3(t)} + \frac{\Omega_{\mathrm{r},0}}{a^4(t)} - \frac{\Omega_k}{a^2(t)} + \Omega_\Lambda\right],$$

where $\Omega_{\mathrm{m},0} = \rho_{\mathrm{m},0}/\rho_{c,0}$, $\Omega_{\mathrm{r},0} = \rho_{\mathrm{r},0}/\rho_{c,0}$, and $\Omega_k = H_0^2/k$. A subscript $0$ denotes quantities at present. This means that radiation is the most important form of energy in the early Universe, whereas matter governs the dynamics of the later Universe. Finally, dark energy plays a major role, as the contributions from radiation and matter become less significant.

Since the decay rates of matter and radiation are different, there exists a special moment at which radiation and matter density become equal. This is called the epoch of matter-radiation equality

$$1 + z_{\mathrm{eq}} = \frac{\Omega_{\mathrm{m},0}}{\Omega_{\mathrm{r},0}} = 2.4 \times 10^4\, \Omega_{m,0} h^2.$$

After this epoch, matter begins to dominate over radiation, and thus density fluctuations (at sub-horizon scales) begin to grow.

It is also interesting to evaluate how the Universe evolves at certain epochs. In the radiation-dominated era, the Universe expands as

$$a = \left(\frac{32\pi G \rho_{\mathrm{r},0}}{3}\right)^{1/4} t^{1/2}.$$

On the other hand, in the matter-dominated era, the expansion becomes

$$a = \left(\frac{3H_0}{2} t\right)^{2/3}. \tag{1.2}$$

The last equation is also called the solution for an Einstein-de Sitter universe.

## 1.2 Structure formation

### 1.2.1 Linear perturbation theory

As a result of inflation, the Universe is thought to have become nearly homogenous, apart from the existence of small density perturbations, which are frozen out after the mass-radiation equality. The fluctuations are usually expressed in terms of density contrast $\delta(\mathbf{x}, t)$

$$\rho(\mathbf{x}, t) = \bar{\rho}_{\rm m}(t)\,[1 + \delta(\mathbf{x}, t)], \tag{1.3}$$

where $\bar{\rho}_{\rm m}$ is the background matter density of the universe.

The perturbed motion of the density field can be described with the linearised Euler equations as

$$\begin{aligned} &\frac{\partial \delta}{\partial t} + \frac{1}{a}\vec{\nabla}\cdot\mathbf{v} = 0 \\ &\frac{\partial \mathbf{v}}{\partial t} + \frac{\dot{a}}{a}\mathbf{v} = -\frac{1}{a}\vec{\nabla}\phi \\ &\nabla^2\phi = 4\pi G\bar{\rho}a^2\delta. \end{aligned} \tag{1.4}$$

where $\phi \equiv \Phi - 2\pi G\bar{\rho}a^2x^2/3$. By taking the divergence of the second equation and replacing the potential term from the third equation, one can get the perturbation equation

$$\frac{\partial^2\delta}{\partial t^2} + 2\frac{\dot{a}}{a}\frac{\partial\delta}{\partial t} = \frac{3}{2}\Omega_{\rm m,0}H_0^2\frac{\delta}{a^3}. \tag{1.5}$$

A general solution of the equation in an Einstein-de Sitter universe includes one decaying ($D_-$) and one growing mode ($D_+$)

$$\delta = A(\mathbf{x})D_+(t) + B(\mathbf{x})D_-(t).$$

Here $D(t)$ is called the growth factor, and the growing mode solution is

$$D_+ \propto t^{2/3} \propto a.$$

Thus, perturbations grow in proportion to the scale factor in an Einstein-de Sitter universe. In a similar manner, it can be shown that the growth factor is proportional to $a^2$ in the radiation-dominated era. For

$\Omega_m \neq 1$, the growth factor is

$$D(z) = \frac{5\Omega_{\mathrm{m},0}H_0^2}{2}H(z)\int_z^\infty \frac{1+z'}{H^3(z')}dz'.$$

Note that the growth of perturbations is slower than in the Einstein-de Sitter universe, because the universe expands more rapidly in this case.

### 1.2.2 Power spectrum and transfer function

The existence of the cosmic web and the solar system means that there must have been some initial density perturbations originating from quantum fluctuations during inflation. These perturbations are, to a large extent Gaussian distributed, allowing us to handle their evolution using Fourier modes.

The Fourier transform of the over-density is written as

$$\delta(\mathbf{x},t) = \frac{V}{(2\pi)^3}\int \delta(\mathbf{k},t)\ \exp(i\mathbf{k}\cdot\mathbf{x})d\mathbf{k}$$
$$\delta(\mathbf{k},t) = \frac{1}{V}\int \delta(\mathbf{x},t)\ \exp(-i\mathbf{k}\cdot\mathbf{x})d\mathbf{x}.$$

For Gaussian random fields, an ensemble average of the real-space over-density is $\langle\delta_{\mathbf{x}}\rangle = 0$, and each Fourier mode is independent. The beauty of Gaussian fields is that their statistical properties can be characterised without loss of information by a power spectrum, which, in the case of the inflation induced fluctuations, can be expressed in power-law form

$$P(k) \equiv \left\langle|\delta(k)|^2\right\rangle = A\,k^{n_s}. \tag{1.6}$$

A spectrum with index $n_s = 1$ is called Harrison-Zeldovich, and yields scale-invariant fluctuations in the gravitational potential ($\delta\Phi \propto k^{[n-1]/2}$). The primordial spectrum, $P_i(k)$, can change over time due to several reasons. First, during the radiation-dominated era, matter fluctuations are tied to radiation, and hence the sub-horizon perturbations do not grow while super-horizon fluctuations can grow as $\delta \propto a^2$. This means that fluctuations on small scales ($k \gg k_{\mathrm{eq}} = 2\pi/\lambda_{\mathrm{eq}}$) will enter the horizon first, and be frozen thereafter until matter governs the dynamics of the universe. Here $\lambda_{\mathrm{eq}}$ is the comoving scale of the horizon at the epoch of matter-radiation equality. Second, during the recombination era, free photons diffused from hot, dense regions are able to damp density and temperature fluctuations on small scales (Silk damping). These kinds of change in the spectrum are subsumed in a function, called the transfer

function $T(k)$, defined as

$$P(k) = P_i(k)\, T^2(k).$$

Note that since perturbations on the super-horizon scale grow with the expansion of the universe, the shape of the primordial spectrum should be preserved on large scales ($T \simeq 1$ for $k \ll k_{\rm eq}$). On the other hand, smaller perturbations cross the horizon earlier (in proportion to $a^2 \propto \lambda^2$) during radiation-dominated era, hence the growth of high frequency perturbations is preferentially modulated ($T \propto k^{-2}$). Thus, once $P_i(0)$ is known, the evolution of density perturbations can be determined by specifying the transfer function. The exact form of the transfer function depends on whether initial fluctuations are adiabatic ($\delta_m = \delta_\gamma$, e.g. Eisenstein & Hu 1998) or isocurvature ($\delta_m = -\delta_\gamma$).

### 1.2.3 Spherical collapse model

The collapse of an object can be determined by solving the Friedmann equation. Let us assume the existence of an over-dense sphere of radius $r$ in a flat universe. According to the Birkhoff's theorem, the over-dense region is subject to the gravity of the total mass inside the sphere, and therefore it is mathematically the same as a closed universe. A solution in this case is given by a parametric form of

$$r = A(1 - \cos\theta) \approx A\left(\frac{\theta^2}{2} - \frac{\theta^4}{24}\right)$$
$$t = B(\theta - \sin\theta) \approx B\left(\frac{\theta^3}{6} - \frac{\theta^5}{120}\right),$$

where

$$A = \frac{3}{10}\frac{r_i}{\delta_i} \quad ; \quad B = \frac{1}{2H_0\Omega_{\rm m,0}^{1/2}}\left(\frac{3a_i}{5\delta_i}\right)^{2/3}.$$

There are two special moments, $\theta = \pi$ and $\theta = 2\pi$. The former indicates the moment at which the radius of the sphere is maximal and begins to shrink. This turnover radius is $r_{\rm max} = 2A$. In the latter case, the radius goes to zero, and hence it represents the collapse of the sphere. The evolution of the sphere is then

$$a = \left(\frac{3}{4}\right)^{2/3}\left(\frac{3a_i}{5\delta_i}\right)(\theta - \sin\theta)^{2/3}$$

At the collapsing point ($\theta = 2\pi$), the above equation becomes

$$a_{\rm coll} \simeq 1.686\frac{a_i}{\delta_i}.$$

This means that a sphere would collapse to a point when $\delta_{\rm coll} = 1.686$.

In reality, particles do not accumulate at the centre, but instead reach virial equilibrium. Using the virial theorem $E = W/2$, where $W$ and $K$ are the potential and kinetic energy, we can find $\theta$ that satisfies $W(r_{\rm max}) = W(r_{\rm vir})/2$. This occurs when $2r_{\rm vir} = r_{\rm max}$, and therefore $\theta = 3\pi/2$. At this point, the density of the sphere with respect to the background density at which the collapse occurs ($t = 2t_{\rm max}$) is

$$\frac{\rho(\theta = 3\pi/2)}{\bar{\rho}(\theta = 2\pi)} = \frac{\rho(t_{\rm max})}{\bar{\rho}(t_{\rm max})}\frac{\bar{\rho}(t_{\rm max})}{\bar{\rho}(2t_{\rm max})}\left(\frac{r_{\rm max}}{r_{\rm vir}}\right)^3 = 18\pi^2 \simeq 178.$$

Thus, for $\Omega_{\rm m,0} = 1$, the virial density contrast is $\Delta_{\rm vir} \equiv 1 - \rho_{\rm vir}/\bar{\rho} \simeq 177$. For a non-zero cosmological constant, the virial theorem should take the energy from the dark energy into account ($K = -W/2 + W_\Lambda$). A useful approximation for a flat universe with a non-zero cosmological constant is

$$\Delta_{\rm vir} \approx (18\pi^2 + 82x - 39x^2)$$

where $x \equiv \Omega(z) - 1$ and $\Omega(z) \equiv \Omega_0(1+z)^3/[\Omega_0(1+z)^3 + \Omega_\Lambda]$ (Bryan & Norman, 1998).

### 1.2.4 Press-Schechter Theory

Press & Schechter (1974) investigated how Gaussian random fields evolve in the linear regime and form structures by considering an over-dense cloud of mass $M$, smoothed on a scale $R$

$$M(\mathbf{r}) = \int \rho(\mathbf{x})\, W(\mathbf{x} + \mathbf{r}; R) d^3\mathbf{x},$$

where $W(\mathbf{r}; R)$ is a window function that sharply decreases at $r \geq R$. The smoothed Gaussian random fields are generally described by[1]

$$p(\delta)d\delta = \frac{1}{\sqrt{2\pi}\sigma_M}\exp\left[-\frac{\delta^2}{2\sigma_M^2}\right]d\delta,$$

where the variance in mass ($\sigma_M$) is

$$\sigma_M^2 \equiv \left\langle |\delta_W(\mathbf{x})|^2 \right\rangle = \frac{1}{2\pi^2}\int P(k)\hat{W}^2(kR)k^2 dk.$$

[1]Rigorously speaking, only a Gaussian random field smoothed with a sharp $k$-space filter is truly Gaussian (Bond et al., 1991; Lacey & Cole, 1993), because the phases of two different $k$ modes remain uncorrelated . This is not the case for Gaussian or spatial top-hat filters which have wings that extend to infinitely large $k$ modes.

Here $\hat{W}$ is the Fourier transform of the window function $W$. Note that the variance is associated with the mass of dark matter haloes through the filtering scale $R$. It is also worth noting that the variance at $R = 8\,h^{-1}\,\mathrm{Mpc}$, $\sigma_8$, can be used to find the normalisation factor $A$ in Equation 1.6.

Integrating the fluctuations from $\delta_{\rm coll}(t)$ to infinity, we have the total fraction in haloes with $M$

$$f = \frac{1}{\sqrt{2\pi}\sigma_M}\int_{\delta_{\rm coll}(t)}^{\infty}\exp\left(-\frac{\delta^2}{2\sigma_M^2}\right)d\delta = \frac{1}{2}\mathrm{erfc}\left(\frac{\nu}{\sqrt{2}}\right)$$

where $\delta_{\rm coll}(t) = \delta_{\rm coll}/D(t)$ and $\nu \equiv \delta_{\rm coll}(t)/\sigma_M$. However, a critical limitation of this linear evolution is that initially underdense regions remain underdense and never collapse. As a result, $f \to 0.5$ even when $\sigma_M \to \infty$, or equivalently $M \to 0$. In reality, underdense regions can collapse, because they are generally gravitationally bound to overdense ones. Press & Schechter (1974) realised the problem, and arbitrarily introduced a factor 2. The differential number density of haloes can then be written as

$$\frac{dn}{d\ln M} = 2\frac{\bar{\rho}_m}{M}\frac{\partial f}{\partial \ln M} = \sqrt{\frac{2}{\pi}}\frac{\bar{\rho}_m}{M}\frac{d\ln\sigma^{-1}}{d\ln M}\nu\exp(-\nu^2/2).$$

Since $\delta_{\rm coll}(t)$ increases with time and $\sigma_M$ decreases with $M$ in a ΛCDM universe, this equation implies that more massive haloes form at later epochs.

### 1.2.5 Acquisition of angular momentum

In the early universe when density fluctuations are sufficiently small, their growth can be written as $\delta(\mathbf{x}, a) = D(a)\,\delta(\mathbf{q})$, where $\mathbf{q} = \mathbf{x}(t_0)$ is the position in comoving coordinates at some initial time ($t_0$). It then follows from Equation 1.4 that $\phi(\mathbf{x}, a) = D\phi(\mathbf{q})/a$. Thus, to first order, once the initial density field is specified, it is possible to predict the displacement of particles from their initial positions (Zel'dovich, 1970), as

$$\begin{aligned}\mathbf{v} &= -\frac{\dot{D}}{4\pi G\bar{\rho}(t)a^2}\nabla\phi(\mathbf{q}) = a\,\dot{b}\,\nabla\phi(\mathbf{q})\\ \mathbf{x} &= \mathbf{q} - \frac{D}{4\pi G\bar{\rho}a^3}\nabla\phi(\mathbf{q}) = \mathbf{q} - b\,\nabla\phi(\mathbf{q}).\end{aligned} \tag{1.7}$$

Here $b(t)(= D(t)/4\pi G\bar{\rho}a^3)$ can be thought as a perturbation parameter that depends on $D(t)$.

The evolution of cosmic angular momentum can then be described based on the Zel'dovich approximation (Peebles, 1969; Doroshkevich, 1970; White, 1984). We follow the derivation presented in White (1984), and consider a lump of matter with mass ($dm = \bar{\rho}_{\rm m}a^3d^3\mathbf{x}(t = t_0)$) in a Lagrangian volume ($V_L$)

at some initial time. By definition, angular momentum is a cross product of a peculiar velocity ($\mathbf{v}$) and a vector ($a\mathbf{x} - a\bar{\mathbf{x}}$), where $\bar{\mathbf{x}}$ is the barycentre of the lump. The angular momentum is then

$$\mathbf{J} = \int_{V_L} d^3\mathbf{q}\, \bar{\rho}_{\rm m} a^3 \, (a\mathbf{x} - a\bar{\mathbf{x}}) \times \mathbf{v} \tag{1.8}$$

$$J_i \approx -a^2 \dot{b}\, \varepsilon_{ijk}\, T_{jl}\, I_{lk}, \tag{1.9}$$

where $\varepsilon_{ijk}$ is the Levi-Civita symbol, and the tidal tensor, $T_{\rm jl}$, and the inertia tensor, $I_{lk}$, are defined as

$$T_{jl} \equiv \left.\frac{\partial^2 \phi}{\partial q_j \partial q_l}\right|_{\bar{\mathbf{q}}} \quad ; \quad I_{lk} \equiv \int_{V_L} dq^3 \bar{\rho}_{\rm m} a^3 (q_l - \bar{q}_l)(q_k - \bar{q}_k).$$

Note that no angular momentum would be generated if the tidal tensor has the same form as the inertia tensor. Note also that the angular momentum stops growing once the matter is detached from the expansion of the universe. In an Einstein-de Sitter universe, the growth factor is proportional to the scale factor, and hence $J \propto a^2 \dot{D} \propto t$. However, since the growth of angular momentum is based on the linear perturbation theory, this approximation may not be valid after shell crossings occur. As pointed out by Vitvitska et al. (2002); Maller et al. (2002), galaxy mergers may play an important role in the acquisition of angular momentum in the non-linear regime.

## 1.3 The structure of this thesis

This thesis presents new advances on the impact of cold flows and feedback on galaxy formation and evolution. For this purpose, I use an Eulerian hydrodynamic code, called RAMSES. Chapter 2 briefly describes numerical methods to solve the Euler-Poisson equations, and gives details of the baryonic physics included in the code, such as star formation and feedback from active galactic nuclei. Using a large-volume cosmological simulation, Chapter 3 discusses the detectability of cold flows based on low-ionisation metal absorption lines. The chapter also gives statistical results of the covering fraction of dense gas, which stimulated the discussion on why cold filaments are not observed. The existence of such cold flows was not expected in the classical galaxy formation theory, and thus Chapter 4 revisits the growth of cosmic angular momentum of baryons, and explains how cold flows change our view on the acquisition of cosmic angular momentum. In Chapter 5, I describe a new implementation of more realistic stellar feedback, based on STARBURST99, and study its impact using isolated galaxy simulations that mimic a high-redshift clumpy galaxy disc. Using simulations of unprecedented resolution, I also

investigate the formation of disc galaxies in a ΛCDM cosmology. Chapter 6 presents the impact of AGN feedback on the stellar assembly of galaxies by comparing hydrodynamic simulations to rest-frame $UV$-optical colours from the Wide Field Camera 3 (WFC3) Early-Release Science. Finally, I summarise the main results and conclusions of this thesis in Chapter 7, along with a future outlook on this research field.

# Chapter 2

# Numerical Method: RAMSES

In the standard ΛCDM cosmology, massive galaxies emerge at the intersection of filamentary structures as gas radiatively cools and form stars. These galaxies undergo violent, non-linear processes, such as mergers and feedback from stars or super-massive black holes. These processes are difficult to depict analytically, hence numerical simulations are the tool of choice to study the formation of galaxies.

These numerical tools are generally divided into two categories depending on which technique is used to solve the Fluid equations.

**Lagrangian** : Hydrodynamical information is tagged on gas particles moving with the flow. The gas particle is represented as a massive particle spread in space, using a spline kernel (e.g. Monaghan, 1992). This is called Smoothed-Particle Hydrodynamics (SPH). An advantage of this method is that some important physical quantities, such as mass, are conserved by construction.

**Eulerian**: The Euler equations are solved on a fixed grid. In this scheme, gas is represented as fluid cells, and the fluid quantities are updated by computing fluxes at the cell interfaces. Specifically designed hydro solvers allow for better capturing of complex instabilities and discontinuities than the standard SPH method (Agertz et al., 2007; Mitchell et al., 2009).

The work in this thesis is based on an Eulerian code, RAMSES (Teyssier, 2002), that uses Cartesian adaptive mesh refinement (AMR). It is massively parallelised with MPI to compute the gravity, hydrodynamics, and magnetic fields on supercomputers. The code is composed of two parts: one for gravity, and the other for hydrodynamics. We describe the key elements of the code in this chapter.

## 2.1 Gravitational force calculations

Despite the fact that billions of stars are in orbit in a galaxy, they are hardly collisional because of their small cross-sections. This is also true for dark matter particles which are assumed to interact only through gravity. Thus, N-body simulations describe the motion of individual particles under the effect of the gravitational force only. Essentially, their common objective is to solve the following equation of motion for each particle

$$\frac{\mathrm{d}\vec{\mathbf{x}}_p}{\mathrm{d}t} = \vec{\mathbf{v}}_p$$
$$\frac{\mathrm{d}\vec{\mathbf{v}}_p}{\mathrm{d}t} = -\vec{\nabla}\Phi,$$

where $\vec{\mathbf{x}}$, $\vec{\mathbf{v}}$, and $\Phi$ are the position, velocity, and gravitational potential, respectively. The most straightforward approach is to calculate the force on each particle by direct summation. This is called the Particle-Particle (PP) method, in which the inter-particle force is calculated as

$$\vec{\mathbf{F}}_{ij} = \sum_{j \neq i} \frac{G\, m_i\, m_j\, (\vec{\mathbf{x}}_j - \vec{\mathbf{x}}_i)}{\left(|\vec{\mathbf{x}}_j - \vec{\mathbf{x}}_i|^2 + \epsilon^2_{\mathrm{soft}}\right)^{3/2}}.$$

Here a softening length, $\epsilon_{\mathrm{soft}}$, is introduced to avoid the singularity which arises when two particles encounter. This pairwise operation is proportional to $N^2$, and thus computationally very costly. Barnes & Hut (1986) realised this problem, and developed a more elegant way of computing the force based on the multipole expansion. Specifically, particles are grouped first, and the force exerted by each group is approximated by a point mass plus an additional term due to the distribution of particles inside each group. The use of the tree code allows to significantly reduce the number of operations ($\sim N \log N$).

While the aforementioned methods rely on a direct force calculation for the interactions, Particle-Mesh (PM) algorithms make use of the fact that the gradient of the gravitational field is the force field (i.e. $\vec{\mathbf{F}} = -\nabla\Phi$). The crucial part of this algorithm is therefore to evaluate the gravitational potential ($\Phi$), which can be done quickly using a Fast Fourier Transform (FFT). However, this method cannot capture short-range forces accurately due to the finite size of the grid it employs to compute the potential. Thus, it is sometimes preferred to calculate the short-range force separately while evaluating the long-range force with the particle-mesh method. This particular type of force computation is called the Particle-Particle-Particle-Mesh ($\mathrm{P^3M}$) algorithm.

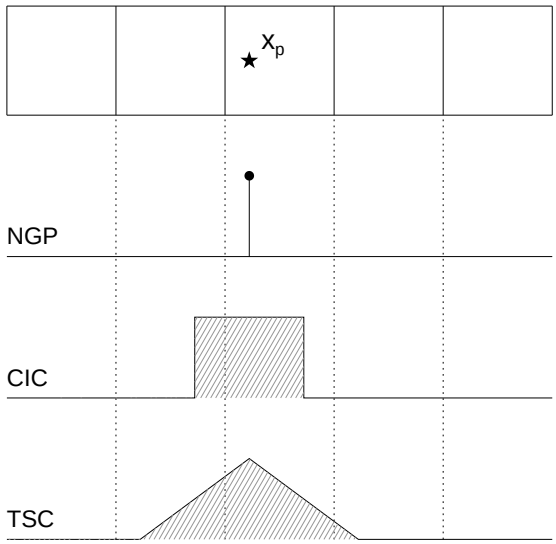


Figure 2.1: Illustration of three different ways of density assignment: the nearest grid point (NGP), cloud-in-cell (CIC), and triangular shape cloud (TSC). A star represents a particle at $x = x_p$.

### 2.1.1 Particle-Mesh method

RAMSES uses an adaptive PM method in which the grids are non-uniform, but locally refined in space. In practice, the gravitational force is computed as follows.

1. compute the density field by assigning particles to grid cells
2. evaluate the gravitational potential from the density field by solving the Poisson equation
3. evaluate the force acting on each particle by interpolating the force defined on the grid
4. update the velocity and position of the particles

More specifically, the first step is to convert a distribution of particles into a dicreet density field, as

$$\rho_i = \frac{1}{\Delta x^3} \sum_{p=1}^{N_p} m_p W(x) W(y) W(z).$$

Here $W$ is the assignment function that depends on a cloud shape function ($\mathcal{S}$), as

$$W(x) = \int_{x_i - \Delta x/2}^{x_i + \Delta x/2} \mathcal{S}(x_p - x) dx.$$

The simplest way to assign particles to grid cells is the nearest grid point (NGP) method (Fig. 2.1), where the cloud shape is the Dirac delta function. However, in this case, the gravitational potential may have

significant discontinuities if the number of particles in a region is small. A better approximation for the inter-particle force is thus to spread the particles over several nearby grid cells. For example, the Cloud-in-Cell (CIC) scheme, which is what RAMSES uses, spreads the mass of particles uniformly across the nearest cells (Fig. 2.1), and the corresponding assignment function is

$$W(x-x_p) = \begin{cases} 1-|x-x_p|/\Delta x & |x-x_p| \le \Delta x \\ 0 & \text{otherwise} \end{cases}.$$

Further improvement (at the expense of CPU time) can be made by using the higher-order triangular shape cloud (TSC), defined as

$$W(x-x_p) = \begin{cases} \frac{3}{4} - |x-x_p|^2/(\Delta x)^2 & |x-x_p| \le \frac{1}{2}\Delta x \\ \frac{1}{2}\left(\frac{3}{2} - |x-x_p|/\Delta x)^2\right) & \frac{1}{2}\Delta x < |x-x_p| \le \frac{3}{2}\Delta x \\ 0 & \text{otherwise.} \end{cases}$$

Once the density distribution is computed, the gravitational potential can be readily obtained by solving the Poisson equation

$$\nabla^2\Phi = 4\pi G\rho.$$

This partial differential equation can be solved by at least three different methods: mesh-relaxation, matrix inversion, and rapid elliptic solvers (Hockney & Eastwood, 1988). The FFT method is a representative example of rapid elliptic solvers, but its requirement of a uniform grid is not suitable for the codes like RAMSES where the size of grid cells varies in space. A popular alternative to FFT is mesh-relaxation methods, which are based on finite differencing on a mesh. The basic idea of these approaches is to solve the following diffusion equation iteratively,

$$\frac{\partial\Phi}{\partial\tau} = \nabla^2\Phi - 4\pi G\rho,$$

until a stable solution is found, i.e. $\partial\Phi/\partial\tau = 0$ (e.g. Bodenheimer et al., 2007), where $\tau$ is a pseudo-time. Expressing the above equation in a two dimensional differential form gives

$$\frac{\Phi^{m+1}_{i,j} - \Phi^m_{i,j}}{\Delta\tau} = \frac{\Phi^m_{i+1,j} + \Phi^m_{i-1,j} - 2\Phi^m_{i,j}}{(\Delta x)^2} + \frac{\Phi^m_{i,j+1} + \Phi^m_{i,j-1} - 2\Phi^m_{i,j}}{(\Delta y)^2} - 4\pi G\rho_{i,j}. \qquad (2.1)$$

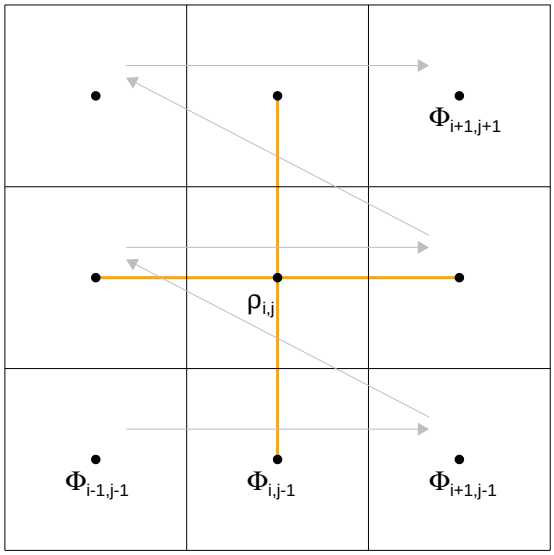


Figure 2.2: Example of the structure of a mesh. Note that a potential and density are defined at cell centres. Orange lines show the stencil of the 5-points finite difference method. Arrows indicate the ordering used in the illustration of the Conjugate Gradient Algorithm.

Note that $m$ indicates $m$-th iteration, not the time step. By arranging the terms, Equation 2.1 reads

$$\Phi_{i,j}^{m+1} = \Phi_{i,j}^{m}\left(1 - \frac{4\Delta\tau}{(\Delta x)^2}\right) + \frac{\Delta\tau}{(\Delta x)^2}\left[\Phi_{i+1,j}^{m} + \Phi_{i-1,j}^{m} + \Phi_{i,j+1}^{m} + \Phi_{i,j-1}^{m}\right] - 4\pi G\rho_{i,j}\Delta\tau.$$

The *Jacobi method* then adopts $\Delta\tau = (\Delta x)^2/4$, in which case the previous equation can be reduced to

$$\Phi_{i,j}^{m+1} = \frac{1}{4}\left[\Phi_{i+1,j}^{m} + \Phi_{i-1,j}^{m} + \Phi_{i,j+1}^{m} + \Phi_{i,j-1}^{m} - 4\pi G\rho_{i,j}(\Delta x)^2\right]. \tag{2.2}$$

While the Jacobi method only uses the potential evaluated at the $m$-th iteration, the *Gauss-Seidel (GS) method* takes advantage of the most recent ($m+1$-th) values of $\Phi$ at each grid point.

The use of the *Successive Over Relaxation* (SOR) in RAMSES further increases the speed of convergence by adopting a linear combination of $\Phi^m$ and $\Phi_{\rm inter}^{m+1}$ computed from the GS method. Here $\Phi_{\rm inter}^{m+1}$ is an intermediate potential, and an updated potential is calculated by imposing an over-relaxation parameter, $\omega$, with a suitable choice of value between 1 and 2, as

$$\Phi_{i,j}^{m+1} = \omega\Phi_{i,j,\rm inter}^{m+1} + (1-\omega)\Phi_{i,j}^{m}.$$

The optimal choice of $\omega$ for adaptive grids is rather complicated, but numerical experiments suggest (Teyssier, 2002; Press et al., 1992)

$$\omega \simeq \frac{2}{1 + \pi\alpha/\langle L \rangle}$$

where $\alpha = 1$ for Dirichlet boundary conditions and $\alpha = 2$ for periodic boundary conditions. $\langle L \rangle$ is the AMR patch size, which is found to be $\sim 20$ cells for cosmological simulations (Teyssier, 2002).

In practice, meshes are not equally spaced in RAMSES, and information may propagate slowly due to the local structure of a stencil in the case of GS or SOR methods. The *Multigrid* method overcomes these difficulties by solving the discrete Poisson equation in sequence, starting from the finest all the way to the coarsest grid.

Let $\Phi_{i,j}$ be the approximate solution and $\Phi_{i,j}^{\rm exact}$ the exact solution, and define two variables, *error* ($\mathcal{E}$) and *residual* ($\mathcal{R}$) as

$$\begin{aligned} \mathcal{E} &\equiv \Phi - \Phi^{\rm exact} \\ \mathcal{R} &\equiv \nabla^2\Phi - 4\pi G\rho. \end{aligned} \tag{2.3}$$

Note that applying the Laplacian to the error yields the same form as the Poisson equation.

$$\nabla^2\mathcal{E} = \mathcal{R} - \left(\nabla^2\Phi^{\rm exact} - 4\pi G\rho\right) = \mathcal{R}. \tag{2.4}$$

The multigrid algorithm then takes advantage of the GS or SOR methods which can reduce errors in high frequency modes (i.e. short wavelength errors) because of the finite resolution of the grid. Low frequency errors are minimised by correcting the high resolution potential based on its coarse grid evaluation. The actual steps of $V$-cycle algorithm are

1. Pre-relaxation: perform a few ($\sim 3$) iterations using the GS or SOR method
2. Restriction: compute the residual by solving Equation 2.3, and restrict the residual to the coarser grid, $\mathcal{R}_l \rightarrow \mathcal{R}_{l-1}$
3. Recursive call: perform 1 – 2 recursively until you reach stability on the coarsest grid
4. Poisson equation: solve Equation 2.4 on the coarsest grid
5. Prolongation: prolong the correction to the finer level, $\mathcal{E}_{l-1}^{\rm exact} \rightarrow \mathcal{E}_l^{m+1}$
6. Correction: correct the potential on the finer level based on the error, $\Phi_l^{m+1} = \Phi_l^m + \mathcal{E}_l^{m+1}$

7. Post-relaxation: perform a few GS or SOR iterations.

If the exact Poisson equation is solved twice per iteration, it is called a $W$-cycle. RAMSES adopts the latter method to obtain the gravitational force on the coarse grids, whereas the Conjugate-Gradient Algorithm (CGA, Hockney & Eastwood 1988) is employed to compute the force on fine level grids.

CGA is an example of the matrix inversion method to solve a set of linear equations, such as 2.2. Given a linear system

$$\mathcal{A}\,\Phi = \rho$$

or in matrix form for a $3 \times 3$ two-dimensional mesh using Equation 2.2 (Fig. 2.2)

$$\begin{bmatrix}
4 & 1 & & -1 & & & & & \\
1 & 4 & 1 & & 1 & & & & \\
 & 1 & 4 & 1 & & -1 & & & \\
-1 & & 1 & 4 & 1 & & -1 & & \\
 & -1 & & 1 & 4 & 1 & & -1 & \\
 & & -1 & & 1 & 4 & 1 & & -1 \\
 & & & -1 & & 1 & 4 & 1 & \\
 & & & & -1 & & 1 & 4 & 1 \\
 & & & & & -1 & & 1 & 4
\end{bmatrix} \otimes \begin{bmatrix} \Phi_{1,1} \\ \Phi_{2,1} \\ \Phi_{3,1} \\ \Phi_{1,2} \\ \Phi_{2,2} \\ \Phi_{3,2} \\ \Phi_{1,3} \\ \Phi_{2,3} \\ \Phi_{3,3} \end{bmatrix} = \begin{bmatrix} \rho_{1,1} \\ \rho_{2,1} \\ \rho_{3,1} \\ \rho_{1,2} \\ \rho_{2,2} \\ \rho_{3,2} \\ \rho_{1,3} \\ \rho_{2,3} \\ \rho_{3,3} \end{bmatrix}$$

one can define a quadratic function, $\mathcal{V}$, such that

$$\begin{aligned}
\frac{\partial \mathcal{V}}{\partial \Phi} &= \frac{1}{2}\Phi^{\mathrm{T}}\mathcal{A}\Phi - \rho^{\mathrm{T}}\Phi \\
\frac{\partial^2 \mathcal{V}}{\partial \Phi^2} &= \mathcal{A}\,\Phi - \rho = \mathcal{R}
\end{aligned} \tag{2.5}$$

where $\mathcal{R}$ is a residual. The last equality indicates that finding the minimum of $\mathcal{V}$ corresponds to finding the best approximate of the potential. Amongst the methods to find this minimum is the method of steepest descent, but the Conjugate gradient method gives an even faster convergence by combining prior knowledge $(m-1)$ of the descent with the descent from the $m$-th iteration.

Once the potential has been obtained, the acceleration at grid points can be calculated using a 5-point finite difference scheme (e.g. Equation 2.2). Finally, the actual force acting on each particle can be

computed by interpolating the mesh-defined force at the particle position, as

$$\vec{\mathbf{F}}(\vec{\mathbf{x}}_p) = m_p \sum_i W(\vec{\mathbf{x}}_p - \vec{\mathbf{x}}_i)\, \vec{\mathbf{F}}_i.$$

## 2.2 Hydrodynamics

### 2.2.1 Euler equations

Unlike collision-less dark matter particles, fluid elements are compressible and subject to a pressure force. The motion of such fluid elements can be described by the Navier-Stokes equations:[1]

$$\frac{\partial \rho}{\partial t} + \vec{\nabla} \cdot (\rho \vec{u}) = 0 \tag{2.6}$$

$$\frac{\partial (\rho \vec{u})}{\partial t} + \vec{\nabla} \cdot (\rho \vec{u} \otimes \vec{u}) = -\vec{\nabla} P + \vec{\nabla} \cdot \vec{\sigma} - \rho \vec{\nabla} \Phi_{\rm g} \tag{2.7}$$

$$\frac{\partial E}{\partial t} + \vec{\nabla} (\vec{u}\,[E + P]) = \vec{\sigma} \cdot \vec{\nabla} u, \tag{2.8}$$

where $\rho$, $u$, $P$, $\sigma$ and $\Phi_{\rm g}$ represent the density, stream velocity, pressure, viscous stress and gravitational potential, respectively. The total energy ($E$) per unit volume can be split into internal and kinetic energy, such that

$$E = E_{\rm int} + E_{\rm kin} = \frac{P}{\gamma - 1} + \frac{1}{2} \rho u^2,$$

where $\gamma$ is the adiabatic index that depends on the composition and state of gas. For example, an ideal atomic gas is characterised by $\gamma = 5/3$. Note that Equations 2.6 – 2.8 are the natural corollary of the mass, momentum, and energy conservation.

In general, astrophysical fluids are turbulent, in which case viscosity becomes negligible ($\sigma \to 0$), and the Navier-Stokes equations are reduced to the Euler equations. Moreover, stars and active galactic nuclei generate energy, while gas can radiatively cool via various atomic processes. The Euler equations then becomes

$$\frac{\partial \rho}{\partial t} + \frac{\partial}{\partial x_j} (\rho u_j) = 0 \tag{2.9}$$

$$\frac{\partial (\rho u_i)}{\partial t} + \frac{\partial}{\partial x_j} (\rho u_i u_j) = -\frac{\partial P}{\partial x_i} - \rho \frac{\partial \Phi_{\rm g}}{\partial x_i} \tag{2.10}$$

$$\frac{\partial E}{\partial t} + \frac{\partial}{\partial x_j} (E u_j) = -P \frac{\partial u_j}{\partial x_j} + \mathcal{H} - \mathcal{C}, \tag{2.11}$$

[1] When viscosity is ignored, the equations are called the Euler equations

where $\mathcal{H}$ and $\mathcal{C}$ represent a heating and cooling term, which are generally computed separately from the Euler equations. We follow the Einstein summation convention. In the absence of gravity, heating, and cooling, the previous equations can be written as generalised advection equations of the form

$$\frac{\partial \mathcal{Q}}{\partial t} + \frac{\partial \mathcal{F}}{\partial x} = 0, \tag{2.12}$$

where $\mathcal{Q} = (\rho, \rho u, E)$ and $\mathcal{F} = (\rho u, \rho u u + P, u\,[E + P])$ represent conservative variables and fluxes, respectively.

We can rewrite Equation 2.12 to highlight the physical meaning of the Euler equations, as

$$\frac{\partial}{\partial t}\begin{bmatrix} q_1 \\ q_2 \\ q_3 \end{bmatrix} + \frac{\partial}{\partial x}\begin{bmatrix} q_2 \\ (\gamma-1)\ q_3 + \left(\frac{3-\gamma}{2}\right)\frac{q_2^2}{q_1} \\ \gamma\frac{q_3\, q_2}{q_1} + \left(\frac{1-\gamma}{2}\right)\frac{q_2^3}{q_1^2} \end{bmatrix} = 0, \tag{2.13}$$

where $(q_1,\, q_2,\, q_3) = (\rho,\, \rho u,\, E)$. By using the chain rule $\frac{\partial \mathcal{F}}{\partial x} = \frac{\partial \mathcal{F}}{\partial \mathcal{Q}}\,\frac{\partial \mathcal{Q}}{\partial x}$, Equation 2.13 can be written as

$$\frac{\partial \mathcal{Q}}{\partial t} + A\frac{\partial \mathcal{Q}}{\partial x} = 0,$$

where $A$ is the Jacobian matrix

$$A = \begin{bmatrix} 0 & 1 & 0 \\ \frac{\gamma-3}{2}u^2 & (3-\gamma)u & \gamma-1 \\ -\frac{\gamma E u}{\rho} + (\gamma-1)u^3 & \frac{\gamma E}{\rho} - \frac{3(\gamma-1)u^2}{2} & \gamma u \end{bmatrix}.$$

The eigenvalues of this Jacobian matrix characterise the velocity of three signals that transmit hydrodynamical information, which we can write

$$\begin{pmatrix} \lambda_1 \\ \lambda_2 \\ \lambda_3 \end{pmatrix} = \begin{pmatrix} u - \sqrt{\frac{\gamma P}{\rho}} \\ u \\ u + \sqrt{\frac{\gamma P}{\rho}} \end{pmatrix}.$$

The middle term represents the motion of the fluid ($u$), and the first and third terms indicate sound waves propagating in a medium moving with $u$. Thus, the Euler equations can essentially be understood as the propagation of hydrodynamical waves.

### 2.2.2 Finite difference method for the advection of fluids

The simplest way to evaluate the basic advection equation, 2.12, is to utilise finite differencing. For illustrative purpose, let $u$ be constant. Equation 2.12 then becomes

$$\frac{\rho_i^{n+1} - \rho_i^n}{t^{n+1} - t^n} + u\frac{\rho_{i+1}^n - \rho_i^n}{\Delta x} = 0$$
$$\rho_i^{n+1} = \rho_i^n - u\Delta t\frac{\rho_{i+1}^n - \rho_i^n}{\Delta x},$$

where $n$ and $i$ represent a different time-step and spatial region, respectively. It is worth noting that Equation 2.1 is also an example of a finite difference method. Although such a numerical scheme is straightforward to apply in many circumstances, there are several critical caveats: 1) mass, velocity, and energy are not accurately conserved, 2) it is diffusive and incapable of sharply capturing discontinuities. The latter point can be problematic especially when dealing with astrophysical phenomena, which often involve shocks and other discontinuities.

### 2.2.3 Finite volume method for the advection of fluids

An entirely different idea based on the Riemann problem[2] was put forward by Godunov (1959), who used cell interfaces to compute the advection of fluids. The essence of this approach is to use the integral form of Equation 2.12 as

$$\iint \left(\nabla_t \, \mathcal{Q} + \nabla \cdot \mathcal{F}\right) \, dx \, dt = 0.$$

Using the divergence theorem, the above equation becomes (for the one-dimensional case)

$$\int_{x_{i-1/2}}^{x_{i+1/2}} \mathcal{Q}(x, t^{n+1}) \, dx = \int_{x_{i-1/2}}^{x_{i+1/2}} \mathcal{Q}(x, t^n) \, dx + \int_{t^n}^{t^{n+1}} \mathcal{F}\left(x_{i-1/2}, t\right) \, dt - \int_{t^n}^{t^{n+1}} \mathcal{F}\left(x_{i+1/2}, t\right) \, dt. \tag{2.14}$$

Since the flux leaving a cell corresponds to the incoming flux for the neighbouring cell, the integral formulation of the advection equation conserves the flux by construction. Note that computing the advection of the flux through cell interfaces is equivalent to solving a set of local Riemann problems. Equation 2.14 itself is not a numerical method, but when the third and fourth term are evaluated using piecewise constant states, it is called a Godunov scheme for hydrodynamics.

[2] A Riemann problem is an example of hyperbolic partial differential equations, defined by two adjacent cells having different density and pressure. A shock tube is a practical example of the Riemann problem.

For a uniform grid simulation, the time and space integration in Equation 2.14 can be replaced with $\Delta t$ and $\Delta x$, and hence

$$\mathcal{Q}_i^{n+1} = \mathcal{Q}_i^n - \frac{\Delta t}{\Delta x}\left(\mathcal{F}_{i+1/2} - \mathcal{F}_{i-1/2}\right). \tag{2.15}$$

Obtaining the last term, the flux difference, is the key to obtaining the solution for the Euler equations. Godunov (1959) suggests to use half-step fluxes, $\mathcal{F}_{i\pm1/2}$, which are computed using inter-cell Riemann solutions, $\mathcal{Q}_{i\pm1/2}$. The inter-cell Riemann problem is defined on the interval $x_i < x < x_{i+1}$ or $x_{i-1} < x < x_i$ and the simplest upwind scheme can be written as

$$\mathcal{Q}_{i+1/2} = \begin{cases} \mathcal{Q}_i^n & \text{if } u > 0 \\ \mathcal{Q}_{i+1}^n & \text{if } u < 0. \end{cases}$$

In this case, the Godunov flux is

$$\mathcal{F}_{i+1/2} = \begin{cases} u\,\mathcal{Q}_i^n & \text{if } u > 0 \\ u\,\mathcal{Q}_{i+1}^n & \text{if } u < 0, \end{cases}$$

and Equation 2.15 becomes

$$\mathcal{Q}_i^{n+1} = \mathcal{Q}_i^n - \frac{u\Delta t}{\Delta x}\left(\mathcal{Q}_i - \mathcal{Q}_{i-1}\right) \quad \text{if } u > 0. \tag{2.16}$$

There exists a variety of ways of determining the Godunov flux, $\mathcal{F}_{i+1/2}$. Among the popular choice is the HLL solver (Harten, Lax, & van Leer, 1983), which assumes that the two fastest waves propagate in opposite directions with velocities

$$S_L = \min(u_L, u_R) - \max(c_{s,L}, c_{s,R})$$
$$S_R = \max(u_L, u_R) + \max(c_{s,L}, c_{s,R}),$$

where $u$ and $c_s$ are the stream velocity and sound speed, respectively. Suppose that one solves a Riemann problem as defined in Fig. 2.3. Then, Equation 2.14 can be simplified as

$$\begin{aligned} \int_{x_L}^{x_R} \mathcal{Q}(x,T)\,dx &= \int_{x_L}^{x_R} \mathcal{Q}(x,0)\,dx + \int_0^T \mathcal{F}(x_L,t)\,dt - \int_0^T \mathcal{F}(x_R,t)\,dt \\ &= x_R\,\mathcal{Q}_R - x_L\,\mathcal{Q}_L + T(\mathcal{F}_L - \mathcal{F}_R). \end{aligned} \tag{2.17}$$

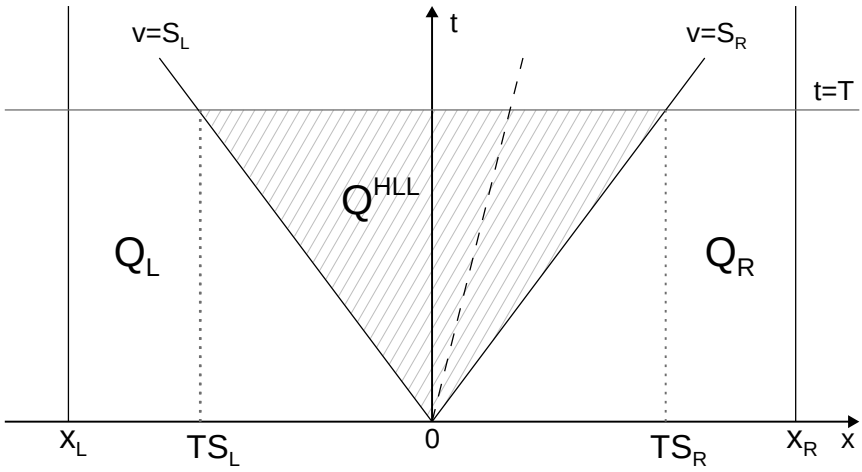


Figure 2.3: Structure of two waves ($v = S_L$ or $S_R$) in the Harten, Lax, and van Leer (HLL) solver. Computational domains can be divided into three regions according to states $\mathcal{Q}_L$, $\mathcal{Q}_R$, and $\mathcal{Q}_{\rm HLL}$. The maximum distances at which the two waves can propagate within the time step $T$ are $TS_L$ and $TS_R$. Also included as a dashed line is the third wave, whose eigenvalue of the Jacobian, $|\partial\mathcal{F}/\partial\mathcal{Q}|_x$, corresponds to the stream velocity $u$. This contact wave or entropy wave is included in the HLLC (HLL Contact wave) Riemann solver.

Since $\mathcal{Q}_L$ and $\mathcal{Q}_R$ are constant in $x_L \le x \le TS_L$ and $TS_R \le x \le x_R$, respectively, the term in the left-hand side of Equation 2.17 can be split as

$$\int_{x_L}^{x_R} \mathcal{Q}(x,T)\,dx = \int_{TS_L}^{TS_R} \mathcal{Q}(x,T)\,dx + (TS_L - x_L)\mathcal{Q}_L - (x_R - TS_R)\,\mathcal{Q}_R. \tag{2.18}$$

Equating Equation 2.17 and 2.18 yields the average state between $TS_L$ and $TS_R$:

$$\frac{1}{T(S_R - S_L)} \int_{TS_L}^{TS_R} \mathcal{Q}(x,T)dx \equiv \mathcal{Q}^{\rm HLL} \equiv \frac{S_R\,\mathcal{Q}_R - S_L\,\mathcal{Q}_L + \mathcal{F}_L - \mathcal{F}_R}{S_R - S_L}. \tag{2.19}$$

Applying the same arguments between 0 and $TS_L$, one obtains:

$$\int_{TS_L}^{0} \mathcal{Q}(x,T)\,dx = -TS_L\,\mathcal{Q}_L + T\,(\mathcal{F}_0 - \mathcal{F}_L) \qquad \text{and}$$
$$= TS_L\,\mathcal{Q}^{\rm HLL},$$

and finally injecting the result (2.19), one obtains the flux at $x = 0$, $\mathcal{F}_0$ or $\mathcal{F}^{\rm HLL}$:

$$\mathcal{F}^{\rm HLL} = \begin{cases} \mathcal{F}_L & \text{if } S_L \ge 0 \\ \mathcal{F}_R & \text{if } S_R \le 0 \\ \frac{S_R\mathcal{F}_L - S_L\mathcal{F}_R + S_L S_R(\mathcal{Q}_R - \mathcal{Q}_L)}{S_R - S_L} & \text{if } S_L < 0 \text{ and } S_R > 0. \end{cases} \tag{2.20}$$

Note that the HLL solver only accounts for the propagation of the two waves out of total three eigenvalues of the Jacobian matrix of $|\partial\mathcal{F}/\partial\mathcal{Q}|_x$, i.e. $u \pm c_s$ and $u$. Due to this limitation, the method tends to smear contact discontinuities, although it is still better than finite difference methods. Toro et al. (1994) realised this problem, and made a modification to the HLL solver by considering the third, i.e. contact or entropy wave. This particular scheme is called HLLC Riemann solver, and is the recommended choice in RAMSES (Teyssier, 2002).

### 2.2.4 Reconstruction of states

The original Godunov scheme discussed above assumes that states in any cell can be approximated by piecewise constants (Fig. 2.4-a). Due to this approximation, the Godunov scheme is first-order accurate in space, and hence diffusive.[3] To improve its accuracy, van Leer (1979) devised the Monotone Upstream-centred Schemes for Conservation Law (MUSCL), in which the states are represented by piecewise linear approximations. This method computes the Godunov flux, $\mathcal{F}_{i+1/2}$, using two reconstructed states at the intercell boundaries, $\mathcal{Q}^L_{i+1/2}$ and $\mathcal{Q}^R_{i+1/2}$, where

$$\mathcal{Q}^L_{i+1/2} \equiv \mathcal{Q}(x = x_i + \Delta x/2)$$
$$\mathcal{Q}^R_{i+1/2} \equiv \mathcal{Q}(x = x_{i+1} - \Delta x/2).$$

To illustrate this idea in more detail, suppose that two neighbouring cells are used to reconstruct states as

$$\bar{\mathcal{Q}}(x) = \mathcal{Q}(x_i) + \sigma_i(x - x_i), \tag{2.21}$$

where $\sigma$ represents the slope of the piecewise approximation. In order to reflect this change, the states at each intercell boundaries are evolved by a half-time step, as

$$\mathcal{Q}^{n+1/2}_{i\pm1/2} = \bar{\mathcal{Q}}_{i\pm1/2} + \frac{\Delta t}{2\Delta x}\left[\mathcal{F}(\bar{\mathcal{Q}}_{i-1/2}) - \mathcal{F}(\bar{\mathcal{Q}}_{i+1/2})\right].$$

From then on, the final procedure is identical to solving the standard Riemann problem, as outlined in the previous subsection, but with $\mathcal{Q}_L = \mathcal{Q}^{R,n+1/2}_{i+1/2}$ and $\mathcal{Q}_R = \mathcal{Q}^{L,n+1/2}_{i-1/2}$.

Fig. 2.4 (b) shows an example of a piecewise linear reconstruction, called the Lax-Wendroff method, where the $i$-th and $i+1$-th cells are used to approximate the true states. RAMSES employs such a linear reconstruction. Further improvement can be made if three cells instead of two are used to reconstruct the

[3] In a different context, the truncation error for the first-order Godunov scheme corresponds to numerical diffusion.

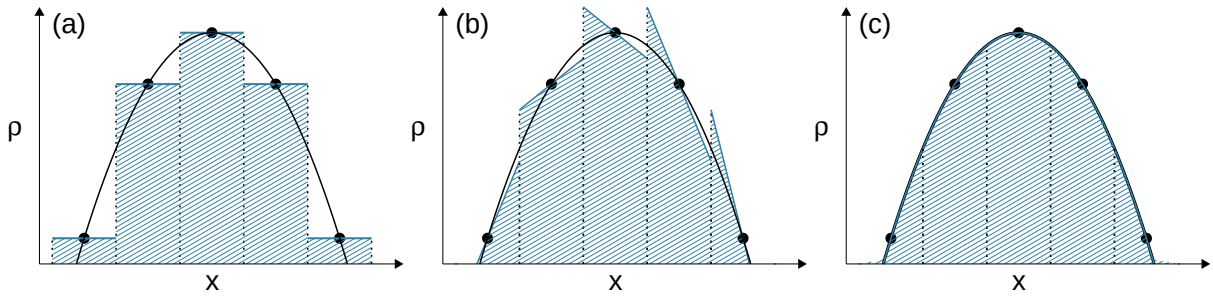


Figure 2.4: Three different schemes for solving partial differential equations: piecewise constant (left), piecewise linear (middle), and piecewise parabolic (right). Black lines indicate the true solution, whereas blue solid lines correspond to reconstructed states. Note that different number of cells are used to reconstruct the states.

state, as shown in Fig. 2.4-(c). This third-order accurate scheme is called Piecewise Parabolic Method (Colella & Woodward, 1984), and widely used in hydrodynamical simulations.

It should be emphasised that high-order schemes are prone to generate undesirable oscillatory features, especially in regions with steep gradients. This is because the slope near a "jump" is either overestimated or underestimated with respect to its true value. To track these oscillatory feature, one defines the Total Variation ($TV$) as

$$TV(\mathcal{Q}) = \sum_i \left(\bar{\mathcal{Q}}_i - \bar{\mathcal{Q}}_{i+1}\right).$$

When spurious oscillations develop, $TV(\mathcal{Q}^{n+1}) > TV(\mathcal{Q}^n)$. In order to prevent such behaviour, slopes are limited. A popular choice of slope limiter is the MinMod limiter, which selects a reduced gradient near a jump according to:

$$\sigma_i = \mathrm{MinMod}\left(\frac{\bar{\mathcal{Q}}_i - \bar{\mathcal{Q}}_{i-1}}{\Delta x}, \frac{\bar{\mathcal{Q}}_{i+1} - \bar{\mathcal{Q}}_i}{\Delta x}\right),$$

where the MinMod function satisfies

$$\mathrm{MinMod}(a,b) = \begin{cases} a & \text{if } |a| < |b| \text{ and } ab > 0 \\ b & \text{if } |a| > |b| \text{ and } ab > 0 \\ 0 & \text{if } ab \leq 0. \end{cases}$$

There are other limiters, such as MonCen, Superbee, and Ultrabee, that can better trace the advection of contact discontinuities, but require more calculations.

## 2.3 Adaptive Mesh Refinement

RAMSES is based on a Fully Threaded Tree (FTT) structure (Khokhlov, 1998), which enables to refine grids on a cell-by-cell basis, as opposed to patch-based AMR codes, such as Enzo (O'Shea et al., 2004) or FLASH (Fryxell et al., 2000). To do so, each cell carries several bits of information pointing to its parent cell, 6 neighbouring parent cells (in 3D), 8 child cells, previous and next grid cell. The last two pointers allow for fast searching of neighbour cells. Each cell also has an identifier indicating whether it is further refined ('split' cell) or not ('leaf' cell). In addition, particles are always linked to the grid cell to which they belong.

RAMSES mainly uses three criteria to trigger the refinement of a cell. First, cells are refined if the mass enclosed within a cell is greater than a certain value set by the user. This is controlled by a parameter called $\mathtt{m_{refine}}$ as,

$$m_{\rm tot} = m_{\rm gas} + m_{\rm dm} + m_{\rm star} \geq \mathtt{m_{refine}}\, \mathtt{m_{sph}}. \tag{2.22}$$

In case of cosmological simulations, the total mass inside a cell is normally chosen as 8 times the mass of a dark matter particle ($\mathtt{m_{sph}}$) to obtain a quasi-Lagrangian refinement of the grid.

However, depending on the purpose of the study, it is sometimes required to resolve the region where physical properties change abruptly. For example, large-scale filamentary structures are better traced when cells are refined on the basis of a pressure gradient (e.g. Rosdahl & Blaizot, 2012). The second refinement condition is hence based on the gradient of any physical variable ($q$), such as density, velocity, or pressure. If the gradient exceeds a fraction ($f_q$) of the value that a cell has, i.e.

$$\Delta q_i \geq f_q \frac{q_i}{\Delta x_i},$$

the cell is refined.

The last condition involves the Jeans instability. Truelove et al. (1997) demonstrated that if the Jeans length is not properly resolved, spurious fragmentation can occur, possibly leading to the formation of binary systems (e.g. Burkert & Bodenheimer, 1996). According to this study, the Jeans length should be resolved with at least 4 cells so as to prevent artificial fragmentation. Thus, the last criterion is

$$\lambda_{\rm J} = \sqrt{\frac{\pi c_s^2}{G\rho}} \geq \mathtt{N_J} \Delta x,$$

where $\mathtt{N_J} \geq 4$.

## 2.4 Time integration and control

Once the acceleration has been evaluated by the multigrid or conjugate gradient method, the position and velocity of particles are updated using a symplectic[4] time integrator. The advantage of symplectic integrators is that they conserve volume in phase space, ensuring that the solution of the differential equation remains numerically stable. As a counter example, Springel (2005) showed that non-symplectic methods, such as the classical Runge-Kutta method, cannot accurately describe a highly eccentric orbital motion (see his Figs 5 – 6). In RAMSES, a second-order midpoint (sympletic) scheme, which is also known as the Kick-Drift-Kick (KDK) leapfrog algorithm, is implemented, as

$$\begin{aligned}
\mathbf{u}^{n+1/2} &= \mathbf{u}^{n} - 0.5\Delta t \left(\frac{\partial \Phi}{\partial \mathbf{x}}\right)^{n} \\
\mathbf{x}^{n+1} &= \mathbf{x}^{n} + \Delta t \mathbf{u}^{n+1/2} \\
\mathbf{u}^{n+1} &= \mathbf{u}^{n+1/2} - 0.5\Delta t \left(\frac{\partial \Phi}{\partial \mathbf{x}}\right)^{n+1}.
\end{aligned}$$

Note that the last equation requires evaluating the potential at $t^{n+1}$, i.e. calculated at the next time step.

The time step used in RAMSES is controlled by four different conditions. First, a particle is not permitted to pass through a cell without interacting with the gas and other particles present. Second, hydrodynamic information cannot propagate across more than one cell in a single time step. Since this information propagates at the speed of sound, the time step must be limited by the time it takes sound waves to cross a cell. This constraint is called the Courant-Friedrichs-Lewy (CFL) condition. Third, in order to model the gravitational collapse of gas properly, the simulation time step should not exceed the free-fall timescale of a gas cell. Last, the time step is limited by the expansion rate of the universe, so that the scale factor does not grow more than 10% in a time step. In particular, this ensures that gravitational clustering is well captured in the high redshift universe. The actual time step for each level is set to the

[4]A linear mapping ($\mathbf{A}$) in two dimensional domains is called symplectic if $\mathbf{A}^T\mathbf{J}\mathbf{A} = 1$, where $\mathbf{J} = \begin{pmatrix} 0 & I \\ -I & 0 \end{pmatrix}$. The symplecticness implies the preservation of the area in physical domains.

minimum of the following four conditions:

$$\begin{aligned}
\Delta t_1^l &= C_1 \times \Delta x^l / \max(v_p^l) \\
\Delta t_2^l &= C_{\rm CFL} \times \Delta x^l / \left(\max[|u_x|,|u_y|,|u_z|] + c_s\right) \\
\Delta t_3^l &= C_3 \times \min(\tau_{\rm ff}^l) \\
\Delta t_4^l &= 0.1 \times a_{\rm exp}/\dot{a}_{\rm exp}
\end{aligned} \tag{2.23}$$

$$\Delta t^l = \min(\Delta t_1^l, \Delta t_2^l, \Delta t_3^l, \Delta t_4^l) \tag{2.24}$$

where $\tau_{\rm ff}$ is the free-fall time of each cell, $a_{\rm exp}$ is the cosmological expansion factor, $C_1 < 1$ and $C_3 < 1$ are free parameters, and $C_{\rm CFL} < 1$ is the Courant factor.

## 2.5 Coordinate System

To account for the cosmological expansion, RAMSES uses the super-comoving coordinate (Martel & Shapiro, 1998) system. Unlike the well-known comoving coordinate, this uses the following set of variables for a non-zero cosmological constant universe:

$$\begin{aligned}
\tilde{\mathbf{r}} &= \frac{\mathbf{r}}{a r_*} \\
\tilde{\mathbf{v}} &= \frac{a \mathbf{v} t_*}{v_*} \\
d\tilde{t} &= \frac{dt}{a^2 t_*} \\
\tilde{\rho} &= \frac{a^3 \rho}{\rho_*} \\
\tilde{\phi} &= \frac{a^2 \phi t_*^2}{\rho_*^2} \\
\tilde{p} &= \frac{a^5 p}{p_*} \\
\tilde{e} &= \frac{a^2 e}{e_*} \\
H(t) &= \frac{1}{a^3 t_*} \frac{da}{d\tilde{t}}
\end{aligned}$$

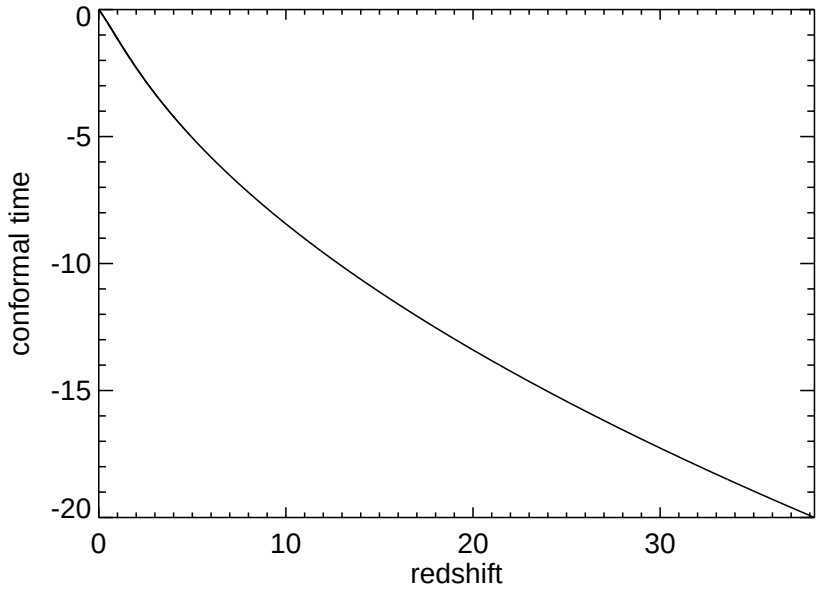


Figure 2.5: Relationship between the conformal time and redshift.

with

$$
\begin{aligned}
t_* \equiv & \frac{1}{H_0} \\
\rho_* \equiv & \rho_c \Omega_m = \frac{3H_0^2 \Omega_m}{8\pi G} \\
v_* \equiv & \frac{r_*}{t_*} \\
\phi_* \equiv & v_*^2 \\
p_* \equiv & \rho_* v_*^2 \\
e_* \equiv & v_*^2.
\end{aligned}
$$

Here, $a$, $\mathbf{r}$, and $\phi$ are the scale factor, position, and peculiar gravitation potential, respectively, and $\mathbf{v} = \mathbf{u} - H\mathbf{r}$ is the peculiar velocity. $r_*$ is a free parameter that depends on a problem, and set as $L_{\rm box}$ in cosmological simulations. The main difference between the super-comoving coordinate system and the comoving system lies in the use of a different time variable, called *conformal time* ($\tilde{t}$). The conformal time can be obtained by solving the Friedman equation (Fig. 2.5).

Note that the super-comoving coordinate has the advantage that the cosmological drag term vanishes in the momentum equation. For example, with the comoving coordinate ($\mathbf{x} = \mathbf{r}/a$), the momentum

equation reads

$$\frac{\partial \mathbf{v}}{\partial t} + \frac{\dot{a}}{a}\mathbf{v} + \frac{1}{a}(\mathbf{v}\cdot\nabla)\,\mathbf{v} = -\frac{\nabla\phi}{a} - \frac{\nabla P}{a\rho},$$

where the middle term on the left-hand side represents the cosmological drag. In super-comoving coordinates, the time and spatial derivatives of a function $f = f(d\tilde{t} = dt/a^2 t_*, \tilde{\mathbf{r}} = \mathbf{r}/aL_{\rm box})$ read:

$$\left(\frac{\partial f}{\partial t}\right)_r = \frac{1}{a^2 t_*}\left[\left(\frac{\partial f}{\partial \tilde{t}}\right)_{\tilde{r}} - \frac{da}{d\tilde{t}}\tilde{\mathbf{r}}\cdot\left(\tilde{\nabla} f\right)_{\tilde{t}}\right]$$
$$(\nabla f)_t = \frac{1}{aL_{\rm box}}\left(\tilde{\nabla} f\right)_{\tilde{t}}.$$

Under these transformations, the fluid equations have the exactly the same form as the standard ones in a non-expanding universe

$$\frac{\partial \tilde{\rho}}{\partial \tilde{t}} + \tilde{\nabla}\cdot(\tilde{\rho}\tilde{\mathbf{v}}) = 0 \tag{2.25}$$

$$\frac{\partial \tilde{\mathbf{v}}}{\partial \tilde{t}} + (\tilde{\mathbf{v}}\cdot\tilde{\nabla})\tilde{\mathbf{v}} = -\frac{\tilde{\nabla}\tilde{p}}{\tilde{\rho}} - \tilde{\nabla}\tilde{\phi} \tag{2.26}$$

$$\frac{\partial \tilde{e}}{\partial \tilde{t}} + (\tilde{\mathbf{v}}\cdot\tilde{\nabla})\tilde{e} + \mathcal{H}(3\gamma - 5)\tilde{e} = -\frac{\tilde{p}}{\tilde{\rho}}\tilde{\nabla}\cdot\tilde{\mathbf{v}} \tag{2.27}$$

with

$$\tilde{p} = (\gamma - 1)\tilde{\rho}\tilde{e} \tag{2.28}$$

$$\tilde{\nabla}^2\tilde{\phi} = 6a\left(\frac{\tilde{\rho}}{\bar{\tilde{\rho}}} - 1\right). \tag{2.29}$$

For an ideal gas with $\gamma = 5/3$, the energy equation above becomes even simpler, leaving the equations identical to the standard fluid ones except for the Poisson equation. A full derivation of these equations is presented in the Appendix of this thesis.

## 2.6 Physical Processes

### 2.6.1 Gas cooling

Plasma interacts with photons, altering the energy of electrons either bound to an atom or free. Specifically, incident light can excite an electron belonging to an atom, and the additional energy that makes the atom unstable can be radiated away isotropically through spontaneous reactions (bound-bound). The same process can free an electron, and the recombination of the electron with a proton is able to re-

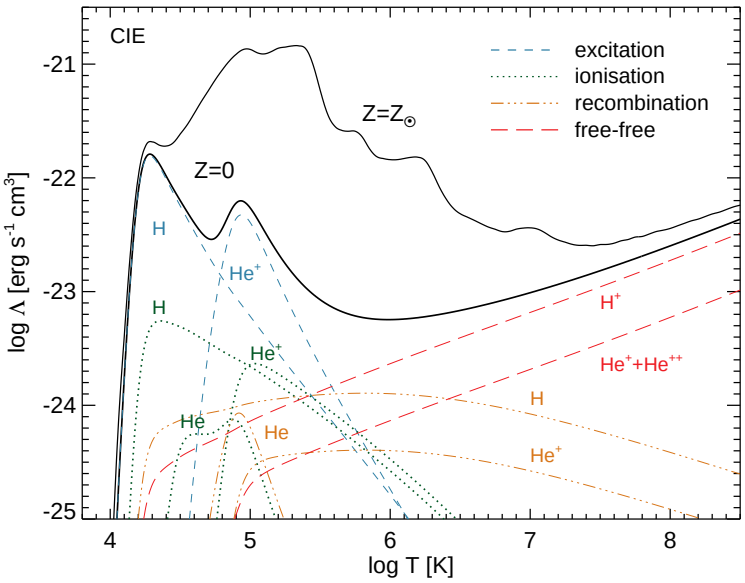


Figure 2.6: Cooling functions as a function of temperature for primordial ($Z = 0$) and solar ($Z = Z_{\odot}$) metallicity in the absence of UV background radiation. Density of the gas in collisional ionisation equilibrium (CIE) is chosen as $n_{\rm H} = 10^{-3}\,{\rm H\,cm^{-3}}$. Cooling rates for primordial composition gas are computed following Katz et al. (1996), while cooling rates for solar abundance gas are taken from Sutherland & Dopita (1993). Note that collisional excitations are important cooling mechanisms in the intermediate temperature range, whereas Bremsstrahlung is dominant at high temperature.

duce the energy of the system (bound-free). When a free electron encounters a proton, its motion is deflected by the electric field of the proton, releasing some of the electron kinetic energy (free-free or Bremsstrahlung) in the process. A free electron can also transfer its energy to a photon by collision, which is known as inverse Compton scattering. The general consequence of these processes is the reduction of the internal energy of the plasma.

These processes are temperature-dependent, except for Compton scattering. Bound-bound transitions are effective only in low temperature environments, because electrons need to remain bound to the nucleus. Bound-free transitions, also known as ionisation/recombination, are dominant for $10^4 \lesssim T \lesssim 10^6$. For hotter plasma ($10^6 \lesssim T \lesssim 10^8$), Bremsstrahlung is the most important process, while Compton scattering becomes the dominant process for extremely hot gas ($T \gtrsim 10^{10}$). As excitations, recombinations and Bremsstrahlung are the key processes for astrophysical fluids, gas cooling depends on the electron number density ($n_{\rm e}$) and proton number density ($n_{\rm p}$), as

$$\dot{e} \propto n_{\rm e} n_{\rm p}. \tag{2.30}$$

Given that almost all hydrogen atoms are ionised at $T \gtrsim 10^5\,{\rm K}$, the electron number density can be approximated by the proton number density. It is conventional to express the loss of energy ($\dot{e}$) in terms

of the number density of hydrogen ($n_{\rm H}$) as

$$\dot{e} = n_{\rm H}^2 \Lambda, \tag{2.31}$$

where $\Lambda$, a cooling function, encapsulates the efficiency of the different cooling processes. Fig. 2.6 displays the cooling functions for a gas density $n_{\rm H} = 10^{-3}\,{\rm H\,cm^{-3}}$, with primordial abundance ($Z = 0$) and solar abundance ($Z = Z_{\odot}$). The cooling function for a pristine gas in collisional ionisation equilibrium is computed following Katz et al. (1996), assuming that there is no UV background radiation (thick solid line). For gas of solar composition, cooling rates are taken from Sutherland & Dopita (1993) (thin solid line). It can be seen that for primordial gas, collisional excitations are the main cooling process in the intermediate temperature range ($10^4 \leq T \leq 10^{5.5}$), whereas Bremsstrahlung dominates the cooling at high temperature ($T > 10^7$). For solar abundance gas, the cooling rates are dominated by collisional excitations of carbon, oxygen, neon, iron, which represent the local peaks at $10^5\,K$, $10^{5.4}\,K$, $10^{5.7}\,K$, and $10^{6.2}\,K$, respectively.

Since the relative contribution from each cooling process differs according to physical conditions, the cooling functions can vary quite a lot with the environment. For example, several authors showed that the presence of a UV background from quasars and galaxies can significantly remove important coolants, such as neutral hydrogen or carbon, in low-density gas (Weinberg et al., 1997; Benson et al., 2002; Wiersma et al., 2009). Cantalupo (2010) also pointed out that photo-ionisation by local soft X-ray and extreme UV can easily reduce the cooling function at $10^4 \lesssim T \lesssim 10^{5.5}$ K by an order of magnitude by suppressing collisional excitation of heavy metals, such as oxygen and iron. An accurate determination of the cooling function requires on-the-fly radiative transfer calculations to infer the electron number density.

### 2.6.2 UV background heating

The presence of the Gunn-Peterson trough (Gunn & Peterson, 1965) in the spectra of distant quasars indicates that hydrogen atoms are already highly ionised at $z \sim 6$ (Becker et al., 2001; Fan et al., 2006). Given that a very small neutral fraction of hydrogen ($x_{\rm HI} \sim 10^{-4}$) can easily form this trough, UV radiation is likely to be abundant even at higher redshifts. Indeed, polarisation data from the *Wilkinson Microwave Anisotropy Probe (WMAP)* suggest $z_{\rm reion} \approx 11$ (Dunkley et al., 2009). This UV light is thought to be produced by quasars and/or hot massive stars, with a higher contribution from stars as redshift increases (e.g. Haehnelt et al., 2001).

In RAMSES, the UV radiation is implemented following Theuns et al. (1998). To briefly recapitulate, these authors first compute the integrated ionisation rates ($\Gamma_\gamma$) and photo-heating rates ($\epsilon_\gamma$) based on integrated spectra of quasars ($J(\nu, z)$) computed by Haardt & Madau (1996) as

$$\begin{aligned}
\Gamma_{\gamma,\mathrm{HI}} &= \int_{\nu_0(\mathrm{HI})}^{\infty} \frac{4\pi J(\nu,z)\sigma_\nu(\mathrm{HI})}{h\nu} d\nu \\
\Gamma_{\gamma,\mathrm{HeI}} &= \int_{\nu_0(\mathrm{HeI})}^{\infty} \frac{4\pi J(\nu,z)\sigma_\nu(\mathrm{HeI})}{h\nu} d\nu \\
\Gamma_{\gamma,\mathrm{HeII}} &= \int_{\nu_0(\mathrm{HeII})}^{\infty} \frac{4\pi J(\nu,z)\sigma_\nu(\mathrm{HeII})}{h\nu} d\nu \\
\epsilon_{\gamma,\mathrm{HI}} &= \int_{\nu_0(\mathrm{HI})}^{\infty} \frac{4\pi J(\nu,z)\sigma_\nu(\mathrm{HI})(h\nu - h\nu_0(\mathrm{HI}))}{h\nu} d\nu \\
\epsilon_{\gamma,\mathrm{HeI}} &= \int_{\nu_0(\mathrm{HeI})}^{\infty} \frac{4\pi J(\nu,z)\sigma_\nu(\mathrm{HeI})(h\nu - h\nu_0(\mathrm{HeI}))}{h\nu} d\nu \\
\epsilon_{\gamma,\mathrm{HeII}} &= \int_{\nu_0(\mathrm{HeII})}^{\infty} \frac{4\pi J(\nu,z)\sigma_\nu(\mathrm{HeII})(h\nu - h\nu_0(\mathrm{HeII}))}{h\nu} d\nu
\end{aligned}$$

where $h\nu_0$ is the ionisation energy, and $\sigma_\nu$ is the photoionisation cross-section. Then, they numerically integrate the above equations using the photoionisation cross-sections from Cen (1992), and determine the fits to the rates as functions of $J_{21}$ and $\alpha$, as

$$J(\nu) = J_{21} \times 10^{-21} \left(\frac{\nu}{\nu_0(\mathrm{HI})}\right)^{-\alpha} \mathrm{erg}^{-1}\,\mathrm{cm}^{-2}\,\mathrm{sr}^{-1}\,\mathrm{Hz}^{-1}. \tag{2.32}$$

Under the assumption of equilibrium between collisional ionisation, photoionisation, and recombination, the ionic balance can be written as

$$\begin{gathered}
\Gamma_{e,\mathrm{HI}}\, n_{\mathrm{HI}}\, n_e + \Gamma_{\gamma,\mathrm{HI}}\, n_{\mathrm{HI}} = \alpha_{\mathrm{HII}}\, n_{\mathrm{HII}}\, n_e \\
\Gamma_{e,\mathrm{HeI}}\, n_{\mathrm{HeI}}\, n_e + \Gamma_{\gamma,\mathrm{HeI}}\, n_{\mathrm{HeI}} = (\alpha_{\mathrm{HeII}} + \alpha_{\mathrm{HeII,d}})\, n_{\mathrm{HeII}}\, n_e \\
\Gamma_{e,\mathrm{HeII}}\, n_{\mathrm{HeII}}\, n_e + \Gamma_{\gamma,\mathrm{HeII}}\, n_{\mathrm{HeII}} + (\alpha_{\mathrm{HeII}} + \alpha_{\mathrm{HeII,d}})\, n_{\mathrm{HeII}}\, n_e \\
= \alpha_{\mathrm{HeIII}}\, n_{\mathrm{HeIII}}\, n_e + \Gamma_{e,\mathrm{HeI}}\, n_{\mathrm{HeI}}\, n_e + \Gamma_{\gamma,\mathrm{HeI}}\, n_{\mathrm{HeI}}
\end{gathered}$$

with the constraints

$$\begin{gathered}
n_{\mathrm{H}} = n_{\mathrm{HI}} + n_{\mathrm{HII}} \\
n_{\mathrm{He}} = n_{\mathrm{HeI}} + n_{\mathrm{HeII}} + n_{\mathrm{HeIII}} \\
n_{\mathrm{e}} = n_{\mathrm{HII}} + n_{\mathrm{HeII}} + 2n_{\mathrm{HeIII}}.
\end{gathered}$$

Here $\Gamma_{e,i}$ and $\alpha_i$ represent the collisional ionisation and recombination rates, respectively. Finally, the heating rate per unit volume can be written as

$$\mathcal{H} = \epsilon_{\gamma,\mathrm{HI}} n_{\mathrm{HI}} + \epsilon_{\gamma,\mathrm{HeI}} n_{\mathrm{HeI}} + \epsilon_{\gamma,\mathrm{HeII}} n_{\mathrm{HeII}}.$$

This heating rate is included in the energy equation (the third equation of Equation 2.11), and it effectively assumes that gas is optically thin everywhere. It should be noted, however, that this is a poor approximation in the high-density regions ($n_{\mathrm{H}} \gtrsim 0.01\,\mathrm{cm}^{-3}$) where self-shielding of gas against UV radiation becomes important (Faucher-Giguère et al., 2010; Rosdahl & Blaizot, 2012).

### 2.6.3 Star formation

It is known that stars form in giant molecular clouds or even denser infrared dark clouds. This suggests a relationship between gas (surface) density and star formation rate (Schmidt, 1959)

$$\dot{\rho}_* \propto \rho_{\mathrm{gas}}^n$$

or

$$\Sigma_* \propto \Sigma_{\mathrm{gas}}^n. \tag{2.33}$$

Based on H$\alpha$, atomic hydrogen (HI), and CO data from 61 normal spiral galaxies, and far infrared (FIR), HI, and CO observations of 36 starburst galaxies, Kennicutt (1998) found a surprisingly tight correlation between the gas surface density and the star formation rate density (see also Kennicutt 1989)

$$\Sigma_* = (2.5 \pm 0.7) \times 10^{-4} \left( \frac{\Sigma_{\mathrm{gas}}}{1\,M_\odot\,\mathrm{pc}^{-2}} \right)^{1.4\pm0.15} M_\odot\,\mathrm{yr}^{-1}\,\mathrm{kpc}^{-2},$$

where $\Sigma_{\mathrm{gas}} \equiv \Sigma_{\mathrm{HI}} + \Sigma_{\mathrm{H_2}}$ is the total gas surface density, which is thought to have a tighter correlation than atomic hydrogen or molecular hydrogen (Kenney & Young, 1988; Kennicutt, 1989; Buat, 1992; Kennicutt, 1998; Schuster et al., 2007). It is worth noting, however, that spatially resolved observations of 7 CO-bright galaxies revealed that the amount of molecular hydrogen seems primarily responsible for the relation (Wong & Blitz, 2002; Bigiel et al., 2008, see, however, Schuster et al. 2007 for an exception). This is probably because the atomic hydrogen surface density ($\Sigma_{\mathrm{HI}}$) saturates around $10\,M_\odot\,\mathrm{pc}^{-2}$, as gas become self-shielded from the incident UV light. Indeed, several authors have found that the transition from atomic to molecular hydrogen gas occurs sharply at $N_{\mathrm{HI}} + 2N_{\mathrm{H_2}} \sim (3-10) \times 10^{20}\,\mathrm{cm}^{-2}$ (e.g.

Savage et al., 1977; Gillmon et al., 2006; Lee et al., 2012).

The exponent close to 1.5 allows to rewrite the equation Equation 2.33 as

$$\dot{\rho}_* = \epsilon_* \frac{\rho_{\rm gas}}{t_{\rm ff}} \propto \rho_{\rm gas}^{1.5}.$$

This simple but very useful formula means that some fraction ($\epsilon_*$) of gas is converted into stars per local free-fall timescale ($t_{\rm ff}$). Therefore, the only free parameter that needs to be determined is the star formation rate per free-fall time ($\epsilon_*$). Although no consensus has been reached yet, observations have shown that only a minute fraction ($\sim 1-4\%$) of dense gas, ranging from $n_{\rm H} \simeq 100$ to $\simeq 10^6\,{\rm cm}^{-3}$, is converted into stars within free-fall time (e.g. Zuckerman & Evans, 1974; Wong & Blitz, 2002; Krumholz & McKee, 2005; Krumholz & Tan, 2007; Evans et al., 2009). The important issue which arises is to understand why the rate is so low. Theoretical studies suggest (e.g. McKee et al., 1993; Nakamura & Li, 2008) that when magnetic energy is greater than gravitational energy (magnetically subcritical ISM), magnetic poloidal fields may prevent gas from collapsing. This would result in a slow collapse controlled by the ambipolar diffusion timescale. However, direct measurements of magnetic field strength by means of the Zeeman effect favour a magnetically supercritical ISM in the Galaxy (Crutcher et al., 2010). As an alternative, turbulence has been widely discussed as a mechanism by which star formation is suppressed (Krumholz & McKee, 2005; Padoan & Nordlund, 2011). The basic idea is that the collapse of the interstellar medium is limited by supersonic turbulence pressure, possibly driven by mechanical stellar feedback (e.g. Ostriker & Shetty, 2011).

Another interesting observational finding is that stars seem to form only if the gas density exceeds a threshold density, $\Sigma_{\rm gas,th} \sim 10\,M_\odot\,{\rm pc}^{-2}$ or $N_{\rm H,th} \sim 10^{21}\,{\rm cm}^{-2}$ (e.g. Kennicutt, 1998; Wong & Blitz, 2002). This corresponds to the transition density from atomic hydrogen to molecular hydrogen, which is, in units of hydrogen number density, $n_{\rm H} \sim 100\,{\rm cm}^{-3}$. This is also comparable to the typical density of giant molecular clouds, $n_{\rm H,GMC} \sim 100\,{\rm cm}^{-3}$ (McKee, 1999). Encouragingly, recent cosmological simulations are beginning to see such giant clumps at high redshift (e.g. Powell et al., 2011; Ceverino et al., 2012; Dubois et al., 2012b). However, one still lacks the spatial resolution to resolve the infrared dark clouds and reach densities $n_{\rm H} \sim 10^5\,{\rm cm}^{-3}$ (see Powell et al. 2011; Geen et al. 2012 for an exception). Unless one resolves such high density gas, one is bound to underestimate the true star formation efficiency, because the free-fall time in such dense regions will be overestimated. In other words, poorly resolved simulations tend to smooth out high-density gas clumps, making the free-fall time longer than it should be on average.

In order to circumvent this high density threshold issue, simulations generally adopt a lower threshold density based on the Jeans density they achieve at maximum resolution. The Jeans length is the critical radius at which a protocloud can collapse by gravity, described as

$$\lambda_J \sim c_s \tau_{\rm dyn} \sim \sqrt{\frac{\gamma_{\rm a} k_{\rm B} T}{\mu m_{\rm H} G \rho}},$$

where $c_s$, $\tau_{\rm dyn}$, $k_{\rm B}$, $m_{\rm H}$ are the speed of sound, dynamical timescale, the Boltzmann constant, mean molecular weight, and the mass of a hydrogen atom. $\gamma_{\rm a}$ is the adiabatic index, which is 5/3 for a monatomic gas. The density threshold is obtained by equating the Jeans length and the size of the finest grid ($\lambda_J = \Delta x_{\rm min}$). This yields

$$\rho_{\rm th} \sim \frac{\gamma_{\rm a} k_B T_{\rm min}}{\mu m_{\rm H} G \Delta x_{\rm min}^2}$$

where $T_{\rm min}$ is the minimum temperature that a gas cell can reach via radiative cooling. As an example, the threshold density for $T_{\rm min} = 100\ K$ and $\Delta x_{\rm min} \simeq 0.4$ pc is $\simeq 6 \times 10^4$ H cm$^{-3}$. It should be noted, however, that the real situation is more complex than the particular configuration used in the Jeans condition (i.e. uniform collapsing sphere and no external pressure), and hence this threshold is, at best, a rough estimate.

In practice, for a gas cell whose density is greater than the threshold, a small fraction is converted into a star particle at a rate defined as

$$\dot{\rho} = \begin{cases} -\epsilon_* \, \rho / t_{\rm ff} & \text{if } \rho \geq \rho_{\rm th}, \\ 0 & \text{otherwise} \end{cases}$$

where $\epsilon_*$ is a free parameter that determines the efficiency for star formation per free-fall time ($t_{\rm ff}$)

$$t_{\rm ff} = \frac{3\,\pi}{32\,G\rho}.$$

Once $\epsilon_*$ and $\rho_{\rm th}$ are chosen, the mass of a stellar particle ($m_*$) forming in a cell per simulation time step ($\Delta t$) is determined as

$$m_* = N_p m_{*,min} = N_p \rho_{\rm th} \Delta x_{\rm min}^3.$$

Here the multiple of the minimum stellar mass ($N_p$) is drawn from a Poisson process, as

$$P(N) = \frac{\lambda_{\rm p}^N}{N!} e^{-\lambda_{\rm p}},$$

where

$$\lambda_{\rm p} = \epsilon_* \left( \frac{\rho \Delta x^3}{m_{*,\rm min}} \right) \frac{\Delta t}{t_{\rm ff}}.$$

### 2.6.4 Supernova Type II[1]

As massive stars ($M \geq 8 M_\odot$) run out of fuel for nuclear reaction by producing an iron core, they begin to contract and soon undergo an implosion caused by several endothermic processes. The inner core of the star stiffens as the collapse progresses, and finally when it gets dense enough to violate Pauli's exclusion principle applied to neutrons, pressure becomes very high owing to the repulsive strong force and a shock wave forms and drives an explosion, releasing $\sim 10^{51}$ erg of energy per supernova event.

Such an explosion can be divided into four distinctive phases (e.g. Shu, 1992).

1 **Free expansion**

In the early stage of the explosion, a spherical shock expands freely. The mass of swept-up material is smaller than the ejected mass, and the energy of the shock is conserved. The free expansion means that the radius of the shock is proportional to its velocity as $r_{\rm sh} = v_{\rm sh} t$

2 **Adiabatic expansion**

When the swept-up gas becomes comparable to the ejected mass, it is no longer free expansion, and the expansion rate declines as the remnant expands. At this stage, however, radiative energy losses are not significant, and the expansion is adiabatic.

3 **Snowplow phase**

Once radiative energy losses become significant, the region behind the shock front cools and forms an expanding dense shell that sweeps up the ambient medium as a snowplough mounted on a winter vehicle does. This phase conserves momentum.

4 **Merging phase**

Finally, when the pressure of the interior region drops and becomes comparable to that of the ambient medium, the shell is dispersed and mixed with the ambient medium.

[1] We discuss other stellar feedback processes (supernova Type Ia, stellar winds, and hypernova) in Chapter 5.

The evolution of shock waves during the adiabatic expansion phase can be accurately determined. This is called the Sedov-Taylor blast wave solution, and described as

$$r_{\rm sh} = A \left( \frac{E_0 t^2}{\rho_0} \right)^{1/5}$$
$$u_{\rm sh} = \frac{2}{5} A \left( \frac{E_0}{\rho_0 t^3} \right)^{1/5} = \frac{2\, r_{\rm sh}}{5\, t} \tag{2.34}$$

where $A$ is obtained numerically by imposing boundary conditions. For $\gamma_{\rm a} = 5/3$, $A = 1.15$. When expressed in astronomical scales,

$$r_{\rm sh} \simeq 2\ {\rm pc} \left( \frac{E_0}{10^{51}\ {\rm erg}} \right)^{1/5} \left( \frac{\rho_0}{10^{-24}\ {\rm g\,cm^{-3}}} \right)^{-1/5} \left( \frac{t}{100\ {\rm yr}} \right)^{2/5}$$
$$u_{\rm sh} \simeq 9000\ {\rm km\,s^{-1}} \left( \frac{E_0}{10^{51}\ {\rm erg}} \right)^{1/5} \left( \frac{\rho_0}{10^{-24}\ {\rm g\,cm^{-3}}} \right)^{-1/5} \left( \frac{t}{100\ {\rm yr}} \right)^{-3/5}.$$

On the contrary, momentum is conserved during the snowplough phase, and the corresponding evolution of the radius of the shock and its expansion rate have a different time dependence as (e.g. Mo et al., 2010)

$$r_{\rm sh} \propto \left( \frac{pt}{\rho_0} \right)^{1/4}$$
$$u_{\rm sh} \propto \left( \frac{p}{\rho_0 t^3} \right)^{1/4},$$

where $p$ is the momentum of the expanding shell.

The initial size of the expanding shell must be the size of a massive star, but current galaxy-scale simulations cannot resolve such tiny scales. A plausible alternative is to make use of the fact that the initial expansion is adiabatic (Equation 2.34). For example, one can estimate the radius at which a fourth of the explosion energy has been radiated away (Mo et al., 2010),

$$r_{\rm sh}(t_{\rm rad}) \simeq 3.3\ {\rm pc} \left( \frac{n_{\rm H}}{100\,{\rm cm^{-3}}} \right)^{-19/45} \left( \frac{E}{10^{51}\ {\rm erg}} \right)^{13/45},$$

assuming gas is of solar metallicity. Note that for a simple stellar population (SSP) of $10^4\,M_\odot$ with a single supernova event, the estimated radius for which the adiabatic assumption is valid is 12 parsec (if the explosion occurs in a typical giant molecular cloud). This is already a challenging resolution to achieve from a galaxy formation simulation point of view.

To circumvent this issue, a larger initial expanding shell radius is adopted with slower expanding

velocities. This requires to specify two free parameters, the fraction of energy lost during the expansion of the shell ($\eta_{\rm loss}$) and the amount of mass entrained with the shell ($\eta_{\rm w}$). Specifically, once the initial radius for a superbubble ($r_{\rm bubble}$) is specified by users, energy and momentum are injected into gas cells. The total energy released ($E_{\rm SN}$) by supernovae from a SSP of $M_*$ is

$$E_{\rm SN} = (1-\eta_{\rm loss})\frac{\eta_{\rm SN} M_*}{m_{\rm SN}} e_{\rm SN},$$

where $m_{\rm SN}$ and $e_{\rm SN}$ are the typical progenitor mass ($10 M_\odot$) and energy released ($10^{51}{\rm erg}$) by a single Type II supernova, and $\eta_{\rm SN}$ represents the mass fraction of massive stars in a SSP. For a Salpeter initial mass function (IMF, $\phi_{\rm Sal}$) with a low-mass cutoff at 0.1 $M_\odot$ and a high-mass cutoff at 100 $M_\odot$, the mass fraction of stars above 8 $M_\odot$ ($\eta_{\rm SN}$) is 0.139, and the number of massive stars per solar mass of stars formed yields

$$\frac{\int_8^{100}\phi_{\rm Sal}(m)dm}{\int_8^{100} m\phi_{\rm Sal}(m)dm} \simeq 0.053\ {M_\odot}^{-1}.$$

The resulting specific frequency of Type II supernova is $0.139 \times 0.053 = 0.0074\, {M_\odot}^{-1}$.

The expansion velocity ($u_{\rm SN}$) of the superbubble can be computed by using this energy and the mass loading factor ($\eta_{\rm w}$), as

$$\begin{aligned} E_{\rm SN} &= \frac{(1+\eta_{\rm w})\,\eta_{\rm SN} M_* u_{\rm SN}^2}{2}, \\ u_{\rm SN} &= \left[\frac{2(1-\eta_{\rm loss})e_{\rm SN}}{(1+\eta_{\rm w})\,m_{\rm SN}}\right]^{1/2}. \end{aligned} \tag{2.35}$$

Given the complex structure of the interstellar medium, the mass loading factor may not be well-defined, but observations suggest that to first order $\eta_{\rm w} = 10$ (e.g. Martin, 1999)[5]. Adopting $\eta_{\rm w} = 10$ gives $u_{\rm SN} \simeq 956\,{\rm km\,s^{-1}}$ for $\eta_{\rm loss} = 0$ and $m_{\rm SN} = 10\,M_\odot$. In practice, the actual velocity of a gas cell can be smaller or larger than this depending on its density. If there is no gas to be entrained (i.e. $\eta_{\rm w} \sim 0$), $u_{\rm SN}$ would reach $\sim\ 3200\,{\rm km\,s^{-1}}$ and the velocity of the cells inside the bubble would be determined by the supernova explosion only. On the other hand, if the density of a gas cell is sufficiently high that there is still plenty of gas in it even after subtracting the mass entrained, the resulting velocity of the cell will be lowered as

$$u = \frac{m_{\rm gas} u_{\rm gas} + (1+\eta_{\rm w})\eta_{\rm SN} m_* u_{\rm SN}}{m_{\rm gas} + (1+\eta_{\rm w})\eta_{\rm SN} m_*}. \tag{2.36}$$

[5]It should be noticed that the symbol $\eta_{\rm w} \equiv \dot{m}_{\rm out}/\dot{m}_{\rm loss}$ is different from the mass-loading factor ($\eta \equiv \dot{m}_{\rm out}/\dot{m}_*$) commonly used in the literature (e.g. Martin, 1999).

Finally, determining the fraction of energy lost $\eta_{\rm loss}$ is not trivial. Using an one-dimensional Eulerian code, Thornton et al. (1998) simulated the supernova-driven expansion of a shell, and concluded $\sim$ 90% of the input energy is radiated away in 3 Myr. However, stars form in a clustered fashion, and the collective action of the supernova-driven winds is likely to be much more efficient simply on the grounds that the duration of adiabatic phase is longer. The situation is even more complicated in galactic-scale simulations, as they are subject to artificial radiative cooling (Katz et al., 1996; Slyz et al., 2005). When supernova explosions are modelled as a thermal input in simulations where the integration time step and cell size are large, the energy from the supernovae is quickly radiated away before gas can actually propagate outwards. Kinetic feedback, as described above, is suggested to improve the propagation of supernova explosions (Aguirre et al., 2001; Springel & Hernquist, 2003; Dubois & Teyssier, 2008; Dalla Vecchia & Schaye, 2008), but it is not entirely immune to artificial cooling either, as fast winds equipartition their energy through shocks (Durier & Dalla Vecchia, 2012). For this reason, current galactic-scale simulations necessitate a low $\eta_{\rm loss}$ to efficiently blow gas away from its host haloes (Peirani et al., 2012, see also Chapter 5).

Another fundamental role of the supernova explosion is the metal enrichment. As discussed in the previous section (Section 2.6.1), cooling rates can easily be enhanced by an order of magnitude by metal cooling, and as such, it is essential to include the metal production by SNe to understand the star formation histories of galaxies. In RAMSES, this is encapsulated by a parameter `yield`, which indicates the amount of metals *newly* processed inside a simple stellar population. The metallicity of the ejecta can then be written as

$$Z_{\rm ejecta} = \texttt{yield} + (1 - \texttt{yield})\, Z_{\rm star},$$

where $Z_{\rm star}$ is the metallicity of the star. Arnett (1996) computed the bulk yield for a Salpeter IMF with a slope $\alpha = 4/3$, and found $\texttt{yield} = 0.0501$.

### 2.6.5 Accretion and feedback from active galactic nuclei

It is generally believed that energy from active galactic nuclei (AGN) is crucial to understand the formation of massive galaxies (e.g. Binney & Tabor, 1995; Ciotti & Ostriker, 1997). Despite the fact that the scale of a super-massive black hole (SMBH) is vastly different from that of its host galaxy, the existence of a tight correlation between the mass of the SMBH and its host galaxy properties (Kormendy & Richstone, 1995; Magorrian et al., 1998; Ferrarese & Merritt, 2000; Gebhardt et al., 2000; McLure & Dunlop, 2002; Marconi & Hunt, 2003; Häring & Rix, 2004; Gültekin et al., 2009; Graham, 2012)

suggests that SMBHs and host galaxies have co-evolved, self-regulating their growth. The basic idea of self-regulation is that AGN feedback controls the growth of SMBHs and spheroids by heating and blowing out gas if the central SMBHs accrete at near Eddington rate (Silk & Rees, 1998; King, 2003). Indeed, there is mounting evidence that AGNs interact with the interstellar/intracluster medium (ISM/ICM), and suppress cooling and star formation in galaxies (e.g. McNamara & Nulsen, 2007). These includes high-velocity galactic outflows commonly observed in quasars (e.g. Turnshek et al., 1988; Hamann et al., 1997; Pounds et al., 2003; Ganguly & Brotherton, 2008) or X-ray cavities inflated by radio jets in cluster centres (Boehringer et al., 1993; Bîrzan et al., 2004; McNamara et al., 2005; Forman et al., 2005; Fabian et al., 2006).

Theoretically, the aforementioned outflows and X-ray cavities appear to have a different physical origin depending on the accretion rate onto the central SMBHs. In the case of high accretion rates, geometrically thin and dense discs form, and efficient local cooling allows gravitational energy to be radiated away (Shakura & Sunyaev, 1973). This radiation may be able to heat up the surrounding gas by inverse Compton heating (Ciotti & Ostriker, 1997, 2001, 2007) or exert pressure on spectral lines (e.g. Murray et al., 1995; Proga, 2007), or dust (Konigl & Kartje, 1994; Roth et al., 2012). This idea is more closely associated with outflows in bright quasars, and hence sometimes referred to as quasar-mode feedback. On the other hand, if the accretion rate is low, the gas radiates inefficiently due to the low density of the disc, and the energy is mainly advected by the flow. This increases the pressure of the gas, leading to the formation of a geometrically thick but optically thin disc (Narayan & Yi, 1994, 1995). The important characteristic of the advection-dominated accretion flow is that the accreting gas is loosely bound and likely to escape, producing a sub-relativistic bipolar jet or wind (Blandford & Begelman, 1999). This wind may be able to blow gas away and inflate hot plasma in clusters (Omma et al., 2004; Dubois et al., 2010). More relativistic jets are thought to form through the extraction of energy from spinning black holes (Blandford & Znajek, 1977), dominating the radio emission.

Motivated by the latter idea, several authors have simulated buoyantly rising hot bubbles driven by relativistic AGN jets (Churazov et al., 2001; Quilis et al., 2001; Brüggen & Kaiser, 2002; Dalla Vecchia et al., 2004; Kawata & Gibson, 2005; Sijacki & Springel, 2006), and concluded that the bubble can reduce radiative gas cooling by heating the surrounding medium as it rises through the intracluster medium. In a similar spirit, Omma et al. (2004) modelled momentum-carrying, sub-relativistic jets launched from the central accretion torus (Blandford & Begelman, 1999), and found that the bipolar outflows, which mainly consist of H/He gas, could successfully create stable X-ray cavities, and offset cooling by pushing cold

gas outwards and mixing it with high-entropy gas in a Hydra-like cluster. While these studies indicate that AGN feedback can prevent strong cooling flows onto massive elliptical galaxies, Di Matteo et al. (2005) also showed that AGN activity during mergers of spiral galaxies could induce strong outflows and quench residual star formation after a merger-induced starburst (see also Springel et al., 2005). This might naturally establish the tight correlation between host galaxy properties and black hole mass (e.g. Kauffmann & Haehnelt, 2000; Di Matteo et al., 2008).

In RAMSES, both quasar-mode and jet-mode feedback are implemented to account for the liberation of energy by gas accretion onto a black hole (Dubois et al., 2010, 2012a). In order to follow the growth of black holes, initial seeds of $10^2 - 10^5 M_\odot$ are created in the finest cell if the Jeans criterion is violated. Truelove et al. (1997) demonstrated that the Jeans length should be resolved with at least four cells to ensure the numerical stability, and thus we assume that a cell is gravitationally unstable and collapses into a black hole if

$$\frac{\Delta x_{\rm min}}{4} > \lambda_{\rm J} = \sqrt{\frac{\pi c_s^2}{G\rho}}.$$

We also assume that black holes can form only if stars are present in a cell. Determining the mass of the initial black hole seed is not trivial, but fortunately the seed tends to grow rapidly by accreting the surrounding cold, dense interstellar medium during its early phase of evolution until it begins to self-regulate its growth. Hence, the choice of the seed mass does not significantly impact the simulation results, provided that it is sufficiently small compared to the mass the SMBH has reached when one analyses these results.

Once a BH forms, it is split into smaller pieces, called cloud particles, in the beginning of each coarse time step so as not to be affected by the stochasticity of local physical properties. For this purpose, 2109 cloud particles are spread regularly inside a sphere of $r = 4\,\Delta x_{\rm min}$ with an interval of $0.5\,\Delta x_{\rm min}$. These cloud particles are used to compute the average density, temperature, and spin axis of the gas around the hole, based on the kernel function $w(r)$ as,

$$w(r) \propto \begin{cases} \exp\left[-r^2/\left(\Delta x_{\rm min}/4\right)^2\right] & r_{\rm Bondi} < \Delta x_{\rm min}/4 \\ \exp\left[-r^2/\left(r_{\rm Bondi}\right)^2\right] & \text{if} \quad \Delta x_{\rm min}/4 < r_{\rm Bondi} < 2\,\Delta x_{\rm min} \\ \exp\left[-r^2/\left(2\,\Delta x_{\rm min}\right)^2\right] & r_{\rm Bondi} > 2\,\Delta x_{\rm min} \end{cases}, \tag{2.37}$$

where $r$ is the separation between black hole and cloud particle. The Bondi radius ($r_{\rm Bondi}$) is given by

$$r_{\rm Bondi} = \frac{G\,M}{c^2_{\rm s,sink}},$$

where $c_{\rm s,sink}$ is the speed of sound of the cell where the black hole is placed.

Gas accretion is modelled with a modified Bondi-Hoyle-Lyttleton accretion rate (Bondi & Hoyle, 1944; Booth & Schaye, 2009), which is a particular solution for the accretion onto a point source moving in a uniform medium. It can be described as

$$\dot{M}_{\rm Bondi} = \frac{4\pi\,\alpha\,G^2\,M_{\rm BH}^2\,\bar{\rho}}{(\bar{c}_s^2+\bar{u}^2)^{3/2}}$$

where $u$ is the average gas velocity relative to the velocity of a BH, $c_s$ is the speed of sound of the nearby gas, and $\alpha$ is a free parameter, called the boost factor, that is required to compensate the accretion in poorly resolved simulations (Springel et al., 2005; Di Matteo et al., 2005; Booth & Schaye, 2009; Choi et al., 2012). The Bondi-Hoyle-Lyttleton rate is often compared with the Eddington accretion rate at which the radiation pressure due to electron scattering can overcome the gravitational force exerted by the central black hole

$$\dot{M}_{\rm Edd} = \frac{4\pi\,G\,M_{\rm BH}\,m_{\rm p}}{\epsilon_r\,\sigma_{\rm T}\,c},$$

where $\epsilon_r$ is the radiative efficiency of the accretion and $\sigma_T$ is the Thomson cross-section. The resulting Eddington ratio ($\chi_{\rm edd}$) is then

$$\begin{aligned}\chi_{\rm edd} \equiv \frac{\dot{M}_{\rm Bondi}}{\dot{M}_{\rm Edd}} &= \frac{\alpha\,GM_{\rm BH}\,\bar{\rho}\,\epsilon_r\,\sigma_{\rm T}\,c}{(\bar{c}_s^2+\bar{u}^2)^{3/2}\,m_{\rm p}} \\ &\simeq 0.35\,\alpha'\,\left(\frac{\bar{n}_{\rm H}}{\rm cm^{-3}}\right)\left(\frac{M_{\rm BH}}{10^6\,M_\odot}\right)\end{aligned}$$

for $\epsilon_r = 0.1$, where

$$\alpha' = \alpha\left[\left(\frac{\bar{c}_s}{10\,\rm km/s}\right)^2+\left(\frac{\bar{u}}{10\,\rm km/s}\right)^2\right]^{-3/2}.$$

As discussed in Booth & Schaye (2009), the boost factor ($\alpha$) is necessary when a simulation cannot resolve dense gas with low temperature. On the other hand, physical properties are properly captured for a hot, low-density gas, and thus it is not required. Following Booth & Schaye (2009), we adopt the density-dependent boost factor:

$$\alpha = \begin{cases} (\rho/\rho_0)^2 & \rho \geq \rho_0 \\ 0 & \rho < \rho_0 \end{cases},$$

where $\rho_0$ is the threshold density for star formation.

Motivated by the analogy between X-ray binaries and AGN (e.g. Körding et al., 2006), we assume that the state of the accretion disc changes at $\chi_{\rm edd} = 0.01$. Specifically, when the gas accretion rate is high ($\chi_{\rm edd} \geq 0.01$, quasar-mode), we inject an amount ($E_{\rm AGN,qso}$) of thermal energy into the AMR cell in which the black hole is located:

$$E_{\rm AGN,qso} = \epsilon_{\rm qso} \dot{M}_{\rm BH} c^2.$$

Otherwise ($\chi_{\rm edd} < 0.01$), we implement an AGN jet with kinetic energy, $E_{\rm AGN,jet}$, which we assume is a bipolar wind blown off the accretion disc (Blandford & Begelman, 1999).

$$E_{\rm AGN,jet} = \epsilon_{\rm jet} \dot{M}_{\rm BH} c^2.$$

Moreover, the fraction of the black hole accretion energy ($\epsilon_{\rm jet}$) which is returned in the form of a bipolar wind has a momentum profile (Omma et al., 2004)

$$\psi(r_{\rm cyl}) = \frac{1}{2\pi r_{\rm jet}^2} \exp\left(-\frac{r_{\rm cyl}^2}{2\, r_{\rm jet}^2}\right),$$

where $r_{\rm cyl}$ is a cylindrical radius measured from the black hole seed particle which sits at $r_{\rm cyl} = 0$, and $r_{\rm jet}$ is the characteristic size that determines the degree of collimation of the jet. The jet axis ($\hat{\mathbf{j}}$) is aligned with the angular momentum of neighbouring gas cells around the black hole seed particle within $4\,\Delta x_{\rm min}$, and hence fluctuates over time. Mass is deposited based on the same exponential profile, as

$$\dot{M}_{\rm jet}(r_{\rm cyl}) = \frac{\psi(r_{\rm cyl})}{\psi_{\rm tot}} \eta_{\rm BH}\, \dot{M}_{\rm BH},$$

where

$$\psi_{\rm tot} = \sum_i^{\rm jet} \psi(r_{\rm cyl,i}).$$

The entrainment of gas due to the outburst is taken into consideration by introducing a mass loading factor ($\eta_{\rm BH}$). Finally, the jet velocity is determined by equating the energy available from the active galactic nuclei and their kinetic energy as

$$\epsilon_{\rm jet} \dot{M}_{\rm BH} c^2 = \frac{1}{2} \eta_{\rm BH}\, \dot{M}_{\rm BH}\, u_{\rm jet}^2$$
$$u_{\rm jet} = \sqrt{\frac{2\epsilon_{\rm jet}}{\eta_{\rm BH}}}\, c.$$

We adopt a jet efficiency of $\epsilon_{\rm jet} = 0.1$ and mass loading $\eta_{\rm BH} = 100$, which yields sub-relativistic

outflows ($u_{\rm jet} \sim 9487\,{\rm km/s}$). Finally, the momentum and kinetic energy corresponding to the velocity and mass of the jet are added to each cell inside $r_{\rm jet}$ as

$$\dot{p}_i = \dot{M}_{\rm jet} u_{\rm jet}\, \hat{\mathbf{r}}_{ij} \cdot \hat{\mathbf{j}}_j$$
$$\dot{E}_{\rm kin} = \left( \sum_{i=1}^{3} \dot{p}_i^2 \right) / 2\dot{M}_{\rm jet}.$$

## 2.7 Identification of structures and substructures

Dark matter halos are identified using HaloMaker (Tweed et al., 2009), which is based on the AdaptaHOP algorithm by Aubert et al. (2004). We briefly describe the algorithm here, and further details can be found in Aubert et al. (2004); Tweed et al. (2009). The method first computes the density ($\rho$) at each particle position by integrating the contribution from the $N_{\rm SPH}$ nearest neighbours using the standard SPH kernel (e.g. Monaghan, 1992). Then, by 'hopping' from one particle to its neighbour having the highest density, it finds the local maxima, and can define peak patches by grouping particles which are located in sufficiently high density regions ($\rho/\bar{\rho} > \rho_{\rm th}$, Eisenstein & Hut 1998) and share the same local maximum. These procedures are the same as the HOP algorithm (Eisenstein & Hut, 1998), and will identify halos. Among the saddle points of two interfacing peak patches belonging to a halo, the dark matter particle with the highest density is used to represent the unique saddle point connecting two peak patches. These unique saddle points are then used to find substructures. As an example, if three peak patches are connected and they belong to a halo, the density of two saddle points will determine the level of each (sub)structure.

Once the structures are found, it is necessary to compute physical properties. The centre of a halo is defined to be the position of the particle having the highest density. For each halo, the principal axes and shapes (a,b,and c) are computed from the eigenvectors and eigenvalues of the inertial tensor. These are then used to compute the mass within concentric ellipsoids ($m_i$). The virial mass of a halo is determined by assessing whether the virial theorem holds better than 20% for particles inside a concentric ellipsoid with $(a_i,\ b_i,\ c_i)$, i.e.

$$\frac{\|2\,E_k + E_p\|}{\|E_k + E_p\|} < 0.2.$$

The corresponding virial radius is chosen as

$$R_{\rm vir} = (a_i\, b_i\, c_i)^{1/3}\,.$$

However, for small halos or satellites, the virial condition may not be satisfied or the mass within the virial radius may be smaller than that predicted by the spherical top-hat model. In these cases, HaloMaker uses the concentric ellipsoid that contains the mass computed from the spherical top-hat model and updates the virial radius, accordingly.

# Chapter 3

# Are cold flows detectable with metal absorption lines?[1]

## 3.1 Introduction

How galaxies get their gas is a long-standing issue. For decades, the standard theoretical picture of galaxy formation has stipulated that all gas accreted into dark matter haloes is shock heated before it radiatively cools and settles into a galactic disk (Silk, 1977; Rees & Ostriker, 1977, although Binney 1977 first suggested this need not be the case). This picture has recently been revisited both by analytic studies (Birnboim & Dekel, 2003; Dekel & Birnboim, 2006) and hydrodynamical simulations (both in 1D: Birnboim & Dekel 2003 and in 3D within an explicit cosmological context, Kereš et al. 2005, 2009; Ocvirk et al. 2008; hereafter OPT08). These studies have established that in haloes below a critical mass shocks are unstable and cannot propagate outwards, so that cold diffuse gas and/or cold filaments can penetrate deep into the halo without experiencing shock-heating. In contrast, at the other end of the mass spectrum, very massive haloes easily sustain a virial shock that is stable against gas cooling so that diffuse/filamentary gas is shock heated to the virial temperature of the halo as it enters. Finally, at intermediate halo masses, either gravitationally shock-heated hot gas and/or a hot galactic wind coexists with cold inflowing filaments (OPT08): some dense cold filaments are stable against the pressure force exerted by the hot gaseous material. In other words, the vast majority of galaxy-size host haloes, especially at high redshift ($z > 2$), are predicted to be threaded by cold gas filaments in the $\Lambda$CDM model of structure formation. Therefore, the questions which naturally arise are whether or not

[1] Kimm, T., Slyz, A., Devriendt, J., Pichon, C., MNRAS, 2011, 413L, 51

the existence of these cold gas filaments can be observationally confirmed, and by which technique.

Since the advent of high-resolution spectroscopy has enabled astronomers to study the kinematics of the intergalactic medium at high redshifts in a wealth of detail (e.g. Pettini et al., 2002; Adelberger et al., 2003; Shapley et al., 2003), and given the fact that cold gas is thought to flow into massive haloes ($10^{12} M_{\odot}$) at $z = 2.5$ along filaments with velocities of $\gtrsim 200\,\mathrm{kms}^{-1}$ (Dekel et al., 2009), it is sensible to think that the spectra of Lyman-break galaxies (LBGs Steidel et al., 1996) might reveal these filaments as redshifted absorption features. Interestingly, a recent study reported that few Lyman-break galaxies (LBGs) show redshifted metal absorption lines, suggesting that inflowing gas in haloes with $4 \times 10^{11} < M_{\mathrm{vir}} < 10^{12} M_{\odot}$ is rare (Steidel et al., 2010). Taken at face value, this appears to contradict the theoretical prediction that cold filaments are prominent in the vast majority of high-z haloes.

However, there exist a variety of reasons as to why these filaments should be very difficult to detect. The first of these is the covering fraction of the filaments. This is estimated in Dekel et al. (2009) to be around $\sim 25\%$ for four massive haloes with $M_{\mathrm{vir}} \sim 10^{12} M_{\odot}$ in the HORIZON-MARENOSTRUM simulation, counting only relatively dense ($N_{\mathrm{H}} > 10^{20}\mathrm{cm}^{-2}$) and cold ($T < 10^{5} K$) gas within a radial distance $20 < r < 100$ kpc from the central galaxy hosted by these haloes. Whereas $25\%$ is indeed a non-negligible covering fraction, its exact dependence on redshift and halo mass remains to be determined. For instance, Faucher-Giguère & Kereš (2011) also measured the covering fraction for a Milky Way-type progenitor LBG in a smoothed particle hydrodynamic simulation but found a significantly smaller value ($\sim 2\%$). Secondly, low-ionisation lines can be produced not only by cold filamentary gas but also by a galaxy's interstellar medium, so that when using a single galaxy to probe the circumgalactic medium, distinguishing absorption produced by filaments from that produced by the ISM is key to prove/disprove the presence of cold filaments. Thirdly, there is the geometry of the accretion: in order to produce a strong absorption signal, a filament needs to be well aligned with the line of sight to maximise its column density. Finally, there is the issue of metallicity: a metal-poor filament will be transparent to metal line observations.

The aim of this study is to quantify the aforementioned effects to better assess the detectability of the absorption signal produced by cold filaments. We show that the actual probability of detecting such flows with metal lines is much smaller than the high covering fraction derived in Dekel et al. (2009) would suggest due to i) the low density and ii) low metallicity of the filaments *compared with the densities and metallicites of the interstellar medium of the host galaxy.*

## 3.2 HORIZON-MARENOSTRUM **simulation**

We use the HORIZON-MARENOSTRUM simulation to investigate the statistical properties of gas accretion at high redshift. The HORIZON-MARENOSTRUM simulation was carried out in a periodic box of comoving size $L = 50\,\mathrm{Mpc}\,h^{-1}$ using an Eulerian adaptive mesh refinement code, RAMSES (Teyssier, 2002). The simulation contains $1024^4$ dark matter particles with $m_{\rm dm} = 1.17 \times 10^7\,\mathrm{M}_\odot$, and the minimum size of a grid cell is kept fixed around $\simeq 0.7\,\mathrm{kpc}\,h^{-1}$. The combination of the large volume of the simulation and relatively fine grid is optimised for studying the statistical properties of gas accretion onto dark matter haloes. The initial conditions of the simulation were generated using the paralleled version of `Grafic` (Bertschinger, 2001), `MPgrafic` (Prunet et al., 2008) with WMAP1 cosmology ($\Omega_m = 0.3$, $\Omega_\Lambda = 0.7$, $h \equiv H_0/(100\,\mathrm{km\,s^{-1}\,Mpc^{-1}}) = 0.7$) (Spergel et al., 2003).

RAMSES uses a second-order Godunov scheme to solve the Euler equations, and an adaptive particle-mesh method is adopted as gravity solver. UV background heating is included as a source term in the energy equation following Haardt & Madau (1996), and atomic gas cooling allows gas to dissipate its energy down to $T \sim 10^4\,\mathrm{K}$ (Sutherland & Dopita, 1993). Star particles are produced based on a Poisson process with a star formation efficiency of 5% per free-fall time (Dubois & Teyssier, 2008; Kennicutt, 1998). We assume that only dense grid cells with $n_{\rm H} > 0.1\mathrm{cm}^{-3}$ can form stars. Massive stars evolve and undergo a supernova phase after 10 Myrs, releasing $10^{51}\,\mathrm{erg}$ of energy into the surrounding interstellar medium (Dubois & Teyssier, 2008). During this phase, heavy elements processed inside stars are dispersed also into their vicinity. AGN feedback is not modelled in this simulation. Due to a limited CPU time availability, the simulation was stopped at $z = 1.5$.

Dark matter haloes are identified using the ADAPTAHOP halo finder (Aubert et al., 2004; Tweed et al., 2009). Of several hundred thousands of dark matter haloes found, we only used massive haloes to measure the physical properties of gas (gas accretion rate, geometry) at the virial radius. More specifically, we excluded haloes whose virial radii were smaller than five times the typical size of the grid cell where cold, dense gas filaments live. Corresponding physical radii are 14, 18, 25, and $34\,\mathrm{kpc}$ at $z = 5.0$, 3.8, 2.5, and 1.5, respectively, and the minimum dark halo mass is $M_{\rm vir} \sim 2.2 \times 10^{10} M_\odot$ over the redshift range. This results in 6655, 11357, 15419, and 15999 host haloes at $z = 5.0$, 3.8, 2.5, and 1.5, respectively. Note that our sample is biased towards haloes in field/group environment, although the virial mass of the most massive halo in the sample is $10^{14}\,M_\odot$ at $z = 1.5$ . In Figs 3.1–3.2, we show five randomly selected regions centred on massive (top two rows) and less massive haloes (bottom two rows).

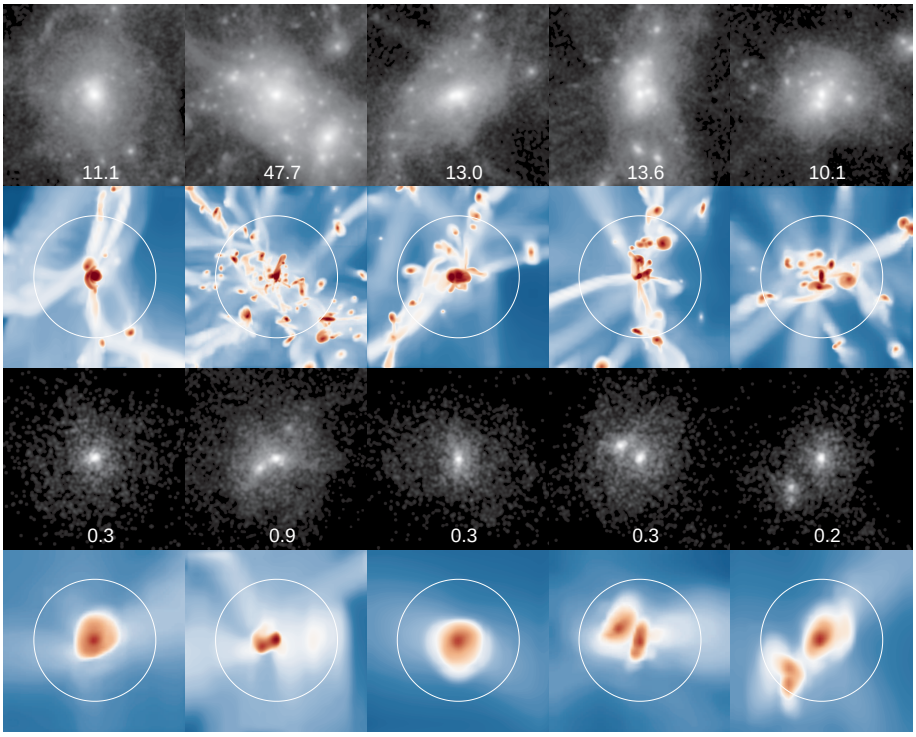


Figure 3.1: Five randomly chosen projected densities of the gas and dark matter at $z = 3.8$ from the HORIZON-MARENOSTRUM simulation. The mass of each halo is indicated at the bottom of each panel in units of $10^{11}\,M_{\odot}$. White circles denote the virial radii. The reddest and bluest colours indicate the gas density of $n_{\rm H} = 1\,{\rm cm}^{-3}$ and $10^{-5}\,{\rm cm}^{-3}$. Gas accretion is largely filamentary.

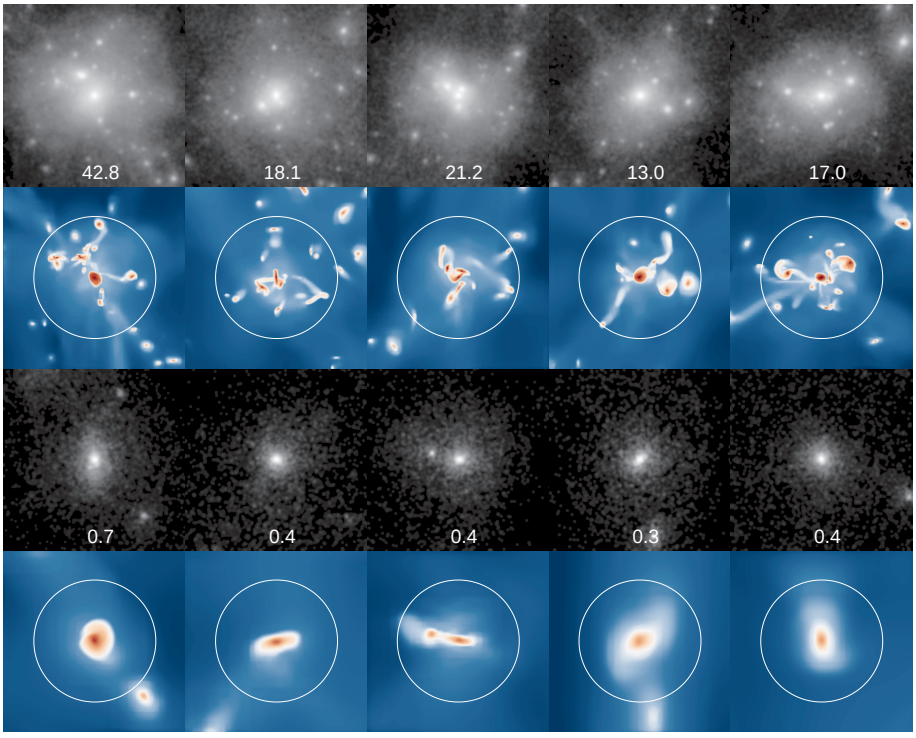


Figure 3.2: Same as Fig. 3.1, but for $z = 1.5$. Gas accretion is now less filamentary and more diffuse, compared to that from high redshift.

## 3.3 Results

### 3.3.1 Covering Fraction of Dense Gas

OPT08 showed that the transition mass ($M_{\rm stream}$) separating cold from hot dominated accretion increases with increasing redshift. According to these authors, by $z \sim 2.5$, the cold streams feeding massive haloes ($M_{\rm vir} \gtrsim 3 \times 10^{11} M_{\odot}$) begin to disappear, but based on measurements of a handful of haloes in the HORIZON-MARENOSTRUM simulation at $z \sim 2.5$, Dekel et al. (2009) find that some massive haloes with $M_{\rm vir} \sim 10^{12} M_{\odot}$ still show high covering fractions ( $\lesssim 25\%$) of dense ($N_{\rm H} > 10^{20} {\rm cm}^{-2}$) and cold ($\rm T < 10^5 K$) inflowing gas within $20 < r < 100$ kpc. In order to obtain statistically significant results on the covering fraction in the HORIZON-MARENOSTRUM simulation, we analyse *all* the haloes in the simulation and show the results in Fig. 3.3. Using the complete sample, we find that the average covering fraction of haloes with $M_{\rm vir} \sim 10^{12} M_{\odot}$ at $z = 2.5$ is $\sim 5\%$, about a factor 5 less than the covering fraction reported in Dekel et al. (2009) for their sub-sample of $M_{\rm vir} \sim 10^{12} M_{\odot}$ haloes at $z \sim 2.5$. We note that this lower value is more consistent with the recent findings of Faucher-Giguère & Kereš (2011). However, whilst low covering fractions ($\sim 5\%$) are computed for most haloes at redshifts $z \lesssim 3$, those of higher redshift ($z \sim 3.8$) haloes are much larger ($\sim 25\%$), as can be seen in Fig. 3.3. This strong redshift evolution in the covering fraction of cold filaments between $z \sim 3.8$ and $z \sim 2.5$ reflects the aforementioned rapid transition from cold to hot dominated accretion. We note that these results are consistent with the OPT08 value of $\sim 10^{13} M_{\odot}$ for $M_{\rm stream}$ at $z = 4$.

An interesting feature present in Fig. 3.3 is that the covering fraction is higher in more massive haloes at a given redshift. This seems to contradict previous findings (OPT08) that it is the small haloes which are mainly fed by cold mode accretion. It should be noted, however, that the covering fraction shown in Fig. 3.3 does not account for the accretion of cold, *diffuse* gas (cold gas with lower column densities) which is only present in haloes with masses incapable of sustaining a virial shock at all. Indeed, these small haloes are usually located within (or around) filaments whose density is low, whereas the filaments around more massive haloes tend to be denser. Furthermore, in massive haloes, satellite galaxies contribute more importantly to the covering fraction, as do extended, warped, galactic disks and dense gas bridges which result from tidal interactions between galaxies. These latter effects partly explain the trend, but the primary driver of the covering fraction increase with halo mass is the density of the accreted gas, which is higher in more massive haloes. Fig. 3.3 (dotted lines) substantiates this claim by showing how the covering fractions drop when the very dense gas ($\rm N_H > 10^{21} cm^{-2}$) which belongs to the ISM of satellite galaxies is excluded from the measurement.

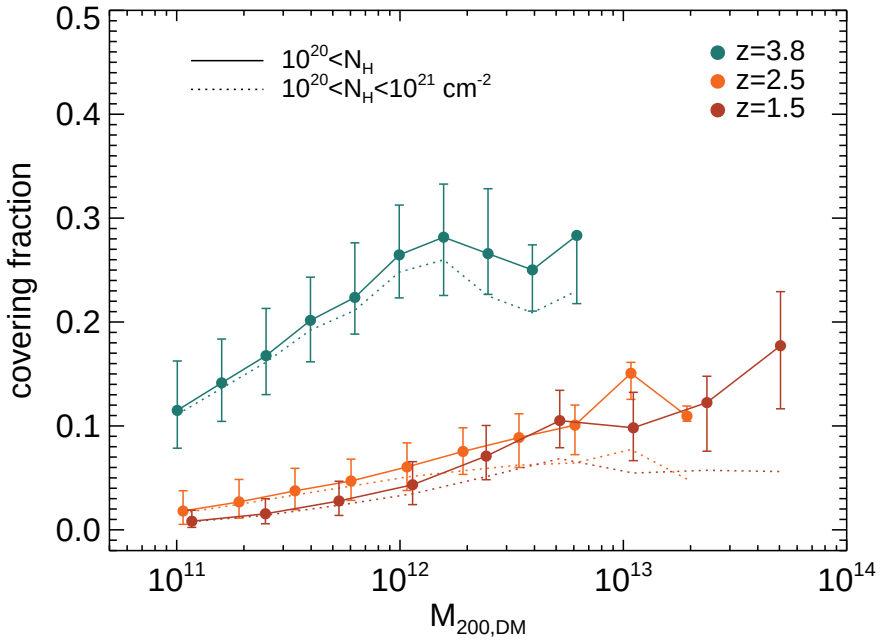


Figure 3.3: The covering fraction of cold ($T < 10^5 K$) and dense ($N_{\rm H} > 10^{20}$) gas within $20 < r < 100$ kpc physical as a function of the virial mass of haloes ($M_{\rm vir}$). Different colours indicate the covering fractions at different redshifts. Solid lines include the contribution from the interstellar medium of satellite galaxies to the covering fraction. To exclude this latter contribution, we also plot the covering fraction with upper density cut ($10^{20} < N_{\rm H} < 10^{21}$ cm$^{-2}$, dotted lines). Error bars correspond to the interquartile range ($25 \leq f \leq 75\%$). For a given halo mass, haloes at higher redshift show larger covering fractions. This can be understood in terms of the rapid development of a virialized hot medium between $z = 3.8$ and $z = 2.5$.

### 3.3.2 CII Absorption

In order to more carefully investigate the possibility of detecting cold filaments using metal absorption lines, we compute the strength of the CII $\lambda1334$ absorption. Our choice of line is dictated not only by the temperature of the filamentary gas which is not high enough to significantly produce more highly ionized metallic elements such as CIV, but also because it is empirically known to yield the strongest absorption feature (Steidel et al., 2010). We do not attempt to model absorption by CII accurately which would require detailed radiative transfer, but instead derive an upper limit by making several extreme assumptions. Firstly, we assume that all the carbon present in filaments is eligible for the CII $\lambda1334$ transition. Secondly, we use the solar abundance ratio ($[C/Z]_\odot \simeq 0.178$, Asplund et al. 2009) to obtain the carbon column density for a given metallicity in the simulation. The optical depth of a grid cell is computed as $\tau = \sigma_{\rm CII} n_{\rm CII} \Delta l$, where $n_{\rm CII}$ is the carbon number density, $\Delta l$ is the size of the grid cell, and $\sigma_{\rm CII}$ is the cross-section for the line transition, which is calculated as

$$\sigma_{\rm CII} = (3\pi\sigma_{\rm T}/8)^{1/2} f \lambda_0 \simeq 1.5 \times 10^{-18} {\rm cm}^2.$$

Here $\sigma_{\rm T}$ is the Thomson cross-section, $\lambda_0$ is the rest-frame wavelength of the transition, and $f$ is the corresponding oscillator strength. We then correct the optical depth by assuming that each grid cell has a Gaussian velocity distribution with a dispersion ($\sigma_{\rm 1D}/2$), which is obtained from the line-of-sight velocity dispersion ($\sigma_{\rm los}$) computed using the closest 27 neighbouring cells. We have tested the validity of the correction by using a high resolution in the NUT series (12 pc resolution, Devriendt et al. *in prep.*), and found that this procedure yields an accurate approximation of the maximum absorption strength and FWHM of the absorption profile that one would derive by using a much higher number of resolution elements. Finally stars are assumed to dominate the UV emission and we use the Maraston (2005) spectral energy distributions to derive the continuum flux around $\lambda \sim 1334\mathring{A}$, which depends on their mass, age, and metallicity. The emission from each star particle in the galaxy is then used to estimate an observed flux, as attenuated by intervening gas present along the line of sight. Note that only the flux emitted by the central 10 kpc$^2$ of a galaxy is used to compute the absorption line so as to mimic the observational resolution of FWHM$\simeq 0.40''$ for galaxies at $z \sim 2$ (Steidel et al., 2010).

Fig. 3.4 shows the HI column density map, projected metallicity distribution, and the corresponding absorption profile for a galaxy residing in a $M_{\rm vir} \sim 10^{12} M_\odot$ halo at $z \sim 3.8$. A dense filament is clearly seen not only in the H column density map, but also in the metallicity map, with metallicity ($\sim 10^{-4} - 10^{-3} Z_\odot$). The filamentary gas is receding from the observer; hence if detectable it should produce a redshifted absorption line. However, it turns out that the absorption signal is dominated by the ISM of the galaxy lighting up the filament. When the absorption due to the ISM is arbitrarily removed by neglecting the opacity from the gas inside the central gas disc ($r < 0.1 r_{200}$), the absorption feature vanishes (green line). Even when the gas outside $r > 0.1 r_{200}$ is assumed to have solar metallicity, the absorption strength is still much smaller (red dotted line) than the absorption produced by the galaxy's ISM (grey and blue dashed lines). This strongly suggests that the primary reason why it is so difficult to detect the cold filament is that the density of the filamentary gas is much lower than that of the galaxy's own ISM. As a result, and since the two absorption lines are not well enough separated in velocity space, the filament absorption signal is completely swamped by the high level of ISM absorption in the red wing of the line.

In order to see if we can bring out the filamentary signal by stacking absorption profiles, we analyse the absorption spectra of 132 and 386 massive galaxies ($M_{200} \geq 10^{12} M_\odot$) at $z = 3.8$ and $z = 2.5$ respectively along 6 projections ($+x, -x, +y, -y, +z, -z$) and find that the optical depth for the CII $\lambda 1334$ transition by the filaments is fundamentally small regardless of redshift. Fig. 3.5 shows that

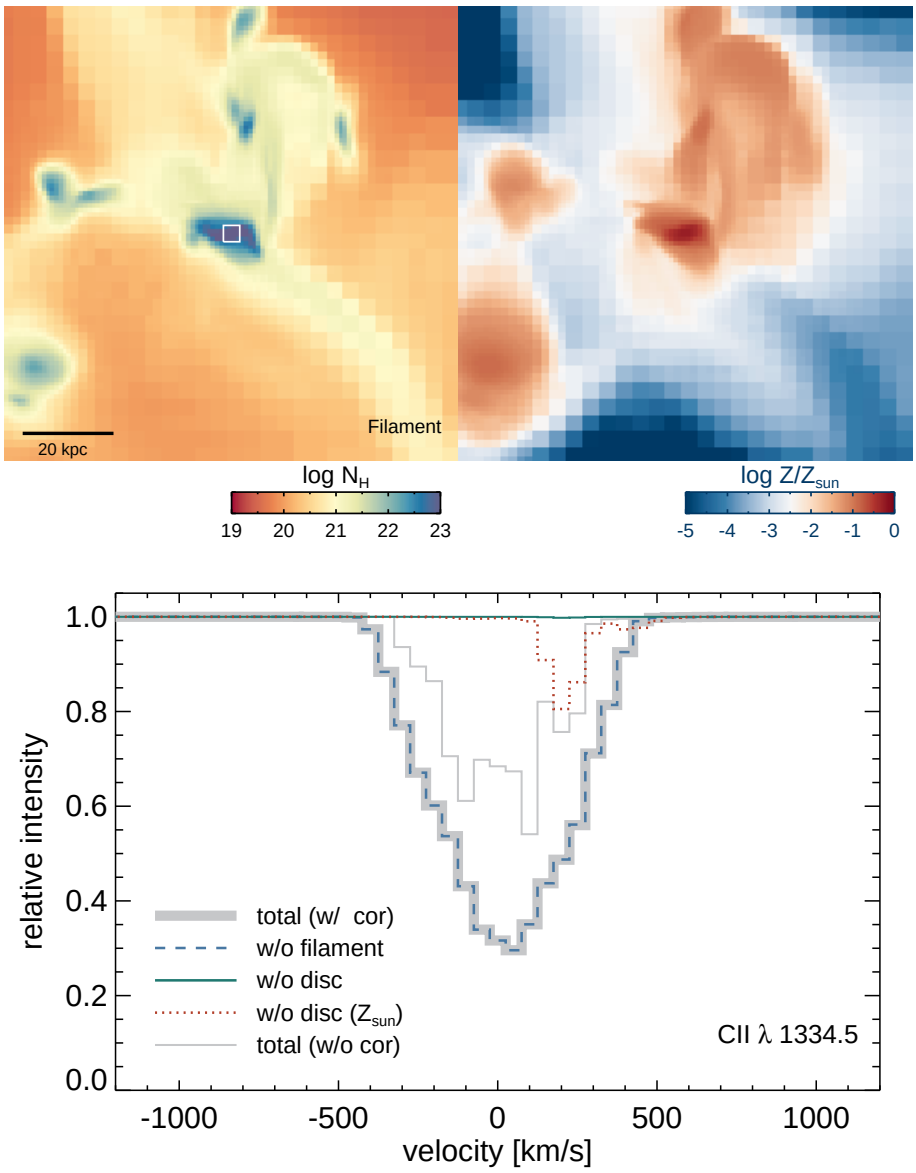


Figure 3.4: An example of the contribution from filamentary gas to the CII $\lambda1334$ absorption. Upper panels show the hydrogen column density and mass-weighted metallicity distributions for a $10^{12}M_{\odot}$ halo at $z \sim 3.8$. A cold filament is indicated on the left panel, which is receding from the observer and therefore should produce a redshifted absorption line. A white square denotes the central $\sim$10 kpc$^2$ region over which the absorption spectrum is obtained. Bottom panel shows an absorption profile of this galaxy (thick grey solid line). We also compute the absorption without the central disc by neglecting the opacity of central cells ($r \leq 0.1r_{200}$) (green solid line) and absorption without the outer gas ($r > 0.1r_{200}$) (blue dashed line). Also included is the absorption produced when the outer gas ($r > 0.1r_{200}$) is assumed to have solar metallicity in the absence of the central disc (red dotted line). It can be seen that the contribution from the filament to the low-ionisation metal line is negligible compared to that of the ISM of the galaxy in every case. An uncorrected spectrum is included to show the effect of the correction applied to the velocity distribution of gas (thin solid grey line).

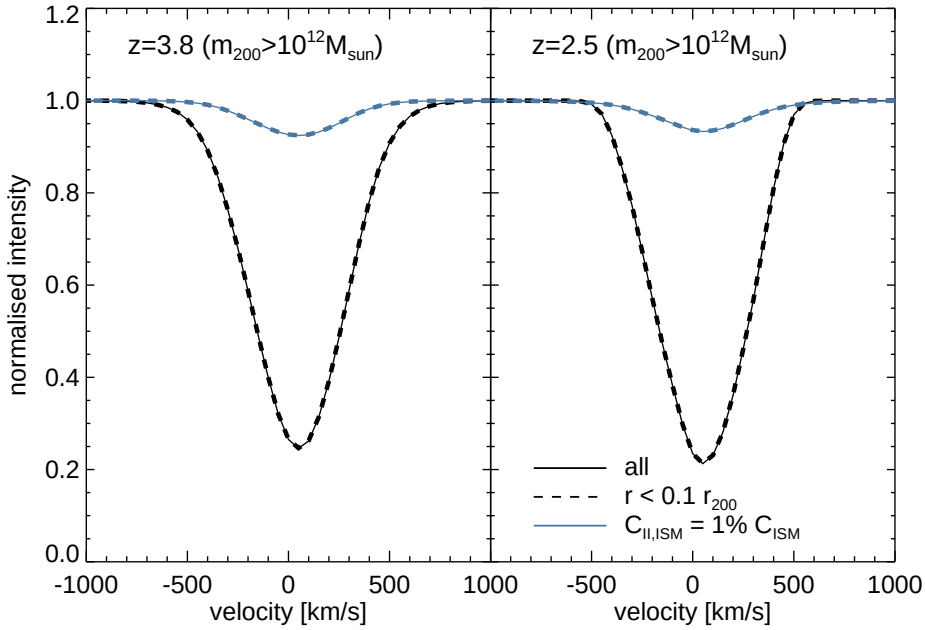


Figure 3.5: Stacked absorption profiles of massive galaxies ($M_{200} \geq 10^{12} M_{\odot}$) at $z = 3.8$ (left) and $z = 2.5$ (right). We take 6 projections ($+x, -x, +y, -y, +z, -z$) for 132 galaxies at $z = 3.8$ and 386 galaxies at $z = 2.5$. The stacked spectra are obtained by taking the mean of the normalised intensity. We also show the absorption spectra expected when only a fraction (1%) of the ISM carbon is assumed to produce the absorption (blue lines, see the text). The contribution from the outer regions (i.e. filament if any) is negligible in the absorption profile.

the stacked (mean) absorption strength is unaffected by the presence of filaments. To check whether the signal from filaments could potentially become noticeable if the ISM was less metal-enriched, we also examined the case where only a tiny fraction (1%) of the carbon in the ISM is eligible for the CII transition (blue lines in Fig. 3.5), but the difference between absorption profiles resulting from all the gas along the line of sight versus the case where we exclude the gas in the central region ($r < 0.1 r_{200}$) is still minute. Therefore, we conclude that the presence of cold filaments is very difficult to confirm with low-ionisation metal absorption lines.

The optical depth of filaments may be under-estimated due to the finite resolution of the HORIZON-MARENOSTRUM simulation. For example, the density of the filamentary structure at $z = 7$ in the HORIZON-MARENOSTRUM simulation ($0.005 \lesssim n_{\rm H} \lesssim 0.1$) is more than an order of magnitude lower than that of the NUT simulation ($0.1 \lesssim n_{\rm H} \lesssim 1$) where the filaments are fully resolved (Powell et al., 2011). However, this increase does not suffice to produce a strong absorption signal. Moreover, we find that the effect of increasing resolution affects the ISM density more considerably (it becomes more than four orders of magnitude higher in the NUT than in the HORIZON-MARENOSTRUM simulation). As a consequence the ISM causes a stronger absorption signal, which more than compensates the increased

contribution from the cold filament.

It should also be noted that finite resolution affects the metallicity of the filamentary gas, so that in the real Universe its metallicity may be higher than the values ($\sim 10^{-4} - 10^{-3} Z_{\odot}$) we report for the HORIZON-MARENOSTRUM simulation. Indeed, our simulation cannot resolve all the small galaxies that might pollute the pristine filamentary gas. Besides, it is well known that the energy from supernovae will artificially be dissipated when simulations are run with an insufficient level of resolution. Indeed, in such a case, supernovae only explode in dense grid cells, resulting in substantial radiative losses and negligible momentum transfer to the surrounding gas. Under these circumstances, metals cannot disperse properly. For comparison, the ultra-high resolution NUT simulation indicates that the metallicity of the filamentary gas around a $\sim 10^{9} M_{\odot}$ galaxy can reach values up to $10^{-2} Z_{\odot}$ already at $z \simeq 7$. Yet, such an increase in metallicity would still be inconsequential for the absorption spectra. Furthermore, we believe that the metallicity in the filaments is not likely to rise appreciably beyond these values, because most of the supernova ejecta escapes in a direction perpendicular to that of the elongated filament, which makes it difficult to efficiently enrich the filamentary gas with metals (Geen et al., 2012). However, for the sake of completeness, we present in Fig. 3.4 the case of a halo for which the gas outside $r > 0.1 r_{200}$ is arbitrarily assumed to have solar metallicity. We find that the absorption strength of the filament (red dotted line) is still much smaller than the absorption produced by the galaxy's ISM.

## 3.4 Conclusions and Discussion

Cosmological simulations predict that high-z galaxies grow by acquiring gas from cold streams (Dekel et al., 2009), but no observational confirmation has been obtained yet. Based on a statistical sample from the HORIZON-MARENOSTRUM simulation, we argue that low-ionisation metal absorption features, such as CII $\lambda 1334$, arising from intervening cold filaments are extremely hard to distinguish from absorption by the ISM of high-z star-forming galaxies. This is primarily because the optical depth for the low-ionisation transition from cold filamentary gas is minuscule, compared with that of the ISM of the host galaxy. Moreover, the filamentary absorption is not redshifted enough with respect to the ISM absorption, so that the residual ISM absorption in the red wing of the line is still prominent. This small optical depth of filaments mainly finds its source in the intrinsically low densities and metallicities of the cold gas when compared to those of the galaxy's ISM. Another factor is the geometry of the flow which lowers the probability of detecting filaments as their column density will rarely be maximised by being aligned with the line of sight.

As an alternative to using a single galaxy, one could probe circumgalactic regions by using a paired background galaxy. This method alleviates the importance of ISM absorption since when probing circumgalactic regions in this way, the absorption by the ISM of the foreground galaxy will occur at a different spatial position from that produced by filaments. Unfortunately, the rare occurrence of suitable foreground-background galaxy pairs makes it difficult to probe more than one line of sight per foreground galaxy. As a result, high resolution individual spectra are hard to obtain and one has to resort to stacking the spectra of multiple galaxies (Steidel et al., 2010). Contrary to what might be expected, stacking will wash out the cold filament absorption signal since absorption by inflowing gas does not neatly separate from that caused by outflows as was the case when probing the circumgalactic region using single galaxies. Indeed, cold filament absorption against the background galaxy light will not only be redshifted, but also blueshifted as one expects that on average as many cold streams will be detected moving towards as away from the observer. Absorption by outflows will also suffer the same fate. This will make it all the more difficult to argue whether the observed absorption features are driven by infalling gas or by outflows from high-z star-forming galaxies. Moreoever, the metal column density of cold filaments is minuscule, as already mentioned. The hydrogen column densities of the cold filaments are distributed around $10^{20}\mathrm{cm}^{-2}$ at these redshifts, yielding corresponding carbon column densities around $10^{16}\mathrm{cm}^{-2}$ if an average $Z = 0.001Z_{\odot}$ is used. Even if all carbon atoms are assumed to be eligible for the CII transition, the optical depth is only around $10^{-2}$ in the line. On the other hand, outflows are expected to be very metal rich, so that even though higher transitions like CIV are expected to dominate the absorption signal, the amount of CII absorption from these outflows might still swamp that produced by the cold filaments.

Finally, we have assessed possible numerical resolution issues on column density and metallicity of the filaments using the very high resolution numerical simulation NUT suite and found that our conclusions remain by and large unchanged.

Based on these considerations, we conclude that the presence of the cold filament is difficult to disprove/prove with low-ionisation metal line absorption. Instead, we note that, in the absence of metal cooling, thermal energy can be effectively converted into Ly$\alpha$ photons at $10^4$–$10^5$ K, which is the typical temperature of cold filaments. Thus, the Lyman $\alpha$ emission route seems more promising to detect cold filaments. Indeed, Rosdahl & Blaizot (2012) predicted using full blown radiative transfer calculations that the large-scale cold filaments would clearly be visible at $I_{\mathrm{Ly}\alpha} = 10^{-19}\,\mathrm{erg\,s^{-1}\,cm^{-2}\,arcsec^{-2}}$ (see their Fig. 14). Future instruments, such as Multi Unit Spectroscopic Explorer (MUSE, Bacon et al.,

2006), are expected to detect a flux of the same order, and will play an important role in probing cold filaments.

# Chapter 4

# Cosmic Angular Momentum of Baryons and Dark Matter

## 4.1 Introduction

Along with mass, angular momentum growth shapes the fundamental properties of galaxies. Using linear theory, one can show that density perturbations acquire angular momentum through their asymmetric interactions with the larger scale tidal field (Peebles, 1969; Doroshkevich, 1970; White, 1984). Thus one expects the angular momentum of the Lagrangian region encompassing a future virialized structure to scale like $a^2(t)\dot{D}(t)$ until it decouples from the Hubble expansion, where $a$ and $\dot{D}$ are the scale factor of the universe and the linear growth rate of density perturbations, respectively (White, 1984). Further assuming that the gas experiences the same tidal field as the dark matter, they should initially share their specific angular momentum. Provided this specific angular momentum is conserved as the gas radiatively cools, early studies were able to reasonably match crucial observed relations, such as the Tully-Fisher relation or the size-rotation velocity relation (Fall & Efstathiou, 1980; Dalcanton et al., 1997; Mo et al., 1998). In spite of several severe shortcomings in the theory pointed out by authors like Hoffman (1986) (including no account of secondary infall and mergers between virialized objects), this success encouraged all (semi-analytic) galaxy formation models published to date (e.g. Cole et al., 2000; Firmani & Avila-Reese, 2000; Hatton et al., 2003; Croton et al., 2006; Monaco et al., 2007; Stringer & Benson, 2007; Somerville et al., 2008; Dutton & van den Bosch, 2009; Firmani & Avila-Reese, 2009; Khochfar & Silk, 2011) to rely on the core assumption that gas and dark matter contained within the same virialized structure split specific angular momentum equally. However, the recent findings that the vast

majority of galaxies are mainly fed gas by cold, thin and dense filaments which penetrate deep inside the virial radius of their host dark matter halo (e.g. Kereš et al., 2005; Ocvirk et al., 2008; Dekel et al., 2009; Powell et al., 2011) begs for a reassessment of the validity of the classical angular momentum scenario.

According to the standard picture of galaxy formation, gas is first shock-heated to the virial temperature of its dark matter halo host as the latter collapses, and subsequent accreted material encounters the resulting virial shock as it penetrates the halo (Rees & Ostriker, 1977; Silk, 1977; White & Rees, 1978). Since the shock-heated gas is more or less spatially re-distributed as the dark matter before it can cool, one is led to logically postulate that its specific angular momentum closely tracks that of the dark matter halo. Non-radiative hydrodynamical cosmological simulations have confirmed that this is the case (e.g. van den Bosch et al., 2002).

However, as soon as the gas is permitted to radiatively cool and form stars, this tight correlation between gas and dark matter spin should break down. For instance, a fraction of gas accreted at earlier times with lower angular momentum will be converted into stars, elevating the specific angular momentum of the remaining gas (Dutton & van den Bosch, 2009). Meanwhile the specific angular momentum of the dark matter halo is expected to either be frozen in after turn around or decline due to the presence of external torques (c.f. Peebles, 1969; Book et al., 2011). Hence it is not very surprising that radiative hydrodynamics cosmological simulations show a difference in the spin parameters between gas and dark matter. Indeed, Stewart et al. (2011b) have recently reported that for a pair of resimulated halos, cold gas had 3 to 5 times more specific angular momentum than dark matter (see also Sales et al., 2010). In this context, the questions which naturally arise are: (i) what are the mechanisms that segregate dark matter and gas angular momenta? (ii) is this segregation universal or does it depend on halo properties? and (iii) does it evolve with redshift? Since the gas is the main agent for transferring angular momentum from (super) halo scales down to central galaxies, it is key to investigate the evolution of its angular momentum in the region extending between the galaxy and the virial radius of the dark matter halo (i.e. $0.1r_{\rm vir} < r \leq r_{\rm vir}$).

Within galaxy size virialised halos, the picture of gas accretion has recently been significantly revised, with the rediscovery of an idea first put forward by Binney (1977) that infalling gas is never shock-heated to the virial temperature but instead flows through an 'isothermal' shock, reaching the galactic disc cold (Fardal et al., 2001; Katz et al., 2003; Birnboim & Dekel, 2003; Kereš et al., 2005; Ocvirk et al., 2008; Brooks et al., 2009). Moreover, this gas is brought along anisotropic narrow streams which persist deep within the halo, contrary to their broader dark matter counterparts which rapidly fade

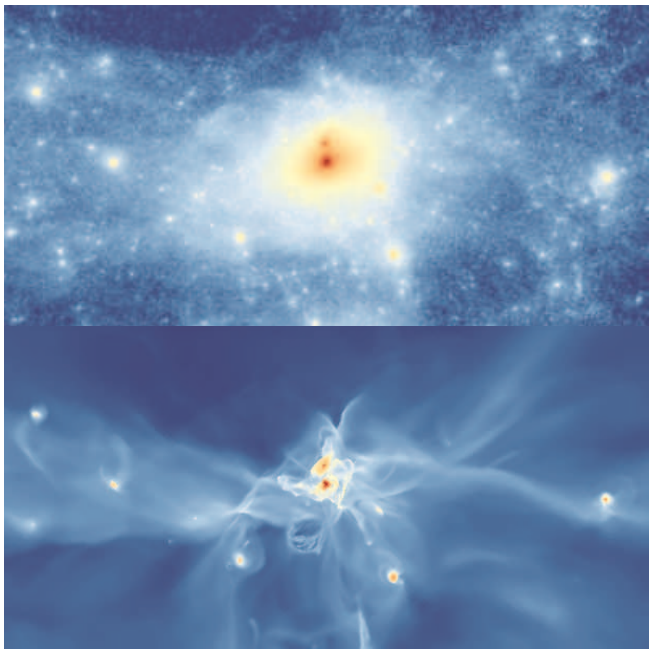

Figure 4.1: Projected densities of the dark matter (top) and gas (bottom) centred on a halo of $\simeq 10^{11} M_{\odot}$ at $z = 3$ from the NUT simulation with supernova feedback (NutFB). A $6r_{\rm vir}$ region is projected and a figure with aspect ratio 1:2 is displayed, where the longer length corresponds to $6r_{\rm vir}$ ($= 224$ kpc). At $z = 3$ the scale-height of the disc as well as the large scale filamentary structure is well resolved in the simulation. It can be seen that dark matter filaments are broader than gas filaments. The gas filaments are not destroyed by supernova explosions.

away at the virial radius (Powell et al., 2011). Therefore, one wonders how differently this filamentary gas advects angular momentum throughout the halo.

With such questions in mind, we use a set of high-resolution cosmological simulations to revisit two key assumptions of disc formation theory, namely that gas carries the same amount of specific angular momentum as its host dark matter halo and that this specific angular momentum is conserved as this material gets accreted onto the central disc. The details of the simulations are described in Section 4.2. In Section 4.3, we review the standard theory of disc galaxy formation and compare angular momentum of gas and dark matter from non-radiative hydrodynamic simulations. In Section 4.4, we investigate the time evolution of angular momentum of baryons and non-baryonic matter along with a comparison to observational data at $z = 0$ and discuss how our results compare with the standard picture. Finally, we discuss the implications and the relevance of feedback and conclude in Section 4.5.

## 4.2 Simulations

We use the Eulerian AMR code, RAMSES (Teyssier, 2002), to investigate the angular momentum evolution of baryons and dark matter. RAMSES uses a second-order Godunov scheme to solve the Euler

Table 4.1: Summary of simulation parameters and physical ingredients. From left to right, columns are as follows: simulation name, comoving box size, number of dark matter particles, minimum grid size, dark matter particle mass, star particle mass, threshold density for star formation, redshift down to which the simulation is carried out, indication of whether supernova feedback is included, and redshift at which UV background heating is initiated.

| Simulations | L (Mpc/h) | $N_{\rm DM}$ | $\Delta x_{\rm min}$ (pc) | $m_{\rm DM}$ ($M_\odot$) | $m_{\rm star}$ ($M_\odot$) | $n_{\rm th}$ (H/cm$^3$) | $z_{\rm end}$ | SN | UV |
|---|---|---|---|---|---|---|---|---|---|
| NutAD | 9 | $1024^3$ | 48 | $5 \times 10^4$ | – | – | 0 | – | z=8.5 |
| NutCO | 9 | $1024^3$ | 48 | $5 \times 10^4$ | $3 \times 10^4$ | 10 | 0 | – | z=8.5 |
| NutFB | 9 | $1024^3$ | 12 | $5 \times 10^4$ | $2 \times 10^4$ | 400 | 3 | Y | z=8.5 |
| MareNostrum | 50 | $1024^3$ | 1090 | $1 \times 10^7$ | $2 \times 10^6$ | 0.1 | 1.5 | Y | z=8.5 |
| Cosmo25 | 25 | $256^3$ | 1090 | $8 \times 10^7$ | $4 \times 10^6$ | 0.1 | 0 | Y | z=10.5 |
| Cosmo50 | 50 | $256^3$ | 2180 | $6 \times 10^8$ | $3 \times 10^7$ | 0.1 | 0 | Y | z=10.5 |

equations, and an adaptive particle-mesh method to solve the Poisson equation. Since the outcome of hydrodynamics simulations is subject to resolution and physical ingredients, we make use of five simulations to draw robust conclusions. These simulations include the NUT series (Powell et al. 2011), the HORIZON-MARENOSTRUM simulation (Ocvirk et al., 2008; Devriendt et al., 2010), and two other cosmological simulations (Cosmo25, Cosmo50; Dubois et al. 2012a) of fairly large volumes but with lower resolution than the HORIZON-MARENOSTRUM simulation. Whereas simulations in the NUT series focus on the evolution of an individual, Milky Way-like galaxy, the HORIZON-MARENOSTRUM, Cosmo25 and Cosmo50 simulations give the statistical properties of galaxies spanning a wide range of halo mass. Physical ingredients common to most of our simulations include reionisation, cooling, star formation and supernova feedback. These are summarised in Table 4.1, along with simulation parameters.

To model the reionisation of the Universe, a uniform UV background radiation field (modelled as a heating term in the energy equation) is turned on at high redshift (see Table 4.1) following Haardt & Madau (1996). Gas dissipates energy through atomic cooling down to $10^4$ K (Sutherland & Dopita, 1993). For the NUT simulations metal line cooling can lower the gas temperature further (below $\sim 10$ K). When the gas density in a grid cell exceeds a given threshold ($n_{\rm th}$, see Table 4.1), star particles are spawned by a Poisson process according to a Schmidt law with a 1% efficiency of the star formation per free-fall time (Kennicutt, 1998; Dubois & Teyssier, 2008). This threshold density is chosen so that it is inferior or equal to the maximal Jeans density reached on the finest level. In the simulations with supernova feedback, after $\sim 10$ Myrs, massive stars undergo Type II supernova explosions, releasing half of their $10^{51}$ ergs into their surroundings as kinetic energy and the other half as thermal energy (Dubois & Teyssier, 2008). During this phase, processed heavy elements are dispersed, enriching the interstellar and intergalactic medium. In what follows, we elaborate on the details of each simulation.

The NUT series make use of the resimulation (also called 'zoom') technique to follow the evolution of a Milky Way-type galaxy in a ΛCDM cosmology. Powell et al. (2011) reported on high redshift results (z $\geq$ 9) from the ultra-high resolution resimulations in the NUT series. These reached a maximum physical spatial resolution of $\sim$ 0.5 pc at all times. To track the evolution of the galaxy down to lower redshifts, the NUT suite also includes three resimulations with lower *spatial* resolution (but identical DM particle mass resolution) and the following physics: (i) adiabatic with a uniform UV background turned on instantaneously at $z = 8.5$ (NutAD) (ii) cooling, star formation, and UV background (NutCO) and (iii) same as (ii) but with supernova feedback and metal enrichment (NutFB). NutAD and NutCO have maximum 48 pc (physical) resolution at all times and reach $z = 0$, whereas NutFB has maximum 12 pc (physical) resolution and only reaches $z = 3$. Figure 4.1 shows a snapshot of the DM (upper panel) and gas (lower panel) of a region centred on a halo hosting a Milky Way-type galaxy at $z = 3$ in NutFB.

We recall the important details of the NUT resimulations here. The simulation volume is a $9h^{-1}$ Mpc comoving periodic box evolving according to a WMAP5 cosmology (Dunkley et al., 2009) ($\sigma_8 = 0.8$, $\Omega_m = 0.258$, $\Omega_\Lambda = 0.742$, $h \equiv H_0/(100\mathrm{kms}^{-1}\mathrm{Mpc}^{-1}) = 0.72$). Initial conditions are generated using `MPgrafic` (Prunet et al., 2008), a parallel version of the Grafic package (Bertschinger, 2001). Within this volume we identify the region where a Milky Way-like galaxy (halo virial mass of $\simeq 5 \times 10^{11} \mathrm{M}_\odot$ at $z = 0$) will form. This region encompasses a volume of side length $\sim$ 2.7 $\mathrm{h}^{-1}$ Mpc. While the root grid for the entire simulation volume is $128^3$, within the ($\sim$2.7 $\mathrm{h}^{-1}$ Mpc)$^3$ region, we place an additional three nested grids, giving an equivalent resolution of $1024^3$ dark matter particles, each with mass $\mathrm{M_{DM}} \simeq 5 \times 10^4 M_\odot$. To fix the maximum physical resolution to a constant value (12 pc for NutFB and 48 pc for NutCO and NutAD) as the universe expands and the simulation evolves, we further refine on the finest fixed grid within the 2.7 $\mathrm{h}^{-1}$ Mpc$^3$ region according to a quasi-Lagrangian strategy, i.e. when the number of dark matter particles in a cell reaches 8 or equivalently when the baryon plus dark matter density in a cell increases by a factor of 8. Table 4.1 lists the maximum level triggered for each simulation. Because of the higher spatial resolution in NutFB it uses a higher density threshold for star formation ($n_{\mathrm{H,th}} = 400\ \mathrm{cm}^{-3}$) than the NutCO run ($n_{\mathrm{H,th}} = 10\ \mathrm{cm}^{-3}$). The star particle mass ($\simeq 2 - 3 \times 10^4 M_\odot$) is determined by the combination of minimum grid size and density threshold for star formation (Dubois & Teyssier, 2008). In NutFB, we assume that every supernova bubble with an initial radius of 32 pc sweeps up the same amount of gas as that initially locked in the star particles. This is usually expressed as a mass loading factor of unity ($\eta = 1$).

The other three simulations are large volume cosmological simulations, and as such are performed

with lower spatial (1–2 kpc) and mass resolution. More specifically, the mass of each dark matter particle is $m_{\rm DM} \simeq 10^7 M_\odot$ for the HORIZON-MARENOSTRUM simulation, $8 \times 10^7 M_\odot$ for the intermediate size run (Cosmo25) and $6 \times 10^8 M_\odot$ for the Cosmo50 run. As in the NutFB run, supernova feedback and UV background heating are included in the simulations, but the radius of the initial supernova bubble is set to twice the minimum size of the grid (see Table 4.1). Note also that the adopted cosmology for the HORIZON-MARENOSTRUM simulation (WMAP1) is different from the others, but as we will show this has very little impact on our results, if at all. We refer interested readers to Ocvirk et al. (2008) and Devriendt et al. (2010) for a detailed description of the HORIZON-MARENOSTRUM simulation set-up.

In all the simulations, we identify (sub) haloes using the ADAPTAHOP algorithm (Aubert et al., 2004), which is based on the detection of peaks and saddle points in the dark matter density field, supplemented by the most-massive subhalo algorithm developed by Tweed et al. (2009). The virial radius of halos is defined as the maximal radius within which the virial theorem is satisfied to better than 20%. We further define gas belonging to a satellite galaxy as gas residing within the half-mass radius of its host DM satellite halo. The centre of a halo, which we use to compute angular momentum, is defined as the centre of mass of dark matter and baryons. The mean motion of the halos is determined by computing the centre of mass velocity of dark matter particles, gas, and stars within their virial radii.

### 4.2.1 Measurement of angular momentum

To understand how galaxies acquire their angular momentum, we study the angular momentum evolution of the different components (gas, dark matter, stars) inside their host halos. We compute the specific angular momentum vectors as:

$$\vec{\mathbf{j}} = \frac{\sum_i m_i \vec{\mathbf{r}}_i \times \vec{\mathbf{v}}_i}{\sum_i m_i},$$

where $\vec{\mathbf{r}}_i$ is the radial distance from the centre of mass of the halo (includes dark matter and baryons), $\vec{\mathbf{v}}_i$ is the peculiar velocity and $m_i$ is the mass of the i-th dark matter (star) particle or gas cell. In what follows, we use different subscripts to denote the specific angular momentum of different components in different regions of the halo. These are summarised in Table 4.2

Note that specific angular momenta measured in different regions of the halo, such as $j_{\rm dm}$ and $j_{\rm gas,out}$, are often compared in this study. Rigorously speaking, this is incorrect and we should only compare quantities measured in the same spatial region of the halo. However, as we show below and as one can easily convince oneself, including/excluding the central part of the dark matter halo has little impact on our conclusions, because the central part ($r < 0.1 r_{\rm vir}$) only accounts for a small fraction $\lesssim 10\%$

Table 4.2: Notations (first column) for specific angular momenta used in this study. The first subscript indicates the component used for the calculation (DM, gas, stars, baryons). The second column specifies the region (normalised to the halo virial radius) over which the specific angular momentum is calculated. The default region over which we measure specific angular momentum is a sphere extending from the centre of mass of the halo to the virial radius. A second subscript indicates whether we exclude ($j_{\rm gas,out}$) or include ($j_{\rm gas,cen}$) the gas in the central region ($r/r_{\rm vir} \leq 0.1$) of the halo for the specific angular momentum calculation. The third column lists the components included in the specific angular momentum calculation.

| Notation | Spatial extent | Component |
|---|---|---|
| $j_{\rm dm}$ | $r/r_{\rm vir} \leq 1$ | dark matter |
| $j_{\rm dm,out}$ | $0.1 < r/r_{\rm vir} \leq 1$ | dark matter |
| $j_{\rm gas}$ | $r/r_{\rm vir} \leq 1$ | gas |
| $j_{\rm gas,out}$ | $0.1 < r/r_{\rm vir} \leq 1$ | gas |
| $j_{\rm gas,cen}$ | $r/r_{\rm vir} \leq 0.1$ | gas |
| $j_{\rm star}$ | $r/r_{\rm vir} \leq 1$ | all stars except those in satellite galaxies |
| $j_{\rm bar}$ | $r/r_{\rm vir} \leq 1$ | all stars (satellite galaxies included) + gas |

of the total halo mass and angular momentum. Hence, in order to facilitate the comparison with previous work in the literature where it is commonly assumed that the halo gas shares either the average or the specific angular momentum profile of its dark matter halo host, we use $j_{\rm dm}$ and $j_{\rm dm,out}$ interchangeably.

## 4.3 Standard Theory of Disc Galaxy Formation and Adiabatic Simulations

We begin our investigation by describing the standard theory of disc galaxy formation. In this picture, gas gains angular momentum through large-scale tidal torquing during the expansion phase of the Lagrangian region which ends up as the virialised halo (Peebles, 1969; Doroshkevich, 1970; White, 1984). As this gas enters the virialised dark matter halo, it gets shock-heated to the virial temperature (e.g. White & Rees, 1978). It then radiatively cools while conserving its angular momentum, forming a rotationally supported gaseous disc at the centre of the halo potential (Efstathiou & Jones, 1979; Fall & Efstathiou, 1980). The two fundamental assumptions which underpin the standard theory can therefore be summarised as follows:

1) the gas that enters the virialised halo having experienced the same tidal torques as the dark matter, it carries the same amount of specific angular momentum as the latter

2) this gas is shock heated and radiates away its energy, sinking down to the central region of the virialised halo while conserving its specific angular momentum

Under these assumptions, a disc galaxy in the standard, *static* model (Fall & Efstathiou, 1980; Mo et al., 1998) can simply be described by two parameters, the angular momentum fraction ($j_{\rm gal} = J_{\rm gal}/J_{\rm vir}$) and the mass fraction ($m_{\rm gal} = M_{\rm gal}/M_{\rm vir}$) of baryons which end up in the galaxy, where $J$ is the total angular momentum and $M$ is the mass. Such a simplification is only possible because the spin parameter (Peebles, 1971; Bullock et al., 2001) of dark matter halos depends very weakly on redshift and mass (e.g. Bett et al., 2007; Muñoz-Cuartas et al., 2011). The fundamental limitations of this standard static approach are twofold: (i) there is no compelling physical argument to decide which values $j_{\rm gal}$ and $m_{\rm gal}$ should have, and (ii) even if there was, the theory would still be unable to predict the evolution of the angular momentum of the galaxy as it grows.

Various solutions to these issues have been presented, which aim to follow the detailed growth of disc galaxies using mass accretion histories measured from either cosmological N-body simulations (Wechsler et al., 2002) or the Extended Press-Schechter formalism (van den Bosch, 2002) (e.g. Avila-Reese et al., 1998; Firmani & Avila-Reese, 2000; Stringer & Benson, 2007; Dutton & van den Bosch, 2009). These semi-analytic models assign rotating gas to concentric shells and compute how much they radiatively cool so as to track their collapse onto the central galaxy. Unfortunately, the angular momentum of such gas shells can be determined in several ways. For instance, Firmani & Avila-Reese (2009) inject an amount of angular momentum at the time of virialisation so that the spin parameter of the halo remains constant and the gas profile matches the universal angular momentum profile of dark matter halos as determined by Bullock et al. (2001). On the other hand, Stringer & Benson (2007) and Dutton & van den Bosch (2009) assume that freshly accreted gas carries angular momentum that is consistent with the angular momentum distribution (AMD) measured in non-radiative cosmological SPH simulations (Sharma & Steinmetz, 2005). The main advantage of these *dynamic* models lies in their predictive power for the self-consistent redshift evolution of observables such as disc galaxy sizes, as a function of mass (see e.g. Dutton & van den Bosch, 2009).

Even though different dynamic models adopt different strategies to study the build-up of galactic discs, their common underlying assumption is that the initially hot gas possesses an angular momentum which follows a similar distribution as that of dark matter. Such an assumption is supported by several non-radiative hydrodynamics simulations which demonstrate a similar AMD between hot gas and dark matter (van den Bosch et al., 2002; Sharma & Steinmetz, 2005). Thus, we refer to a model as 'standard' in this study if it is based on the two fundamental assumptions previously listed at the beginning of this section and *if its gas angular momentum matches the angular momentum distribution (AMD) or profile*

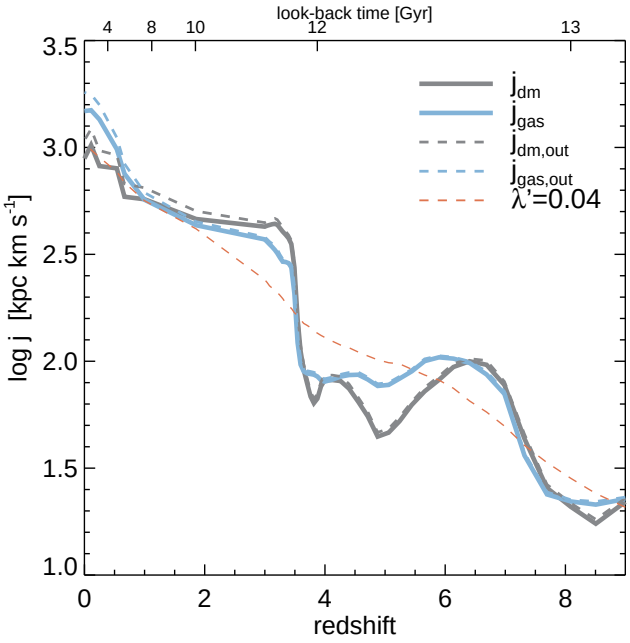


Figure 4.2: Evolution of the specific angular momentum ($j$) of a dark matter halo hosting a Milky Way-type galaxy in the adiabatic run (NutAD). Different colours denote different components: dark matter ($j_{\rm dm}$, solid grey), dark matter at $0.1 \leq r/r_{\rm vir} \leq 1$ ($j_{\rm dm,out}$, dashed grey), gas ($j_{\rm gas}$, thick blue), and gas at $0.1 \leq r/r_{\rm vir} \leq 1$ ($j_{\rm gas,out}$, dashed blue). We also display the specific angular momentum corresponding to a reduced spin value $\lambda' = 0.04$ (red dashed line) for the dark matter halo. The specific angular momentum of the halo gas ($j_{\rm gas,out}$) closely follows that of the dark matter halo ($j_{\rm dm}$) in this non-radiative simulation.

*(AMP) of dark matter haloes (Bullock et al., 2001) or 'adiabatic' gas (Sharma & Steinmetz, 2005) profiles.*

In principle, the two assumptions, i.e. the same tidal torquing and angular momentum conservation, cannot be violated in the Lagrangian point of view. However, a dark matter halo is an open system, and therefore one must consider the misalignment between different accretion events. In the standard theory of disc galaxy formation, the misalignment is neglected for simplicity by assuming that the spin vectors of concentric shells are well aligned. For this reason, it only focuses on the *net* angular momentum, which conveys incomplete information about how gas angular momentum is advected inside a dark matter halo. Moreover, since gas accretion process onto a galactic disc can be markedly different depending on the presence of radiative cooling, careful examination is called for to better understand the advection of angular momentum onto the central disc. If we relax the assumption to allow the misalignment between different concentric shells and radiative cooling, the gas may not share the same angular momentum profile or distribution as dark matter, as we will show in later sections.

### 4.3.1 Adiabaticity and the cosmic origin of angular momentum

In this study, we use a different computational technique, AMR, to solve hydrodynamic equations, as opposed to the previous works based on SPH technique. Therefore, we first reproduce the results of Sharma & Steinmetz (2005) and discuss the gross feature of the angular momentum evolution of a halo by analysing our non-radiative NutAD run.

Since gas cannot cool radiatively in this simulations, newly accreted material is shock-heated by the pressure supported intra-halo medium. As a result, its radially oriented initial velocity is isotropised, and drives the gas density field towards spherical symmetry. Accreted dark matter particles are also more or less isotropically redistributed within the host halo by the collisionless phase mixing and violent relaxation process. Given that (i) gas and dark matter within the halo experience the same larger-scale torques (e.g. Peebles, 1969; Book et al., 2011), and (ii) gas and dark matter are driven by the gravitational collapse to a very similar equilibrium distribution (i.e. to a good approximation that of an isothermal sphere since the total amount of angular momentum provided by tidal torques is very limited), we expect them to have similar $j$. Indeed, Figure 4.2 shows that $j_{\rm gas}$ or $j_{\rm gas,out}$ closely tracks $j_{\rm dm}$ regardless of whether or not mergers, easily identified by large jumps in $j$ (e.g. Vitvitska et al., 2002; Maller et al., 2002; Peirani et al., 2004), occur, reproducing the results from the earlier works (e.g. van den Bosch et al., 2002). When the dark matter angular momentum is expressed in terms of the spin parameter ($\lambda' = j_{\rm dm}/\sqrt{2}r_{\rm vir}V_{\rm c}$, Bullock et al. 2001), we recover the typical value of $\lambda' \simeq 0.04$ at all times with fluctuations of up to a factor of $\sim 2$ around this value. We have also found that our $z$-axis AMDs, $p(j_z)$, of the gas can be well fitted with the gamma function of Sharma & Steinmetz (2005) (Figure 4.6), where $j_z$ is defined as the component of specific angular momentum aligned with the total angular momentum vector of either dark matter or the gas. Although we have not included in this study, when a thermal broadening is applied to gas velocities using the temperature of each cell, we reproduce the results of van den Bosch et al. (2002) that the $z$-axis AMDs of the gas and dark matter are indistinguishable.

An interesting feature in Figure 4.2 is that $j_{\rm dm}$ increases with time (albeit at a reduced rate below $z = 3$), implying that late infall carries a larger amount of angular momentum. This is not a completely unexpected result given that dark matter haloes are known to experience little evolution of spin parameter with time (e.g. Peirani et al., 2004; Muñoz-Cuartas et al., 2011). As their mass and radius grow, so must their angular momentum. However, it is not trivial to understand *why* the late accretion has larger $j$. A naive answer is that material with larger angular momentum takes more time to reach the potential well, but this does not explain *how* it acquired such a large angular momentum in the first place. We discuss

in detail the cosmic evolution of the angular momentum of halos (which necessarily goes beyond tidal torque theory) in a companion paper (Pichon et al., 2011), but for completeness' sake, we briefly outline the main idea in the paragraph below.

The dynamics of the gas and dark matter flowing along what has been dubbed the 'cosmic web' can be understood as the anisotropic time evolution of the initial Gaussian random gravitational field. Cosmological structures originate as peaks in the associated initial density field (Bond et al., 1996), which are connected to other peaks through peak patches. The bulk motion of a peak patch is determined by the gradient of the large-scale potential. The latter also drives the motions of filaments which exist at the intersection of at least three void patches and connect peaks. As a consequence of the asymmetry between voids, the gas and dark matter flowing out of these voids acquire a transverse velocity when they intersect at a filament. This transverse velocity is the seed of a halo's angular momentum which is then advected along the filaments all the way into the halo sitting on the peak. Since the transverse velocity along a filament is constant to zeroth order approximation, the material initially located further away from the peak will naturally contribute more angular momentum. Note that the infall of matter along such filaments will *coherently* contribute an increasing amount of angular momentum as time goes on (shown in Figure 4.2), since the filament preserves its orientation over long stretches of time.

In summary, we have confirmed the earlier results that the non-radiative gas and dark matter share the similar AMD and hence the total specific angular momentum inside a halo (van den Bosch et al., 2002; Sharma & Steinmetz, 2005), supporting the standard picture of disc formation theory.

## 4.4 Simulations with Radiative Cooling

In the real Universe, gas can radiatively cool and form cold, dense filamentary structures at high redshift (Kereš et al., 2005; Ocvirk et al., 2008; Dekel et al., 2009; Brooks et al., 2009). The cold flows are efficiently brought in to a dark matter halo without being shock-heated at the virial radius. Even at lower redshift, gas accretion onto a dark matter halo is likely to have a preferential direction in that matter accretion is mainly driven by the dynamics of the large-scale cosmic web (e.g. Codis et al., 2012). Given the dissimilarity in the accretion process from the adiabatic case, it is necessary to reassess several assumptions made in the disc formation models.

For this purpose, we make use of the cooling run (NutCO) and feedback run (NutFB)[1]. The mass of the dark matter halo at $z = 0$ is $M_{\rm vir} \simeq 4 \times 10^{11} M_{\odot}$ (see Appendix A.3 for a time evolution of the halo

[1]Run with identical initial conditions and mass resolution, but with higher (12 pc) spatial resolution and supernova feedback

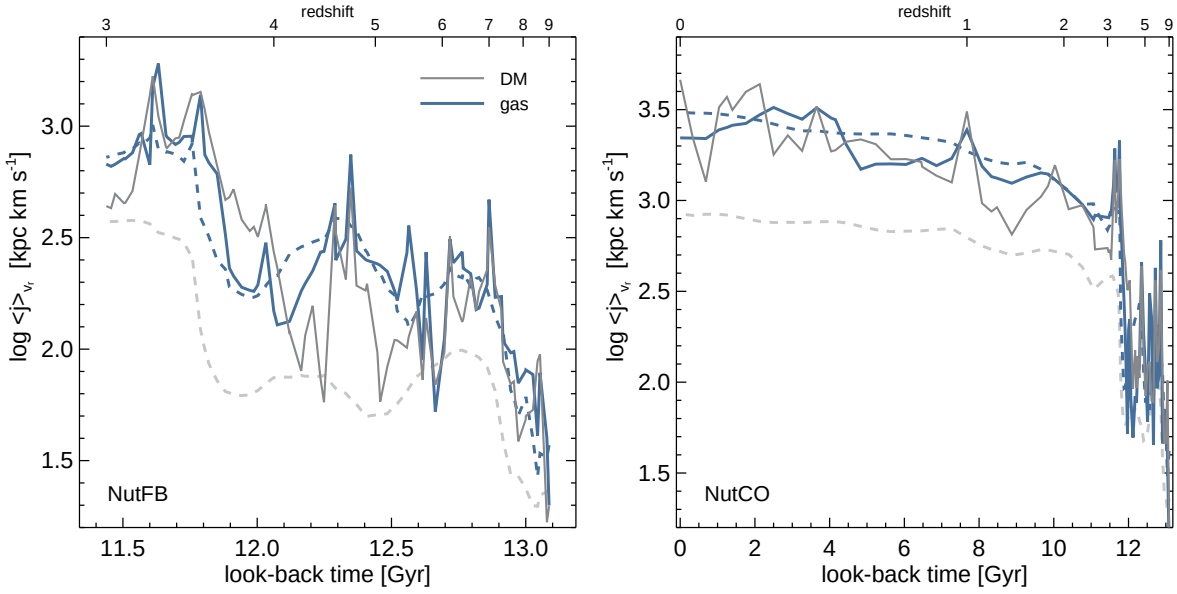


Figure 4.3: Accretion-weighted specific angular momentum for dark matter (black solid line) and gas (blue solid line) at the virial radius in the feedback (left panel; NutFB) and the cooling (right panel; NutCO) runs. The net specific angular momenta of the dark matter halo ($j_{\rm dm}$) and the halo gas ($j_{\rm gas,out}$) are included as grey dashed and blue dashed lines. Note the similar evolution of the specific angular momentum of the halo gas and of both accreted gas and dark matter.

mass), which is thought to be close to the mass at which gas accretion transitions from the cold mode to the hot mode (Birnboim & Dekel, 2003; Ocvirk et al., 2008). The most significant *halo* merger occurs at $z \simeq 2.6$ (satellite to host halo mass ratio $M_{\rm sat}/M_{\rm host} \sim 0.25$), while the second most significant merger ($M_{\rm sat}/M_{\rm host} \sim 0.12$) happens at $z \simeq 3.5$. The majority (75%) of the other 20 minor mergers ($0.01 \leq M_{\rm sat}/M_{\rm host} \leq 0.1$) take place between $6 < z < 10$. In addition to these mergers, material accreted along filaments also contributes to the rapid variation of $j$ since the density in the gas filaments varies (see also Figure 2 of Brooks et al. 2009).

### 4.4.1 Reassessment of the assumptions used in the standard disc formation theory

In order to test whether the gas carries the same amount of specific angular momentum as the dark matter when it is accreted by the halo, we compute the accretion-weighted specific angular momentum modulus of both components at the virial radius as

$$\langle j \rangle_{v_r} = \left| \frac{\sum_i m_i v_r \Theta(-v_r) \vec{\mathbf{r}}_i \times \vec{\mathbf{v}}_i}{\sum_i m_i v_r \Theta(-v_r)} \right|,$$

where $\Theta$ is the Heaviside step function. This is done by calculating the contribution of infalling ($v_r < 0$) gas or DM particles located within the thin shell defined by $0.95 \leq r/r_{\rm vir} \leq 1.05$. Since the collisionless

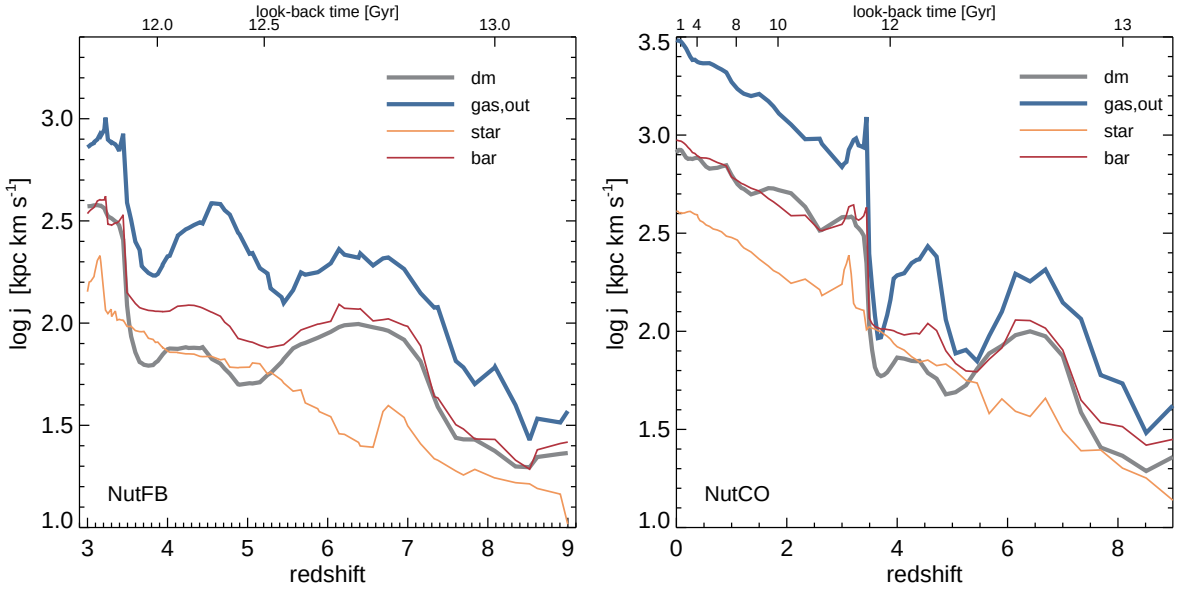


Figure 4.4: Evolution of the specific angular momentum modulus ($j$) from the high-resolution (12pc) feedback (NutFB; left) run and low-resolution (48pc) cooling (NutCO; right) run. Different colours denote different components: dark matter ($j_{\rm dm}$, thick grey), gas at $0.1 \leq r/r_{\rm vir} \leq 1$ ($j_{\rm gas,out}$, thick blue), stars ($j_{\rm star}$, thin orange), all baryons in the halo ($j_{\rm bar}$, red). Note that the specific angular momentum calculations for dark matter ($j_{\rm dm}$), gas ($j_{\rm gas,out}$) and baryons ($j_{\rm bar}$) includes the contribution from satellite galaxies, while it is excluded for the measurement of $j_{\rm star}$. The specific angular momentum of gas ($j_{\rm gas,out}$) is larger than that of its host dark matter halo ($j_{\rm dm}$), suggesting that the angular momentum of the gas is not acquired during the collapse of the latter. Specific angular momentum of the total baryons ($j_{\rm bar}$) is comparable to that of the dark matter halo ($j_{\rm dm}$) in both runs.

dark matter particles can potentially get accreted several times as they come in and out of the halo, we track each particle individually and flag them the first time they cross the virial sphere so as not to re-accrete them later. For the collisional gas, this problem does not arise as it remains in the center of the halo unless blown out/evaporated by feedback or shock-heating, so a simple radial velocity cut suffices.

Figure 4.3 demonstrates that the specific angular momenta of the accreted gas and dark matter agree reasonably well both in the feedback (NutFB) and cooling (NutCO) run, at all times. Although we have not included it in this study, this turns out to be the same in the non-radiative (NutAD) run. It is noteworthy that both freshly accreted gas and dark matter bring in a larger amount of specific angular momentum than that of the dark matter halo, $j_{\rm dm}$ (grey dashed lines). The fact that $j_{\rm gas,out}$ (blue dashed lines) carries nearly the same large amount of specific angular momentum as $\langle j \rangle_{v_r}$ supports the view that the angular momentum of the gas accreted by the central galaxy is acquired *before* it enters the dark matter halo (e.g. Peebles, 1969; White, 1984; Pichon et al., 2011). These confirm that gas acquires the same specific angular momentum as dark matter through tidal torquing (e.g. Book et al., 2011).

We then measure the specific angular momentum of the *total* baryonic component, i.e. gas and stars,

($j_{\rm bar}$: thin red line in the left panel of Figure 4.4), as a function of time. We find that its amplitude most closely tracks that of the specific angular momentum of the DM ($j_{\rm dm}$, thick grey solid line) which we know reflects the mass assembly history of the halo. We are not implying that $|\vec{\mathbf{j}}_{\rm dm}|$ of individual dark matter particles is conserved during the collapse, but simply that, as the baryon angular momentum is advected deep within the halo, we can only probe the accretion history of the gas by including all baryons within the inner region. When this effect is accounted for, there is no indication in our simulation that baryons lose more (or less) specific angular momentum amplitude than DM during gravitational collapse of the halo, as postulated in the standard theory.

It is also worth noting that stellar components contain smaller specific angular momentum than $j_{\rm gas,out}$ or $j_{\rm dm}$. Since the global star formation timescale is much longer than the dynamical timescale of the central region (e.g., Kennicutt, 1998), most of the stars will form from older gas, with a lower angular momentum amplitude. Even though newly formed stars carry more angular momentum, they represent a smaller fraction of the total stellar mass than the central gas mass compared to that of the total halo gas. Therefore, a supplementary time delay to reach a given level of $j$ and a smoother growth in specific angular momentum amplitude of the stellar component is inevitable (Dutton & van den Bosch, 2009).

Finally, we test a commonly adopted premise in evolutionary (semi-) analytic models that gas follows the angular momentum profile of dark matter (Bullock et al., 2001) or adiabatic gas (Sharma & Steinmetz, 2005). Figure 4.5 shows the radial profiles of the $j$ distributions of gas and dark matter within the virial radius of the dark matter halo, normalised to the average specific angular momentum of the DM halo at each redshift, $j_{\rm dm}(z)$. These profiles are split in a low and a high redshift bin ($z < 1$ and $z > 3$) and stacked. Two striking features emerge from the analysis of Figure 4.5. First, the dependence of the shape of *all* the specific angular momentum profiles on redshift is minor. Second, while the $j$ of the dark matter component drops almost proportionally with radius, the $j$ profile of the gas is flat in the outer parts of the halo ($r \gtrsim 0.1\ r_{\rm vir}$) as indicated by the solid light blue line on the figure which represents the fit:

$$j_{\rm gas}(r) \simeq \begin{cases} 3\ j_{\rm dm} & \text{if } r \geq 0.08\, r_{\rm vir} \\ 43.6\ (r/r_{\rm vir})^{1.06} j_{\rm dm} & \text{if } r < 0.08\, r_{\rm vir} \end{cases} \tag{4.1}$$

to these simulation data. This is in stark contrast with the behaviour of the gas specific momentum in the NutAD run (grey solid line) which more closely follows the $j$ profile of the dark matter halo (see also Sharma & Steinmetz, 2005). This implies that as long as the gas can radiatively cool, its specific angular momentum is conserved whilst it is being advected to the inner region ($r \lesssim 0.1 r_{\rm vir}$), regardless

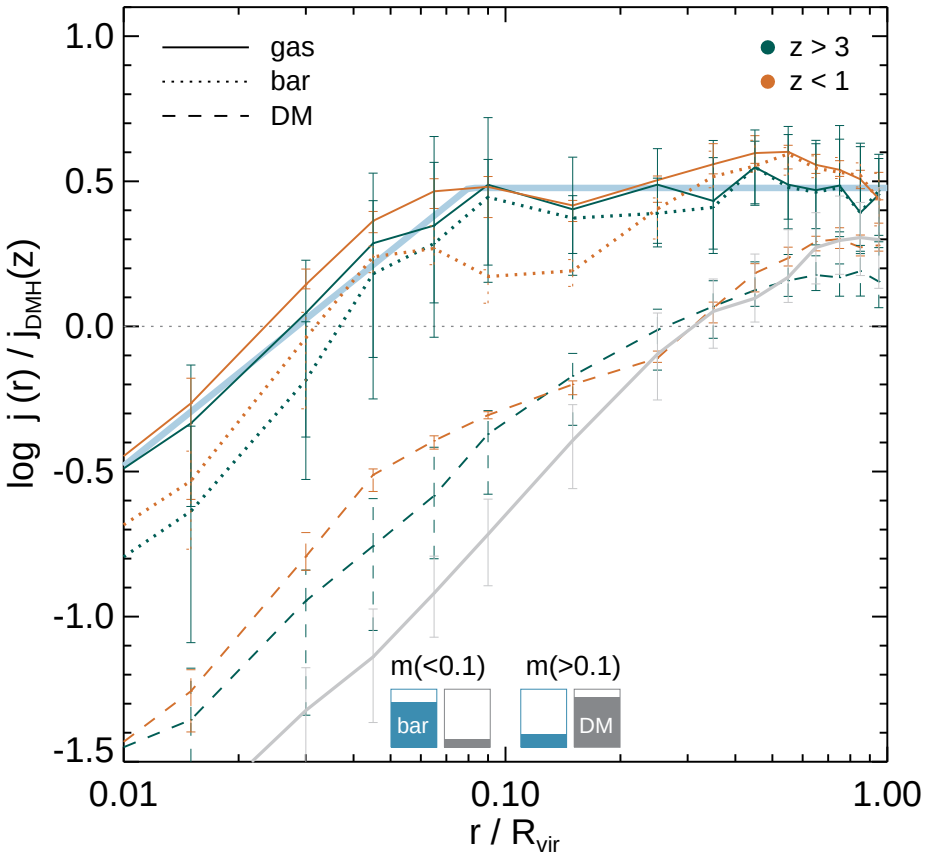


Figure 4.5: Stacked distributions of specific angular momentum as a function of radius from the NutCO run. Profiles are normalised with respect to the averaged specific angular momentum of the dark matter halo at a given redshift, $j_{\rm DMH}(z)$.The specific angular momentum of gas, baryon (gas+star), and dark matter is shown as solid, dotted, and dashed lines, respectively. Dark blue lines display $j$ at high redshift ($z > 3$), while orange lines show $j$ at low redshift ($z < 1$). The solid grey line shows the gas specific angular momentum profile in the NutAD (adiabatic) run at ($z < 10$) and the thick light blue line represents the analytic fit to the gas in the NutCO run as specified in the text (Eq. 4.1). Each point corresponds to the median and error bars indicate interquartile ranges. We also include the relative mass fraction (median) of the inner ($r < 0.1r_{\rm vir}$) and outer ($r > 0.1r_{\rm vir}$) baryons (or dark matter) at the bottom of the panel. Note that these mass fractions are only weakly dependent on redshift. The normalised $j$ of gas is flat at $0.1 \lesssim r/r_{\rm vir} \leq 1$, and gently diminishes in the region where the galactic disc is located, demonstrating that, contrarily to the DM, the angular momentum of the gas is not significantly redistributed outside of a sphere of radius $r \sim 0.1r_{\rm vir}$.

of whether shock heated gas is present or not. Therefore, any redistribution of angular momentum (i.e. mixing with the gas having different $j$) must happen within the central region of the halo, close to the galactic disc. The detailed analysis of this complex process is beyond the scope of the current study and will be presented elsewhere (Tillson et al. *in prep.*).

The trend that $j_{\rm gas}(r)$ is greater than $j_{\rm dm}(r)$ is not unexpected in the sense that it is the low-$j$ gas that is preferentially converted into stars. Thus, $j$ of the remaining gas in the halo will naturally be higher than that of the dark matter halo which includes dark matter with small $j$ as well as large $j$. However, it should be noted that the specific angular momentum of gas in the outer region, $j_{\rm gas}(r \gtrsim 0.1r_{\rm vir})$, is remarkably larger than the net specific angular momentum of the dark matter halo or the specific angular momentum of dark matter at the virial radius. Even if the gas angular momentum were increased by the consumption of low-$j$ gas, a factor of three difference could not be explained by this if gas were assumed to share the specific angular momentum of the dark matter halo. As shown in Figure 4.4, the total specific angular momentum of gas in the outer region ($j_{\rm gas,out}$: blue lines) is systematically larger than that of dark matter ($j_{\rm dm}$: gray lines) by a factor of a few (see also Sales et al., 2010; Stewart et al., 2011b).

As a complement to the radial distribution of $j$ presented in Figure 4.5, we also present angular momentum probability distributions, $P(j_z)$, of baryons and dark matter in Figure 4.6. The $z$-direction of specific angular momentum, $j_z$, is defined as in Sharma & Steinmetz (2005), i.e. it corresponds to the direction of the net specific angular momentum of each component considered (DM, gas or baryons, i.e. gas plus stars). Note that we have not added thermal random motions to gas velocities, but have simply taken streaming motions defined in each cell. As discussed by Sharma & Steinmetz (2005), such a broadening hinders a fair comparison of angular momentum distributions between dark matter and gas in the sense that any underlying $j$ distribution is likely to be wiped out by the broadening. Moreover, since the thermal motions will be suppressed in a realistic situation where radiative cooling drops the temperature of the gas, we neglect the thermal motions and use the streaming motions for the comparison of angular momentum.

Several interesting conclusions can be gleaned from Figure 4.6. Firstly, even though we follow hydrodynamics with an entirely different technique from Sharma & Steinmetz (2005) (grid based instead of SPH), we obtain very similar probability distributions of gas and dark matter angular momentum in our adiabatic run (compare our Figure 4.6 with their Figure 17). We therefore confirm their result that these two components do not share exactly the same $P(j_z)$ distribution. This suggests that the different

virialisation processes acting on the gas (shock-heating) and the dark matter (violent relaxation/phase mixing) do not redistribute angular momentum in the same manner, although the average specific angular momenta of these components are similar. In particular, shock-heating strongly suppresses the negative angular momentum tail of the distribution for the gas, which corresponds to dark matter particles on counter-rotating orbits. Secondly, the angular momentum distribution of baryons (stars plus gas) and/or gas in the presence of cooling are markedly different from both that of adiabatic gas and dark matter, at all redshifts. These former show a broader double peaked shape which is incompatible with the gamma based analytic function fit proposed by Sharma & Steinmetz (2005) (their equation 27) in the adiabatic case. The ability of gas and/or stars to counter rotate is restored in the run with cooling, and an excess probability of higher $j_z$ material, especially at $r > 0.1r_{\rm vir}$ appears. This lends further support to our claim that gas/baryons carry more specific angular momentum than the dark matter halo at any given radius (Figure 4.5), contrarily to what happens in the adiabatic case. These results corroborate that one cannot simply assume that gas follows the angular momentum profile or distribution of dark matter or adiabatic gas (Bullock et al., 2001; Sharma & Steinmetz, 2005), as was done in several (semi-) analytic models.

To summarise, we find that the general assumptions made in the standard theory of disc formation, i.e. the same tidal torquing and angular momentum conservation, are reasonable, and previous results based on the 'static' approach are likely to be robust. Yet the advection of gas angular momentum in the presence of radiative cooling turns out to be distinctive from that of the adiabatic case, suggesting that the angular momentum profile (or even distribution) of adiabatic gas should be used with caution in any 'evolutionary' models.

### 4.4.2 Radiative cooling as the origin of the discrepancy in angular momentum profiles

Why is the gas specific angular momentum profile markedly different compared to that of dark matter? Cold, dense filamentary gas rapidly flows onto the central gaseous disc. As Brooks et al. (2009) discussed, this can take place faster than the free-fall time since the gas is accreted with roughly the circular velocity of the halo. Accordingly, the outer region ($0.1 \lesssim r/r_{\rm vir} \leq 1$) is occupied by gas recently accreted, which has a large amount of specific angular momentum. On the other hand, dark matter particles pass through the central region of the halo and depending on their exact orbital properties, and can end up populating the outer regions despite having entered the halo at earlier times with smaller angular momentum. Thus, despite the fact that dark matter first falls into the halo with a similar amount of specific

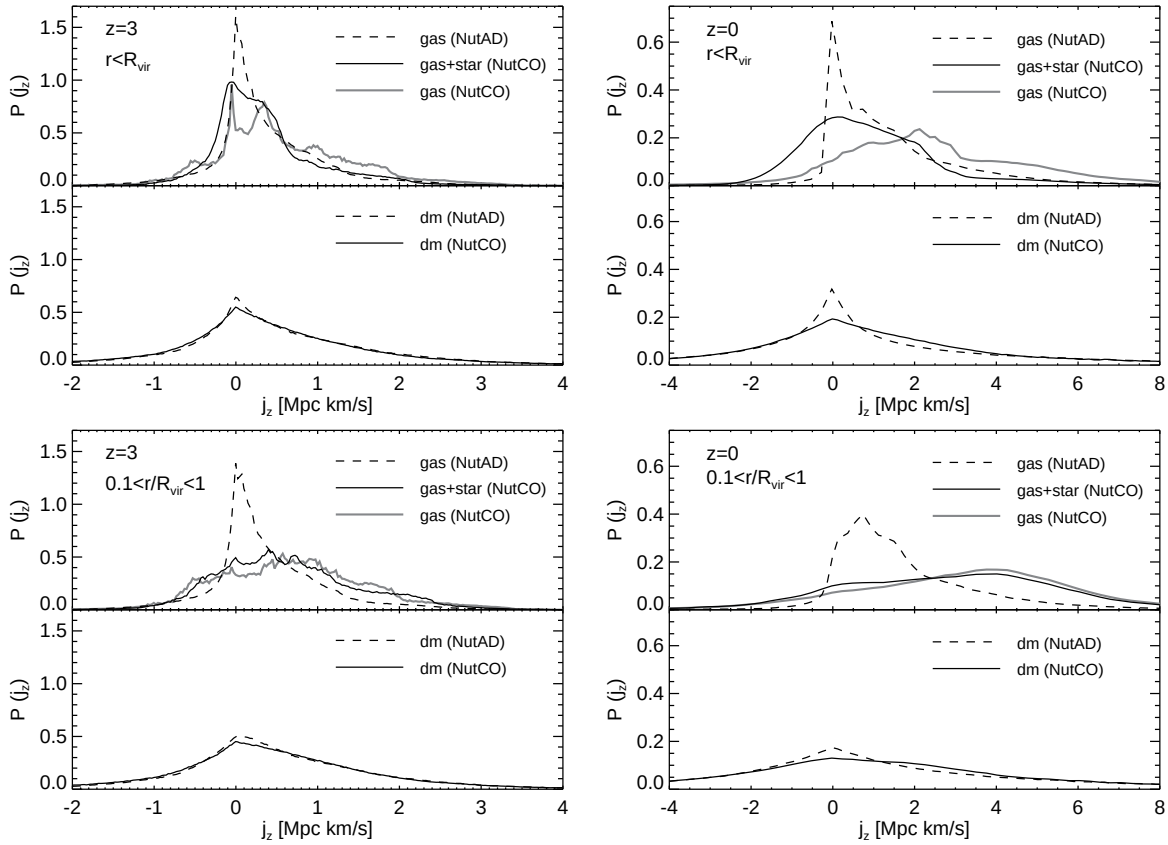


Figure 4.6: Comparison of angular momentum distributions ($P(j_z)$) of baryons and dark matter between the adiabatic run (NutAD) and the cooling run (NutCO). The $z$-direction specific angular momentum ($j_z$) for gas and dark matter is obtained by calculating the dot product between $\vec{j}$ of each mass element and the net spin orientation ($\hat{j}_{\rm gas}$ or $\hat{j}_{\rm dm}$) as in Sharma & Steinmetz (2005). Left and right panels show the comparisons at high redshift ($z = 3$) and at low redshift ($z = 0$), respectively. Angular momentum distributions are shown for the whole halo, ($r < r_{\rm vir}$; top panels) and its external regions only ($0.1 \leq r/r_{\rm vir} < 1$; bottom panels). Different lines correspond to different components, as indicated in each panel. It can be seen that angular momentum distribution of baryons (stars plus gas) and/or gas in the NutCO run is markedly different (broader double peaked shape) from that of dark matter or that of gas in the NutAD run which are well fitted by the analytic formula (27) of Sharma & Steinmetz (2005) based on the gamma function.

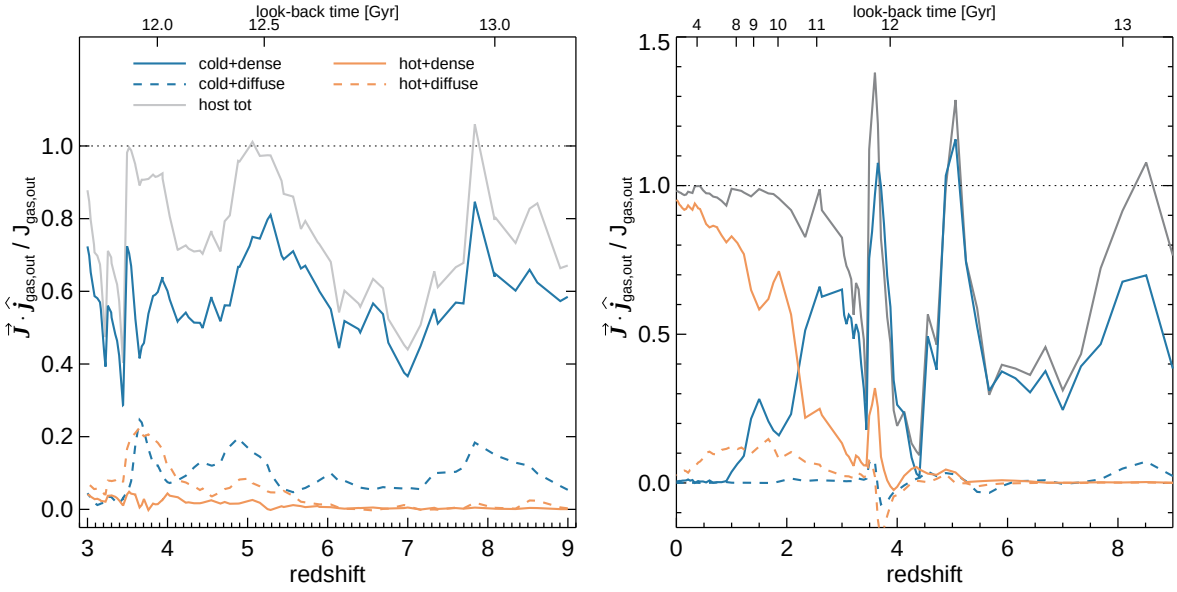


Figure 4.7: Fraction of total angular momentum of gas at $0.1 \leq r/r_{\rm vir} \leq 1$ from various components. Left and right panels correspond to the fraction from the feedback run (NutFB) and cooling run (NutCO), respectively. We divide the gas into four different phases: i) cold ($T < 10^5$K), dense filamentary ($n_{\rm H,fil} \leq n_{\rm H} < n_{\rm H,th}$), ii) cold diffuse ($n_{\rm H} < n_{\rm H,fil}$), iii) hot ($T > 10^5$K) dense, and iv) hot diffuse component (see Equation (4.2) for the definition of $n_{\rm H,fil}$). Note that these quantities do not include the gas belonging to satellite galaxies. Grey solid line corresponds to the total fraction of angular momentum of gas belonging to the host halo. Cold, dense filamentary accretion accounts for most of the angular momentum in the halo. The hot gas phase (orange lines) begins to develop at $z \sim 3$ in the cooling run (right panel), and accounts for almost all of the angular momentum in $0.1 \leq r/r_{\rm vir} \leq 1$ by $z = 0$.

angular momentum as the gas, mixing with 'older' particles makes $j_{\rm dm}$ become systematically smaller than $j_{\rm gas,out}$. Note that this also explains the similar evolution of the specific angular momentum of the halo gas ($j_{\rm gas,out}$) and the newly accreted gas at high redshift (Figure 4.3).

Apparently, the cold filaments are nearly radial, and one might wonder how much angular momentum is transported through the filaments at high redshift. To substantiate the idea that the larger $j_{\rm gas,out}$ relative to $j_{\rm dm}$ is associated with the dense filamentary component, we divide the gas into four different phases according to temperature and density as

- cold dense ($T < 10^5$K and $n_{\rm H,fil} \leq n_{\rm H} < n_{\rm th}$)
- cold diffuse ($T < 10^5$K and $n_{\rm H} < n_{\rm H,fil}$)
- hot dense ($T \geq 10^5$K and $n_{\rm H,fil} \leq n_{\rm H} < n_{\rm th}$)
- hot diffuse ($T \geq 10^5$K and $n_{\rm H} < n_{\rm H,fil}$).

where we define the cold dense filamentary structure using the $n_{\rm H,fil} \leq n_{\rm H} < n_{\rm H,th}$ gas density cut. The

lower density bound ($n_{\rm H,fil}$) is chosen as

$$n_{\rm H,fil} \equiv \delta_{\rm f}\,\bar{\rho}\,f_{\rm bar}X_{\rm H}/m_{\rm H}, \tag{4.2}$$

where $f_{\rm bar}$, $X_{\rm H}$, and $m_{\rm H}$ are the universal baryon fraction ($\Omega_{\rm b}/\Omega_{\rm m}$), the primordial hydrogen mass fraction and the mass of the hydrogen atom, respectively. The dependence of the lower bound of the filament density on the background density ($\bar{\rho}(z)$) is motivated by the fact that the filamentary structure acquires its properties on large scales which are not gravitationally decoupled from the expansion of the Universe. The parameter $\delta_{\rm f}$ determines the overdensity of the filamentary gas. We find that $\delta_{\rm f} \sim 100$ reasonably identifies the filamentary structure in the NUT simulations, which corresponds to hydrogen number densities higher than $n_{\rm H} \simeq 0.02$ and $\simeq 0.001$ cm$^{-3}$ at z=9 and z=3, respectively. Note that, although this is not a worry in the NUT simulations because we spatially resolve the filaments, $\delta_{\rm f}$ will generally be resolution-dependent in cosmological simulations. In a rather obvious fashion, a lack of spatial resolution will artificially broaden the filamentary structure and thus reduce its density as mass needs to be conserved.

Figure 4.7 shows the contributions from the four different phases to the *total* angular momentum of the gas located at $0.1 \leq r/r_{\rm vir} \leq 1$. We emphasise that gas belonging to satellite galaxies is excluded from the measurements. It is clear from this figure that cold filamentary accretion is primarily responsible for the larger $j_{\rm gas,out}$. The cold filamentary gas alone accounts for more than half of the gas angular momentum in the region. Thus, it can safely be concluded that the cold, dense filamentary accretion carries material with larger $j$ than the dark matter halo from outside the virial radius to the inner region of haloes without the gas having much time at all to interact with the dark matter. Gas belonging to satellite galaxies occasionally contributes a significant fraction of $J$ (difference between the solid grey line and a horizontal line drawn for $\vec{\mathbf{J}} \cdot \hat{j}_{\rm gas,out}/{\rm J}_{\rm gas,out} = 1$ in Figure 4.7). However, its impact on the specific angular momentum is less significant than that of the cold, dense filamentary accretion at $z \geq 3$ for two reasons. First, whilst cold, dense filamentary gas flows into the central gaseous disc rapidly, gas gravitationally bound to a satellite galaxy orbits around it for the time it takes dynamical friction to drag the satellite galaxy down. As a consequence of this process, satellite gas angular momentum in Figure 4.7 cannot be directly converted into the actual angular momentum of gas accreted onto the central galaxy. Second, satellites are accreted along the gas filaments, and hence part of the gas which we conservatively assigned to these satellite galaxies could be regarded as filamentary gas. In this sense, the estimate of $J$ for the satellites in Figure 4.7 should be considered as an upper bound, and thus the actual fraction

of the total angular momentum contributed by cold filamentary accretion may be slightly higher than reported in this work. Since the NutCO run does not include supernova feedback, satellite galaxies can retain more gas than in the NutFB run, and thus the resulting relative contribution from the cold, dense filamentary gas to the total angular momentum gets slightly smaller at high redshift than the feedback run (right panel of Figure 4.7). However, there is little difference in $j_{\rm gas,out}$ or $j_{\rm dm}$ between these two runs for $z \geq 3$. Finally, the contribution to the total angular momentum from other phases (hot diffuse, hot dense, and cold diffuse) to $J$ turns out to be minor for a DM halo of this mass at high redshift. Whilst the lack of angular momentum of the cold diffuse phase originates from its almost isotropic accretion which cancels its angular momentum to a high degree, that of the hot gas phase is mainly caused by the small mass fraction of hot gas. This result is not very surprising because our DM halo, at $10^{11}M_{\odot}$ is not massive enough to sustain a stable virial shock (Birnboim & Dekel, 2003; Kereš et al., 2005), and supernova explosions in simulations are notoriously inefficient at ejecting large amounts of hot gas in the halo (Mac Low & Ferrara, 1999; Dubois & Teyssier, 2008; Powell et al., 2011; Faucher-Giguere et al., 2011).

Obviously, the cold, dense filamentary gas accretion disappears at low redshift (e.g. Kimm et al., 2011; Faucher-Giguère & Kereš, 2011; Stewart et al., 2011a), and therefore one expects that the high redshift segregation of specific angular momentum between gas and dark matter previously advocated becomes weaker as time elapses. Indeed, in the extreme case where gas is prevented from cooling (NutAD run: Figure 4.2 and 4.5) the evolution of its specific angular momentum radial profile closely follows that of the dark matter, indicative of a similar distribution of low and high specific angular momentum material for both components. Considering that the post-shock temperature for an isothermal sphere of mass a few times $10^{11}M_{\odot}$ (our halo reaches 2 $\times 10^{11}M_{\odot}$ at $z \simeq 2$, c.f. Appendix A.3) is $T_{\rm shocked} \gtrsim 3T_{\rm vir}/8 \sim 10^5$K (Dekel & Birnboim, 2006), where $T_{\rm vir}(\simeq 35.9 \times (V_{\rm c}/[{\rm km \cdot s^{-1}}])^2)$ is the virial temperature, and that the run does not feature any SN feedback, we can safely identify the halo hot gas at $z \lesssim 2$ with material which has been shock-heated. Nonetheless, as Figure 4.5 clearly demonstrates, this hot halo gas within $0.1 \leq r/r_{\rm vir} \leq 1$ still has a specific angular momentum higher than that of the dark matter, indicating that shock-heating of the accreted cold gas, even when it takes place as early as $z = 2$, does not erase the difference in specific angular momentum of dark matter and gas. Note that the shock-heated material at the centre of the halo, which has a lower specific angular momentum than that in the outer regions, is cooled and accreted onto the central disc on timescales shorter than the sound crossing time of the halo ($\sim 1$ Gyr at $z = 0$ for our halo). Therefore, it cannot significantly mix with

higher specific angular momentum gas accreted at later times. This creates a 'cooling flow' towards the central galaxy and as a result preserves the distribution of gas specific angular momentum that was set in at high redshift (Figure 4.5) or through recent mergers.

### 4.4.3 Generalisation of the results

Now that we have established that gas in a Milky Way-like halo has a larger specific angular momentum than dark matter, and with a different radial profile, it is vital to know whether this property is generic or not. To build a statistically representative sample of haloes, we make use of three large cosmological hydrodynamics simulations called HORIZON-MARENOSTRUM, Cosmo25, and Cosmo50. The HORIZON-MARENOSTRUM simulation contains 326, 1921, 3307, and 4015 haloes with $M_{\rm vir} \geq 10^{11} M_{\odot}$ at $z = 6.1, 3.8, 2.5$, and $1.5$. Since the simulation has only been carried out down to $z = 1.5$, we use the Cosmo25 and Cosmo50 run to supplement the sample at lower redshifts. The number of haloes with $M_{\rm vir} \geq 10^{11} M_{\odot}$ in the Cosmo25 run is 378 and 459 at $z = 1.5$ and $z = 0$ respectively. For the Cosmo50 run, we restrict our analysis to 481 more massive haloes ($M_{\rm vir} \geq 10^{12} M_{\odot}$) at $z = 0$ because of the poorer resolution of the simulation.

The middle panel of Figure 4.8 shows the median and the interquartile range of the spin parameter distribution of the dark matter haloes. As is well known in the literature, it shows that the typical value for the spin is $\lambda \simeq 0.04$ with very little dependence on halo mass and redshift. On the other hand, the spin parameter of gas in the HORIZON-MARENOSTRUM simulation (filled circles) is 2–4 times higher in general than that of the dark matter halo and clearly depends on halo mass. As the halos become larger, cooling timescales increase (because of higher gas temperatures and smaller central densities) allowing more and more mixing between low and high specific angular momentum gas to occur. As a result, the gap between $j_{\rm gas,out}$ and $j_{\rm dm}$ is reduced for the most massive objects. The ratio turns out to be even more significant at $z = 0$ in the Cosmo25 (asterisks) and Cosmo50 run (diamond), demonstrating that our finding that gas has larger specific angular momentum extends to *all* halos over the *entire* redshift range. As discussed in Sec. 4.4.2, since the cooling permits the gas to flow into the centre, $j_{\rm gas,out}$ tends to reflect $j$ of newly accreted gas. This means that, for any dark matter halo of a given mass, its gas content at lower redshift will be composed of material carrying larger specific angular momentum. In other words, the redshift dependence of gas spin shown in Figure 4.8 is understood as a large scale structure driven increase in the specific angular momentum of freshly accreted gas. For practical purposes, we compute a redshift-dependent fit to the specific angular momentum gas to dark matter ratio for halos with $M_{\rm vir} \leq 10^{13} M_{\odot}$

$$\frac{\lambda'_{\rm gas,out}}{\lambda'_{\rm DM}} \simeq \max[3.5 + 24.3(1+z)^{-0.8} - 1.97(1+z)^{-0.7} \log M_{\rm vir}, 2]. \tag{4.3}$$

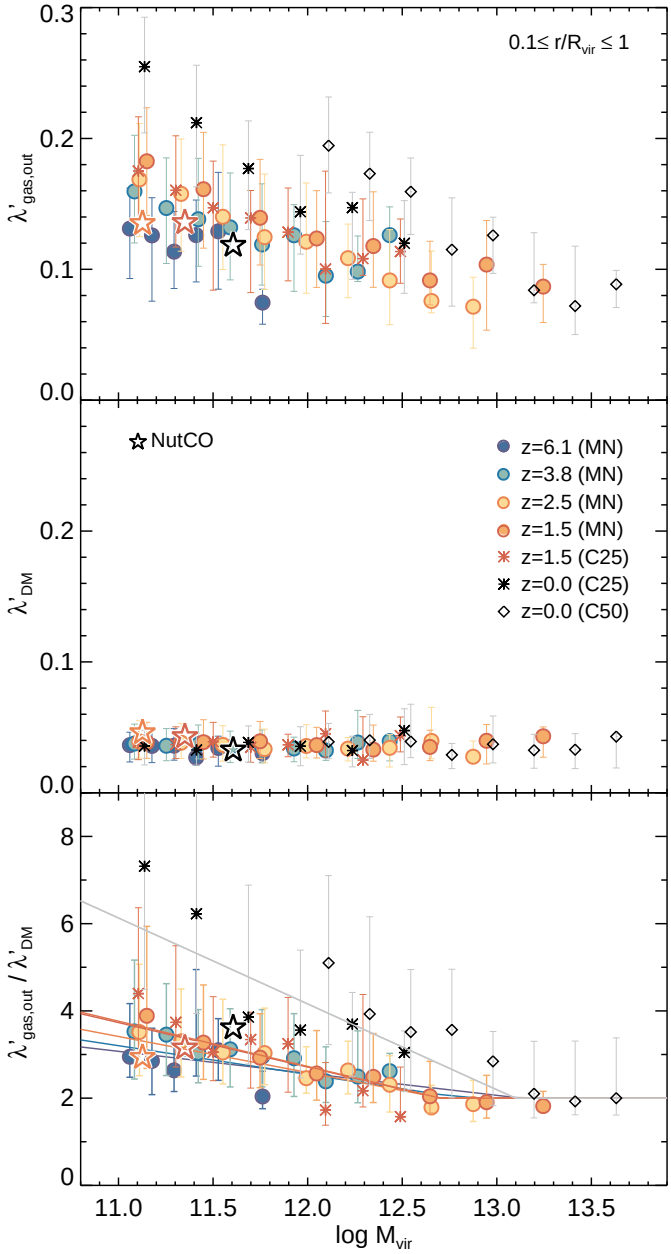


Figure 4.8: Spin parameter distributions of the gas within $0.1 \leq r/r_{\rm vir} \leq 1$ (top), the dark matter halo (middle), and the ratio of the two (bottom). Filled circles correspond to the results from the HORIZON-MARENOSTRUM simulation, and asterisks and diamonds show the results from the Cosmo25 and Cosmo50 run, respectively. Different colours denote different redshifts as indicated on the figure. The results from the NutCO run are also included as stars with the same colour-coding. Solid lines show linear fits to the simulated data at different redshifts as given by Equation. (4.3). Statistically, the specific angular momentum of the gas within $0.1 \leq r/r_{\rm vir} \leq 1$ is at least twice that of the dark matter halo host, at all redshifts.

Note that since the HORIZON-MARENOSTRUM and Cosmo25 simulations are run using different cosmologies (WMAP1 and WMAP5 respectively) and different mass resolutions, we included data at a common redshift ($z = 1.5$) to ensure that the differences between the z=1.5 HORIZON-MARENOSTRUM and the $z = 0$ Cosmo25 halos does not arise from a different choice of cosmology/simulation parameters.

We emphasise that all the extra specific angular momentum brought in by the gas will not be devoted to spinning up the central galactic disc, given that its typical misalignment with the central gaseous disc is measured to be $\approx 40^{\circ}$ for intermediate mass halos ($M_{\rm vir} \sim 10^{11} M_{\odot}$) in the HORIZON-MARENOSTRUM simulation. In the vicinity of the central disc, hydrodynamical interactions with the circum-galactic gas will become important and may substantially redistribute angular momentum. A careful numerical investigation of angular momentum advection in the central region is therefore needed to determine whether or not a simple semi-analytic approach is capable of correctly describing the evolution of angular momentum of disc galaxies using the new initial conditions we provide with this fit.

We also note that limited spatial resolution of our large volume cosmological simulations will lead to an artificial increase of the gas angular momentum, especially in low mass halos. Indeed, the softening of the gravitational force produces very extended discs at the centre of these halos, which would probably be contained within 0.1 $r_{\rm vir}$ at higher resolution. However, comparing the spin of the gas in the NutCO halo (large empty stars in Figure 4.8) at various redshifts with that measured for a sample of halos of comparable mass available in these cosmological simulations (solid circles and asterisks in Figure 4.8), we conclude that resolution effects most likely account for a minor fraction of the gas spin ($\sim 20\%$).

A caveat to bear in mind is that the physical processes that can prevent the cooling catastrophe in cluster environments are likely to change the ratio $\lambda_{\rm gas,out}/\lambda_{\rm dm}$. For example, as extensively discussed in the literature, feedback from active galactic nuclei is thought to stir/heat a large amount of cooling gas, redistributing it in the outer parts of the halo. As previously argued, such a mixing mechanism will contribute to narrow the gap between gas and dark matter spin. Such a potent feedback mechanism is not included in the cosmological simulations presented here, and thus a larger fraction of baryons than observed are converted into stars in massive haloes (Dubois et al., 2010). This should be taken into account before concluding that the ratio ($\lambda_{\rm gas,out}/\lambda_{\rm dm}$) for massive haloes has converged to $\sim 2$ as Figure 4.8 (bottom panel) advocates.

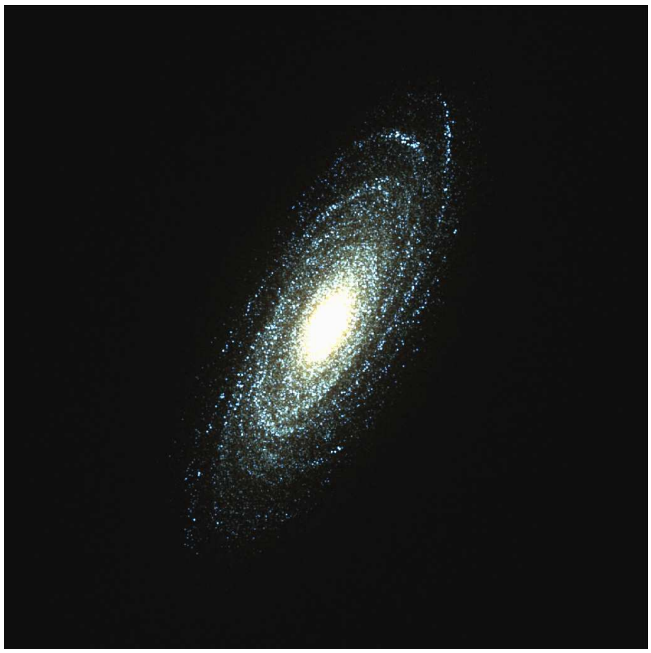

Figure 4.9: True colour composite image of the NutCO galaxy in the U, B and V at $z = 0$. The image measures 15 kpc on a side. Note that internal extinction by dust is not accounted for in this image. Notice the presence of a large bulge (I-band B/D ratio 0.78) typical of a galaxy with morphological type Sa/b (see text for detail).

### 4.4.4 Comparison with observations

Ultimately, to decide whether or not our simulations yield realistic galaxies, we have to compare their properties with observations. Unfortunately, with the high resolution we need to properly address the issues related to angular momentum, cooling and feedback, we can only perform such a comparison at $z = 0$ with one of our runs (NutCO) for the time being. As this simulation does not model any feedback mechanism, by $z = 0$ the simulated galaxy has formed too many stars ($M_{\rm star} = 6.8 \times 10^{10} M_{\odot}$). At $z = 0$, the $I$-band bulge-to-disc ratio ($B/D$) of the central galaxy in the NutCO run is $\simeq 0.78$ (see Figure 4.9). Such a value is close to the typical $B/D$ of Sa/Sb type spirals, but the disc scale length (2.0 kpc) turns out to be smaller than those observed (Graham & Worley, 2008).

Nevertheless, bearing this caveat in mind, we present in Figure 4.10 measurements of the $j$ versus $V$ relation for the NutCO galaxy at various redshifts, compared to the observational bright disc galaxy sample gathered by Kassin et al. (2006) (at $z \simeq 0$). Kassin et al. derived the specific angular momenta for these galaxies from Halpha + HI rotation curves and radial stellar mass distributions given in Kassin et al. (2006). The average errors in $j$ measured from the data are $\approx 60\,{\rm kpc\,km\,s^{-1}}$. As is done in the observations, both the amount of specific angular momentum and the velocity of the simulated galaxy ($V_{\rm max}$, maximum of the rotation curve) are estimated using the stellar component, except for the filled

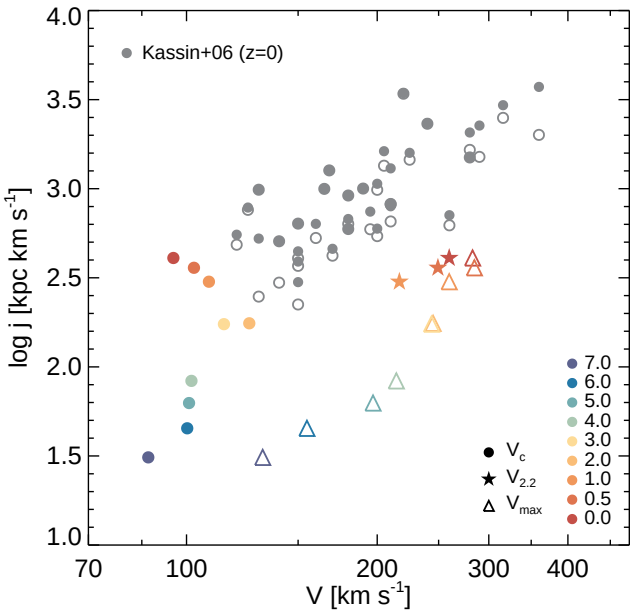


Figure 4.10: Comparison between the NutCO galaxy and the observational bright disc galaxy sample described in Kassin et al. (2006). Observational data is in grey (lower and upper estimates of $j$ are given by empty and solid circles respectively, see Kassin et al. 2012 for details). For the simulation data, different symbols (circles and right arrows) stand for different estimates of the velocity of the galaxy (circular velocity and maximum rotation velocity). We also include estimates of $V_{2.2}$, the velocity measured at 2.2 times the exponential scale length in $I$ band, for $z \leq 1$. Note that the simulated galaxy displays a dense large bulge which overgrows, at least partially, because of the lack of modelling of any kind of internal feedback (radiation, stellar winds, supernovae, cosmic rays, etc.) in the NutCO run.

circle symbols where the velocity is measured as the circular velocity at the virial radius of the dark matter halo. For a fair comparison with observations, we also include velocities measured at 2.2 times the disc scale length, the radius at which the rotation curve of a self-gravitating exponential disk is expected to show a peak (Freeman, 1970), in the $I$ band ($V_{2.2}$) at $z \leq 1$.

Looking at Figure 4.10, one clearly sees that the velocity estimate plays a crucial role in our ability to assess whether simulated galaxy stars have the correct amount of angular momentum. This is because the observed slope of the relation ($\approx 2$) is quite large so any error on the velocity will translate into a much larger error on the specific angular momentum. More specifically, our simulation suffers from forming too many stars and as a result any velocity estimated in the central region of the halo is bound to be too large. If, on the other hand, we use the circular velocity at the virial radius of the halo to bypass the problem (note that this is current practice, see e.g. Dutton & van den Bosch 2009), we find that the level of angular momentum of the simulated stars is in fair agreement with the observations (Figure 4.10). We point out that this is a consequence of the lossless transport of a large amount of specific angular momentum by gas from super halo scales right into the inner regions, followed by its

redistribution in the vicinity of the disc, as discussed in the previous section. As a result of this effect and the low efficiency of the star formation process on disc scales, stars end up with a factor 2 to 3 less angular momentum than their dark matter halo counterpart which is very close to the discrepancy between dark matter only simulations and observations, as pointed out by Navarro & Steinmetz (2000) and Kassin et al. (2012).

Finally, it is interesting to note that when we use the $V_{\rm max}$ estimates for the velocity of the galaxy, although we do not match the zero point of the relation, simulated data points at different redshifts move along the observed sequence, suggesting that we would predict very little time evolution of the sequence. On the contrary, $V_{\rm c}$ estimates suggest there exists a strong evolution of the relation with redshift as the flat velocity profile of the dark matter halo is already in place very early on.

## 4.5 Conclusions and Discussion

In this study, using high-resolution cosmological hydrodynamic re-simulations of individual galaxies and large scale cosmological hydrodynamic simulations, we have revisited the standard theory for angular momentum evolution of gas and dark matter within virialised structures.

According to this standard picture, gas acquires angular momentum through nearby tidal fields in the same way as dark matter and is shock-heated to the virial temperature during the collapse of the halo. This gas then radiatively cools and settles into a rotationally supported disc, conserving its specific angular momentum in the process (Fall & Efstathiou, 1980; Dalcanton et al., 1997; Mo et al., 1998). Such assumptions naturally lead to predict that dark matter and halo gas share the same specific angular momentum. Investigating the issue, our main conclusions can be summarised as follows:

- Indeed, gas and dark matter bring in a similar specific angular momentum ($\langle j \rangle_{v_r}$) when they are accreted regardless of the radiative cooling.

- When radiative cooling is turned on, provided one compares the dark matter with the total baryon (gas and stars) specific angular momentum, their amplitudes are similar at all times. In other words, we find no evidence of baryons losing more (or less) angular momentum than dark matter within the virialised halo at any epoch, consistent with the standard picture of disc formation.

- The time evolution of the halo gas specific angular momentum is quite comparable to that of the dark matter, but only when gas is not permitted to radiatively cool, i.e. it is artificially forced to shock- heat during the collapse (NutAD run).

- When radiative cooling is turned on, the radial profile of gas angular momentum becomes distinctively different from that of dark matter (NutCO and NutFB run). The accreted specific angular momentum ($\langle j \rangle_{v_r}$) is well preserved for the gas between $0.1 \lesssim r/r_{\rm vir} \leq 1$, and systematically larger than the specific angular momentum of the dark matter within the entire virialised halo *at all times* (e.g. Figure 4.5). As a result, the modulus of the averaged angular momentum of the gas ($j_{\rm gas,out}$) is higher than that of the DM halo ($j_{\rm dm}$ or $j_{\rm dm,out}$) by a factor 2 to 6, depending on redshift and halo mass (see also Stewart et al. 2011b).

- Regardless of whether cooling is turned on or not, the *modulus* of the net specific angular momentum inside the virial sphere is not conserved for dark matter or gas. We attribute this continuous loss of angular momentum amplitude to a 'vector cancellation' effect (the angular momentum of newly accreted material is never perfectly aligned with the angular momentum of the whole halo) augmented by an accretion history effect (material accreted earlier carries less angular momentum so it weighs the average modulus of the specific angular momentum down at any epoch).

More specifically, our analysis reveals that at high redshift, the discrepancy between gas and dark matter specific angular momentum within $0.1 \lesssim r/r_{\rm vir} \leq 1.0$ ($j_{\rm gas,out}$ and $j_{\rm dm}$, respectively) arises because the angular momentum-rich freshly accreted gas flows into the central region through cold, dense filamentary accretion without being redistributed throughout the halo by shock-heating or supernovae feedback (NutFB run). As the dark matter halo grows at lower redshifts, a progressively larger amount of gas undergoes shock-heating, but since the central dense gas can still cool and collapse onto the disc on timescales shorter than a halo sound crossing time, the difference between $j_{\rm gas,out}$ and $j_{\rm dm}$ is, by and large, preserved. This competition between central cooling and redistribution of gas through shock heating and/or feedback induces a mass dependence of the discrepancy between gas and dark matter specific angular momentum: it is reduced for more massive halos where shock heating dominates. However, for a halo of fixed virial mass, this discrepancy is also larger at low redshifts than it is at high redshifts because the amount of specific momentum carried by the newly accreted material grows faster than the halo average with time (c.f. Pichon et al. (2011) for the origin of this effect). This generic behaviour is encapsulated in Equation. (4.3), which provides a fit to our simulated data.

We remark that the systematic discrepancy between $j_{\rm dm}$ and $\langle j \rangle_{v_r}$ measured in the NutCO run at *all* times means that the dark matter component of the halo (and its baryons as a whole) loses somewhere between half and two thirds of its specific angular momentum *amplitude*, depending on redshift (Figure 4.3). We note that even though this result seems in agreement with the measures of Book et al.

(2011) for a handful of well resolved dark matter halos in pure N-body simulations, we do not find, like these authors, that it can be attributed to external torques, following the original argument of Peebles (1969). The reason for this disagreement lies in the *continuous* nature of the specific angular momentum loss of the dark matter component. As Figure 4.3 demonstrates, the accretion weighted specific angular momentum of dark matter is higher than the specific angular momentum of the dark matter halo at *all redshifts*, regardless of whether we are in a phase where tidal torque theory predicts the angular momentum of the halo should grow or not. We are therefore pushed to conclude that the angular momentum 'loss' suffered by the halo has to be attributed primarily to a 'vector cancellation' effect: particles with similar amounts of angular momentum (modulus) but pointing away in opposite directions contribute only a small amount to the 'net' angular momentum of the virialised halo (e.g. Vitvitska et al., 2002). Note that the accretion history effect will also play a role in reducing the modulus of $\vec{\mathbf{j}}_{\rm dm}$ but cannot account for all the decrease.

Our efforts to probe the spatial distribution of angular momentum within the virialised halo also led us to define an inner region ($r/r_{\rm vir} \leq 0.1$). Gas in the outer region, $j_{\rm gas,out}$, generally has more specific angular momentum (by a factor 3 or so) than the dark matter halo as a whole, and only stars have less (by about a factor 2). We attribute this dichotomy within the baryon component to the long global star formation timescale of the disc compared to the gas accretion time scale, driving stars to preferentially form from gas accreted at a much earlier stage with lower angular momentum (see also Dutton & van den Bosch (2009) who reach similar conclusions with a SAM). As a result, a comparison with the data at $z = 0$ reveals that the level of specific angular momentum of our high resolution simulated stellar disc matches quite well that of the observations. However the difficulty of obtaining realistic galaxy rotation curves still prevents us from satisfactorily reproducing the observed $j$ versus $V$ relation (see Figure 4.10). Part of this failure is to blame on the fact that the only re-simulation we have been able to run down to $z = 0$ so far (NutCO run) does not include any modelling of feedback (stellar winds, supernovae, cosmic ray, etc.) (as pointed out by e.g. Governato et al., 2007; Agertz et al., 2011; Brook et al., 2011; Piontek & Steinmetz, 2011). For this reason, too many baryons (the universal fraction $\Omega_B/\Omega_m$) remain in the host halo and concentrate in the galaxy, potentially affecting the morphology of our galaxy which features a large bulge (morphological type Sa/Sb) but in any case leading us to overestimate disc rotational velocities.

Using a couple of cosmological hydrodynamics resimulations, one of a bulge-dominated galaxy and another of a disk-dominated galaxy at redshift 0, Zavala et al. (2008) show that the specific angular

momentum of the disc galaxy closely follows that of its dark matter halo. They argue that this is because the stellar feedback in the simulation which produces the disk-dominated galaxy is strong enough to heat the gas within the halo thereby preventing it from cooling too much at early times, fragmenting into sub-galactic clumps, and transferring its angular momentum to the dark matter halo by dynamical friction. Instead this hot gas accumulates in the halo where it acquires the specific angular momentum of the dark matter before it eventually cools and re-collapses onto the central galactic disc, all the while conserving its angular momentum. However, in the first cosmological resimulation where individual supernovae remnants are resolved, very little gas is heated by stellar feedback at high redshift (Powell et al., 2011). Moreover, these authors show that the cold filaments which supply most of the gas to the galaxy (Kereš et al., 2005, 2009; Dekel & Birnboim, 2006; Ocvirk et al., 2008; Brooks et al., 2009) are not disrupted by supernova feedback. This result has been independently confirmed by Faucher-Giguere et al. (2011) who used the constant velocity wind model of Springel & Hernquist (2003) to model feedback and found that at high redshift ($z \geq 3$) their supernova-driven galactic winds with low mass loading ($\eta = 1$) were not able to suppress the accretion of cold, dense gas in intermediate-mass haloes ($M_{\rm vir} \sim 10^{11-12}\ M_{\odot}$). Only when they assumed extreme parameters for their wind (i.e. loaded them with double the mass that is turned into stars, and drove them with double the amount of energy than that available from their supernova explosions) were they able to shut down cold, dense accretion. However this took place at the expense of the baryonic mass function which ended up dramatically undershooting the observations of e.g. Bell et al. (2003) at $z = 0$. Purely based on energetic grounds, feedback from active galactic nuclei may be able to blast the filamentary structure (Dubois et al., 2012b; van de Voort et al., 2011), but it is unclear how geometrical effects will affect their capacity to do so. A collimated jet for instance will not, in general, deposit enough of this energy in the vicinity of the filaments because of their small covering factor (a few percent, Kimm et al. 2011). In any case, in the simulation presented here, and contrary to the conclusions of Zavala et al. (2008), the specific angular momentum of the gas *in the galaxy* (thin blue line in the left panel of Figure 4.4) is similar (slightly larger) to that in its DM halo host, even though supernova feedback is moderate. This raises the question of the importance of the numerical technique employed to assess the fragmentation and transfer of angular momentum in disks. Although this is beyond the scope of this study, as we are chiefly interested in the outer parts of the halo, we believe that our simulation provides a more correct answer simply because we have better resolution. We refer the interested reader to the recent paper by Commerçon et al. (2008) for a thorough comparative study between SPH and AMR as to how a high artificial viscosity and numerical noise undermine the capacity

of the SPH technique to conserve angular momentum of disks when the number of particles (total and in the kernel) is not high enough.

Overall, our results demonstrate the need for the standard picture of galaxy disc formation and evolution to be revisited. Even though the general principles upon which it is based are sound (gas acquires its angular momentum along with DM through tidal torquing and conserves it when cooling), the fundamental assumption that it makes (specific angular momentum distribution of the gas and dark matter are the same until virialisation) does not hold because gas is not necessarily shock-heated during the gravitational collapse of the halo. A more comprehensive picture we advocate should take into account the fact that gaseous cold flows effectively carry larger than previously thought amounts of angular momentum originating from the large-scale motion of the cosmic web down to the central region of virialised structures at high redshift. Since the rotation axis of the central disc can change rapidly due to violent accretion at this redshift, the gas flows encounter a misaligned component in the vicinity of the disc, and only a fraction of the angular momentum will contribute to spinning up the disc. Gas cooling at low redshift tends to preserve this transport of angular momentum, but the presence of a pervasive shock-heated corona which entirely fills the virialised halo will make the specific angular momentum of the gas in the outer region more aligned to the central gaseous disc. Careful numerical investigation of how angular momentum is transported and/or cancelled in the central region of the halo will further help shed light into this fundamental aspect of disc formation theory.

# Chapter 5

# Simulating galaxies with more realistic stellar feedback processes

It has been known for some time that stars are not quiescent. Even though most stars appear dormant, they have actually been emitting streams of charged particles from their upper atmosphere, as illustrated by the explosive flares undergone by our very own Sun. Moreover, when massive stars end their life, their undergo a tremendous explosion, releasing a huge amount of energy, sometimes leaving a black hole at the centre. These magnificent eruptions of energy and matter are of vital importance to the evolution of galaxies, not only because they affect the fate of the surrounding gas by heating or blowing it out, but also because atoms heavier than Helium, which constitute the human body, are processed and dispersed via these phenomena.

## 5.1 Introduction

The modelling of stellar feedback processes has been a difficult task. This is mainly because with current computational capability we cannot resolve the complex behaviour of the interstellar medium (ISM) along with the evolution of individual stars. The direct consequence of this limited resolution is the formation of single warm gas phase rather than the multiphase ISM (McKee & Ostriker, 1977), causing stars to explode in a denser medium than they should. In this case, the feedback energy per unit mass decreases precipitously as it is injected in the bulk of the gas, and ends up being radiated away before it actually impacts dynamical properties of the gas.

This artificial cooling problem has been recognised and discussed in many different contexts (Katz, 1992; Thacker & Couchman, 2000; Kay et al., 2003; Slyz et al., 2005; Dalla Vecchia & Schaye, 2008;

Creasey et al., 2011; Dalla Vecchia & Schaye, 2012). Thacker & Couchman (2000) studied the impact of different prescriptions of supernova explosions in a Milky Way-like isolated galaxy and a smaller one using a SPH code, HYDRA (Thacker et al., 2000), and found that the heating temperature primarily determines the effectiveness of the feedback. Based on a modified version of the HYDRA code (Theuns et al., 1998), Kay et al. (2003) also argued that they could match the X-ray properties of galaxy groups (e.g. Ponman et al., 1999; Xue & Wu, 2000) when a sufficiently high heating temperature ($\sim 2 \times 10^7\,\mathrm{K}$) is adopted to model supernova explosions. Recently, Dalla Vecchia & Schaye (2012) investigated the emergence of galactic outflows using the GADGET code (Springel, 2005), and concluded again that stochastic supernova explosions, which ensure the minimum heating temperature of $10^{7.5}\,\mathrm{K}$, are able to drive highly mass-loaded outflows in dark matter haloes of $10^{10}$ and $10^{12}\,M_\odot\,h^{-1}$. These studies demonstrate that the cooling time of each wind particle into which energy is injected from a supernova explosion should be long enough compared to the sound crossing time-scale of the ISM where the explosion occurs (Creasey et al., 2011; Dalla Vecchia & Schaye, 2012).

An alternative way of ameliorating the overcooling problem was devised by Navarro & White (1993), who modelled the explosions by imparting momentum directly to the surrounding gas particles. An advantage of the scheme is that the injected energy is not immediately radiated away until the wind particles get shock-heated and convert their kinetic energy into internal energy. Dalla Vecchia & Schaye (2008) showed that kinetic feedback can effectively suppress the star formation by a factor of 4 in a dwarf-sized galaxy or by a factor of $\approx 1.5$ for a Milky-way prototype. They also measured that the mass loading of the wind is 5 times larger than the star formation rate for the dwarf-sized galaxy, while the factor drops to $\approx 0.2$ for the Milky way prototype. Given that their input mass loading factor ($\eta = \dot{M}_\mathrm{load}/\dot{M}_*$) is 2, the mass loading in the former case corroborates the argument that wind particles drag nearby gas particles along as they flow out of the galaxy (see also Hopkins et al., 2012b). Note, however, that the exact amount of mass loading likely depends on the details of feedback scheme. For example, Dubois & Teyssier (2008) studied the mass loading induced by kinetic supernova feedback using an AMR code, RAMSES, and came to the conclusion that the mass loaded along the outflow is only $\sim 10\,\%$ of the star formation rate. It is also worth noting that the kinetic feedback can transport metals into the intergalactic medium easily, as low-density gas can be launched with speeds on the order of $\sim 1000\,\mathrm{km\,s^{-1}}$ (e.g. Dalla Vecchia & Schaye, 2008; Powell et al., 2011; Geen et al., 2012). Owing to these benefits, the method has been used in many galactic-scale or cosmological simulations (Mihos & Hernquist, 1994; Springel & Hernquist, 2003; Oppenheimer & Davé, 2006; Cen & Ostriker, 2006;

Dubois & Teyssier, 2008; Powell et al., 2011; Kimm et al., 2012; Hopkins et al., 2012c).

Instead of trying to offset artificial cooling, several authors adopt a practical approach in which radiative cooling is simply switched off or reduced for a brief period of time (Mori et al., 1997; Thacker & Couchman, 2000; Brook et al., 2004; Stinson et al., 2006; Governato et al., 2007; Piontek & Steinmetz, 2011). This is based on the idea that the early phase of the supernova explosion is adiabatic (e.g. Chevalier, 1974). With the method adopted, Governato et al. (2007, 2009, 2010) have performed cosmological simulations using a SPH code, GASOLINE (Wadsley et al., 2004). They showed that simulated galaxies became more realistic, matching observed rotation curves of disc galaxies or forming bulgeless dwarf galaxies. Using the ENZO code (Bryan & Norman, 1997; O'Shea et al., 2004), Hummels & Bryan (2012) have also shown that suppressing the cooling for 50 Myr indeed significantly reduces the peak in the rotation curve, although it is still higher than observations.

Finally, in an effort to avoid the dilution of explosion energy by sharing it with a large amount of gas, Marri & White (2003, see also Springel & Hernquist 2003; Scannapieco et al. 2006) decoupled the hydrodynamic interactions of wind particles for a brief period of time ($\sim 50\,\mathrm{Myr}$). An advantage of the method is that metals are dispersed into the intergalactic medium quite easily, but, as pointed out by Dalla Vecchia & Schaye (2008), such a decoupling tends to produce dwarf galaxies with a smoothly distributed ISM rather than the dwarfs with irregular morphologies which are observed, because wind particles cannot intervene in the evolution of the ISM.

Physically, the two approaches, kinetic and thermal feedback models, should converge to the same numerical solution, given that the equipartition of energy is likely to lead to the same blast wave solution (Durier & Dalla Vecchia, 2012). However, since the ISM is not properly resolved, different methods yield dissimilar results in current cosmological simulations. Although the thermal model coupled with disabled cooling seems to be most effective in blowing gas out, we use the kinetic feedback in this work on the ground that the type of energy estimated for supernova explosions as well as stellar winds is mechanical energy, not thermal energy (Leitherer et al., 1992; Woosley & Weaver, 1995; Nomoto et al., 2006).

It should also be emphasised that predictions of the impact of the feedback processes are model-dependent. For example, Ceverino & Klypin (2009) argued that allowing for delayed explosions (10–100 Myr) can solve the over-cooling problem producing the multiphase ISM despite the fact that they inject the energy in a thermal form[1] (see also Slyz et al., 2005). On the other hand, Hopkins et al. (2012c,b,a) argued that all mechanisms involved should be included so as to correctly capture the mul-

[1]Note, however, that we do not see such a dramatic impact in our isolated simulations (See Section 5.3)

tiphase ISM. They demonstrated that radiation pressure by infrared photons is crucial in the driving of galactic outflows in starburst galaxies, whereas mechanical input from supernova and stellar wind is the most important process in normal spiral and dwarf galaxies.

Many previous works are based on a single supernova explosion per star particle to lessen the computational cost (e.g. Dubois & Teyssier, 2008). However, especially from a chemical enrichment point of view, this is certainly an oversimplification. A significant fraction of stellar mass is in fact lost through various phases of stellar evolution, such as Wolf-Rayet stars or the asymptotic giant branch (Leitherer et al., 1992). Thus, stellar feedback should be modelled more realistically by taking into account stellar winds, supernova type II, and type Ia (see also Kobayashi & Nakasato, 2011; Hopkins et al., 2012a). To this end, we implement continuous kinetic feedback processes in RAMSES, considering the chemical enrichment along the lines of STARBURST99 (Leitherer et al., 1999, 2010). Sec. 5.2 describes physical ingredients and our implementation of the feedback processes. In Sec. 5.3 we examine the impact of feedback models in an isolated gaseous disc embedded in a NFW-type dark matter halo (Navarro, Frenk, & White, 1997). In Sec. 5.4 we investigate the formation of realistic disc galaxies in the ΛCDM cosmology by carrying out several cosmological zoom simulations. We conclude and discuss our results in Sec. 5.5.

## 5.2 Physical Ingredients

### 5.2.1 Stellar winds and supernova type II

The observation of Wolf-Rayet stars, which resemble the spectral features of P Cygni stars, initiated the idea that stars lose mass (Adams & Burwell, 1920; Beals, 1929). More observational hints supporting mass loss were reported by Adams & MacCormack (1935), who showed that M-type supergiants exhibit blueshifted metal absorption lines with $\sim 5\,\mathrm{km\ s^{-1}}$. Deutsch (1956) found that a M supergiant, $\alpha$ Herculis, has a prominent envelope being ejected with $10\,\mathrm{km\ s^{-1}}$. A similar conclusion was reached by Weymann (1962), who studied the circumstellar lines in $\alpha$ Orionis. Studying about a hundred giants, Reimers (1975) later found a correlation between stellar parameters and mass-loss rate as

$$\dot{M} = 4 \times 10^{-13}\, \eta \left(\frac{R}{R_\odot}\right) \left(\frac{L}{L_\odot}\right) \left(\frac{M_\odot}{M}\right)\ [M_\odot/yr] \tag{5.1}$$

where $\eta$ is an empirical correction factor that ranges from 1/3 to 3. More evolved stars, such as supergiants or AGB, showed a higher mass-loss rate of $\sim\ 10^{-6}\, M_\odot\,\mathrm{yr}^{-1}$ (Morton, 1967). Luminous blue

variables (LBV) even reveal mass-loss rates of $\sim 10^{-5} - 10^{-4}\,M_{\odot}\,\mathrm{yr}^{-1}$ (e.g. Humphreys & Davidson, 1994). These indicate that the mass-loss rate depends on the evolutionary phase of a star.

To model stellar winds, the "evolutionary model" of the STARBURST99 (Leitherer et al., 1999, 2010) is adopted. For the sake of completeness, we recapitulate the details of the model here. Leitherer et al. (1992) divided stars into four classes, and applied observed terminal velocities for each class to derive the mechanical luminosity of the wind. These include

- Wolf-Rayet star ($\log T_{\rm eff} > 4.4$, $X_{\rm H,surf} < 0.4$, and $M_{\rm initial} > M_{\rm WR}$),
- LBV ($3.75 < \log T_{\rm eff} < 4.4$ and $\log \dot{M} > -3.5$),
- normal OB stars ($\log T_{\rm eff} > 3.9$),
- red super giant (RSG, $\log T_{\rm eff} < 3.9$).

Here $M_{\rm WR} \sim 20 - 60 M_{\odot}$ is the initial stellar mass of a star that can undergo a WR phase, and $X_{\rm H,surf}$ is the hydrogen mass fraction on the stellar surface.

Specifically, RSG stars with solar metallicity are assumed to release mass at a velocity of $30\,\mathrm{km\ s^{-1}}$ (Drake, 1986), while a larger velocity ($200\,\mathrm{km\ s^{-1}}$) is used for LBV stars (e.g. Humphreys & Davidson, 1994). On the other hand, the terminal velocity of OB stars is determined according to stellar properties ($v_{\infty} = f(L, M, T, Z)$), and is on the order of $\sim 1000\,\mathrm{km\ s^{-1}}$ (Howarth & Prinja, 1989). Based on radiation hydrodynamic calculations, Leitherer et al. (1992) assumed that more metal-rich stars have a larger terminal velocity ($v_{\infty} \propto Z^{0.13}$). This is expected because the line-driven force becomes stronger at higher metallicity (e.g. Castor et al., 1975). Finally, the velocity of the WR stars ($\sim 1500 - 3500\,\mathrm{km\ s^{-1}}$) is calculated depending on the surface abundance (Prinja et al., 1990). The resulting wind power is then easily calculated as $P = 0.5 \dot{M} v_{\infty}^2$, where $\dot{M}$ is the mass-loss rate given by stellar evolutionary tracks (e.g. Girardi et al., 2000) and/or empirical estimates (e.g. Vassiliadis & Wood, 1993). Using Maeder (1990) stellar tracks, Leitherer et al. (1992) demonstrated that OB and WR stars account for most of the power due to their energetic outflows, whereas LBVs are less important because such massive stars are rare. RSG stars are more numerous, but their terminal velocities are not large enough to dominate the total mechanical power.

A significant mass loss occurs around the AGB tip in the HR diagram (i.e., Mira variables). For a sample of 43 Galactic Mira variables, Vassiliadis & Wood (1993) derived a fit between the pulsating period and the mass loss rate. This empirical loss is then added to the mass loss occurred during the late

stages of stellar evolution of the Padova tracks (Girardi et al., 2000). We use the Salpeter initial mass function (Salpeter, 1955) with a low-mass cutoff at 0.1 $M_{\odot}$ and a high-mass cutoff at 100 $M_{\odot}$.

The left panels of Fig. 5.1 show the properties of the stellar winds as a function of time. The stellar mass-loss rate peaks early ($\sim 10^6 - 10^7$ yr) as a substantial fraction of mass of massive stars is ejected. On the other hand, intermediate stars (1-5 $M_{\odot}$) that undergo the thermally pulsing AGB phase dominate the mass loss rate at later epochs ($t > 10^8$ yr). Stars with a higher metallicity exhibit stronger mass loss and mechanical power due to effective radiation pressure driving. The total power released over the lifetime of individual stars ranges from $1.6 \times 10^{47}\,\mathrm{erg}$ to $2 \times 10^{48}\,\mathrm{erg}$, depending on metallicity. Notice that the metallicity shown in the second row of panels is the *net* metallicity of mass loss from supernova Type II and stellar winds.

We also present the ejecta and mechanical energy from Type II supernovae in the right panels. In contrast to the simple supernova feedback modelling described in Section 2.6.4, supernovae now occur as early as $\simeq 4$ Myr and continue to be produced until $\simeq 40$ Myr. It is also interesting to note that the total mass loss fraction is smaller for a more metal-rich population, which can be attributed to the fact that metal-rich stars lose more mass before they enter the supernova phase. The total mechanical luminosity of the supernovae (fifth panel, right column) is $\simeq 6.3 \times 10^{48}\,\mathrm{erg}$, which is about an order of magnitude larger than that of stellar winds.

We note that the total stellar mass loss obtained when adding the two sources (stellar wind and supernovae) is only $\approx 20\%$. This is smaller than Leitner & Kravtsov (2011), who estimated the mass loss fraction ($\approx 30\%$) from the empirical initial-final mass relation of Kalirai et al. (2008)[2]. The difference arises because the total mass loss fraction of intermediate stars from Vassiliadis & Wood (1993) is smaller than that of Kalirai et al. (2008). But the scatter in the initial-final mass relation and/or mass loss rate is too large to rule out one or the other.

### 5.2.2 Supernova Type Ia

While Type II supernovae contribute to the enrichment of alpha elements *and* the iron-peak elements, Type Ia supernovae preferentially synthesise iron-peak elements. Due to this behaviour, the alpha enhancement, $[\alpha/\mathrm{Fe}] = \log(\alpha/\mathrm{Fe}) - \log(\alpha/\mathrm{Fe})_{\odot}$, carries critical information about the duration of star formation and is of great importance in constraining the stellar assembly history of massive galaxies.

[2]Kalirai et al. (2008) obtained the mass of white dwarfs and their cooling time by fitting the Balmer lines of the observed spectra to a model atmosphere (see also Weidemann, 2000). Since the cluster age can be computed by fitting the main sequence, subtracting the dwarf cooling time from the cluster age gives the lifetime of the progenitor main sequence. Then, one can get the mass of the star on the main sequence by using the relation between its mass and lifetime

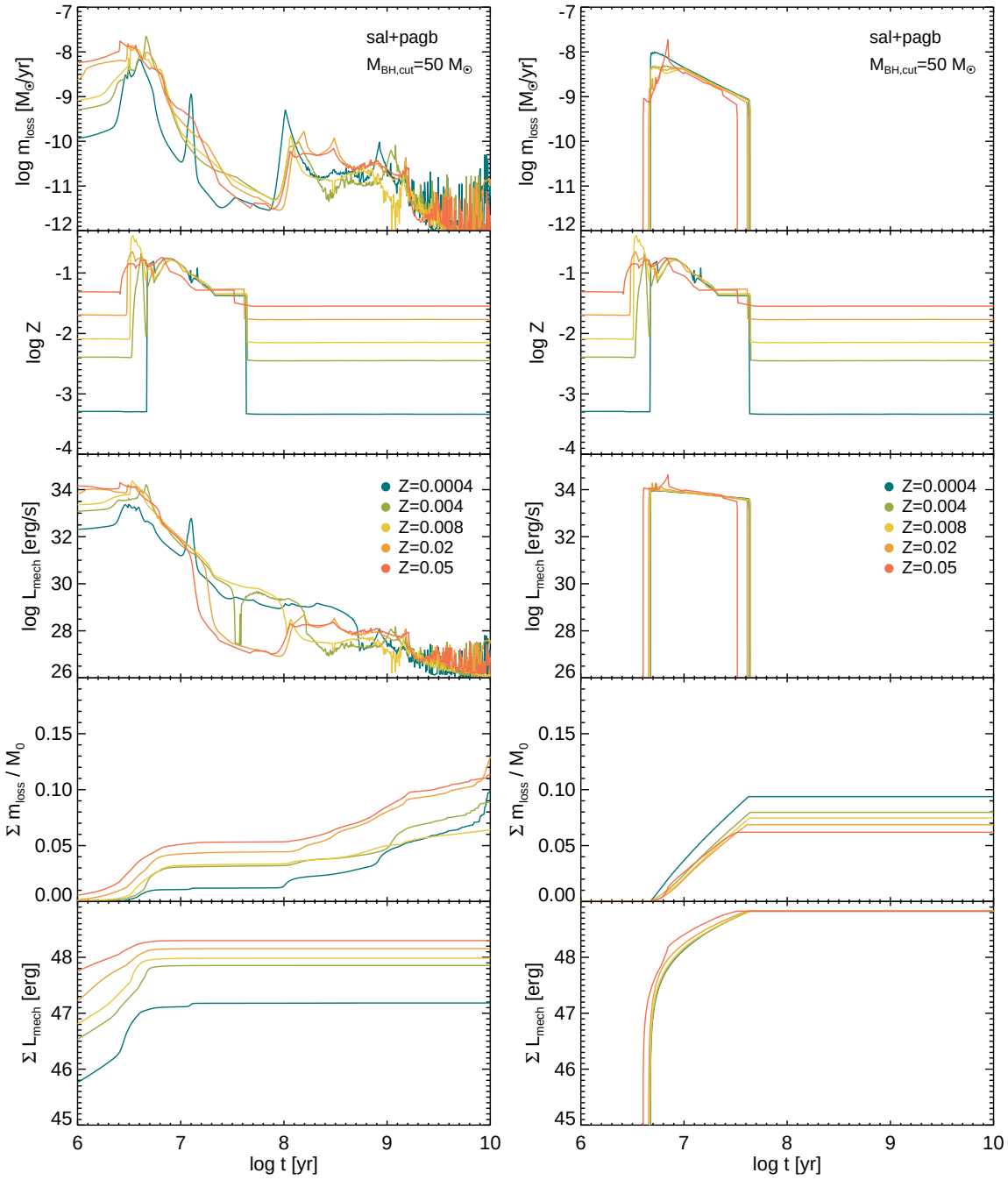


Figure 5.1: Stellar mass loss ($m_{\rm loss}$), metallicity of the ejecta ($Z$), and mechanical luminosity ($L_{\rm mech}$) generated by STARBURST99 (Leitherer et al., 2010) using a Salpeter IMF with a low-mass cutoff at 0.1 $M_\odot$ and a high-mass cutoff at 100 $M_\odot$. Also included are the integrated fraction of mass loss (fourth row of panels) and the mechanical energy (fifth row of panels) as a function of time. The left panels represent the contribution from stellar winds, which are computed using the Padova stellar tracks (Girardi et al., 2000) including the empirical mass loss rate from AGB stars (Vassiliadis & Wood, 1993). The mass and energy released by supernova Type II are shown in the right panels. We assume that stars above 50 $M_\odot$ implode and form a black hole and thus do not produce a supernova. Different colours denote different metallicities, as indicated in the legend. Notice that the metallicity shown in the second row of panels is the *net* metallicity of mass loss from supernova Type II and stellar winds, and thus the left and right panels are identical.

Several scenarios have been suggested to explain the occurrence of Type Ia supernovae (SN Ia). The most popular idea is that a carbon-oxygen white dwarf undergoes a thermonuclear explosion when additional mass is accreted from a companion and triggers explosive carbon burning in a degenerate core (Hoyle & Fowler, 1960). The carbon ignition thin shell then propagates outward subsonically (deflagration) or supersonically (detonation), disrupting the entire white dwarf (see Hillebrandt & Niemeyer, 2000, for a review). Merging carbon-oxygen white dwarfs may also give rise to SN Ia when the Chandrasekhar mass is reached (Iben & Tutukov, 1984), although it appears that an off-centre carbon or oxygen deflagration tends to induce a collapse rather than explosion (Nomoto & Kondo, 1991). Another possible origin is a carbon-oxygen white dwarf with sub-Chandrasekhar mass for which the detonation of helium accreted from a He-rich companion triggers a secondary carbon detonation in the core (Woosley & Weaver, 1994).

In this study, we use the carbon-deflagration model (W7) of Nomoto, Thielemann, & Yokoi (1984), which gives good agreement with the observed spectra of SN 1992A and SN 1994D (Nugent et al., 1997). In this scenario, the binary system consists of a carbon-oxygen carbon dwarf and a post main sequence star, and thus the emergence of SN Ia is largely determined by the lifetime of the secondary star. Since stars more massive than 8 $M_{\odot}$ would not form a carbon-oxygen white dwarf, this sets the maximum progenitor mass ($M_{\rm max}$) for the primary star. To model the frequency of SN Ia explosions ($R_{\rm Ia}$), we follow the standard method of Greggio & Renzini (1983, see also Matteucci & Greggio 1986) as

$$R_{\rm Ia}(t) = \frac{\rm d}{{\rm d}t}\left[A_{\rm Ia}\int_{M_{\rm b,low}}^{M_{\rm b,upp}} f\left[\frac{M_2(t)}{M_b}\right]\,\phi(M_{\rm b})\,\frac{{\rm d}M_{\rm b}}{M_{\rm b}}\right],$$

where

$$M_{\rm b,low} = \max\left[2M_2(t), M_{\rm min}\right]$$
$$M_{\rm b,upp} = M_{\rm max} + M_2(t).$$

Here $M_b$ is the total mass of the binary system, $M_2(t)$ is the mass of the secondary star that transfers its mass to the carbon-oxygen white dwarf at some epoch $t$, and $\phi$ is the Salpeter initial mass function. The minimum mass for SN Ia ($M_{\rm min}$) is set to 3 $M_{\odot}$ to ensure that the total mass of the white dwarf and its companion reaches the Chandrasekhar limit. The main sequence lifetime of a star is computed following

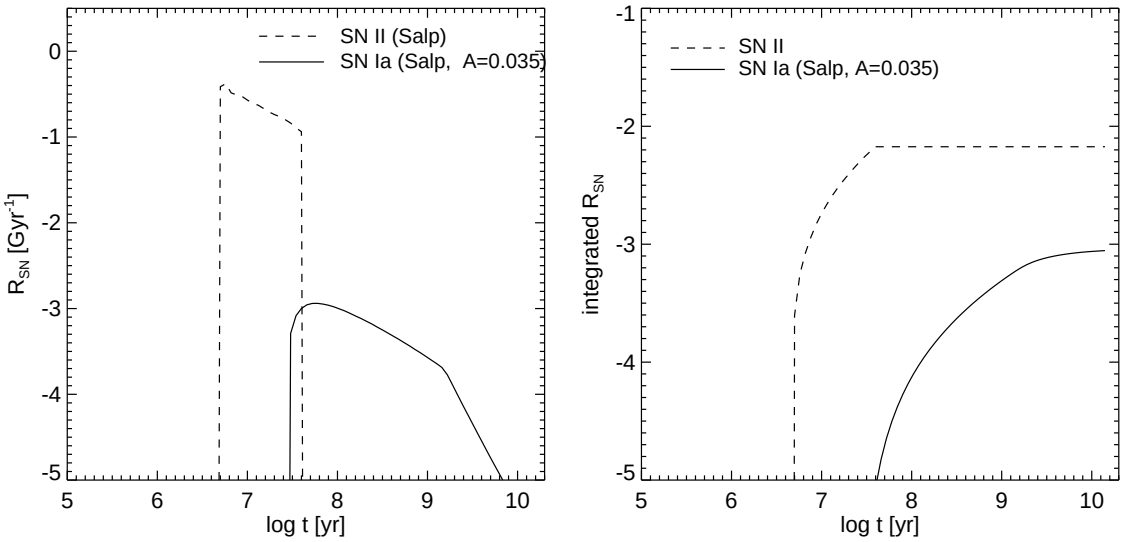


Figure 5.2: Frequency of Type Ia and II supernovae per unit mass (left) and their integrated rates (right). SN Ia explosions commence from $\simeq 30\,\mathrm{Myr}$ onwards due to the presence of massive binaries composed of two 8 $M_\odot$ stars. The total number of SN Ia explosions is smaller than its SN II counterpart.

Padovani & Matteucci (1993),

$$\log \tau_m\,[\mathrm{yr}] = \left[1.338 - \sqrt{1.79 - 0.2232\ (7.764 - \log m)}\right] /0.1116.$$

We adopt the following functional form for the distribution of secondary stars ($\mu \equiv M_2(t)/M_b$) as

$$f(\mu) = 2^{1+\gamma}(1+\gamma)\mu^\gamma \quad (0 < \mu \leq 0.5),$$

with a parameter $\gamma = 2$ (e.g. Greggio & Renzini, 1983), which favours equal-mass binary systems (Tutukov & Iungelson, 1980). Finally, a free parameter $A_{\mathrm{Ia}}$ represents the fraction of binary systems entering the SN Ia phase relative to the total number of stars in the mass range. It is model-dependent, and should be calibrated on the observed SN Ia rate (e.g. Mannucci et al., 2006).

Fig. 5.2 shows the rate of SN Ia explosions with $A_{\mathrm{Ia}} = 0.035$ (solid lines), which is the value required to match the abundance ratios of the Milky Way (c.f. Thomas et al., 1998; Matteucci & Recchi, 2001). Also included is the rate for Type II computed with the main sequence lifetime from the Padova track (Girardi et al., 2000), as is done in STARBURST99. The SN Ia explosions commence from $\simeq 30\,\mathrm{Myr}$ onwards due to the presence of massive binaries composed of two 8 $M_\odot$ progenitor stars. SN II explosions outnumber SN Ia, meaning that the contribution from SN Ia is negligible to the total energy budget. Indeed, Fig. 5.3 shows that although the energy from SN Ia is comparable to that of stellar winds,

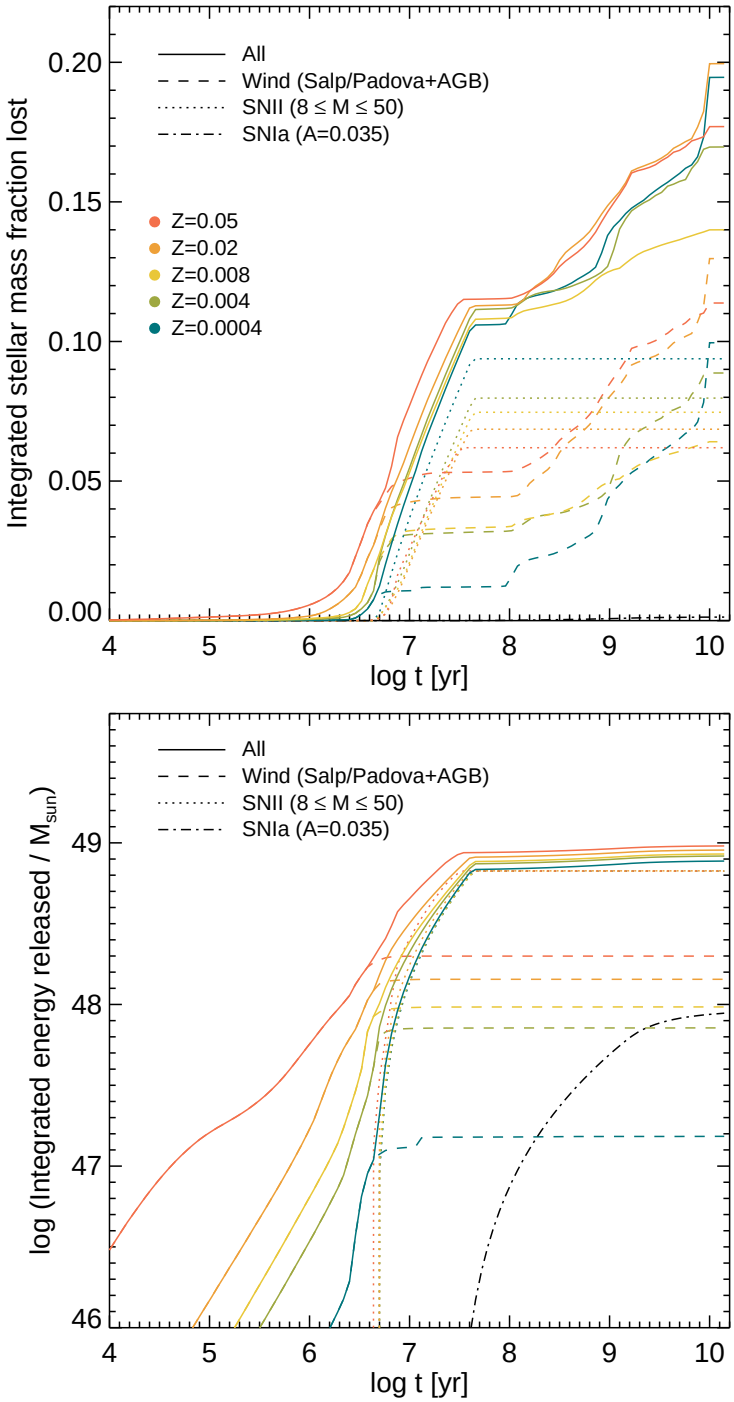


Figure 5.3: Mass loss and energy release from stellar winds, SN II, and Ia. The rate of SN II explosions is computed with a lower mass bound of 8 $M_\odot$ and higher mass bound of 50 $M_\odot$. We assume that 7% of binaries composed of a CO-WD and post-main sequence star produce SNIa. The mass loss rate for stellar winds is the same as Fig. 5.1. It can be seen that contributions from stellar winds and SN II to the total mass loss are comparable, whereas SN Ia accounts for less than $10\,\%$ of the total loss. The dominant energy source is SN II, which is an order of magnitude larger than the energy from stellar winds or SN Ia.

it is an order of magnitude smaller than the energy from Type II supernovae. The same figure also shows that the mass loss from the SNIa is negligible, while stellar winds and SN II equally contribute to the total mass loss.

### 5.2.3 Hypernovae

It is observationally known that some supernova explosions release an order of magnitude more energy than core-collapse supernovae such as SN 1987A. These are called hypernovae (HNe), and reported in several cases: SN 1997ef (Iwamoto et al., 2000; Mazzali et al., 2000), SN 1998bw (Patat et al., 2001; Nakamura et al., 2001), SN 2002ap (Mazzali et al. 2002), SN 2003dh (Stanek et al., 2003; Hjorth et al., 2003), and SN 2003lw (Malesani et al., 2004; Thomsen et al., 2004). These authors have compared the time evolution of observed synthetic spectra and bolometric luminosity with the light processed by stratified expanding shells (e.g. Mazzali & Lucy, 1993), and come to a conclusion that the isotropic kinetic energy liberated from the explosions of a massive star (20–50 $M_\odot$) amounts to $10\text{–}50 \times 10^{51}\,\mathrm{erg}$.

Because of the energetic explosion, HNe are thought to be effective at synthesising some iron-peak elements, such as Zn or Co (Tominaga, Umeda, & Nomoto, 2007). Umeda & Nomoto (2002) first argued that highly energetic explosions are required to match [Co/Fe] and [Zn/Fe] ratios observed in very metal-poor halo stars. With updated hydrodynamic and nucleosynthesis models of HNe, Tominaga, Umeda, & Nomoto (2007) were indeed able to reproduce the anomalous abundance ratios of extremely metal-poor ($[\mathrm{Fe/H}] = -3.7$) stars in the Galaxy (Cayrel et al., 2004). These HN explosions are known to be rare in the local universe, and thus inconsistent with the scenario in which all the massive stars with $20 \leq M \leq 50\ M_\odot$ end as HNe (Podsiadlowski et al., 2004). The frequency of HNe is around 1% of the total supernova type II rate (Podsiadlowski et al., 2004). Therefore, an appealing and observationally viable scenario for all these studies is that HN explosions are frequent in the early universe where the metallicity of stars is very low, whereas such explosions are inhibited in metal-rich systems.

Motivated by these considerations, we tested the possibility that a fraction of massive stars ($20 \leq M \leq 50\ M_\odot$) can explode as HN, releasing $E_{\mathrm{HN}} = 10^{52}\,\mathrm{erg}$ of energy. Following Kobayashi et al. (2011), stars above 50 $M_\odot$ are assumed to implode without producing metals. When no upper limit is set, massive stars increase the [$\alpha$/Fe] ratio and the [$\alpha$/Fe] plateau observed in low metallicity stars cannot be reproduced (Kobayashi et al., 2006). We also use a metal-dependent fraction of HN explosions for stars in the mass range ($20 \leq M \leq 50\ M_\odot$), as in Kobayashi & Nakasato (2011) (see the left panel of Fig. 5.4). For metal-rich stars, a fraction consistent with local observations (1%) is adopted. However, since heavy

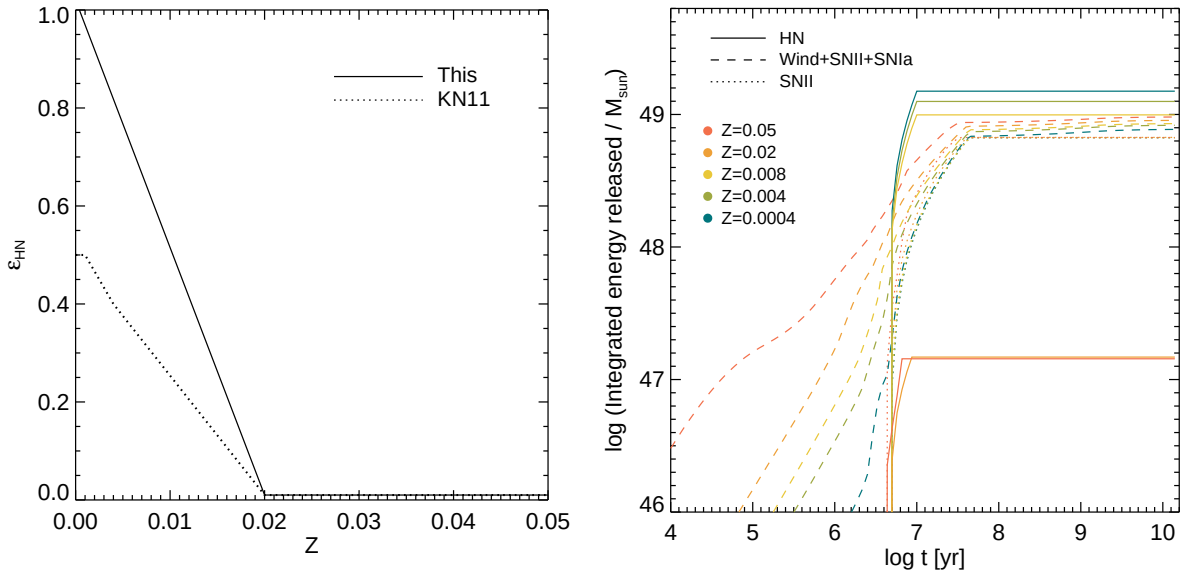


Figure 5.4: *Left:* Metal-dependent fraction of hypernovae (HNe) in the mass range 20–50 $M_{\odot}$. The HN fraction used in the chemodynamic simulation by Kobayashi & Nakasato (2011) is presented as a dotted line. *Right:* Comparison between the energy released by "normal" stars (SN II+Ia+SW) and the energy from HNe. For metal-poor stars, the explosion energy from HNe is approximately two times larger than the total energy released by standard stellar feedback processes.

elements such as titanium are still underproduced in Kobayashi & Nakasato (2011), who assumed that half of the massive stars with primordial abundance will undergo HN explosions, we increase the fraction to unity for zero metallicity stars. In principle, the latter is equivalent to assuming twice the energy from the HNe, i.e. $E_{\rm HN} = 2 \times 10^{52}$ erg, while keeping the maximum HN fraction to half, as we do not use different metal yields for the HNe for the sake of simplicity.

The resulting energy distribution for a simple stellar population is shown in the right panel of Fig. 5.4. We note that, in effect, the inclusion of HNe with the Salpeter IMF has the same consequence as boosting the specific supernova energy by a factor of $\sim$3 at high redshift. At low redshift, the contribution from HNe must be negligible as newly formed stars would be metal-rich. Since Type II SN explosions per unit mass are already taken into account by employing the STARBURST99 model, only additional energy is added through the parameter `e_HN`, as

$$\max(\varepsilon_{\rm HN})\, E_{\rm HN} - 10^{51}\,{\rm erg} = \texttt{e\_HN}\ 10^{51}\,{\rm erg}.$$

### 5.2.4 Implementation of multiple explosions

An ultimate goal of any theoretical model on stellar feedback is to simulate individual supernovae in a turbulent medium, but this is not feasible with the current computing power. Thus, almost all cosmolog-

ical or non-cosmological simulations have used massive star particles weighing more than $10^4$–$10^6\,M_\odot$ (e.g. Springel & Hernquist, 2003; Slyz et al., 2005; Scannapieco et al., 2006; Dalla Vecchia & Schaye, 2008; Dubois & Teyssier, 2008), and assumed that a star particle hosts a single supernova explosion. For example, Dubois & Teyssier (2008) assumed that each star particle releases $m_{\rm star}\eta_{\rm SN}\,10^{51}\,{\rm erg}$ 10 Myr after the star particle has been created, where $m_{\rm star}$ is the mass of the star particle, $\eta_{\rm SN}$ is the mass fraction that can enter the Type II SN phase. A similar approach is employed by Ceverino & Klypin (2009), who used 40 Myr instead for the delay time. Given that even a simple stellar population has a wide spectrum in mass, the single explosion is an oversimplification. The next step towards a realistic modelling of stellar feedback should include multiple supernova explosions.

To this end, we implement multiple discrete explosions which occur every coarse time step, based on the same technique used in Dubois & Teyssier (2008). To sum things up, kinetic energy is injected into gas cells within a bubble radius in such a way to explicitly conserve mass and linear momentum. The ejecta from the explosions is uniformly distributed inside the bubble as

$$\rho_i^{n+1} = \rho_i^n + \rho_{\rm ejecta} + \rho_{\rm load} = \rho_i^n + (1+\eta_w)\,M_{\rm ejecta}/V_{\rm bub},$$

where $n$ represents the $n$-th time step, $M_{\rm ejecta}$ is the mass loss during $\Delta t$, and $\Delta V_{\rm bub}$ is the total volume of the cells inside the bubble radius. The amount of gas entrained with the stellar ejecta ($\rho_{\rm load} = \eta_w\rho_{\rm ejecta}$) is accounted for by introducing a mass-loading factor $\eta_w$, and subtracted from the leaf cell where the star particle sits. Note that the size of the bubble is forced to be larger than $2\,\Delta x$, where $\Delta x$ is the size of the finest cell, so that the expanding shell can form an approximately spherical bubble in a low-density, uniform medium (Fig. 5.5). Since AMR cells are discretised and their distribution with respect to a star particle is bound to be asymmetric, velocity and energy need be corrected to ensure conservation of linear momentum. The correction factor for a velocity ($\Delta\vec{\mathbf{q}}$) can be calculated as

$$(1+\eta_w)\sum_i^{\rm bub}\rho_{\rm ejecta}V_i\,(\vec{\mathbf{u}}_{\rm exp}\cdot\hat{\mathbf{r}}) = \vec{\Delta q}\,|\vec{\mathbf{u}}_{\rm exp}|\,(1+\eta_w)\,\rho_{\rm ejecta}V_{\rm bub}$$

where the expansion velocity is

$$u_{\rm exp} = \sqrt{\frac{2E}{(1+\eta_w)\,m_{\rm ejecta}}}. \tag{5.2}$$

The actual momentum added to each cell ($\Delta\vec{\mathbf{p}}$) is then

$$\Delta\vec{\mathbf{p}} = (1+\eta_w)\,\rho_{\rm ejecta}\,(\mathbf{I}-\Delta\vec{\mathbf{q}})\cdot\vec{\mathbf{u}}_{\rm exp} + \rho_{\rm ejecta}\vec{\mathbf{u}}_{\rm ejecta} + \eta_w\rho_{\rm ejecta}\vec{\mathbf{u}}_{\rm load}.$$

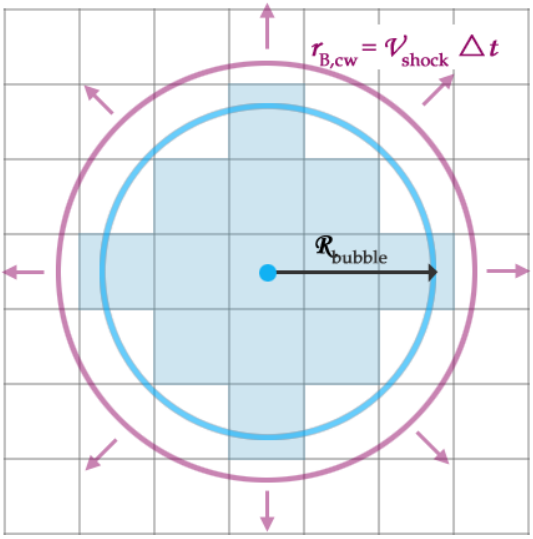


Figure 5.5: Illustration of the condition for launching a blast wave. A blast wave is allowed to propagate only if a shock advances enough to reach the bubble radius set by the user. If the condition is not met, the energy is stored until the next time step.

The second term represents the original momentum of a star particle ejecting mass, and the last term indicates the linear momentum of the gas entrained from the cell in which SNe or stellar winds occur. Finally, the amount of kinetic energy corresponding to the increase in velocity in each cell is added to the energy hydrodynamic variable to ensure energy conservation.

The improvement made over Dubois & Teyssier (2008) is that we inject the energy only if a blast wave propagates far enough to reach the bubble radius set by the user. Thus, we pile up the energy, mass, and metals during $\Delta t = t - t_{\rm last}$ for each star, where $t$ is the current time step and $t_{\rm last}$ is the time at which the last blast wave is allowed to propagate into the interstellar medium. If the energy stored is large enough to make the shock radius ($r_{\rm B,cw}$) bigger than the bubble radius ($r_{\rm bubble}$), then a blast wave will be launched. The size of the shock front is determined assuming a blast wave propagating self-similarly in a uniform medium, and can be described as

$$r_{\rm B,cw} \simeq 44\ {\rm pc} \left[ \left( \frac{E_{\rm wind}}{10^{47}\ {\rm erg}} \right) \left( \frac{0.1\ {\rm H/cm^3}}{n_{\rm H}} \right) \right]^{0.2} \left( \frac{\Delta t}{10^7\ {\rm yr}} \right)^{0.4} \tag{5.3}$$

for a typical set of parameters around star forming regions. The problem of this condition is that although the wind velocity is fixed, the estimate of the radius can be artificially large if the density of a cell is too small. This is evidently unphysical and should be avoided. The maximum radius is thus limited by the free expansion velocity as,

$$r_{\rm B,min} = \min \left[ r_{\rm B,cw}, v_{\rm wind} \Delta t \right].$$

Unlike thermal feedback models, kinetic feedback requires that we compute the average density for every star particle, which is computationally expensive. Fortunately, almost all of the energy available from a simple stellar population is released during the first several tens of Myrs, so we adopt the kinetic feedback for stars younger than a certain age ($t \leq t_{\rm ctw}$[3]). A reasonable choice is $t_{\rm ctw} = 50\,{\rm Myr}$, given that $\simeq 90\,\%$ of the total energy is released during this time. This roughly corresponds to the time at which Type Ia supernovae come into play. After $t_{\rm ctw}$, the energy is input thermally.

Since stars form in a clustered fashion, young stars are likely to be located in small regions of the simulation volume. Moreover, given that the simulation cannot resolve better than the size of the finest cell, it is more sensible to evaluate Equation 5.3 on a cell-by-cell basis. This also has the benefit of reducing the computation time. Thus, our stellar feedback represents collective winds from stellar winds, SNe II, Ia, and sometimes HNe.

[3]The subscript 'ctw' means the onset of Continuous Thermal Winds, which are injected at each fine time step.

## 5.3 Stellar feedback in isolated disc simulations

### 5.3.1 Simulation set-up

With the physical ingredients specified in the previous section, we are now in a position to investigate the impact of stellar feedback processes by simulating the evolution of an isolated disc galaxy. Since star formation is more vigorous and stellar feedback is likely to be more important at high redshift (e.g. Daddi et al., 2007; Elbaz et al., 2007; Stark et al., 2009; Genzel et al., 2010), we choose initial conditions that mimic clumpy discy galaxies that are often observed in the early Universe (e.g. Elmegreen et al., 2007; Genzel et al., 2011). We assume that gas follows a double exponential gas density profile as

$$\rho(r,z) = \rho_{\rm max} \exp\left[-\left(\frac{r}{2\ {\rm kpc}}\right) - \left(\frac{r}{10\ {\rm kpc}}\right)^5\right] {\rm sech}^2\left(\frac{z}{200\ {\rm pc}}\right) + \rho_{\rm min},$$

where the minimum density ($\rho_{\rm min}$) is $3.3 \times 10^{-7}\ {\rm m_H/cm^3}$ and the maximum density ($\rho_{\rm max}$) is $\simeq 13\ {\rm m_H/cm^3}$. The initial velocity field of the gas is given assuming Kepler rotation:

$$\begin{aligned} v_x &= \left[\frac{GM(x^2+y^2)}{R^3}\right]^{1/2} \frac{-y}{R} \\ v_y &= \left[\frac{GM(x^2+y^2)}{R^3}\right]^{1/2} \frac{x}{R} \\ v_z &= 0, \end{aligned} \tag{5.4}$$

where $M = M_{\rm gas} + M_{\rm halo} \simeq 6.4 \times 10^{10}\ M_\odot$. We set the initial temperature of the gas to $10^4$ K.

The simulation is run on $64^3$ coarse grid, and three further levels of adaptive refinements are triggered when the mass of a cell exceeds $\simeq 5.5 \times 10^6\ M_\odot$. The length of the simulation box measures $\simeq 36$ kpc, and the maximum resolution of the AMR grid is $\Delta x = 70\,{\rm pc}$. Gravitational forces due to a NFW dark matter halo with $V_c = 50\,{\rm km\,s^{-1}}$ and $c_{\rm NFW} = 10$ (corresponding to $M_{\rm vir} \simeq 6 \times 10^{10}\,M_\odot$) are taken into consideration analytically. The Euler equations are solved using the HLLC solver (Toro et al., 1994) with radiative cooling turned on. The initial metallicity of the gas is assumed to be $10^{-3} Z_\odot$, and a typical Courant number of $C_{\rm cfl} = 0.8$ is used. Gas can cool down to 1 K owing to metal cooling, and stars can form out of dense gas ($n_{\rm H,thres} \geq 25\ {\rm cm^{-3}}$) with 1% efficiency per free-fall time in the case of intermediate resolution runs. Since the simulation cannot resolve the multiphase interstellar medium, we adopt a polytropic equation of state with an index $\gamma = 4/3$ for gas denser than $n_{\rm H,thres}$. To account for metal enrichment by SN Ia, we adopt $A_{\rm Ia} = 0.07$. Parameters associated with stellar feedback processes

Table 5.1: Summary of simulation parameters. From left to right, columns are as follows: the name of the simulation, the number of explosions from a simple stellar population, the minimum grid size, the threshold density for star formation, the minimum mass of star particles, the mass-loading factor, the delay time for the single explosion model, the time from which thermal energy is injected, and remarks. The first (second) letter of simulation names represent the resolution, i.e. High, Medium, or Low (the number of explosions, i.e. Single or Multiple).

| Model | No. of Explosions | $\Delta x_{\rm min}$ [pc] | $n_*$ [$\rm cm^{-3}$] | $\epsilon_*$ | $m_*$ [$M_\odot$] | $\eta_w^1$ | Delay [Myr] | $t_{\rm ctw}$ [Myr] | Remarks |
|---|---|---|---|---|---|---|---|---|---|
| MS-w10 | single | 70 | 25 | 0.03 | $2.7\times10^5$ | 10 | 10 | – | |
| MM-w10 | multiple | 70 | 25 | 0.03 | $2.7\times10^5$ | 10 | – | 50 | |
| MM-w1 | multiple | 70 | 25 | 0.03 | $2.7\times10^5$ | 1 | – | 50 | |
| MM-w5 | multiple | 70 | 25 | 0.03 | $2.7\times10^5$ | 5 | – | 50 | |
| MM-w20 | multiple | 70 | 25 | 0.03 | $2.7\times10^5$ | 20 | – | 50 | |
| MM-w50 | multiple | 70 | 25 | 0.03 | $2.7\times10^5$ | 50 | – | 50 | |
| MM-t00 | multiple | 70 | 25 | 0.03 | $2.7\times10^5$ | 10 | – | 0 | thermal |
| MM-HN | multiple | 70 | 25 | 0.03 | $2.7\times10^5$ | 10 | – | 50 | hypernovae |
| MM-e5 | multiple | 70 | 25 | 0.03 | $2.7\times10^5$ | 10 | – | 50 | strong |
| HS-w10 | single | 17.5 | 400 | 0.01 | $6.8\times10^4$ | 10 | 10 | – | |
| HM-w5 | multiple | 17.5 | 400 | 0.01 | $6.8\times10^4$ | 5 | – | 50 | |
| HM-w10 | multiple | 17.5 | 400 | 0.01 | $6.8\times10^4$ | 10 | – | 50 | |
| HM-w20 | multiple | 17.5 | 400 | 0.01 | $6.8\times10^4$ | 20 | – | 50 | |
| LM-w10 | multiple | 140 | 6 | 0.07 | $5.3\times10^5$ | 10 | – | 50 | |

are altered to determine their impacts on gas dynamics. We also present simulations with higher and lower resolution ($\Delta x = 18\,\rm pc$ or $140\,\rm pc$) to quantify the importance of numerical resolution. In order to resolve the Jeans length self-consistently, we vary the threshold density for star formation based on the Jeans instability condition by setting $\lambda_J = \Delta x$, as

$$\lambda_J = \sqrt{\frac{15\,k_B\,T}{4\pi\mu m_{\rm p} G\rho}} = \Delta x_{\rm min}$$

$$n_{\rm H,thres} \simeq \frac{X_{\rm H}\,\rho_{\rm thres}}{m_{\rm p}} = \frac{15\,k_B\,X_{\rm H} T_0}{4\pi\mu m_{\rm p}^2 G(\Delta x_{\rm min})^2} \propto \frac{T_0}{\Delta x_{\rm min}^2}.$$

We note that resolution can play an important role in predicting the star formation rate in galaxies that are gravitationally unstable, such as merging galaxies (Teyssier, Chapon, & Bournaud, 2010). In order to ensure a similar star formation history, different efficiencies for star formation are used for the runs with different resolution (see the left panel of Fig. 5.6). The parameters used in each simulation are summarised in Table 5.1.

[1]Notice that the symbol $\eta_{\rm w} \equiv \dot{m}_{\rm out}/\dot{m}_{\rm loss}$ is different from the mass-loading factor ($\eta \equiv \dot{m}_{\rm out}/\dot{m}_*$) commonly used in the literature (e.g. Martin, 1999).

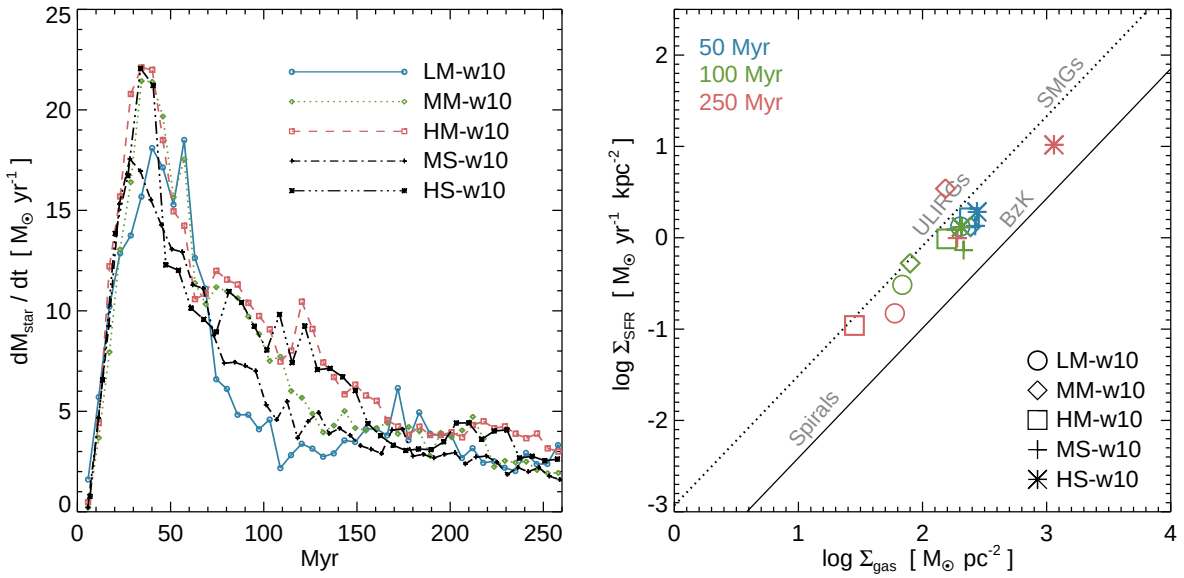


Figure 5.6: Left: Evolution of SFRs in models with different resolution and ingredients, as indicated in the legend. Right: SFR density as a function of the gas surface density of simulated galaxies at 50 Myr (blue), 100 Myr (green), and 250 Myr (red). Solid line shows a fit to the normal spirals and BzK galaxies (Eq. 5.5), whereas the dotted line represents starburst galaxies, which is 0.9 dex larger than the normal star forming sequence (Daddi et al., 2010).

### 5.3.2 Results

Our initial galactic disc is purely gaseous, and thus it first collapses and form stars vigorously. The peak SFR reaches $\sim 20\,M_\odot\,\mathrm{yr}^{-1}$ around 30 Myr, but it declines quickly and settles to $2-4\,M_\odot\,\mathrm{yr}^{-1}$ (Fig. 5.6, left panel). Note that this is at least a factor of a few larger than the SFRs observed in the local normal spiral galaxies (Salim et al., 2007). To compare the level of the SF activity with the empirical relations by Daddi et al. (2010, see also Genzel et al. 2010 for molecular surface density relations), we compute the SFR surface density and gas surface density within the half-(stellar) mass radii (Fig. 5.6, right panel). We find that the simulated galaxies are indeed placed above the normal star forming sequence composed of normal spirals and BzK galaxies (Daddi et al., 2004), which is represented as a fit (Daddi et al., 2010)

$$\Sigma_{\mathrm{SFR}} = 1.48\times10^{-4}\,M_\odot\,\mathrm{yr}^{-1}\,\mathrm{kpc}^{-2}\left(\frac{\Sigma_{\mathrm{gas}}}{M_\odot\,\mathrm{pc}^{-2}}\right)^{1.42}. \tag{5.5}$$

However, the SF activities of the simulated galaxies are not active enough to be classified as starburst galaxies, such as ultra luminous infrared galaxies (ULIRGs, Sanders & Mirabel, 1996) or sub-millimetre galaxies (SMGs, Barger et al., 1998). Although a high-resolution run, `HS-w10`, exhibits a very high gas surface density and high SFR at 250 Myr, the large values turn out to occur because gas fragments into clumps and SF is confined exclusively to the very central region. As can be seen in the left panel

in Fig. 5.6, the actual SFR does not rise to $\sim 1000\,M_{\odot}\,\mathrm{yr}^{-1}$, as observed in SMGs (e.g. Barger et al., 1998), and therefore it should be considered to be an actively star forming galaxy rather than a starburst.

#### 5.3.2.1 Single versus multiple explosions

We first compare the impact of the number of explosions on the properties of the interstellar medium. Fig. 5.7 shows projected densities of gas, and slices of gas density, temperature, and metallicity from different models at $t = 200\,\mathrm{Myr}$. Stellar feedback is able to blow gas away not only in the single explosion run (`MS-w10`, the first row) but also in the multiple explosion run (`MM-w10`, the second row), increasing the temperature up to $10^8\,\mathrm{K}$. However, gas clumps turn out to be robust against feedback processes, and no clumps with depressed central densities can be found, which would be a clear sign of effective feedback processes. The metallicity of the ejecta is super-solar and thus effective at enriching the intergalactic medium in both models. The morphology of gas, temperature, and metallicity is found to be largely indistinguishable between the two runs. This is not unexpected, given that the star formation occurs in a clustered fashion in both runs (see Fig. 5.7), and thus the multiple explosions do not appear to make a significant difference compared to the single explosion in terms of the morphology.

Fig. 5.8 shows the phase diagrams for the two high-resolution runs, `HS-w10` and `HM-w10`, at $t = 200\,\mathrm{Myr}$. Red (blue) colours indicate high (low) gas metallicity. Both runs show prominent warm-hot diffuse gas component characterised by $10^5 \lesssim T \lesssim 10^7\,\mathrm{K}$ and $n_{\mathrm{H}} \lesssim 1\,\mathrm{cm}^{-3}$ and cold dense gas with $T \lesssim 10^3\,\mathrm{K}$ and $n_{\mathrm{H}} \gtrsim 1\,\mathrm{cm}^{-3}$. It can be seen that the hot gas is very metal-rich, implying that it is the gas parcel into which the energy and mass are injected directly. Note that the star forming gas ($n_{\mathrm{H}} \geq 400\,\mathrm{cm}^{-3}$) is highly enriched as well ($Z \simeq 0.5\,Z_{\odot}$). A notable difference of the two runs is that even though its mass fraction is negligible, only `HM-w10` exhibits hot and very diffuse gas with $T \gtrsim 10^6\,\mathrm{K}$ and $n_{\mathrm{H}} \lesssim 10^{-4}\,\mathrm{cm}^{-3}$. This arises because the energy release is much more extended in the `HM-w10` run and stars can directly deposit their energy into very diffuse gas, whereas the SN explosions always occur in relatively dense medium in the `HS-w10` run. As a result, the maximum temperature of the gas is higher in the `HM-w10` run, and the simulation took longer to run due to a more stringent Courant condition. For example, when run on an SGI Altix ICE cluster featuring Intel Xeon E5650 processors (2.67 GHz), `HM-w10` required 312 hours of CPU wall clock time, i.e. twice longer than that of `HS-w10` (168 hours).

We also quantify the impact of stellar feedback by measuring the outflow rate ($\dot{m}_{\mathrm{out}}$), which is defined as the addition of fluxes through two planes parallel to the disc of the galaxy and located $\pm 9\,\mathrm{kpc}$

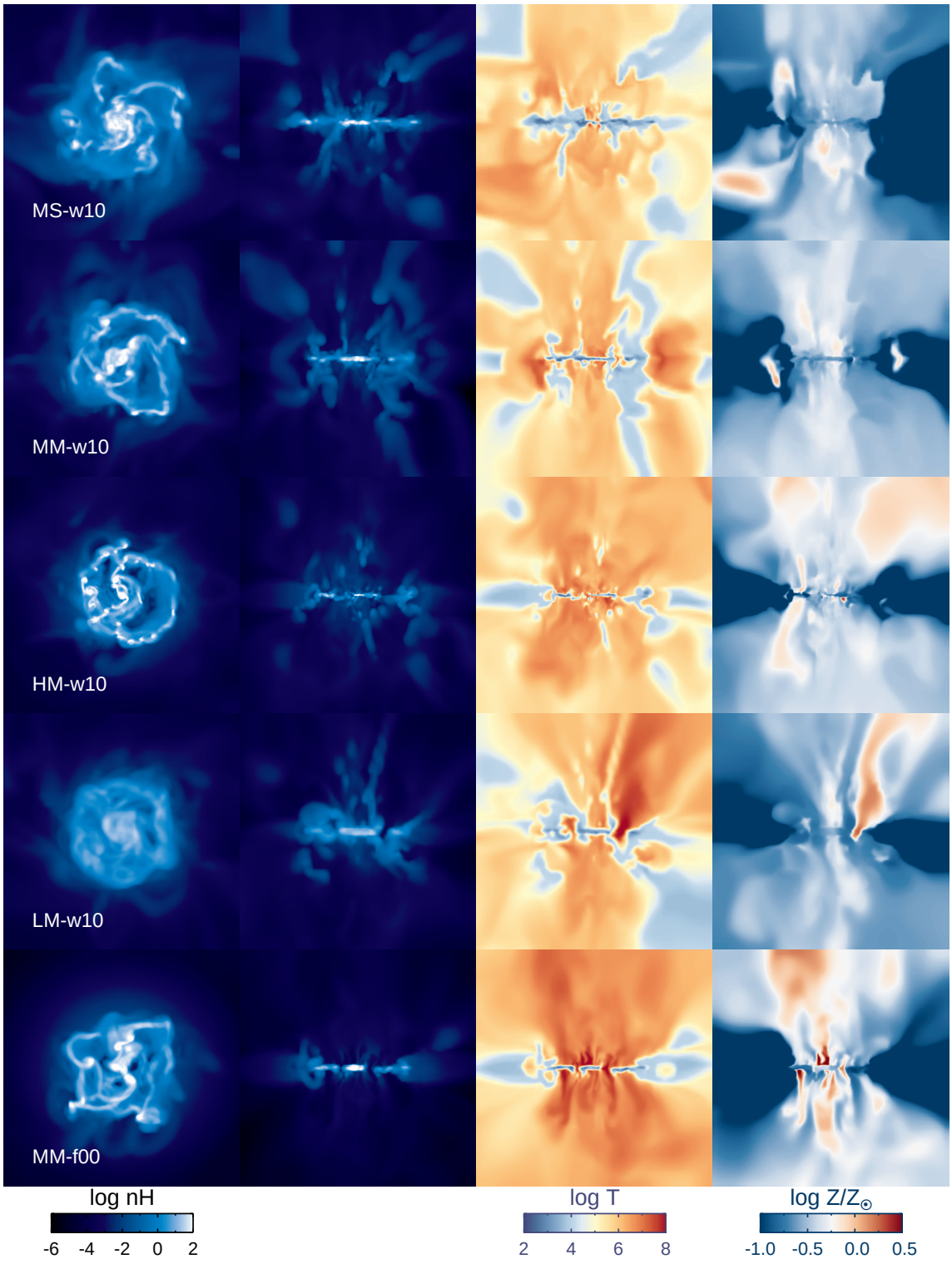


Figure 5.7: Distribution of gas density, temperature, and metallicity at $t = 200\,\mathrm{Myr}$. The first columns show projected densities of gas along the z-axis, while the other three columns present a slice of gas density (second), temperature (third), and metallicity (fourth). The solar metallicity is assumed to be $Z_\odot = 0.02$. The first two rows correspond to models with a single explosion (`MS-w10`) and multiple explosions (`MM-w10`). The panels in the third row (`MM-f00`) show the gas properties in the model with thermal feedback. Models with lower (`LM-w10`) and higher (`HM-w10`) resolution are also included in the fourth and fifth rows. The image measures $18\,\mathrm{kpc}$ on a side.

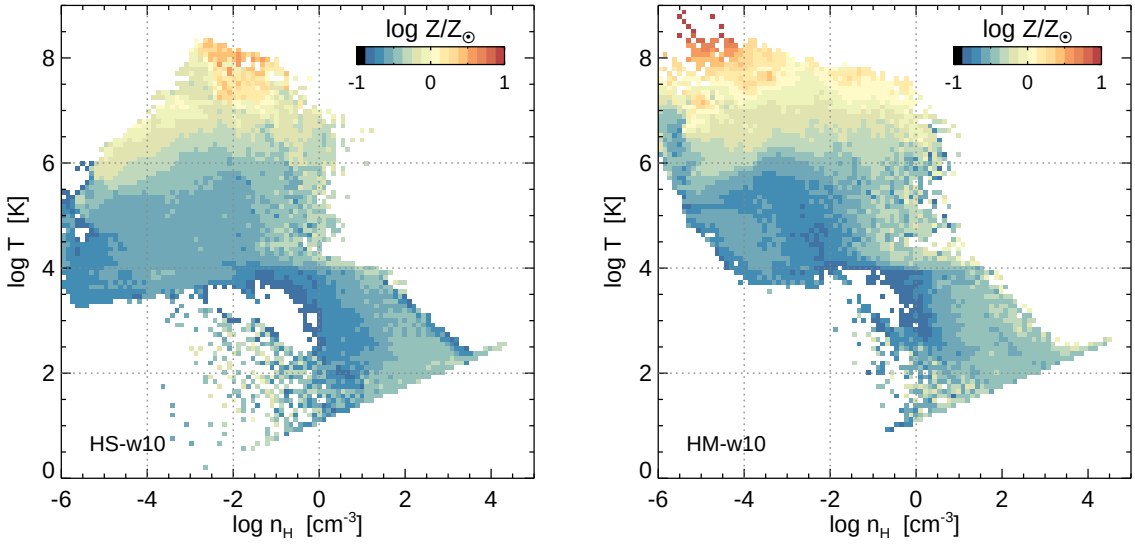


Figure 5.8: Phase diagram of the `HS-w10` (left) and `HM-w10` run (right) at $t = 200\,\mathrm{Myr}$. Colour-coding indicates the mass-averaged gas metallicity. It can be seen that hot diffuse gas is metal-rich, sometimes reaching more than twice the solar metallicity ($Z_\odot = 0.02$). The extremely metal-rich gas corresponds to the gas parcel into which the energy and mass loss from stars are directly injected.

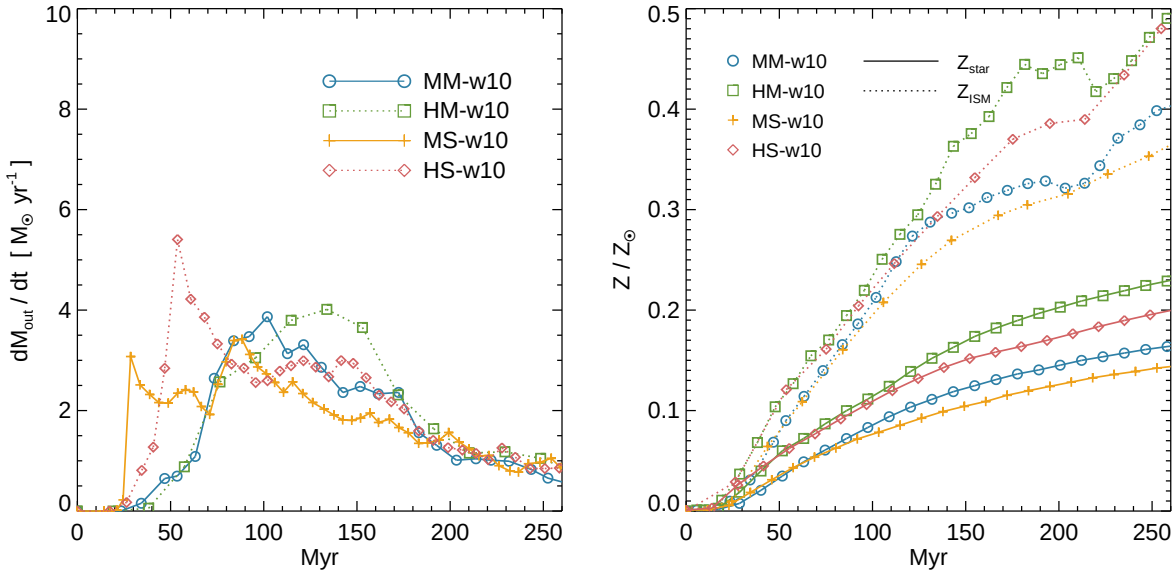


Figure 5.9: *Left:* Effect of different feedback models on the outflow rate measured through planes parallel to the disc of the galaxy and located $\pm 9$ kpc away from it. Models with a single burst per star particle (`MS-w10` and `HS-w10`) are denoted with orange crosses and red lines, while multiple explosion models (`MM-w10` and `HM-w10`) are shown with blue and green lines, respectively. Due to the short time delay in SN explosions ($t_{\mathrm{delay}} = 10\,\mathrm{Myr}$), the outflow emerges earlier in the single burst model than in the multiple explosion models. However, the total amount of outflow from the four different runs are found to be similar (see text). *Right:* The mass-averaged metallicity of stars (solid lines) and the star-forming gas (dotted lines). The runs with the multiple explosions per star particle show a higher metallicity than the runs adopting a single SN explosion owing to metal-rich stellar winds.

away from it. Fig. 5.9 (left panel) shows that the outflow in the single explosion models, i.e. `MS-w10` and `HS-w10`, emerges earlier than in the models with multiple explosions owing to its short time delay adopted ($\Delta t = 10\,\mathrm{Myr}$). A strong outburst ($\dot{m}_{\rm out} \sim 5\,M_\odot\,\mathrm{yr}^{-1}$) occurs first due to the high level of star formation activity in the early period, and a mild outflow of $\dot{m}_{\rm out} \sim 1\,M_\odot\,\mathrm{yr}^{-1}$ ensues. On the other hand, `MM-w10` and `HM-w10` reach their peak outflow $\simeq 70\,\mathrm{Myr}$ after the peak SFR. Note that the difference in the peak SFR and outflow between the two models can potentially result in different mass loading factors. Nevertheless, we find that the total outflow rates are in good agreement between the single burst and multiple burst models. The integrated amount of outflow during the first $250\,\mathrm{Myr}$ are $4.3 \times 10^8\,M_\odot$, $5.0 \times 10^8\,M_\odot$, $4.2 \times 10^8\,M_\odot$, and $3.9 \times 10^8\,M_\odot$ for `MS-w10`, `HS-w10`, `MM-w10`, and `HM-w10`, respectively.

We find that the runs with multiple explosions predict higher stellar and ISM metallicities than those adopting a single explosion (right panel in Fig. 5.9). Given that we used the metal yield, `y`=0.1, twice larger than the bulk yield suggested by Arnett (1996) to account for enrichment by stellar winds in `MS-w10` and `HS-w10`, the smaller metallicity in these runs thus indicates that the metals processed by stars directly escape from the galaxy without being mixed with the interstellar medium. This is different from the `MM-w10` and `HM-w10` run, in which roughly half of the metals are dispersed via the stellar wind channel first and SNe blow some metals out at a later stage.

#### 5.3.2.2 Effect of mass loading

The observational finding that at least half of the baryons of local spiral galaxies are missing from their host dark matter halo (McGaugh et al., 2010) suggests that a substantial fraction of gas is blown out by stellar feedback processes. Given that the ejecta from SN explosions and stellar winds can account for at most $\sim 20\%$ of the mass of newly formed stars, the baryon deficiency implies that the outbursts entrain a large amount of gas before they leave the dark matter halo. For 14 dwarf galaxies and a starburst galaxy, M82, Martin (1999) obtained a rough estimate of the mass of the hot wind in super shells based on H$\alpha$ fluxes, and found indeed that the amount is comparable to the star formation rate[4] (see also Strickland & Heckman, 2009). By performing two dimensional Eulerian hydrodynamical simulations with the ZEUS code (Stone & Norman, 1992), Fujita et al. (2009) argued that broad Na I D features often observed in starburst galaxies (e.g. Martin, 2005) arise from multiple shell fragments seen at sub-parsec scales, indicating the importance of resolving the shell fragments. However, simulating galaxies with sub-parsec

[4]Rupke et al. (2005) also studied the mass loading in 78 starburst galaxies (35 infrared galaxies, 30 low-z ULIRGs, and 13 high-z ULIRGs) by fitting Na I D features, but found a smaller median mass loading factor of $\dot{M}_{\rm out}/\dot{M}_* \simeq 0.1$, although it ranges from 0.01 to 10.

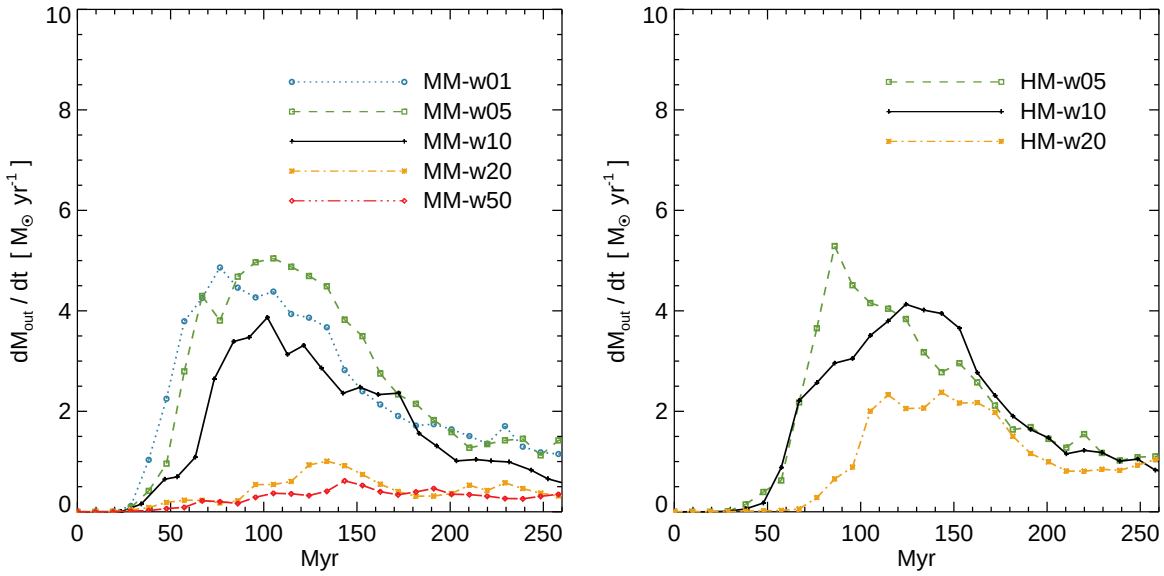


Figure 5.10: Dependence of the outflow rate measured through planes parallel to the disc of the galaxy and located $\pm 9$ kpc away from it on the mass loading factor. Different colour-codings denote different mass-loading factors, as indicated in the legend. Highly entrained ejecta ($\eta_w \geq 2$) hardly escape the galaxy, while the outflow is found to be relatively stronger in the runs with low mass loading.

scales at $z = 0$ is practically not tractable, and thus the mass loading is put in by hand, as described in Section 5.2.4, motivated by observational studies available in the literature.

However, given the lack of spatially resolved observations of the mass loading, it is important to test how the mass-loading factor adopted in the simulation impacts the properties of outflows during the evolution of the clumpy disc galaxies. Fig. 5.10 shows the resulting outflow rates from runs with different mass-loading factors spanning $1 \leq \eta_w \leq 50$. As in Fig. 5.9, the outflow rate is measured through two planes parallel to the disc of the galaxy and located $\pm 9$ kpc. Several trends can be identified in the left panel of the figure. First, the runs with a low mass-loading factor ($1 \leq \eta_w \leq 10$) show relatively strong outflows, whereas less significant outflow is observed in the models with a high mass-loading factor ($\eta_w \geq 20$). This trend is also found in high-resolution runs (see the right panel of the same plot). In both resolution runs, the maximum outflow is observed in the case with $\eta_w = 5$. Although it is difficult to single out the main cause of the trend because of the non-linear, clumpy structures of the simulated galaxy, this can be partially ascribed to the fact that the kinematical impact from the stellar ejecta is more mitigated when the limited energy is shared with a larger amount of entrained gas. Second, the three runs with low entrainment show a more or less similar outflow rate in spite of an order of magnitude difference in the loading factor (1–10). Interestingly, the mass loading during the burst phase ($50 \lesssim t \lesssim 100$ Myr) turns out to be larger than the input value $\dot{M}_{\rm out}/\dot{M}_* \simeq 0.1$. The ratio of the peak SFR ($\simeq 23\ M_\odot\,{\rm yr}^{-1}$

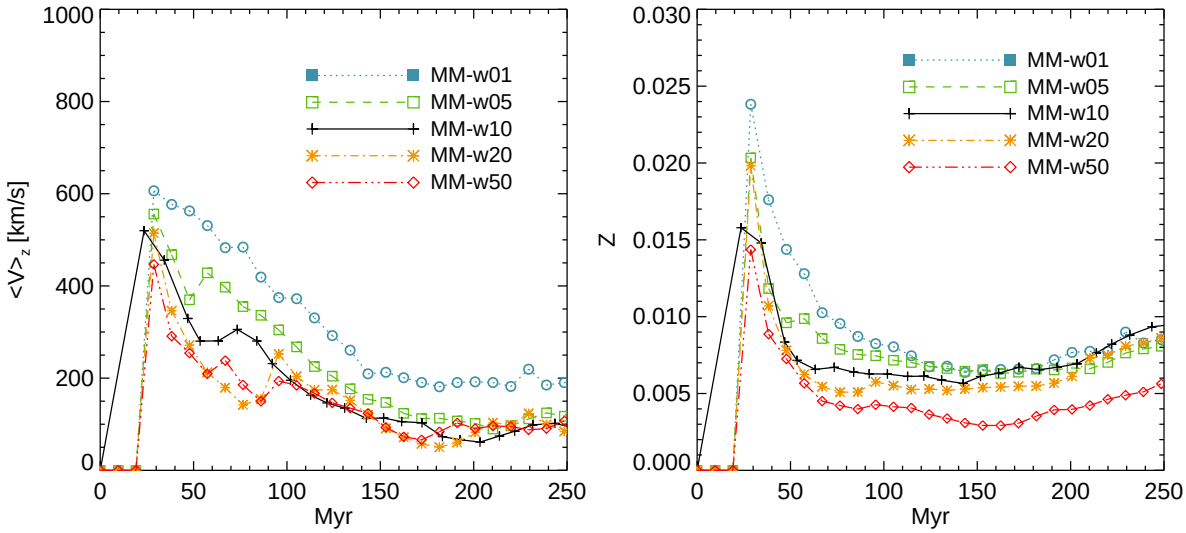


Figure 5.11: Properties of outflows in the models with different mass-loading factors. The left panel shows a mass-averaged $z$-axis outflow velocity measured at $z = \pm 9\,\mathrm{kpc}$. The mass-averaged metallicity is also shown in the right panel. It can be seen that outflows tend to be faster and more metal-rich in the run with lower $\eta_w$.

at $t = 30$ Myr) and the peak outflow rate ($\simeq 5\ M_\odot\,\mathrm{yr}^{-1}$ at 100 Myr) is found to be 0.2, indicating that the stellar ejecta indeed entrain some gas. Lastly, our experiments suggest that the loading factor is likely to vary over time, because there is a time delay between the peak SFR and the peak outflow. For example, in case of `MM-w10`, $\dot{M}_{\rm out}/\dot{M}_*$ at $t = 50$ Myr is $\simeq 0.1$, whereas the ratio increases to $\simeq 0.5$ at $t = 100$ Myr. However, we find that it never exceeds unity at any time. Although the mass loading can increase in principle when the outflow is measured at lower altitudes, e.g. $z = \pm 5$ kpc, it seems necessary for the stellar feedback to actually blow gas out of the host dark matter halo in order to stand a reasonable chance of matching the abundance of baryons measured in local spiral galaxies. Hence, the low mass loading at high altitudes is an issue which needs to be addressed in the future.

Inspection of the velocity and metallicity of the outflow gives further insight into how the mass-loading factor affects the gas dynamics in the galaxy. Ideally, it is best to track individual gas parcels into which the momentum is directly injected, but this is very difficult in Eulerian simulations. Instead, we present a mass-weighted average of velocity and metallicity of the outflow measured at $z = \pm 9$ kpc in Fig. 5.11, bearing in mind that the gas cells in which we measure the physical properties of the outflow may not represent the same dynamical component between two different runs. As can be inferred from Eq. 5.2, a higher mass loading generally leads to a lower outflow velocity (left panel). Although it appears no longer true at $t \gtrsim 150$ Myr for the runs with $\eta_w \geq 5$, it should be noted that the average density of the outflowing gas, $\langle\rho\rangle \propto \dot{M}_{\rm out}/\langle V_z\rangle$, in `MM-w50` is lower than that in the `MM-w10` run. This means

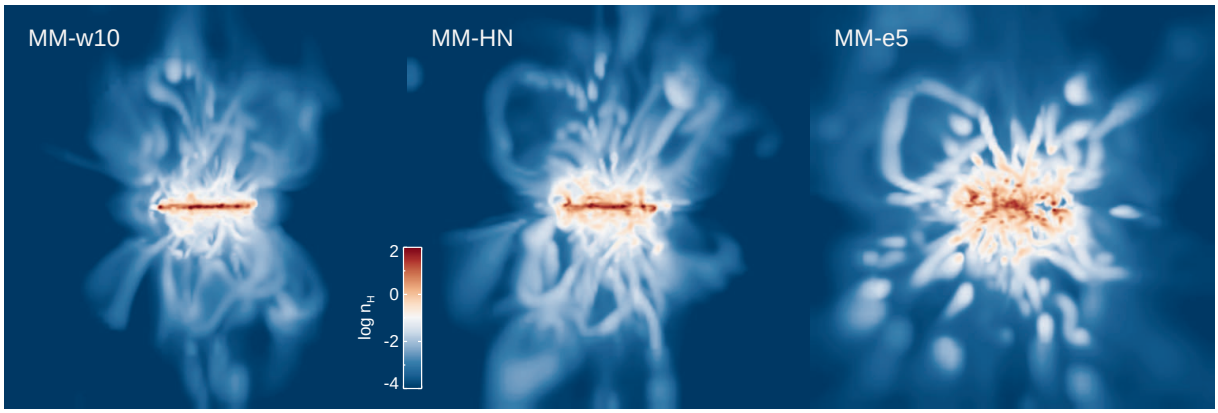


Figure 5.12: Projected gas density maps in the runs with different feedback strength at $t = 100$ Myr: from left to right, the normal feedback, the run with the HNe, and the run with a five times the energy from the normal feedback run. Giant gas loops are visible in all three cases, but their density tends to get higher with increasing energy input. Small density blobs of density $n_{\rm H} \gtrsim 10\,{\rm cm}^{-3}$, moving with $v \lesssim 100\,{\rm km\ s}^{-1}$, are only seen in the the extreme feedback run (`MM-e5`). The image measures 36 kpc on a side.

that the gas elements accelerated to high speeds are preferentially crossing the plane at $z = \pm 9$ kpc in the `MM-w50` case. Thus, it is sensible to argue that, for a given density, the outflow velocity is larger in the run with a lower $\eta_w$ .

Fig. 5.11 also shows that the metallicity of outflow peaks around $t \sim 30$ Myr, which precedes the peak outflow rate. This can be attributed to the fact that low-density gas, which is highly enriched and accelerated by stellar winds, first crosses the planes located $\pm 9$ kpc from the disc of the galaxy. More importantly, we find that the mean metallicity of the outflow is generally higher in the low mass-loading runs at $t \lesssim 150$ Myr, mainly because the stellar ejecta is less diluted than the high mass-loading runs by construction. The clear trend at $t \lesssim 150$ Myr also suggests that the mixing of the outflowing gas with the ambient gas is not substantial in the early phase of the outflow. As metals from stellar ejecta are recycled, the metallicity of star-forming gas and stars rises (i.e. $Z_{\rm ISM} \geq 0.006$, see the right panel in Fig. 5.9), and as a consequence, the net metallicity of the outflow increases.

#### 5.3.2.3 Effect of extreme feedback sources

As we discussed in Section 5.2.3, hypernovae can provide approximately two times more energy than normal supernovae if all the massive stars in the range $20 \leq M_{\rm star} \leq 50$ undergo HNe explosions. An interesting question to answer is then whether the feedback from hypernovae can increase the mass loading. In Fig. 5.12, we present the projected gas densities when the outflow is the most significant (at $t = 100$ Myr). The run with the hypernova clearly exhibits more pronounced outflows than `MM-w10`,

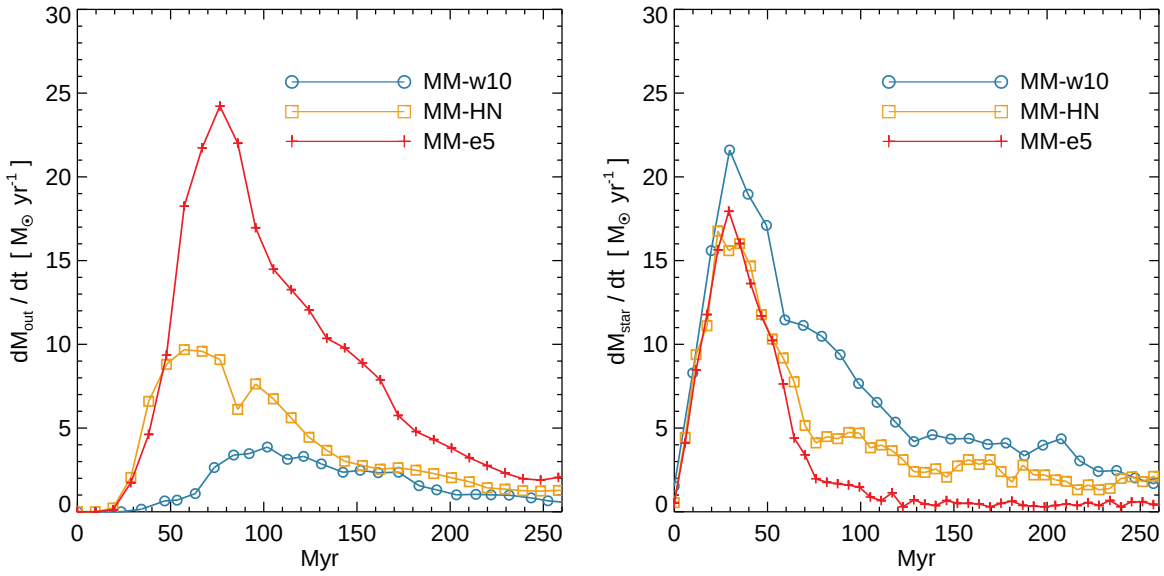


Figure 5.13: Properties of outflows in the models with strong stellar feedback. The left panel shows the outflow rate measured for the normal feedback run (blue circles), HNe run (orange squares), and extreme feedback model (red crosses). Corresponding star formation histories are presented in the right panel. Although the HNe run reveals a higher mass loading than the normal feedback run, it is still smaller than what several observational studies suggest. We find that such a high level of mass loading is attainable only when we adopt extremely strong feedback (`MM-e5`).

creating several loops of gas with a number density of $\sim 0.1\ \mathrm{cm}^{-3}$. When we calculate all the energy available from stars, i.e. stellar winds+SN II+Ia+HNe, by taking into account the metallicity-dependent HN fraction for `MM-HN`, we find that it releases 2.2 times larger energy than that from the `MM-w10` run.

As an extreme model, we have also investigated a case in which the energy from stars (without HN) is artificially increased by a factor of five. Visual inspection of Fig. 5.12 suggests that the disc structure is considerably disrupted by the strong feedback. Some dense blobs of gas with $n_{\mathrm{H}} \geq 10\ \mathrm{cm}^{-3}$ are now pushed out of the galactic disc and visible in the density map.

In order to quantify the impact of the feedback, we measure the outflow rate in Fig. 5.13. Although the outflow rate in `MM-HN` is augmented by a factor of two, it turns out to be still insufficient to account for a large mass-loading factor, as suggested by several observations (e.g. Martin, 1999). We find that mass loading factor values comparable to these observations can only be achieved when an artificially large amount of energy is fed to the ISM, as in the `MM-HN` run. As a result of the strong feedback, the star formation is notably suppressed as well.

It is interesting to note that the dense blobs seen in the `MM-e5` run, which are plausible candidates for molecular clouds, are leaving the galaxy at $\sim 100\ \mathrm{km\,s}^{-1}$. This is much slower than the fast molecular winds moving at speeds of order $1000$ km s$^{-1}$, observed through CO emission lines in the local ULIRG

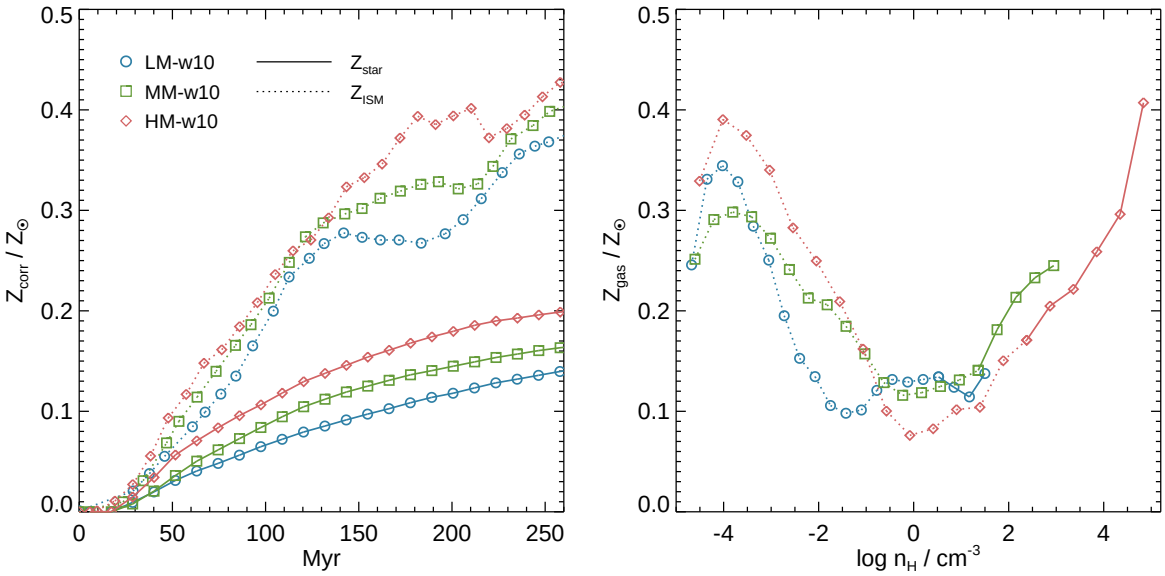


Figure 5.14: Effect of resolution on metal enrichment. Mean metallicities of the star (solid lines) and star-forming gas (dotted lines) are shown in the left panel after applying a correction factor to offset small differences in SFHs between the various runs. Different runs are denoted with different colour-codings and symbols. In the right panel, we plot gas metallicity as a function of gas density at $t = 100$ Myr. The higher resolution run is slightly more efficient at recycling the metals synthesised from stars.

population (Chung et al., 2011). Although the star formation rate in our simulated galaxy is much smaller than that of ULIRGs, which form stars at rates $\sim 100\,M_{\odot}\,\mathrm{yr}^{-1}$, the high-velocity molecular winds appear to be difficult to reconcile with starburst-powered winds, considering that even the extreme model fails to generate fast and dense winds. An AGN-powered wind may be able to explain this, given that for such winds, even a larger amount of energy can be liberated in a very short period of time (e.g. Choi et al., 2012).

#### 5.3.2.4 Effect of numerical resolution

Finally, it is important to assess the effect of numerical resolution on our results. It is worth remembering that although the lower resolution run has a factor of four smaller grid size, we choose a larger initial radius for the expanding bubble to compensate for the difference in resolution. Fig. 5.9 indeed argues that the prediction for the outflow rate is not significantly affected by the different resolution. The runs with 17.5 pc or 70 pc resolution result in a more or less similar outflow rate.

Yet we find that higher resolution runs yield slighltly higher mean metallicities for stars and star-forming gas (Fig. 5.14, left panel). Since the number of stars producing metals is slightly different in the three runs, we apply a simple correction to the metallicities for a fair comparison in the left panel, such

that

$$Z_{\rm corr}(t) = Z(t)\frac{M_*(t)}{M_*^{\texttt{MM}}(t)}$$

where $M_*^{\texttt{MM}}(t)$ is the integrated stellar mass of the `MM-w10` run at time $t$. The systematic trend shown in Fig. 5.14 originates from the fact that the metal-rich stellar ejecta is more diluted than it should be in the low-resolution run. If an AMR cell were infinitesimally small, then the metallicity of the dense regions surrounding a star would be highly enriched first, and part of the metals would be subsequently dispersed as the supernova remnants carry them further away in the ISM. A prediction from this thought experiment is that dense gas will be preferentially enriched at higher resolution. This is substantiated by Fig. 5.14 (right panel), which presents the mass-weighted average of gas metallicity as a function of density at $t = 100$ Myr. The metallicity of the dense cells in the `HM-w10` run is indeed found to be at least twice as large as that of `LM-w10`, supporting the idea that higher resolution causes the stellar ejecta to be recycled more efficiently.

Nevertheless, the resulting mean stellar metallicity differs by a small amount ($Z \sim 0.05 Z_\odot$ or $Z = 10^{-3}$). Such a minute difference may easily be washed out by mixing processes, such as a galaxy merger or turbulence.

## 5.4 Forming a disc galaxy in a ΛCDM universe

Observational studies suggest that a significant amount of baryons is missing in the local Universe (Persic & Salucci, 1992; McGaugh et al., 2010). Several authors assert that heating by gravitational collapse and galactic superwinds are responsible for hiding a sizeable fraction ($f_{\rm bar}$ =50–60%) in the warm-hot intergalactic phase characterised by $10^5 < T < 10^7\,K$ (Cen & Ostriker, 1999; Davé et al., 2001; Cen & Ostriker, 2006) which is very difficult to detect. An important prediction from these simulations is that the warm-hot intergalactic medium (WHIM) is a diffuse phase, which extends far from galaxies. Anderson & Bregman (2010) tried to pin down the amount of gas in the WHIM or an even hotter phase using the dispersion measure of pulsars in the Large Magellanic Cloud, X-ray detections, and non-detections of O VIII absorption, and came to the conclusion that hot gas inside the dark matter halo hosting the Milk Way can only account for a small amount, 0.02–0.13 $f_{\rm uni}$, requiring the existence of outflows which expel baryons way beyond its virial radius.

Indeed, such far-reaching outflows are often detected in actively star-forming galaxies, such as Lyman break galaxies (LBGs) at high redshift (Steidel et al., 1996; Adelberger et al., 2003; Shapley et al., 2003; Steidel et al., 2010). Steidel et al. (2010) reported that the interstellar absorption lines (e.g. C IV or Si II) in 87 LBGs are generally blueshifted with respect to the system redshift, which is a signature of metal-rich outflows. Ultra luminous infrared galaxies, which are known to show a high level of star formation activity ( $\gtrsim$ 100 $M_\odot\,{\rm yr}^{-1}$), also often reveal outflows of $\sim$ 1000 km s$^{-1}$ (e.g. Sanders & Mirabel, 1996; Martin, 2005; Chung et al., 2011). These observations provide tantalising evidence for a close link between star formation and outflow, supporting the claim that small to intermediate halos suffer from a shortfall in baryons.

Outflows are thought to play a pivotal role in the formation of disc galaxies. Ever since Navarro & Benz (1991) raised the concern that simulated gas discs are too compact, many attempts have been made to understand how spiral galaxies with extended disc form in an explicit cosmological context (Abadi et al., 2003; Sommer-Larsen et al., 2003; Governato et al., 2004; Robertson et al., 2004; Okamoto et al., 2005; Governato et al., 2007; Croft et al., 2009; Scannapieco et al., 2009; Joung et al., 2009; Piontek & Steinmetz, 2011; Agertz et al., 2011; Guedes et al., 2011). The consensus of these works is that when feedback is neglected, gas cooling and star formation become too efficient and the simulated galaxy ends up being bulge-dominated. The most appealing remedy is to blow low angular momentum gas out of the dark matter potential well through stellar feedback processes at high redshift, but the conclusion on how this should happen depends on the details of the simulation. Using unprecedented high resolution

simulations and the more realistic feedback processes laid out in Section 5.1, we investigate the impact of feedback and resolution in forming a realistic disc galaxy in this section.

### 5.4.1 NUT simulations

As we briefly described in Chapter 4, the NUT simulations are a series of hydrodynamical, cosmological zoom simulations of a volume of side length $9\,h^{-1}$ Mpc, which is run with RAMSES (Teyssier, 2002). It is designated to study the formation and evolution of a Milky Way-like galaxy with very high resolution. The initial conditions are generated using `MPgrafic` (Prunet et al., 2008), a parallel version of the `grafic` code (Bertschinger, 2001), with the WMAP5 cosmological parameters ($\sigma_8 = 0.8$, $\Omega_m = 0.258$, $\Omega_\Lambda = 0.742$, $h \equiv H_0/100\,\mathrm{km\ s^{-1}} = 0.72$) (Dunkley et al., 2009). A sphere of diameter $2.88\,h^{-1}$ Mpc encompassing the galaxy is refined to achieve higher resolution when the mass of each cell (gas+star+dark matter) exceeds the eight times the mass of a dark matter particle. A root grid of $128^3$ elements is used to cover the entire simulation volume, with 3 extra nested levels present in the high resolution sphere from the start. Further refinement levels are added during run time to keep the minimum cell size fixed to 12 or 48 pc. In order to resolve small-mass halos of $\sim 10^8 M_\odot$, dark matter particles of $5.5 \times 10^4 M_\odot$ are employed in the refined region, equivalent to $N_{\rm dm} = 1024^3$. The Euler equations are solved using the HLLC scheme (Toro et al., 1994) with a typical Courant number of 0.8, and the conjugate gradient solver (see Sec. 2.1, Hockney & Eastwood 1988) is adopted to solve the Poisson equation.

The NUT simulations also include many other important physical ingredients. Gas can radiatively cool down to $\sim 10^4$ K due to the atomic transitions and thermal Bremsstrahlung, and the temperature can decrease further down to 1 K when metals are present (Sutherland & Dopita, 1993). Note that the expansion of the universe can also lower the temperature of low-density gas by adiabatic expansion. The initial gas metallicity is set to $10^{-3}\,Z_\odot$. If the cooled gas collapses into a small region exceeding a certain threshold density ($n_{\rm H,thres}$), a star particle is created based on the Schmidt law (Schmidt, 1959) with 1% efficiency per local free-fall time, as suggested by Krumholz & Tan (2007). Each star particle represents a simple stellar population and is assumed to release $10^{51}$ erg per supernova explosion or $\simeq 10^{49}$ erg per unit solar mass after several tens of Myrs from the birth of the star particle. We use one third of the energy to increase the internal energy of the gas cell where the star particle sits in, and the other two thirds to increase the momentum inside a bubble of radius 32 pc, as described in Section 5.2.4. It is assumed that each explosion entrains 10 times as much mass as the stellar ejecta ($\eta_w = 10$). A uniform

Table 5.2: Summary of simulation parameters and physical ingredients. From left to right, columns are as follows: simulation name, minimum grid size, mass of a dark matter particle, mass of a star particle, threshold density for star formation, redshift at which UV background heating is turned on, redshift of the last snapshot, and feedback processes included.

| Simulation | $\Delta x_{\rm min}$ [pc] | $m_{\rm dm}$ [$10^4\,M_\odot$] | $m_*$ [$10^4\,M_\odot$] | $n_{*,\rm thres}$ [cm$^{-3}$] | $z_{\rm reion}$ | $z_{\rm end}$ | Feedback |
|---|---|---|---|---|---|---|---|
| NutAD | 48 | 5.5 | – | – | 8.5 | 0 | – |
| NutCOLR | 48 | 5.5 | 3.5 | 10 | 8.5 | 0 | – |
| NutCO | 12 | 5.5 | 2.3 | 400 | 8.5 | 3 | – |
| NutSFB | 12 | 5.5 | 2.3 | 400 | 8.5 | 3 | SNII + Ia +SW |
| NutHFB | 12 | 5.5 | 2.3 | 400 | 8.5 | 1.5 | SNII + Ia +SW + HNe |

UV background is instantaneously turned on at $z = 8.5$ following Haardt & Madau (1996). Feedback from an active galactic nuclei is not yet included in the NUT simulations.

In order to assess the impact of various feedback processes, we use three existing simulations from the NUT suite. The NutAD run is the most basic model in which star formation and feedback processes are inhibited. As gas cannot cool, its collapse does not occur. Accordingly, no refinement is triggered above `level=18` ($\Delta x = 48$ pc), even though the refinement is permitted up to `level=20`. The NutCO run includes cooling and star formation, but feedback is not taken into consideration. NutCOLR is identical to NutCO, but we limit the refinement to 48 pc to run the simulation to $z = 0$.

We carry out two extra NUT simulations in which the new implementation of the multiple explosion of stellar feedback is used, NutSFB and NutHFB. These now include stellar winds and SN Ia as well as SN II. In particular, the energy from hypernovae is also considered in the NutHFB run, and as such it can be regarded as an extreme feedback model. As the feedback energy increases the temperature of the interstellar medium, the courant time step becomes very small, and the simulations take much longer than the cooling run. Thus, we run these two simulations to $z = 3$ for NutSFB and $z = 1.5$ for NutHFB. In order to assess how serious the missing baryon problem is (McGaugh et al., 2010), we use approximately 1.5 times the energy available from STARBURST99 (Leitherer et al., 1999, 2010) per stellar mass unit, which is $1.3 \sim 10^{49}\,{\rm erg}\,{M_\odot}^{-1}$. The binary fraction for SN Ia is chosen to be $A_{\rm SNIa} = 0.07$. Dark matter halos are identified using HaloMaker (Tweed et al., 2009), which is based on the AdaptaHOP algorithm by Aubert et al. (2004). We summarise the parameters adopted in the simulations in Table 5.2.

### 5.4.2 Results

#### 5.4.2.1 General features of the Nut halo in the absence of feedback

We begin our investigation by describing the general properties of the Milky Way-like galaxy we simulate with the zoom-in technique, which we call the Nut galaxy. In Fig. 5.15 we show the growth of the host dark matter halo and stars in the Nut galaxy from the simulations without feedback processes (i.e. NutAD, NutCOLR, and NutCO). Since the dark matter drives the gravitational collapse on large scales, the mass of the dark matter halo shows an excellent agreement in the three runs. Note that the final mass of the Nut halo is $\simeq 4 \times 10^{11}\,M_{\odot}$, which roughly corresponds to the transition mass that demarcates the halos fed by cold streams from the halos filled with gravitationally shock-heated gas (Birnboim & Dekel, 2003; Kereš et al., 2005; Ocvirk et al., 2008; Brooks et al., 2009). As we have shown in Chapter 4, the virial shock develops at $z \lesssim 2$, when the virial mass of the halo becomes larger than $\simeq 2 \times 10^{11}\,M_{\odot}$. The stellar mass of the NutCO galaxy is $6.5 \times 10^{10}\,M_{\odot}$ at $z = 0$, which is comparable to the stellar mass of the Milky Way ($6.61 \times 10^{10}\,M_{\odot}$) obtained from a Bayesian fitting method to photometrically and kinematically derived constraints, such as disc scale-length or terminal velocities (McMillan, 2011). Yet McMillan argues that the best estimate of the dark matter halo hosting the Milky Way is $1.4 \times 10^{12}\,M_{\odot}$, which is about 3 times more massive than the Nut halo. Given that the NutCO and NutCOLR runs do not take feedback processes into account, it is highly likely that the cooling runs over-predict the amount of stars, and therefore the Nut halo probably represents a smaller halo than the dark matter halo hosting the Milky Way.

The star formation rate of the most massive progenitor in the cooling runs ranges from a few $M_{\odot}\,\mathrm{yr}^{-1}$ to several tens of $M_{\odot}\,\mathrm{yr}^{-1}$ (Fig. 5.15, right panel). In particular, we find that the specific SFR measured at $z = 6$ is $\simeq 2\ \mathrm{Gyr}^{-1}$ for both runs, which appears to be in excellent agreement with the empirical estimate of the star formation rate ($\simeq 1.8\ \mathrm{Gyr}^{-1}$) of the Lyman Break galaxies with $\simeq 2 \times 10^{9}\,M_{\odot}$ at similar redshifts (McLure et al., 2011). Even though it is possible that the agreement is obtained because of the large stellar mass of the NutCO galaxy, we expect that both the SFR and stellar mass will decrease when feedback processes are included, and thus that the predicted *specific* SFR would not change dramatically, as we show in the next section. Fig. 5.15 also shows that the halo has a relatively rich merging history, as marked with filled squares. In order to identify a halo merger, we compare the members of each dark matter halo in two subsequent snapshots, and find a halo which has lost more than 50% of its member DM particles. Of 22 relatively significant mergers ($M_{\mathrm{cen}}/M_{\mathrm{sat}} \leq 100$) identified in the NutCOLR run, we find that a $\simeq$1:8 merger occurs at $z \simeq 3.5$, and that a 1:4 major merger follows at

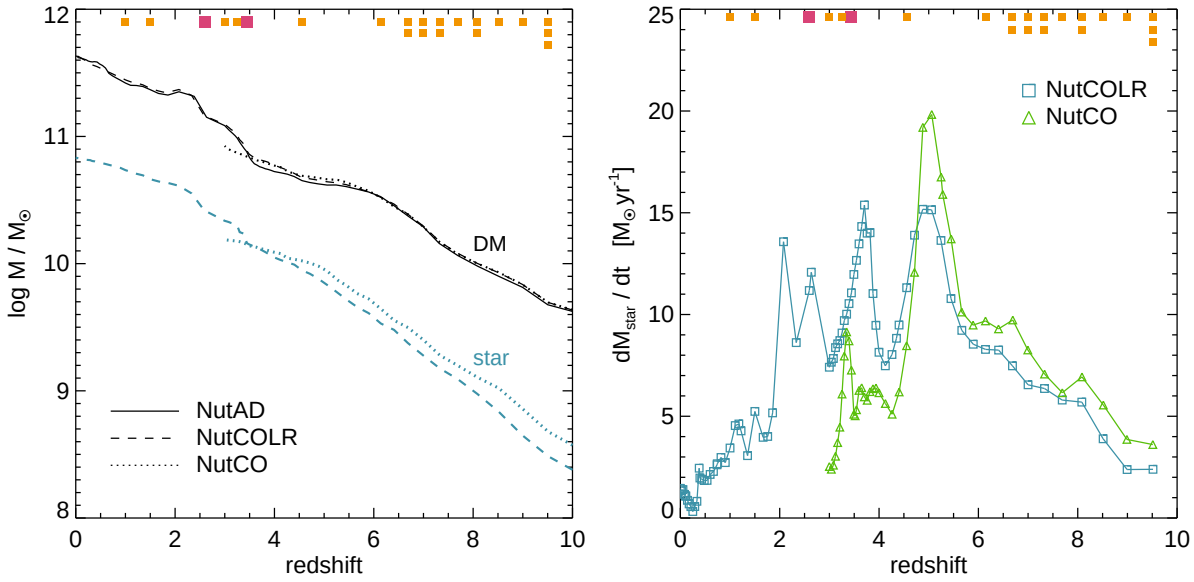


Figure 5.15: *Left:* Evolution of dark matter halo (black lines) and stellar component (blue lines) in the adiabatic (NutAD), high resolution cooling (NutCO) and lower resolution cooling runs (NutCOLR). Different line styles correspond to different runs, as indicated in the legend. Since the gas cannot cool and collapse to form stars in the adiabatic simulation, stellar growth is omitted for NutAD. The mass of the dark matter halo hosting the Nut galaxy agree well in the three runs. The orange (red) squares shown in the upper region of the panel indicate halo mergers with $10 < M_{\rm cen}/M_{\rm sat} \leq 100$ ($M_{\rm cen}/M_{\rm sat} \leq 10$). *Right:* Star formation rates of the most massive progenitor galaxies in the cooling runs. Blue squares (green triangles) represent the SFH of the Nut galaxy in the NutCOLR (NutCO) run. The Nut galaxy grows slightly faster in the NutCO than the NutCOLR, but the difference in total stellar mass becomes smaller with decreasing redshift.

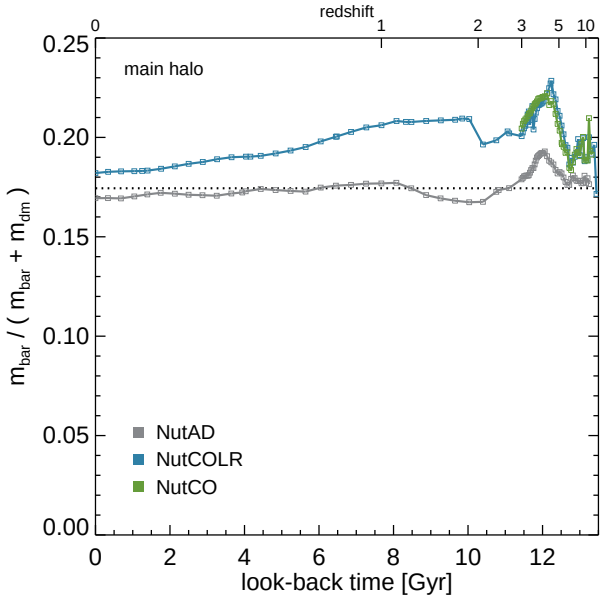


Figure 5.16: Evolution of the fraction of baryons within the Nut halo in the adiabatic and cooling runs. The fraction of baryons in the NutAD run (grey lines) remains more or less equal to the universal baryon fraction ($f_{\rm uni}$, dotted line), whereas the NutCOLR (blue) and NutCO (green) runs predict higher values than $f_{\rm uni}$.

$z \simeq 2.6$. In general, the peaks in the SFR can be associated with merging events. For example, satellite galaxies accreted at $6 \lesssim z \lesssim 7$ merge with the central galaxy at $z \simeq 5$, enhancing its star formation.

It is also interesting to note that the NutCO run predicts more enhanced star formation at high redshift ($z \gtrsim 5$) than its lower resolution counterpart (NutCOLR), indicating that star formation may be resolution-dependent. Indeed, when the force resolution is not good enough, dark matter particles constituting small haloes become loosely bound to the halo and cannot provide a gravitational well deep enough for gas to condense and form stars. The outcome of the poor force resolution is a delay in star formation in small halos (Rasera & Teyssier, 2006), and the gas which could not form stars will eventually collapse when the mass of the host dark matter halo becomes large enough to compensate the resolution effect. Nevertheless, the difference in stellar mass between the two cooling runs does not appear to be substantial (Fig. 5.15, left panel), and equality in stellar mass between NutCOLR and NutCO is established at $z \simeq 3.5$. Note, however, that this equality does not imply that the simulated galaxies share the same kinematic properties. We will discuss this issue later in this section.

Recently, McGaugh et al. (2010, see also Persic & Salucci 1992) argue that intermediate mass halos fall short of the universal amount of baryons predicted by the standard ΛCDM cosmological models (e.g. Dunkley et al., 2009). Based on flat rotation velocities and stellar masses measured from extended 21 cm emission and $B$-band or $K'$-band photometry (McGaugh, 2005), these authors showed

that galaxies with $V_c \simeq 100 - 200\,\mathrm{km\ s^{-1}}$ have $f_d \equiv \Omega_m M_{\rm bar}/\Omega_b M_{500} \sim 0.15 - 0.3$, where $M_{500} = 250^{-1/2}\,(GH_0)^{-1}\,V_{500}^3$ and $M_{\rm bar} = M_{\rm star} + M_{\rm gas}$. In order to understand how the observed value compares with the prediction from the basic models without feedback, we measure the fraction of baryons, $f_{\rm bar}$ ($\equiv M_{\rm bar}/[M_{\rm bar} + M_{\rm dm}]$), for the adiabatic and cooling runs in Fig. 5.16. It is apparent from the figure that if gas gets shock-heated as it crosses the virial radius (NutAD), the fraction of baryons is kept more or less equal to the universal baryon fraction ($f_{\rm uni} = \Omega_b/\Omega_m = 0.174$, dotted line), consistent with an independent study by Crain et al. (2007). On the other hand, the cooling runs reveal an even higher fraction of baryons than the adiabatic case. The result that the fraction tends to be larger at higher redshift ($z > 2$) can be interpreted as follows. At high redshift, cold filaments form in the region where radiative cooling is significant, and carry a large amount of baryons. Since halos are primarily fed by a set of cold filaments at high redshift, the fraction of baryons in the halos becomes higher than the universal baryon fraction. On the other hand, the dark matter does not lose energy via radiative cooling and therefore gets redistributed over a large region by the virialisation process. As the halo grows, the virial shock finally develops and then the baryons cannot penetrate deep in the halo anymore: a significant amount stays between $R_{\rm vir}$ and $2\,R_{\rm vir}$ due to the virial shock, so the fraction of baryons $f_{\rm bar}$ drops at low redshift. The final baryon fraction in the halo from the NutCOLR run is $f_{\rm bar} \simeq 0.18$, which is at least three times larger than observational estimates (e.g. McGaugh et al., 2010). This suggests that, in the LCDM universe, roughly three fourths of the baryons should be ejected from Milky Way-like galaxies.

#### 5.4.2.2 Feedback-regulated star formation and baryon fraction

Now that we know feedback is essential to match the observed baryon fraction, we evaluate the effect of different feedback processes by carrying out two zoom-in simulations. The NutSFB run includes feedback from SN II, Ia, and stellar winds, while the energy from hypernovae is considered in addition to the standard feedback processes in the NutHFB run. Note that our feedback scheme does not include any artificial treatment that disables the radiative cooling (e.g. Stinson et al., 2006; Guedes et al., 2011). In an attempt to resolve the early evolution of supernova bubbles, both simulations are run at high resolution (12 pc), but they are run only to $z = 3$ (NutSFB) or $z = 1.5$ (NutHFB) because of the trade-off between resolution and computational costs. We emphasise that the Nut galaxies in the cooling runs are already almost too massive for their host haloes at $z = 3$ ($M_{\rm star}[z = 3]/M_{\rm dm}[z = 0] \simeq 2 \times 10^{10}\,M_\odot/4 \times 10^{11} M_\odot = 0.05$), and thus it is sensible to focus on the influence of feedback processes at $z \geq 3$. Given the fact that the star formation activity is more vigorous and the dark matter halo is less massive

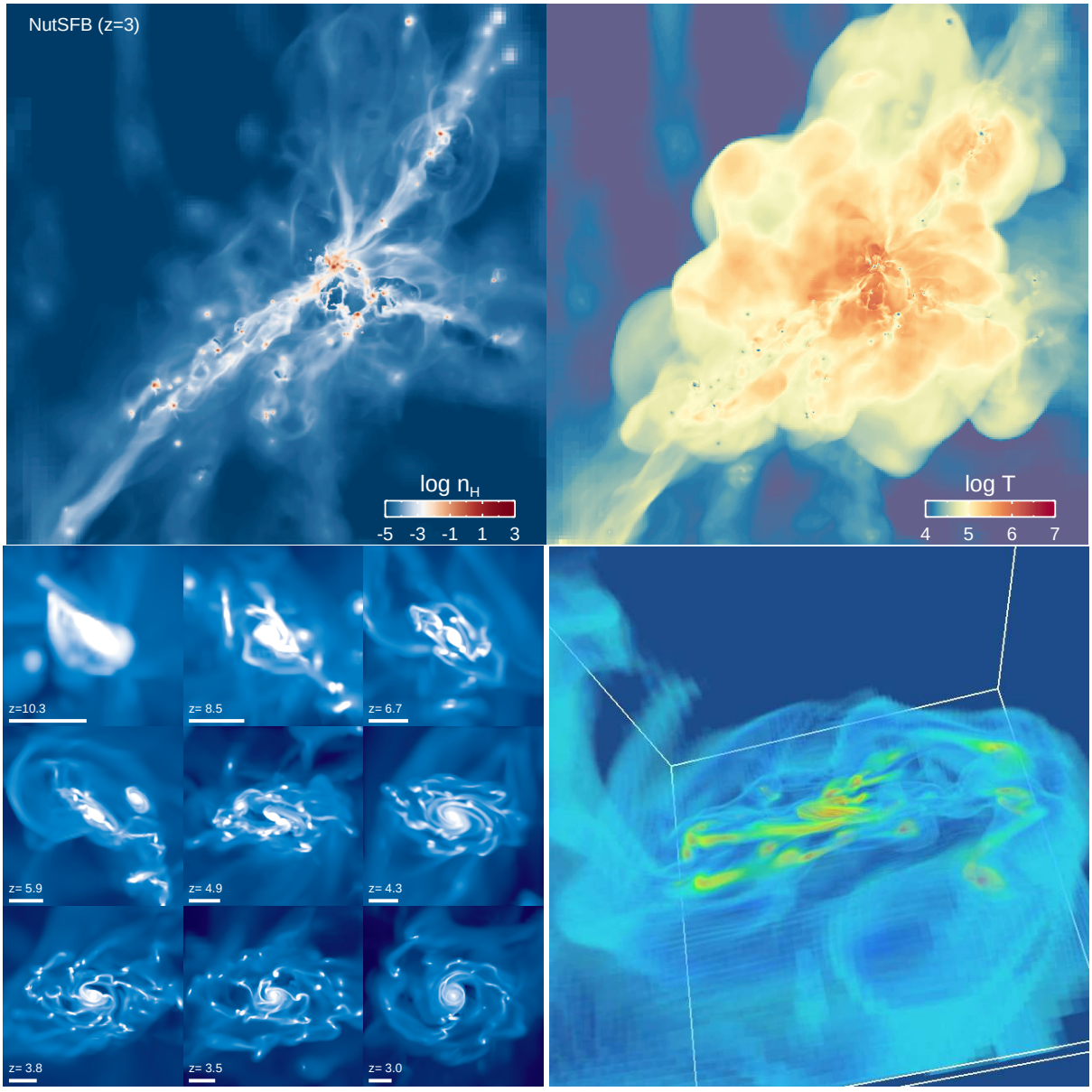


Figure 5.17: Projected densities and temperatures of the gas from NutSFB. Top panels show a snapshot of the gas density and temperature of the zoomed-in region ($\simeq$ 800 kpc on a side) at $z = 3$. Far-reaching, hot bubbles are clearly visible. The left bottom panels display projected densities of regions centred on the Nut halo at different redshifts. A $0.1\,R_{\rm vir}$ region is projected with a scale bar corresponding to 300 pc. The right bottom panel shows a three-dimensional view of the projected gas density of the Nut galaxy at $z = 3$. Redder colours indicate denser gas.

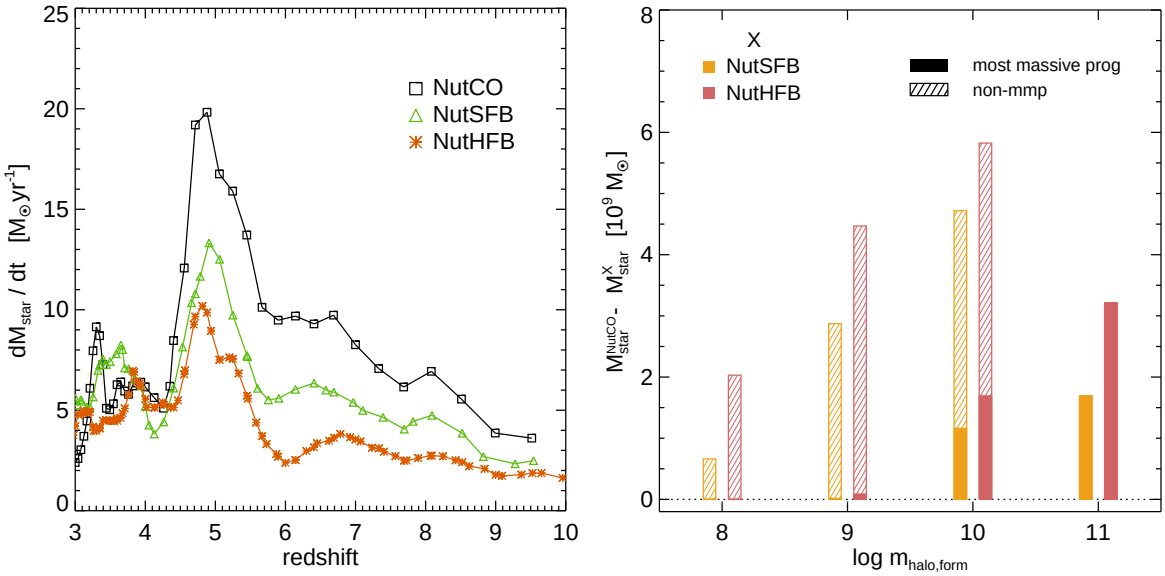


Figure 5.18: Impact of feedback processes on star formation history. *Left:* Star formation histories from the simulations with different feedback processes, as indicated in the legend. *Right:* The amount of quenched star formation in dark matter halos of different mass until $z = 3$, compared to the star formation measured in the NutCO run, i.e. $M_{\rm star}^{\rm NutCO} - M_{\rm star}^{X}$. Here, $M_{\rm star}^{X}\,(m_{\rm halo,form})$ indicates the total amount of stars formed in halos with $m_{\rm halo,form}$ over the redshift range $3 \leq z \leq 500$. Note that we only count stars belonging to halos that constitute the Nut halo at $z = 0$. The contribution from the most massive progenitor (mmp) to the quenched star formation is displayed as filled bars, while the contribution from non-most massive progenitor galaxies is shown as dashed bars. We find that the stellar mass of the Nut galaxy is reduced by $\simeq 30\%$ in NutSFB and 50% in NutHFB at $z = 3$.

at these epochs (Fig. 5.15), we expect that any impact of stellar feedback on the Nut galaxy should be noticeable in the high redshift universe. Fig. 5.17 shows a snapshot of the gas density and temperature of the zoomed-in region and complex clumpy discs at different redshifts. It can be seen that hot outflows are far-reaching, sometimes propagating out to $\sim 10\ R_{\rm vir}$ ($\sim 400$ kpc).

Fig. 5.18 (left panel) examines the suppression of star formation by stellar feedback processes. The SFRs are measured in the most massive progenitor of the Nut galaxy by averaging over 100 Myr. We find that inclusion of the stellar feedback is able to suppress the SFR by $\sim 30\%$ compared to the NutCO run. The level of star formation activity is further modulated by HNe, which provides $\simeq 66\%$ more energy per solar mass than the NutSFB at $z = 3$.[5] The resulting galaxy stellar masses at $z = 3$ are $\simeq 1.5 \times 10^{10}\,M_\odot$, $1.0 \times 10^{10}\,M_\odot$, and $0.76 \times 10^{10}\,M_\odot$ for the NutCO, NutSFB, and NutHFB runs, respectively. In other words, approximately $2.1 \times 10^{49}$ erg $\ {M_\odot}^{-1}$ is required to reduce the stellar mass by a factor of 2 at $z = 3$.

In the ΛCDM cosmology, the accretion history of a galaxy is dictated not only by smooth accretion,

[5]The maximum integrated energy from a simple stellar population is $3.2 \times 10^{49}$ erg ${M_\odot}^{-1}$ when HNe are included, but the contribution from HNe becomes negligible as star particles become metal-rich.

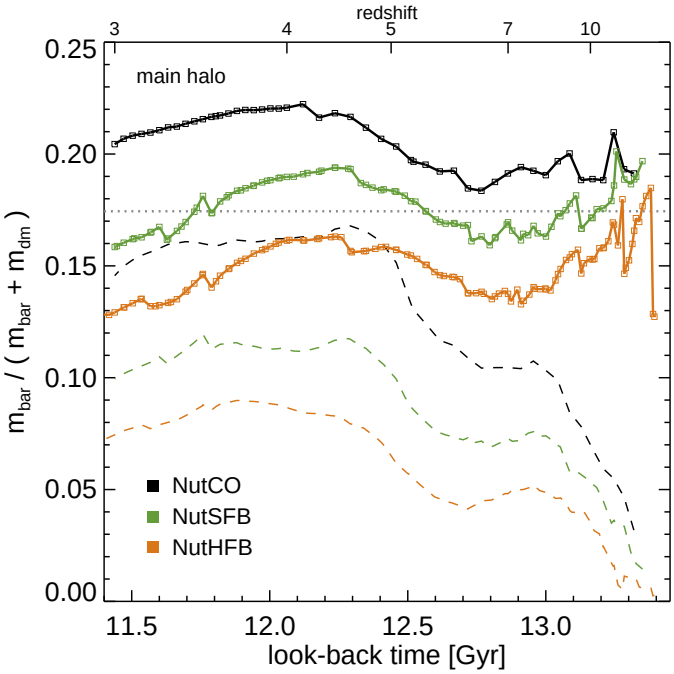


Figure 5.19: Baryon fractions in the Nut dark matter halo in feedback runs. Different colour-codings indicate different models, as indicated in the legend. The dotted line denotes the universal baryon fraction ($\Omega_b/\Omega_m$, dotted line). The dashed lines represent the contribution from stars ($m_{\rm star}/[m_{\rm bar}+m_{\rm dm}]$). The feedback from stars does not seem to reduce the baryon fraction sufficiently enough to accommodate the empirical estimate at $z = 0$ ($f_{\rm bar} \sim 0.04$), even accounting for a decline of 0.03 in the baryon fraction between $z = 3$ and $z = 0$ (see Figure 5.16)

but also by satellite infall. Thus, it is of interest to quantify where star formation quenching primarily occurs. To do so, we make use of the dark matter particles that constitute the Nut halo at $z = 0$ in the NutCOLR run, and identify halos at $z = 3$ that will later be merged to the central halo by matching particle identifications. Star particles in these halos are then traced back to find the mass of the dark matter halo where each star formed ($m_{\rm halo,form}$). In this way, we compute the amount of stars formed in halos of different masses for NutCO, NutSFB, and NutHFB. As an example, we find that the total amount of stars formed in the Nut galaxy or other merging candidates outside the Nut halo is $2.9 \times 10^{10}\,M_\odot$ at $z = 3$ in case of NutCOLR, which is half the stellar mass predicted at $z = 0$. The right panel of Fig. 5.18 displays the amount of quenched star formation compared with the NutCO run. It is apparent that a majority of star formation quenching happens in halos with $M_{\rm vir} \gtrsim 10^9\,M_\odot$. For comparison, 70–90% of the stars present at $z = 3$ are formed in such halos. In particular, we find that the most massive progenitors account for only $\simeq 30\%$ of the total star formation quenching, indicating that the primary site in which the suppression occurs is satellite galaxies.

A question that naturally arises is whether the feedback blows gas away from the dark matter potential well ("blow-away") or simply delays the SFR by only blowing gas out of the galaxy ("blowout"), creating

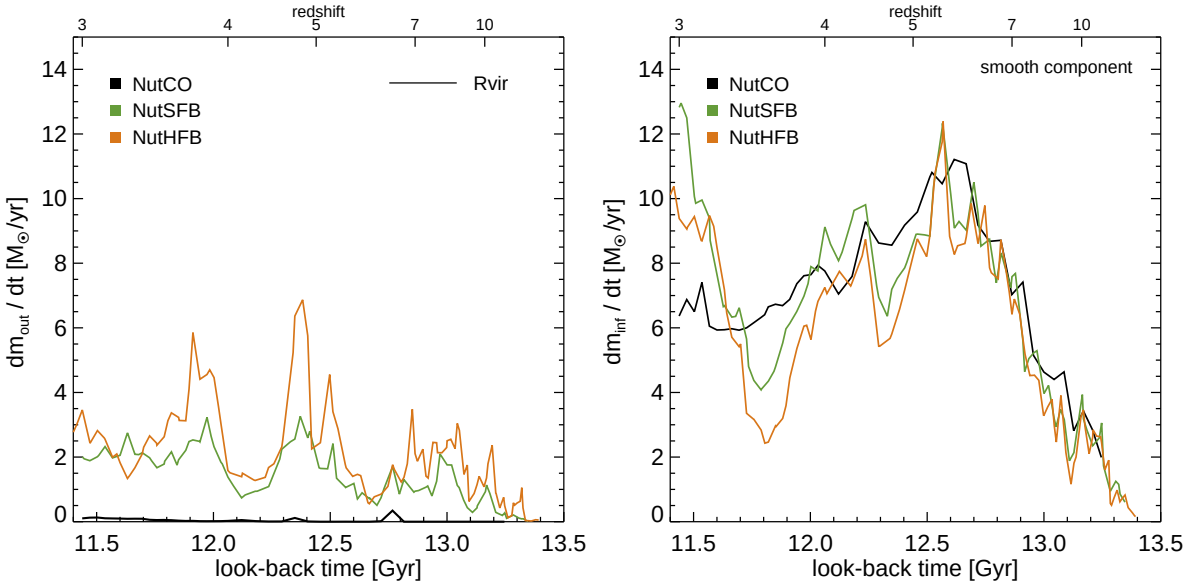


Figure 5.20: Outflow (left panel) and inflow rates (right panel) measured at the virial radius in runs with different input physics. Different colour-codings indicate the runs with different input physics, as indicated in the legend. In order to avoid contamination due to satellite galaxies, we remove the contribution from the gas belonging to substructures. It can be seen that higher energy explosions lead to higher outflow rates, occasionally reducing the amount of smooth accretion. However, gas accretion remains, by and large, unaffected by feedback processes in general.

a galactic fountain. Fig. 5.19 demonstrates that both "blow-away" and "blowout" occur. The fact that the baryon fractions in the Nut halo from the feedback runs are systematically smaller than that from the cooling run (NutCO) indicates that gas indeed escapes from the dark matter halo, as we have shown in Fig. 5.17. Stellar fractions in the Nut halo ($M_{\rm star}/[M_{\rm bar}+M_{\rm dm}]$, dashed lines) are also diminished by stellar feedback, but their differences between the cooling run and feedback runs are found to be larger than those in the baryon fraction. This means that some explosions which could not blow gas away were able to prevent forming dense gas clumps by blowing it out.

In Fig. 5.20 we quantify the outflow and inflow rates at the virial radius, measured as

$$\dot{m}_{\pm} = 4\pi R_{\rm vir}^2\, \rho_{\pm}\, V_{r,\pm},$$

where $\rho_+$ and $V_{r,+}$ are the average density and velocity of outflowing gas within a thin shell of $0.95 \leq r/R_{\rm vir} \leq 1.05$. In order to avoid contamination from satellite galaxies orbiting around the virial sphere, we neglect the contribution from gas belonging to any substructure for outflow and inflow. Several interesting features can be noticed in the figure. First, although sporadic, outflow is ubiquitous during the entire lifetime of the galaxy, sometimes reducing the amount of smooth accretion. Although the outflow rate ($\sim 2M_\odot\,{\rm yr}^{-1}$) is about a factor of 2 smaller than the SFR in NutSFB, more energetic

explosions (NutHFB) lead to rates comparable to the SFR. Second, the smooth accretion dominated by cold filaments is largely unaffected by stellar feedback processes[6], agreeing with the conclusion that the only way to accommodate the empirically derived baryon fraction is to blow away a substantial amount of gas from the host halo.

Despite the fact that we use a large amount of energy to launch galactic winds, the standard feedback processes could not lower the baryon fraction by more than 0.04 at $z = 3$. Even with the energetic explosions (HNe), the predicted baryon fraction turns out to be still large ($\simeq$ 13%), compared to the empirical estimates ($f_{\rm bar} \sim$ 4%, McGaugh et al., 2010), suggesting that too many stars have already formed at this redshift. Although we do not include in this thesis, we also find that the baryon fraction in the NutHFB run remains $\simeq$ 13% until $z \simeq 1.5$. Even if we simply apply the 0.03 decrease driven by cosmic infall from $z = 1.5$ to $z = 0$ (see Fig. 5.16), we still predict $f_{\rm bar}$ $\simeq$10%, a factor of two larger than the empirical estimate at $z = 0$. Although this value is still lower than the prediction from the Eris simulation ($f_{\rm bar}$ =0.12–0.16) which claims to produce realistic galaxy rotation curves (Guedes et al., 2011), our models do not yield satisfactory results when the kinematics of the galaxy are compared with observations. We will discuss this critical issue in detail in the next section.

#### 5.4.2.3 Impact of feedback processes on the kinematics

Spiral galaxies are often characterised by a flat rotation curve with a steep nuclear rise (e.g. Sofue & Rubin, 2001). Reproducing the rotation curves is a challenging task for numerical galaxy formation, given that complicated baryonic processes are involved in the kinematics of a galaxy.

Fig. 5.21 shows circular velocities inside a dark matter halo at $z = 3$ (left), measured as

$$V_c(r) = \sqrt{\frac{GM(< r)}{r}},$$

where $M(< r)$ is the total mass (DM+star+gas) inside the radius $r$. As reported in many other studies, the cooling runs (NutCO and NutCOLR) produce a very prominent central peak (up to 500 km s$^{-1}$) in the velocity curve. It should be noted, however, that the peak velocity differs depending on resolution. As mentioned, this is essentially because better force resolution provides a deeper potential for gas to collapse, allowing star formation to commence earlier. An important consequence of the early star formation is to convert low-angular momentum gas into stars, leading to the formation of a prominent

[6]Recently, Dubois et al. (2012a) have shown using high resolution AMR simulations that powerful outbursts from active galaxy nuclei residing in a massive halo ($5 \times 10^{11}\ M_\odot$) can destroy dense, cold streams at $z = 6$.

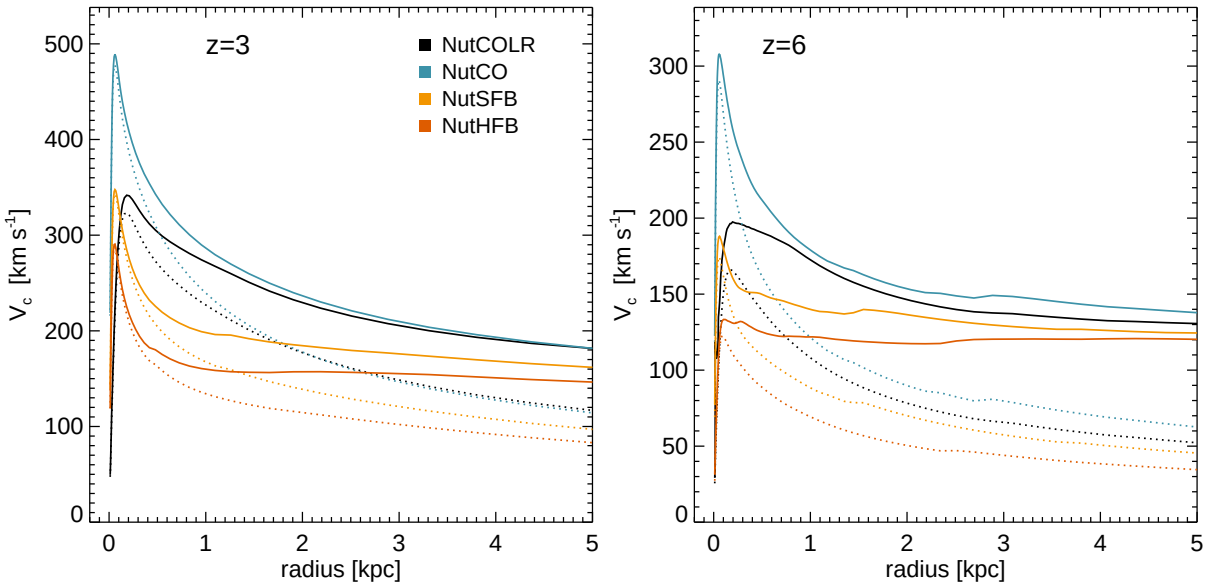


Figure 5.21: Comparison of rotation curves of the Nut galaxies at $z = 3$ (left) and $z = 6$ (right). Different colour-codings display the simulations with different input physics and resolution, as indicated in the legend. Solid lines are the circular velocities derived from the total mass inside each radius $r$, while the contribution from stars is represented by dotted lines. The central peaks in the rotation curve are clearly visible in all models already at $z = 3$.

bulge. Indeed, we find that the central peak already exists at high redshift ($z = 6$) in the cooling run. Using the same code but with 8 times lower dark matter mass resolution and 14 times larger grid cells (170 pc), Agertz et al. (2011) showed that in the absence of feedback their Milky Way-like spiral galaxy rotates at $\sim 400$ km s$^{-1}$ at 1.5 kpc radius at $z = 0$. On the contrary, our Nut galaxy with a spatial resolution of 48 pc (NutCOLR) shows a maximum velocity of 450 km s$^{-1}$ at 0.5 kpc at $z = 0$. Given that our Nut halo is roughly three times smaller than their halo, the difference in the peak velocity implies that the prediction of rotation curves is resolution-dependent.

Agertz et al. (2011) have also argued that low star formation efficiency ($\epsilon_* = 0.01$) with the standard feedback, i.e. $E_{\rm SNII} = 10^{51}$ erg, yields a realistic galaxy rotation curve. However, although the peak velocity is decreased to $\simeq 350$ km s$^{-1}$ (NutSFB) or 290 km s$^{-1}$ (NutHFB) and the velocity curves in the feedback runs are flatter within the inner radius than those of the cooling runs, we find that the central peak still exists in the simulation with efficient stellar feedback or even extreme feedback. Note that the Nut simulations adopt the same star formation efficiency as in Agertz et al. (2011), and therefore adopting the low star formation efficiency is not the key to success in producing a realistic galaxy. On the other hand, Guedes et al. (2011) claimed that changing the star formation threshold from $n_{\rm H} = 0.1\,{\rm cm}^{-3}$ to $n_{\rm H} = 5\,{\rm cm}^{-3}$ ensures that stars are formed in a clustered fashion, making the feedback more efficient. Their rotation curve at $z = 0$ is also found to be reasonably flat. Yet our simulations

adopt an even higher star formation threshold, $n_{\rm H} = 400\,{\rm cm}^{-3}$, which is close to the transition density from atomic to molecular hydrogen. In light of our results that the central peak still exists in the feedback runs, we conclude that the clustered star formation does not guarantee to form realistic galaxy rotation curves. Rather, we note that radiative cooling is prevented briefly in Guedes et al. (2011), and as a consequence, star-forming gas might have been more heavily affected by supernova explosions than its twin run adopting a lower star formation threshold.

Even though modelling techniques and details are entirely different in the two simulations (Agertz et al., 2011; Guedes et al., 2011), realistic rotation curves are found in both when the SFRs are significantly reduced at high redshift ($z \gtrsim 3$). This suggests that the crucial factor determining the kinematics of a galaxy is SFH. But the question is how effective a star formation quenching is needed. Even though our NutHFB run produces a factor of 2 less massive galaxy at $z = 3$, it is unable to remove the compact central bulge that generates the central peak in the rotation curve. Given that both NutSFB and NutHFB runs show signs of mass concentration already at $z = 6$, even more effective feedback is required at such high redshifts. However, since we already used a stellar feedback up to two times more energetic than normal supernova explosions, this sort of solution may not be fully satisfactory, although feedback from a larger fraction of Hypernovae or an active galactic nuclei could provide the additional amount of energy. There exists also the possibility that the high density of the interstellar medium ($400 \leq n_{\rm H} \lesssim 10^4\,{\rm cm}^{-3}$) may have led to excessive radiative cooling during the early phase of stellar explosions. Indeed, when we compare the energy injected from stars and the actual amount of energy used to blow gas out by the galactic wind at virial radius as

$$f_{\rm wind} \equiv \frac{\dot{E}_{\rm wind}}{\dot{E}_{\rm star}} = \frac{0.5\,m\,v_r^2 + G\,M_{\rm vir}\,m/R_{\rm vir}}{\dot{E}_{\rm star}},$$

we find that only a tiny fraction of energy ($f_{\rm wind} \sim 0.01$–$0.02$) is used in both NutSFB and NutHFB. Therefore, the problem we face may be to find a way to capture the early phase of the stellar explosions properly.

## 5.5 Conclusions and discussion

In this chapter, we have tested a new implementation of multiple, collective stellar explosions based on STARBURST99. The model now includes the energy release and mass ejecta not only from SN II but also from SN Ia and stellar winds. Motivated by the chemical enrichment in the Milky Way (Kobayashi et al., 2011), we have also considered very energetic explosions arising from massive stars. As opposed to the single blast model developed by Dubois & Teyssier (2008), multiple kinetic bubbles are launched from each star particle self-consistently without violating energy, mass, and momentum conservation. In order to examine the impact of the choice of stellar feedback parameters on the evolution of a galaxy, we have performed 14 isolated disc simulations, which mimic star forming galaxies at high redshift, varying the input parameters. Our main findings can be summarised as follows.

- Due to the weak impact, the main role of stellar winds is to enrich the star-forming gas slightly more efficiently than the single explosion model. However, outflow rates as well as the morphologies of gas density and temperature fields are largely indistinguishable between the single and multiple explosion model.

- The simulations with a low mass loading ($\eta_w \leq 10$) showed relatively strong outflows. The model in which 5 times the ejecta is entrained ($\eta_w = 5$) is found to be most effective in blowing gas out of the galaxy. On the contrary, large mass loading resulted in slower winds and less metal-rich outflows.

- Inclusion of hypernovae increased the outflow rate by a factor of $\sim 2$, but the ratio of mass loading and star formation turns out to be still smaller than unity, in disagreement with several observations. Such high mass-loading was only obtained in the simulation in which we inject 5 times more energy than the normal feedback run.

- We find that the runs adopting two different resolutions yield more or less similar outflows. On the other hand, the metallicity of stars and star forming gas is slightly underestimated in lower resolution simulations because metals are artificially diluted within AMR cells.

In order to understand how disc galaxies form in a $\Lambda$CDM universe, we have made use of two existing NUT simulations without feedback (NutCOLR, NutCO), and carried out two zoom-in cosmological simulations with feedback, which are also part of the NUT project. The NutSFB run includes the mass loss and energy release from normal SN II, Ia, and stellar winds, while hypernovae explosions are included in addition to the normal feedback processes (NutHFB). Our conclusions are as follows:

- In the presence of radiative cooling, the baryon fraction in the Nut halo is systematically higher than the universal amount predicted from cosmology. This can be attributed to the fact that galaxies form at the intersection of cold, dense filaments which are baryon-rich. However, the baryon fraction is restored to the universal baryon fraction at low redshift, as the hot shock mode of baryon accretion becomes dominant.

- The impact of efficient feedback processes are investigated using very high resolution simulations (12 parsec). In an attempt to form a realistic disc galaxy, we use 1.5 times more energy than the prediction from STARBURST99, but we nevertheless find that the baryon fraction in the Nut halo is kept high, close to the universal baryon fraction. Even when the feedback from HNe is included, the simulation still predicts too many baryons in the Milky Way-like halo at $z = 3$ ($f_{\rm bar} \simeq 0.13$). The resulting stellar masses of the Nut galaxy are reduced by a factor of $\simeq 1.5$ in NutSFB and $\simeq 2$ in NutHFB at $z = 3$, compared to the stellar mass from NutCO.

- A majority of star formation quenching occurs in halos with $M_{\rm vir} \gtrsim 10^9\,M_\odot$, which are also the main site of star formation. Of the global amount, we find that 70% is suppressed in satellite galaxies.

- Even though outflows are far-reaching, the mass-loading factor at the virial radius in the feedback runs is found to be generally lower ($\eta \lesssim 0.5$) than the empirical estimate (e.g. Martin, 1999). We also find that the smooth accretion is impervious to these stellar-driven outflows.

- Contrarily to what several authors argued, adopting low star formation efficiency (Agertz et al., 2011) or high threshold density for star formation (Guedes et al., 2011) does not guarantee to form a realistic galaxy rotation curve. The rotation curves of our simulated galaxies with stellar feedback (NutSFB or NutHFB) showed a pronounced central peak of $\sim 300\,{\rm km\,s^{-1}}$ at $z = 3$. Surprisingly, we find that the peak is already in place at $z = 6$ for NutSFB.

- Even though lower force resolution leads to a delay in star formation, we find that the stellar masses in simulations with different resolution are more or less the same at low redshift ($z \lesssim 4$). However, a higher-resolution simulation yielded a more peaked rotation curve as more low-angular momentum gas is converted into stars at high redshift.

It would be certainly worrisome if simulation results are contingent on numerical resolution. However, the trend that higher resolution runs produce a more pronounced peak is likely to be simply an

artefact of numerical simulation due to incomplete modelling of feedback processes. With efficient feedback, low angular momentum gas will be blown out of the central region of the galaxy, allowing for star formation in a more extended disk, in which case resolution may not be such a critical issue.

Given that only $\sim 2\%$ of the total energy is used to blow gas out of the dark matter halo in our feedback runs, it is necessary to understand why the process is inefficient. Even though our simulated galaxies produce a multiphase ISM, we find that dense gas clumps, including the core, are immune to feedback processes. As long as such dense clumps/core are robust against feedback processes, it will be difficult to form a realistic galaxy, and therefore one must find a way to make the feedback more efficient so that it can disrupt such dense clumps or prevent forming them in the first place. The most straightforward solution is to inject more energy. Hopkins et al. (2012b,a) recently tested the impact of several feedback processes for disc galaxies composed of stars, dark matter, and gas particles. They showed that in a small magellanic cloud-like galaxy, the mechanical feedback from stars, drawn from STARBURST99, is enough to create large-scale, heavily entrained winds, which is inconsistent with our findings based on the purely gaseous disc (Section 5.3). This implies that mechanical feedback is only ineffective in clumpy environments. Indeed, they showed that the mechanical feedback alone could not drive highly entrained outflow in a starburst prototype ($\eta \sim 0.1$), and they had to invoke radiation pressure from dust by multiple absorption/scattering of infrared photons (Hopkins et al., 2011). Another possible way involves counterbalancing the self-gravity in individual gas clumps or clouds. An example of this approach is to disable the radiative cooling in the system, which is equivalent to implicitly exerting additional pressure. However, this simple argument is not easy to justify, because the condition of adiabacity depends on the local density and temperature on much smaller scales than a simulation can resolve. Moreover, Thornton et al. (1998) demonstrated using one-dimensional simulations of a supernova explosion in a uniform medium that more than 90% of the input energy is radiated away in a dense, propagating shell. In a different context, Scannapieco & Brüggen (2010) developed a model in which supernovae deposit their energy as supersonic turbulence. Scannapieco & Brüggen (2010) argued that the supersonic turbulence can help drive strong bipolar outflows through hot, diffuse gas in dwarf-sized galaxy without disrupting dense regions. Unfortunately, they did not compare their results with other previous studies, so it is difficult to assess whether this can be a solution to the peaked rotation curve problem. Finally, our simulations as well as others ignore the effect of magnetic fields. This may be a bold approximation, given that the magnetic pressure is of the same order as the thermal pressure in molecular clouds (e.g. McKee & Ostriker, 2007). Moreover, given that supernova explosions are

a reasonable origin for galactic magnetic fields (e.g. Dubois & Teyssier, 2010), the interplay between magnetic fields and outflows may be of crucial importance in predicting how outflows entrain gas and how energy dissipates in a turbulent medium. These issues should be tackled in the future.

# Chapter 6

# Constraining stellar assembly and AGN feedback at the peak epoch of star formation[1]

## 6.1 Introduction

The present-day galaxy luminosity function shows a rapid turnover at luminosity $L_*$ (Cole et al., 2001), while ΛCDM cosmology predicts a power-law form for the dark matter halo mass function (Jenkins et al., 2001). The low mass-to-light ratio in low- and high-mass halos is interpreted as evidence for the existence of baryonic feedback, that regulates star formation (e.g. Binney, 2004). Consensus favours a picture in which energy from active galactic nuclei (AGN) regulates the formation of massive galaxies (e.g. Ciotti & Ostriker, 1997; Kaviraj et al., 2011a), despite the significant difference in the scale of a supermassive black hole (SMBH) from that of its host galaxy. This picture appears to be supported by the tight observed correlation between SMBH mass and the bulge of its host galaxy (e.g. Häring & Rix, 2004), evidence for the suppression of gas cooling and star formation due to AGN interaction with the interstellar/intracluster medium (e.g. McNamara & Nulsen, 2007), high-velocity galactic outflows that are commonly detected in quasars (Pounds et al., 2003; Ganguly & Brotherton, 2008) and X-ray cavities inflated by radio jets, associated with AGN, that are observed in cluster centres (Fabian et al., 2006). Nevertheless, it is still unclear as to how, to what extent, and at what epochs, AGN feedback shapes the star formation history (SFH) of galaxies in the Universe.

[1]Kimm, T., Kaviraj, S., Devriendt, J., Cohen, S., Windhorst, R., Dubois, Y., Slyz, A., Hathi, N., Ryan, R. Jr, O'Connell, R., Dopita, M., Silk, J., 2012, MNRAS, 425L, 96

Several studies have used semi-analytic or fully hydrodynamic models of galaxy formation, to understand the effect of negative feedback on the cosmic SFH (e.g. Fontanot et al., 2009). While detailed physical ingredients and prescriptions differ in each model, such studies agree on the importance of AGN feedback for reproducing the masses, colours, and star formation rates (SFRs) of local massive galaxies (e.g. Kimm et al., 2009). However, the comparisons are almost exclusively performed in the nearby Universe, while the bulk of the stellar assembly in these galaxies takes place at high redshift ($z > 1$). Unfortunately, 8-10 Gyrs of evolution can easily wash out many of the *details* of stellar assembly, and thus it is necessary to investigate the epoch *at which the bulk of the star formation takes place (*$1 \lesssim z \lesssim 3$*)* (Madau et al., 1998). Confronting the observed galaxy colours with the models at these epochs represents a more stringent test of their reliability.

In this Chapter, we study the stellar assembly in massive galaxies, by comparing a fully hydrodynamical cosmological simulation to *rest-frame* UV-optical galaxy colours from the WFC3 Early Release Science (ERS) programme (Windhorst et al., 2011). The rest-frame UV (shortward of 3000Å), which is sensitive to even residual amounts of star formation, is a powerful tracer of how quiescent a galaxy is (e.g. Kaviraj et al., 2011b; Rutkowski et al., 2012), enabling us to constrain the quenching of star formation due to AGN and stellar feedback. By contrast, the rest-frame optical colours constrain the average epoch of stellar mass assembly. This is the first direct comparison to simulations of rest-frame UV-optical colours at the epoch of peak star formation. We describe the data and simulations in § 6.2 and 6.3 respectively. We present the comparison between observations and models in § 6.4, and discuss the implications of our results on galaxy formation in § 6.5. Throughout, we adopt $(h_0,\, \Omega_m,\, \Omega_b,\, \Omega_\Lambda,\, \sigma_8) = (0.7,\, 0.26,\, 0.045,\, 0.74,\, 0.8)$ following the WMAP-3 results (Hinshaw et al., 2009). All fluxes are based on the AB magnitude system.

## 6.2 Observations

The WFC3 ERS programme (Windhorst et al., 2011) has imaged ∼1/3 of the GOODS-South field (∼45 arcmin$^2$), using the WFC3 F225W, F275W, F336W, F098M, F125W, and F160W filters, with exposure times of 1-2 orbits per filter. In combination with the existing GOODS BViz coverage (Giavalisco et al., 2004), this provides 10-filter panchromatic coverage (0.2–1.7 $\mu m$) to point source depths of AB ∼26.5–27.5 mag (UV–IR, 5$\sigma$). Here, we study 188 and 151 galaxies with $M_{\rm star} \geq 10^{10} M_\odot$, for comparisons at $0.8 \leq z \leq 1.2$ and $1.7 \leq z \leq 2.3$ respectively. Note that the ERS sample is complete down to $\sim 10^9 M_\odot$ and the observed images that trace both the rest frame UV and the rest frame optical are deep

enough for all massive galaxies to be detected (Windhorst et al., 2011). For every galaxy, photometric redshifts were calculated using EAZY, based on all 10 filters with all possible combinations of pairs of the EAZY_v1.0 templates (Brammer et al., 2008). The absorption due to intervening intergalactic HI clouds is taken into consideration. No redshift prior probability distribution specific to these fields is used. The resulting mean reduced $\chi^2$ of the fit is 0.94, and the typical redshift uncertainty of the sample is $\Delta z = |z_{\rm spec} - z_{\rm phot}| \simeq 0.15$. We note that no k-correction is applied to the observed sample, and that we refer the rest-frame UV and optical fluxes to the fluxes through the WFC3/ACS bandpass that *roughly* trace the GALEX $NUV$ or Johnson $B/V$. Thus our estimated rest-frame $NUV$ or optical fluxes are slightly different from GALEX $NUV$ or Johnson $B/V$ fluxes.

In addition, the full suite of WFC3/ACS photometry of each galaxy is compared to a library of exponentially decaying model star formation histories, based on the Bruzual & Charlot (2003) stellar models. A wide range of ages (0.001–13 Gyr), decay timescales (0.1–9 Gyr), metallicities (0.005–2 $Z_{\odot}$) and dust extinctions $0 < E(B-V) < 2$ are employed, with the normalisation of the models yielding the stellar mass. The likelihood of individual models ($\chi^2/2$) are calculated and parameters are marginalised. The median of the marginalised probability distributions are taken to be the best estimates, with the 25 and 75 percentile values (which enclose 50% of the total probability) providing an associated uncertainty (see e.g. Kaviraj et al., 2011b). Specific SFRs (SSFRs) and stellar masses thus derived have uncertainties of $\sim$0.3 dex.

## 6.3 Simulation

In this paper, we use the octree-based Eulerian hydrodynamics code, RAMSES (Teyssier, 2002). Metal-dependent radiative cooling is modelled based on Sutherland & Dopita (1993), and a uniform UV background is instantaneously turned on at $z = 10.5$ following Haardt & Madau (1996). Star particles are created following a Schmidt law with 2% efficiency, when the density of a gas cell reaches a critical density, $\rho_0 = 0.4$ H/cm$^3$. We use the polytropic equation of state for the gas above the threshold density, with the minimum temperature of $10^4$ K. Massive stars are assumed to lose their mass through stellar winds and a supernova phase, dispersing gas and metals (18% and 2% by mass, respectively) into their surroundings. Feedback is modelled as an isotropic kinetic outflow, which carries matter amounting to ten times the mass loss from the stars (Dubois & Teyssier, 2008).

Our model assumes that seed BHs of $10^5 M_{\odot}$ form in regions of high gas density, ensuring that only one BH is formed per galaxy (Dubois et al., 2012a). The growth of the BH is tracked self-consistently,

based on a modified Bondi-Holye-Lyttleton accretion rate. We adopt a density-dependent boost factor $\alpha_{\rm BH} = (\rho/\rho_0)^2$, following Booth & Schaye (2009). When gas accretes onto BHs, we assume that a central BH can impact the ambient gas in two ways, depending on the Eddington ratio ($\chi \equiv \dot{m}/\dot{m}_{\rm edd}$). For a high accretion rate ($\chi \geq 0.01$), 1.5% of the accretion energy is injected as thermal energy (quasar-like mode), whereas sub-relativistic ($v = 10^4$ km/s) momentum-imparting collimated winds are launched for a low accretion rate ($\chi < 0.01$) event with 10% efficiency (Dubois et al., 2012a). The parameters are chosen to match the fraction of stars in groups and clusters of galaxies (Dubois et al. *in prep*). In order to avoid artificial cooling and maximise the impact of AGN feedback, we store the thermal energy and kinetic energy until it either reaches $10^8$K or the energy corresponding to 10% of the BH mass. Therefore, the efficiency of the two modes should be regarded as a rough estimate, not a true efficiency.

We have performed two cosmological simulations with the same initial conditions generated by `mpgrafic` (Prunet et al., 2008), a parallel version of the `grafic` package (Bertschinger, 2001). The simulations contain $256^3$ dark matter particles with $m_{\rm dm} \simeq 4 \times 10^9 M_\odot$ in a 50 $h^{-1}$ Mpc comoving periodic box. We fix the maximum spatial resolution to $\simeq 0.38$ kpc/h in physical units. The minimum mass of the star particles is $1.65 \times 10^6 M_\odot$. The virial mass of the most massive halo in our simulated volume is $3.3 \times 10^{13} M_\odot$ at $z = 1$. Note that the mass of dark matter halos used to compare with the observation in Section 6.4 is in the range $12 \lesssim \log M_{\rm vir} \lesssim 13.5$, and hence our sample represents massive galaxies ($M_{\rm star} \geq 10^{11} M_\odot$ at $z = 1$) forming in group/field environments. This allows for a fair comparison with the ERS sample, which is known to have few cluster galaxies (Windhorst et al., 2011). It is also worth mentioning that 36% of the simulated massive galaxies are bulge-dominated at $z = 1$, which seems compatible with the observed morphological fraction in the GOODS fields (Bundy et al., 2005).

*Predicted colours of simulated galaxies are generated by folding the stellar spectra of individual star particles with the stellar population models of Bruzual & Charlot (2003).* The optical depth is calculated following the empirical calibration of Guiderdoni & Rocca-Volmerange (1987), and dust attenuation is calculated using the Cardelli et al. (1989) extinction curve (Devriendt et al., 2010, Eq. 1). We emphasise that *the attenuated spectra of the simulated galaxies are redshifted to either $z = 1$ or $z = 2$ before convolving them with the throughput of WFC3/ACS filters* to directly compare with ERS galaxies.

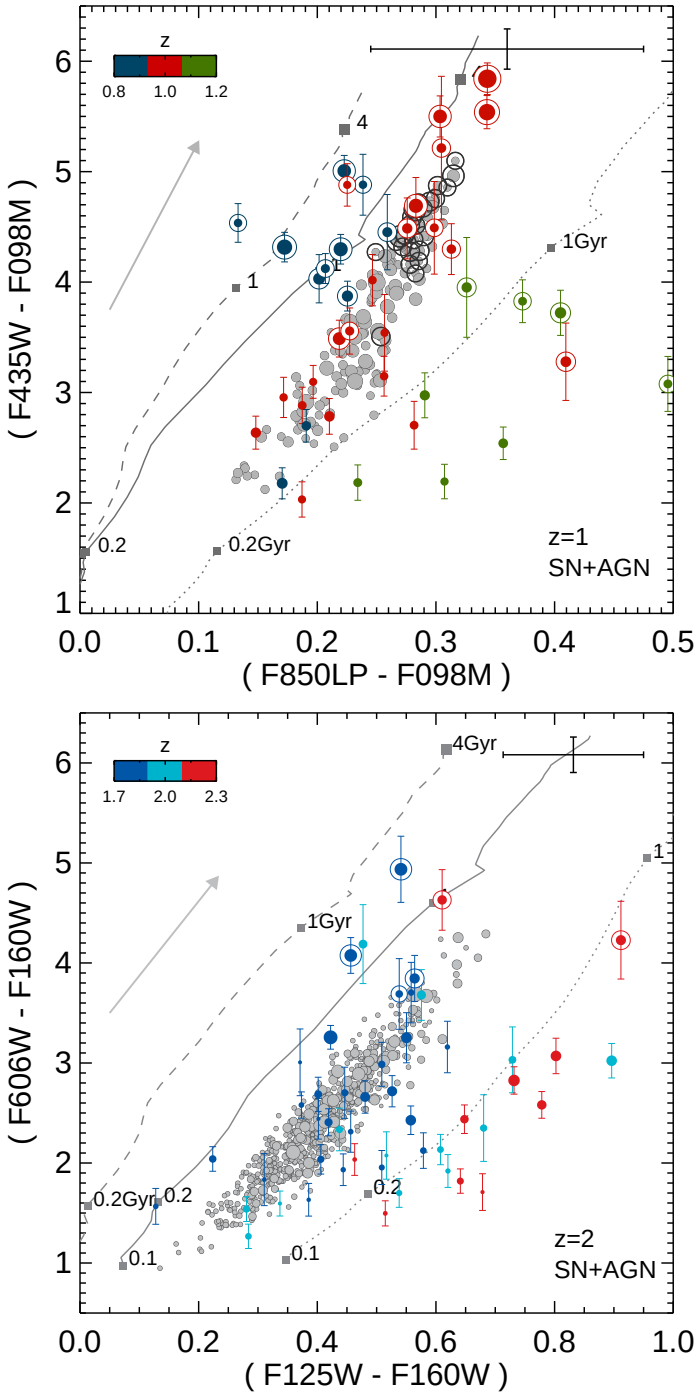


Figure 6.1: Colour comparisons of massive galaxies at $z = 1$ (top; $m_{\rm star} \geq 10^{11}\,M_{\odot}$) and $z = 2$ (bottom; $m_{\rm star} \gtrsim 10^{10.5}\,M_{\odot}$) with simulations that include AGN+supernova feedback. The observed colours on the x and y axes trace rest-frame $(B - V)$ and $(NUV - V)$, respectively (see text for more details). Filled circles with error bars indicate the WFC3 ERS data, while simulated galaxies are shown using filled grey circles. The size of the symbol scales with stellar mass. The three lines represent the expected colours of simple stellar populations (SSPs) with different ages at different redshift: in the upper panel, $z$ =0.8 (dashed), 1.0 (solid), and 1.2 (dotted), in the lower panel: $z$ =1.7 (dashed), 2.0 (solid), and 2.3 (dotted). For clarity, the colours of SSPs with different ages (0.1, 0.2, 1, and 4 Gyr) are indicated by filled square symbols. Points with a concentric circle denote galaxies with low specific star formation rate (SSFR$< 0.01$ Gyr$^{-1}$). We indicate the median uncertainty of the observed colours in the top right and the typical extinction vectors of the simulated galaxies in the left of each panel.

## 6.4 Results

In Fig. 6.3 we present the rest-frame UV and optical colours of ERS galaxies around $z \simeq 1$. We use the ACS F435W, F850LP, and WFC3 F098M filters to trace the *rest-frame* $NUV$ ($\sim$2300Å), $B$, and $V$ bands, respectively. In order to test the influence of AGN feedback, we restrict our sample to galaxies more massive than $m_{\rm star} \geq 10^{11}\,M_{\odot}$ because SN feedback is ineffective in such large potential wells, leaving AGN feedback as the most plausible mechanism for modulating star formation. Three reference lines are included in the figure to help distinguish the age and redshift sequence. Each line corresponds to a simple stellar population (SSP) with various ages (marked next to the line). Differences between the lines indicate the change in the colours when a spectrum is redshifted to different values before it is convolved with the filter throughputs ($z = 0.8$, 1.0, and 1.2 [left panel] or $z = 1.7$, 2.0, and 2.3 [right panel]). Observed galaxies show a large scatter in $(NUV - V)$ and $(B - V)$ colours, partly because no k-correction is applied. When the redshift interval of the sample is constrained around $z \simeq 1$, a colour sequence is apparent (red points), with massive galaxies being redder in both UV and optical colours.

To make a detailed comparison, we study the SSFRs derived from SED fitting (see Section 2), marking 'quiescent' (SSFR $\equiv \dot{m}_{\rm star}/m_{\rm star} \leq 0.01\,{\rm Gyr}^{-1}$) galaxies in our sample with a concentric circle in Fig. 6.3. We find that almost all massive galaxies with $(NUV - V) \gtrsim 4$ mag are quiescent. It is worth emphasising here that this provides a stringent test for any cosmological galaxy formation model, since such low SSFRs are comparable to those of nearby 'red and dead' galaxies (e.g. Kimm et al., 2009). *Thus, any process that shapes the star formation history of massive galaxies must be powerful enough to quench star formation at this early epoch.*

We find that the simulated galaxies with AGN feedback agree reasonably well with the observed sequence at $z = 1$. The left-hand panel of Fig. 6.3 indicates that a majority of model galaxies with $(NUV - V) \gtrsim 4$ mag are indeed quiescent (double circles), but not due to dust reddening, indicating that AGN feedback is a plausible explanation for the emergence of quiescent galaxies at $z \simeq 1$. However, in the absence of AGN feedback almost all model galaxies are predicted to be actively star forming (Fig. 6.2), suggesting that gravitational heating by substructure alone (e.g. Khochfar & Ostriker, 2008) is not able to account for the build-up of quiescent galaxies in group/field environments at this epoch (see also Johansson et al., 2012). Note that such interactions between infall of substructure and the interstellar/intracluster medium is automatically accounted for in our hydrodynamic calculations. We also see that the model with AGN feedback reproduces the observed trend of blue galaxies ($(NUV - V) \lesssim 3$ mag) being less massive. However, there is an indication that massive galaxies with intermediate

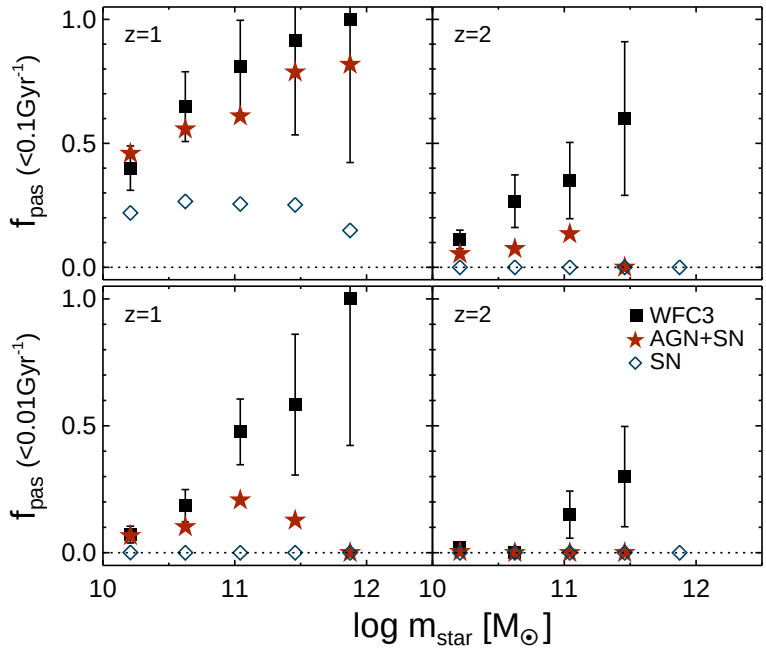


Figure 6.2: The fraction of passive galaxies for the observations (black squares), the model with supernova and AGN (red stars), and the model with supernova (blue diamonds). Top panels show the fraction of galaxies showing SSFR$< 0.1$ Gyr$^{-1}$, while bottom panels display the fraction of galaxies which are an order of magnitude less active SSFR$< 0.01$ Gyr$^{-1}$. Poisson errors are indicated by error bars.

colours ($(NUV - V) \simeq 3.5$ mag) are more frequent than observed in the data (see the left panel in Fig. 6.3).

In Fig. 6.3 (right panel), we show the corresponding colour comparisons at $z \simeq 2$. We only show galaxies with masses greater than $3 \times 10^{10} M_{\odot}$, which form more than 90% of the progenitors of our model galaxy sample at $z = 1$. Since the redshift of the galaxy sample has changed, we now use the ACS F606W and the WFC3 F125W and F160W filters to trace the rest-frame $NUV$, $B$, and $V$ bands respectively. We find that our simulated galaxies at $z \simeq 2$ compare better with WFC3 galaxies at $1.7 \leq z < 1.9$ rather than $1.9 \leq z < 2.1$. We suspect that this is due, in part, to a systematic underestimation of the photometric redshifts at these epochs (see also Williams et al., 2009). Note that the observed galaxies at $1.7 \leq z < 1.9$ are comparable to the model galaxies at $z = 2$, given the typical uncertainty of EAZY redshifts at these epochs ($\Delta z \sim 0.15$). At $z \simeq 2$ we find that there exists a non-negligible number of massive galaxies with a very low level of star formation activity, which are absent in the run with AGN feedback. The massive galaxies ($M_{\rm star} \gtrsim 10^{11} M_{\odot}$) in the model are actively star forming (SSFR$\sim 0.3$ Gyr$^{-1}$), leading to colours ($(NUV - V) \lesssim 3$) that are inconsistent with the observations.

Fig. 6.2 shows the fraction of passive galaxies, which confirms that the modelled recent star formation

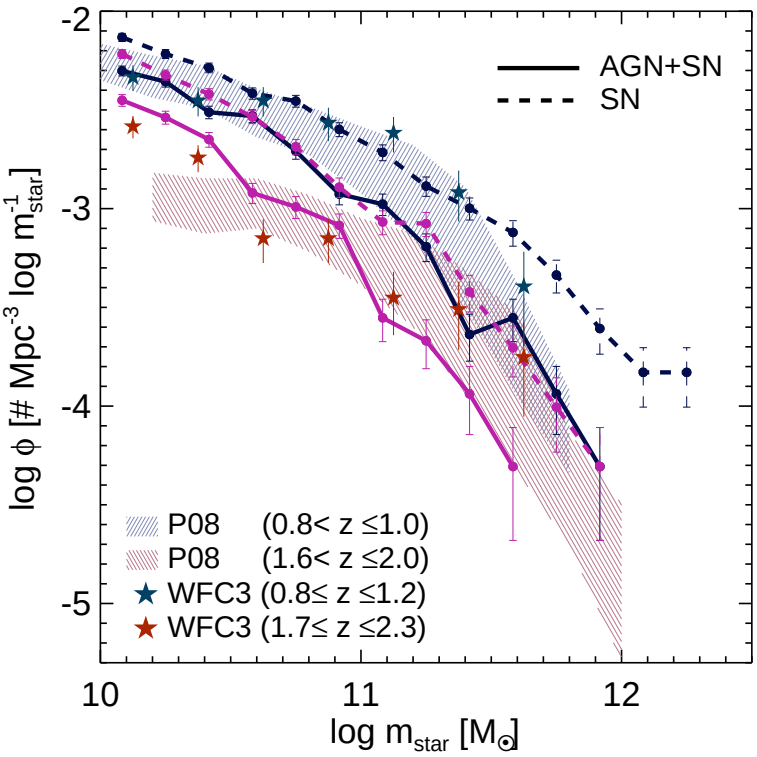


Figure 6.3: The stellar mass functions of galaxies at $z = 2$ (reddish colours) and $z = 1$ (bluish colours). Our estimations at each redshift intervals for simulated galaxies with and without AGN feedback are plotted as solid and dashed lines, respectively. Error bars indicate Poisson errors in the counts. For comparison, we display the mass functions at $0.8 < z \leq 1.0$ (blue shading) and $1.6 < z \leq 2.0$ (red shading) from Pérez-González et al. (2008). Also included as stars are the simple number counts from the WFC3 sample.

needs to be further suppressed in massive galaxies at $z \simeq 2$. While our simulation predicts that $\lesssim$ 20 % of massive galaxies have SSFR$< 0.1$ Gyr$^{-1}$ at $z \simeq 2$, the observations suggest that 30–60% of the massive galaxy population is passive (top right). At $z \simeq 1$, a majority (60–80%) of the massive galaxies in the model have become passive (top left), but when a more conservative definition for a passive galaxy is used (SSFR$< 0.01$ Gyr$^{-1}$), we find that the passive fraction in the model drops to approximately 0–20% (bottom left). This is inconsistent with the observations, which suggest that 50–100% of massive galaxies are quiescent at this epoch.

Nevertheless, the impact of AGN feedback becomes clearly visible in the stellar mass functions (see Fig. 6.3). The number of massive galaxies in the AGN run ($m_{\rm star} \gtrsim 10^{11} M_{\odot}$; solid lines) are systematically smaller than the run without AGN (dashed lines) by a factor of $\sim 3$. Comparing twin halos that share position and mass in the feedback/no feedback runs, we find that the stellar masses of the galaxies they host are reduced by a factor of 2–5, meaning that the mass functions are shifted horizontally (to the left) due to AGN feedback. The mass functions are in reasonable agreement with

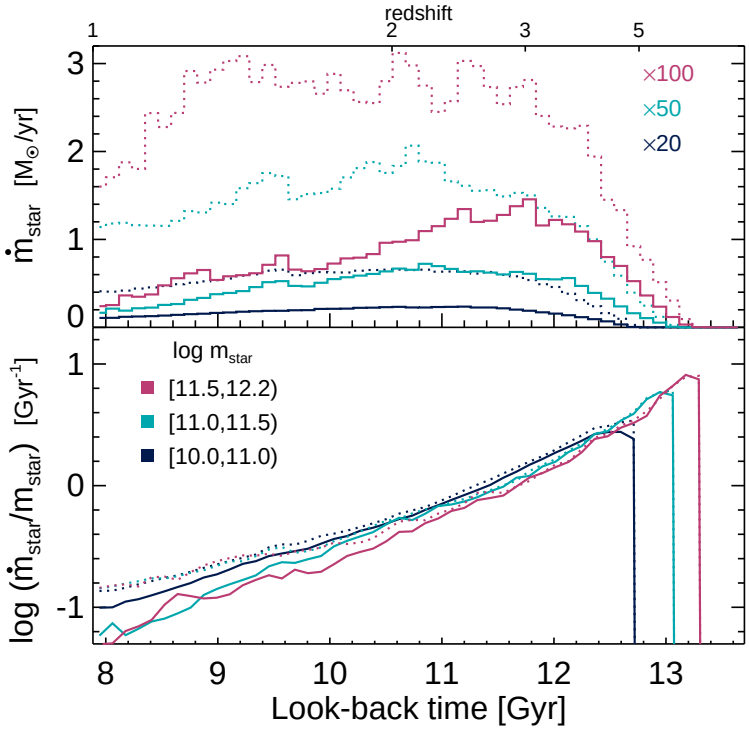


Figure 6.4: The median star formation history of simulated galaxies at $z = 1$ in the run with (solid) and without (dotted) AGN feedback. *Top*: the median star formation rates of galaxies in three different mass bins. For clarity, the SFRs are scaled down by 100 for galaxies with $10^{11.5} \leq m_{\rm star} < 10^{12.2}$ (red), 50 for galaxies with $10^{11.0} \leq m_{\rm star} < 10^{11.5}$ (cyan), and 20 for galaxies with $10^{10} \leq m_{\rm star} < 10^{11}$ (blue). *Bottom*: The specific star formation rates (SSFRs) as a function of look-back time.

the stellar mass function estimated by Pérez-González et al. (2008) (red and blue shadings), and also compatible with the simple number counts from the WFC3 galaxies at $1.7 \leq z \leq 2.3$ (orange stars) or $0.8 \leq z \leq 1.2$ (blue stars).

One may wonder whether our AGN feedback recipe is too strong, given the apparent deficit of the most massive galaxies. However, this can be partly attributed to the absence of density fluctuations on scales comparable to the size of the simulation (Sirko, 2005; Gnedin et al., 2011). Moreover, the fact that we need further quenching of residual star formation in massive galaxies does not appear to favour moderating the impact of AGN feedback. We discuss this issue further in the next section.

Finally, in agreement with the downsizing picture (Cowie et al., 1996), we find that in the run with AGN feedback, the star formation histories of more massive galaxies are peaked at higher redshift (solid lines in the upper panel of Fig. 6.4). This can also be seen in the bottom panel, where we plot the median SSFR of 1127, 117, and 29 galaxies in three mass bins, $10^{10} \leq m_{\rm star} < 10^{11}\,M_\odot$, $10^{11} \leq m_{\rm star} < 10^{11.5}\,M_\odot$, and $10^{11.5} \leq m_{\rm star} < 10^{12.2}\,M_\odot$, as a function of look-back time. If we compare the galaxy SFHs in the runs with (solid lines in the top panel) and without AGN feedback (dotted lines), we see that star formation is preferentially suppressed at $1 \lesssim z \lesssim 3$ at which the bulk of the star formation takes

place (Madau et al., 1998).

Interestingly, we see that the most massive galaxies have an extended SFH, which may, at first sight, seem inconsistent with the high observed [$\alpha$/Fe] ratios in local systems (e.g. Thomas et al., 2005). However, we note that it is the star formation timescale in the *subunits* that finally merge to form the larger galaxy that determines its average [$\alpha$/Fe]. In other words, it is not possible to directly infer the [$\alpha$/Fe] from a 'composite' SFH of the various subunits (such as the one shown in Fig. 6.4), because much of the broadness of the SFH is driven by the fact that star formation peaks at different epochs in different subunits. Hence, the degree of the discrepancy may not be as substantial as it appears, and will be tested with more detailed chemo-hydrodynamic simulations in a forthcoming paper.

## 6.5 Discussion and Conclusions

We have presented the first direct comparison of the rest-frame UV-optical colours of massive galaxies at $1 \lesssim z \lesssim 2$ to the predictions of hydrodynamic simulations that include AGN feedback. We have shown that massive galaxies in the simulations are actively star forming at this redshift in the absence of a strong source of energetic feedback. In an attempt to estimate the stellar assembly of massive galaxies, we have incorporated a simple, jet/quasar-mode AGN feedback (Dubois et al., 2012a), and found that it reproduces a reasonable fraction of *moderately* quiescent galaxies in both rest-frame UV and optical colours at $z = 1$. However, the model slightly overpredicts the level of recent star formation activity in massive galaxies at $z = 1$ and 2, compared with the observations. Despite this, the stellar mass functions in the model with AGN feedback agree reasonably well with the WFC3 ERS data (within the statistical uncertainties), due to the efficient quenching of star formation during the epoch of peak star formation.

The lack of massive, quiescent galaxies in the model seems to require *further* suppression of residual star formation without significantly altering the stellar mass function. This suggests that the peak epoch of the stellar assembly in massive galaxies should commence earlier than we have predicted, while the residual star formation must decline more sharply over time. Although further star formation quenching is attainable by introducing more enhanced feedback or other processes that we have ignored (e.g. photoionisation of gas coolants due to soft X-ray and extreme UV photons from stars, Cantalupo 2010), changing the peak epoch of stellar assembly, while keeping the stellar mass function fixed may require well-balanced interplay between feedback and star formation.

Regarding the extended nature of the predicted SFHs, a different approach, involving a higher level of star formation activity in the very early universe (e.g. Stark et al., 2009) is also appealing. The advantages

of this idea are 1) it does not violate the stellar mass functions at $z \leq 2$, 2) it alleviates the discrepancy in [$\alpha$/Fe] ratio in massive galaxies to some degree (e.g. Pipino et al., 2009), although other routes, such as the use of a top-heavy IMF may offer more promising solutions (Arrigoni et al., 2010)), and 3) star formation can be efficiently suppressed with the same amount of energy released from the black holes by consuming gas earlier on. Even though the physical origin of such high specific star formation rates is unclear, we note that proper modelling of gas fragmentation in galaxy mergers can easily elevate star formation by an order of magnitude (Teyssier et al., 2010), and may even be able to match the observed high SSFRs in the early universe (e.g. Khochfar & Silk, 2011).

We also note that the mass and spatial resolution of a simulation plays a role in determining the star formation history of the model galaxies. Adopting a better resolution allows us to resolve smaller halos in the early universe ($z \gtrsim 5$), leading to earlier star formation, with an order of magnitude enhancement in the star formation activity at this epoch (Rasera & Teyssier, 2006). This will naturally increase the mean age of the massive galaxies (e.g. Johansson et al., 2012). However, the question is how many stars form during this epoch, compared to the total stellar mass at $z \simeq 1$ or 2. Inspection of the top panel of Fig. 6.4 shows that an order of magnitude increase in the SFR at $z \geq 5$ will not significantly affect the overall SFHs.

Given the simplicity of our modelling of AGN feedback, the agreement between observations and models is encouraging. An important challenge will be to match chemical abundance ratios in massive galaxies, while producing the correct number of red and dead galaxies at high redshift. In a forthcoming paper we will investigate these issues in detail, focussing on more realistic modelling of the starburst phases and the interplay between feedback and star formation at high redshift.

# Chapter 7

# Conclusions

For decades, the standard paradigm of galaxy formation stipulated that gas first got shock-heated as it crossed the virial radius of a virialised dark matter halo, and that the resulting hot gas slowly settled as a cold rotationally supported disc by radiating away its internal energy whilst conserving its angular momentum (Rees & Ostriker, 1977; Silk, 1977; White & Rees, 1978). However, recent hydrodynamic simulations have shown that in the early universe such a virial shock does not always exist, but instead gas freely flows into the halo through cold, dense filaments until it reaches the vicinity of the central galaxy (Kereš et al., 2005; Ocvirk et al., 2008; Dekel et al., 2009). Progress in high-performance computing has allowed us to study internal galactic properties in more detail, shedding light on the importance of feedback processes in regulating star formation. In this thesis, we have investigated the two issues (cold flows and feedback) using Eulerian hydrodynamic simulations. More specifically, the main questions we addressed were:

- Are cold flows detectable with low-ionisation metal absorption lines? What are the typical covering fractions of cold flows?
- How is angular momentum transported inside the dark matter halo? How does the presence of cold flows change our view on the acquisition of angular momentum during the evolution of disc galaxies?
- Is more realistic stellar feedback able to blow out a substantial amount of gas from galaxies or disrupt cold flows? How sensitive are these results to the specific choice of feedback subgrid models/parameters? Can we form a realistic disc galaxy in the ΛCDM universe? Is resolution of the simulation the key to success in forming a realistic disc galaxy?

- Can AGN feedback account for the emergence of massive quiescent galaxies at $1 \lesssim z \lesssim 2$? How do the stellar assembly histories of simulated galaxies compare with those deduced from observations?

This chapter summarises the main results of this thesis, and suggests possible directions along which it could be further developed.

## 7.1 Summary of the thesis

Cosmological simulations have shown that dark matter haloes are connected to each other by large-scale filamentary structures. Cold gas flowing within this 'cosmic web' is believed to be an important source of fuel for star formation at high redshift. However, the presence of such filamentary gas has never been observationally confirmed despite the fact that its covering fraction within massive haloes at high redshift is predicted to be significant ($\sim$ 25%), (Dekel et al., 2009). In Chapter 3, we investigated in detail whether such cold gas is detectable using low-ionisation metal absorption lines, such as CII $\lambda$1334, as this technique has a proven observational record for detecting gaseous structures. Using a large statistical sample of galaxies from the HORIZON-MARENOSTRUM N-body+AMR cosmological simulation, we found that the typical covering fraction of the dense, cold gas in $10^{12}$ $M_{\odot}$ haloes at z $\sim$ 2.5 is lower than expected ($\sim$ 5%). In addition, the absorption signal by the interstellar medium of the galaxy itself turns out to be so deep and so broad in velocity space that it completely drowns that of the filamentary gas. A detectable signal might be obtained from a cold filament exactly aligned with the line of sight, but this configuration is so unlikely that it would require surveying an overwhelmingly large number of candidate galaxies to tease it out. Finally, the predicted metallicity of the cold gas in filaments is extremely low ($\leq$ $10^{-3}$ $Z_{\odot}$). Should this result persist when higher resolution runs are performed, it would significantly increase the difficulty of detecting filamentary gas inflows using metal lines. However, even if we assume that filaments are enriched to $Z_{\odot}$, the absorption signal that we compute is still weak. We are therefore led to conclude that it is extremely difficult to observationally prove or disprove the presence of cold filaments as the favourite accretion mode of galaxies using low-ionisation metal absorption lines. The Ly$\alpha$ emission route looks more promising but due to the resonant nature of the line, radiative transfer simulations are required to fully characterise the observed signal.

The presence of cold gas flows, at least in hydrodynamic simulations, suggests that angular momentum transport by gas may differ from that by dark matter. In Chapter 4, we revisited this issue using a series of high resolution cosmological hydrodynamics simulations of a Milky Way-sized galaxy, called

NUT. We found that at the time of accretion, gas and dark matter do carry a similar amount of specific angular momentum, which is systematically and significantly higher than that of the dark matter halo as a whole. At high redshift, freshly accreted gas rapidly streams into the central region of the halo, directly depositing this large amount of angular momentum within a sphere of radius $r \sim 0.1 r_{\rm vir}$. In contrast, dark matter particles pass through the central region unscathed, and a fraction of them ends up populating the outer regions of the halo ( $r/r_{\rm vir} \gtrsim 0.1$), spatially redistributing angular momentum in the process. As a result, the gas angular momentum profile never follows that of its virialised dark matter halo host. This generic result holds for halos of all masses at all redshifts, as radiative cooling ensures that a significant fraction of baryons remain trapped at the centre of the halos. In light of our results, we argued that the standard theory of disc formation needs to be revisited, such that gas efficiently carries its large angular momentum generated by large-scale structure motions deep inside dark matter halos, re-distributing it only in the vicinity of the disc. The redistribution process lowers the high specific angular momentum of the fresh gas by mixing it with pre-existing, misaligned central gas disc and/or circum-galactic gas, resulting in a total specific angular momentum of baryons (stars+gas) in broad agreement with the prediction of standard disc formation theory (Fall & Efstathiou, 1980; Mo et al., 1998). As a consequence, despite this injection of angular momentum enriched gas, we predict an amount for stellar discs which is in broad agreement with observations at $z = 0$.

In Chapter 5, we investigated the impact of stellar feedback on the properties of outflows in a star forming, clumpy disc galaxy. In an attempt to model more realistic kinetic stellar feedback than previous studies, we implemented continuous, collective galactic winds by considering a wide spectrum of stellar lifetimes, based on STARBURST99. Our feedback model includes not only supernova Type II (SN II), but also supernova Type Ia (SN Ia) and stellar winds from massive stars. Although the energy from stellar winds is less significant than that from SN II, stellar winds account for $\sim 50\%$ of the total mass loss, releasing metals mildly in the surrounding gas. As a consequence, the metallicity of the gas phase increases faster than the single explosion case during the evolution of an isolated clumpy disc galaxy. Except for the metallicity, other physical quantities (outflow rates and morphologies of gas density or temperature fields) do not show a significant difference between the run with our new feedback model and the run with the single explosion model. We also found that outflow rates do not strongly rely on the adopted resolution and input mass-loading factor, provided that sufficiently small mass-loading factors ($\eta_w \leq 10$) are used. High mass-loading factor ($\eta_w \geq 20$) produced slower and weaker outflows, as the energy of explosions is shared with too much gas in the early phase of the expansion. However, the

measured outflow rates are significantly smaller than star formation rates, as opposed to observations showing the two are comparable (Martin, 1999). We could only achieve such high levels of entrainment when we pumped five times more energy than the normal stellar feedback per unit mass in the ISM.

We also explored the formation of disc galaxies in a ΛCDM universe by using several high-resolution zoom simulations of a Milky way-sized galaxy. As already discussed in the literature, we found that the rotation curve is strongly peaked towards the centre of the galaxy in the absence of feedback, meaning that too many stars formed too early as our galaxy forms inside-out. Interestingly, higher resolution runs produced a more pronounced rotation peak. We attributed this to the fact better force resolution allows us to capture early star formation histories by providing deeper potential when the dark matter halo is small. As a result, low-angular momentum gas is more effectively converted into stars at high redshift in the higher resolution, leading to the formation of compact bulge at the centre. Inclusion of stellar feedback (NutSFB), which assumed 1.5 times larger energy ($\sim 1.3 \times 10^{49}\,\mathrm{erg\,s^{-1}}$) than the normal stellar feedback, is able to suppress star formation by $\sim 30\%$ at $z = 3$, compared to that from the cooling run, but it still produced a peaked rotation curve. Although inclusion of hypernovae (NutHFB) further suppresses star formation ($\sim$ 20%) at $z = 3$, it is unable to quench the formation of low-angular momentum stars enough to remove the peaked rotation curve. In general, cold filamentary accretion turns out to be impervious to the stellar feedback processes. Our results are inconsistent with the recent claim that a low star formation efficiency is essential to produce a realistic disc galaxy (Agertz et al., 2011), given that we used the same star formation efficiency and more effective kinetic feedback. Enforcing a clustered star formation (Guedes et al., 2011) does not appear to be satisfactory either, because star formation is already limited to very dense regions ($n_{\rm H} \geq 400\,\mathrm{cm^{-3}}$) in our simulations. Nonetheless, the discrepancies imply that the key to success in making a realistic galaxy is to regulate the star formation from very early on ($z > 6$), blowing a significant amount of gas out of the halo in the process. Indeed, when we computed the baryon fractions inside the dark matter halo from the feedback runs (NutSFB and NutHFB), they are significantly higher than the empirical estimates by McGaugh et al. (2010). Therefore, the stellar feedback should be more effective or another efficient source of feedback is required to solve the peaked rotation curve *and* the high baryon fractions. The question remains, however, what is the possible but physically sensible way of doing so without invoking artificial numerical treatment.

In Chapter 6, we studied stellar assembly and feedback from active galactic nuclei around the epoch of peak star formation ($1 \leq z \leq 2$), by comparing hydrodynamic simulations to rest-frame $UV$-optical galaxy colours from the Wide Field Camera 3 (WFC3) Early-Release Science (ERS) Programme. Our

Adaptive Mesh Refinement simulations included metal-dependent radiative cooling, star formation, kinetic outflows due to supernova explosions, and feedback from supermassive black holes. Our model assumes that when gas accretes onto black holes, a fraction of the energy is used to form either thermal winds or sub-relativistic momentum-imparting collimated jets, depending on the accretion rate. We found that the predicted rest-frame UV-optical colours of galaxies in the model that includes AGN feedback is in broad agreement with the observed colours of the WFC3 ERS sample at $1 \leq z \leq 2$. The predicted number of massive galaxies also matches well with observations in this redshift range. However, the massive galaxies are predicted to show higher levels of residual star formation activity than the observational estimates, suggesting the need for further suppression of star formation without significantly altering the stellar mass function. A promising solution may be to achieve a faster stellar assembly through enhanced star formation during galaxy mergers while star formation at the peak epoch is still suppressed by the AGN feedback.

## 7.2 Future works

There are several interesting areas which can be further investigated to understand the formation and evolution of galaxies.

First, the impact of active galactic nuclei on the formation of disc galaxies should be investigated. There have been many studies to comprehend the connection between super massive black holes and star formation in massive galaxies. However, no attempts has been made so far whether a relatively small black hole can impact the star formation in Milky Way-sized galaxies. This is possibly because the Milky Way black hole is much smaller than the supermassive black holes sitting in clusters. Yet this does not mean that the impact of AGN feedback is negligible. In fact, in the case of Milky way, the total energy available from stellar feedback processes is comparable to that from the intermediate mass black hole if the mass-to-energy conversion efficiency of 0.1 is assumed. Given that AGN feedback is more bursty than stellar feedback processes, it cannot be simply concluded that stellar feedback processes would be more efficient than AGN feedback in Milky Way-type galaxies. An advantage of AGN feedback from a numerical point of view is that since a large amount of energy is released in a short period of time, spurious numerical radiative cooling may not be as important an issue as for stellar feedback (e.g. Dalla Vecchia & Schaye, 2012). This will be of great importance in understanding the missing baryon problem as well as the formation of a realistic disc galaxy.

The next step towards simulating more realistic galaxy is to include magnetic fields. Although we

have ignored the impact of magnetic fields in the NUT simulations for simplicity, magnetic fields can provide an additional support against the gas cooling through magnetic pressure. For example, the magnetic pressure for gas having the magnetic field strength of 1$\mu$G is $\sim 4 \times 10^{-14}$ dyn cm$^{-2}$. This is comparable to the thermal pressure of gas with $n_{\rm H} = 0.1$ and $T = 10^4\,K$. Since the magnetic pressure scales as $B^2$, locally enhanced magnetic fields by supernova ejecta may be even more effective at suppressing the cooling towards the galaxy centre. This may be a more physically sensible alternative to disabling atomic cooling for a brief period of time in the dense interstellar medium (e.g. Stinson et al., 2006).

Finally, chemo-hydrodynamic simulations will shed light on the stellar assembly history of elliptical galaxies. As discussed in Section 5, [$\alpha$/Fe] abundance ratios convey important information about the timescale of star formation. Yet none of the models based on the hierarchical formation scenario could explain high [$\alpha$/Fe] ratios observed in massive elliptical galaxies (Trager et al., 2000; Thomas et al., 2005) with the standard Salpeter-type initial mass function (Thomas, 1999; Pipino et al., 2009; Arrigoni et al., 2010). Arrigoni et al. (2010) argued that in order to obtain the high ratios, the slope of the initial mass function should be reduced so that more massive stars can produce $\alpha$ elements. Unfortunately, observational studies favour bottom-heavy initial mass functions for elliptical galaxies (van Dokkum & Conroy, 2010; Cappellari et al., 2012), implying that the high [$\alpha$/Fe] ratios is likely to be associated with bursty star formation histories. Therefore, confronting chemical abundances predicted from cosmological hydrodynamic simulations to the observed [$\alpha$/Fe] ratios will be useful to constrain the stellar assembly histories of elliptical galaxies. In particular, given the lack of existing numerical studies, the experiment will also provide insight into the chemical mixing on small scales. The chemical enrichment in H, He, C, N, O, Mg, and Fe is already implemented based on STARBURST99, and we are currently running the simulations.

# Appendix A

# Appendix

## A.1 Euler equations in the super comoving coordinate system

RAMSES uses the super comoving coordinate system to account for the cosmological expansion. We derive Equations 2.25–2.29 in this section (see also Doumler & Knebe, 2010).

The super comoving coordinate system is based on the following change of variables.

$$\boxed{\begin{aligned} d\tilde{t} &\equiv H_0 \frac{dt}{a^2} \\ \tilde{\mathbf{r}} &\equiv \frac{\mathbf{r}}{aL} \\ \tilde{\rho} &= \frac{a^3}{\rho_c \Omega_m} \rho \end{aligned}}$$

where $\rho_c$ and $\Omega_m$ are the critical density of the Universe and the matter density parameter at $z = 0$, respectively.

The time and spatial derivatives in the super comoving coordinate system can be written as

$$\begin{aligned} \nabla_r f|_t &= \frac{1}{aL} \nabla_{\tilde{r}} f \Big|_{\tilde{t}} \\ \frac{\partial f}{\partial t}\Big|_{\mathbf{r}} &= \frac{1}{a^2 H_0} \frac{\partial f}{\partial \tilde{t}}\Big|_{\mathbf{r}} = \frac{1}{a^2 H_0} \left( \frac{\partial f}{\partial t}\Big|_{\tilde{\mathbf{r}}} + \frac{\partial \tilde{\mathbf{r}}}{\partial \tilde{t}} \cdot \tilde{\nabla} f \Big|_{\tilde{t}} \right) \\ &= \frac{1}{a^2 H_0} \left( \frac{\partial f}{\partial t}\Big|_{\tilde{\mathbf{r}}} - \mathcal{H} \tilde{\mathbf{r}} \cdot \tilde{\nabla} f \Big|_{\tilde{t}} \right), \end{aligned}$$

where $\mathcal{H} \equiv da/d\tilde{t}/a$.

Rewriting the velocity ($v$), pressure ($p$), and energy ($\varepsilon$) in the super comoving coordinate system, we

have

$$\begin{aligned}
\tilde{\mathbf{v}} &= \frac{d\tilde{\mathbf{r}}}{d\tilde{t}} = \frac{a}{H_0 L}\left(\mathbf{u} - H\mathbf{r}\right) = \frac{a}{H_0 L}\mathbf{v} \\
\tilde{p} &= \frac{\tilde{n} m \tilde{\mathbf{v}}^2}{3} = \frac{a^5}{\rho_c \Omega_m H_0^2 L^2} p \\
\tilde{\varepsilon} &= \frac{\tilde{p}}{(\gamma-1)\tilde{\rho}} = \frac{a^2}{H_0^2 L^2}\varepsilon,
\end{aligned}$$

where $\mathbf{u} = d\mathbf{r}/dt$ and $\mathbf{v} = d\mathbf{x}/dt$.

The gravitational potential in the super comoving coordinate system can be written as

$$\begin{aligned}
\frac{d\tilde{\mathbf{v}}}{d\tilde{t}} &= \frac{a^2}{H_0}\frac{d\tilde{\mathbf{v}}}{dt} = \frac{a^2}{H_0}\frac{d}{dt}\left(\frac{a\mathbf{u} - \dot{a}\mathbf{r}}{H_0 L}\right) = \frac{a^2}{H_0^2 L}\left(a\frac{d\mathbf{u}}{dt} - \ddot{a}\mathbf{r}\right) \\
&= \frac{a^2}{H_0^2 L}\left(-\frac{1}{L}\tilde{\nabla}\phi - a\ddot{a}L\tilde{\mathbf{r}}\right) \\
&= \frac{a^2}{H_0^2 L}\left[-\frac{1}{L}\tilde{\nabla}\phi + a\ddot{a}L\left(-\tilde{\nabla}\frac{1}{2}\tilde{r}^2\right)\right] \\
&= -\tilde{\nabla}\left[\frac{a^2}{H_0^2 L^2}\left(\phi + \frac{1}{2}a\ddot{a}L^2\tilde{r}^2\right)\right] \\
&= -\tilde{\nabla}\tilde{\phi},
\end{aligned}$$

and

$$\boxed{\phi = \frac{H_0^2 L^2}{a^2}\tilde{\phi} - \frac{1}{2}a\ddot{a}L^2\tilde{r}^2.} \tag{A.1}$$

### A.1.1 Continuity Equation

The continuity equation means mass conservation and reads

$$\frac{\partial \rho}{\partial t} + \nabla\cdot(\rho\mathbf{u}) = 0. \tag{A.2}$$

The first and second terms can be replaced with the super comoving time derivative and the super comoving density as

$$\begin{aligned}
\left.\frac{\partial\rho}{\partial t}\right|_{\mathbf{r}} &= \frac{H_0}{a^2}\left(\left.\frac{\partial\rho}{\partial\tilde{t}}\right|_{\tilde{\mathbf{r}}} - \mathcal{H}\tilde{\mathbf{r}}\cdot\tilde{\nabla}\rho\Big|_{\tilde{t}}\right) \\
&= \frac{H_0}{a^2}\left[\left(\frac{\rho_c\Omega_m}{a^3}\left.\frac{\partial\tilde{\rho}}{\partial\tilde{t}}\right|_{\tilde{\mathbf{r}}} - 3\tilde{\rho}\frac{\rho_c\Omega_m}{a^4}\frac{da}{d\tilde{t}}\right) - \mathcal{H}\frac{\rho_c\Omega_m}{a^3}\tilde{\mathbf{r}}\cdot\tilde{\nabla}\tilde{\rho}\Big|_{\tilde{t}}\right] \\
&= \frac{\rho_c\Omega_m H_0}{a^5}\left(\left.\frac{\partial\tilde{\rho}}{\partial\tilde{t}}\right|_{\tilde{\mathbf{r}}} - 3\mathcal{H}\tilde{\rho} - \mathcal{H}\tilde{\mathbf{r}}\cdot\tilde{\nabla}\tilde{\rho}\Big|_{\tilde{t}}\right),
\end{aligned}$$

and

$$\begin{aligned}\nabla \cdot (\rho \mathbf{u}) &= \frac{1}{aL}\tilde{\nabla} \cdot \left[\frac{\rho_c \Omega_m}{a^3}\tilde{\rho}\frac{H_0 L}{a}\left(\tilde{\mathbf{v}} + \mathcal{H}\tilde{\mathbf{r}}\right)\right] \\ &= \frac{\rho_c \Omega_m H_0}{a^5}\tilde{\nabla} \cdot (\tilde{\rho}\tilde{\mathbf{v}} + \mathcal{H}\tilde{\rho}\tilde{\mathbf{r}}) \\ &= \frac{\rho_c \Omega_m H_0}{a^5}\left(\tilde{\nabla} \cdot \tilde{\rho}\tilde{\mathbf{v}} + \mathcal{H}\tilde{\mathbf{r}} \cdot \tilde{\nabla}\tilde{\rho} + 3\mathcal{H}\tilde{\rho}\right).\end{aligned}$$

Here we have used the relation $\mathbf{u} = H_0 L(\tilde{\mathbf{v}} + \mathcal{H}\tilde{\mathbf{r}})/a$ and $H = H_0\mathcal{H}/a^2$. Putting these into Equation A.2, we have

$$\boxed{\frac{\partial \tilde{\rho}}{\partial \tilde{t}} + \tilde{\nabla} \cdot (\tilde{\rho}\tilde{\mathbf{v}}) = 0.} \tag{A.3}$$

### A.1.2 Momentum Equation

The second Euler equation is

$$\frac{\partial (\rho \mathbf{u})}{\partial t} + \nabla \cdot (\rho \mathbf{u} \otimes \mathbf{u} + p\mathbf{I}) = -\rho \nabla \Phi. \tag{A.4}$$

As has been done in the previous section, each part is transformed to the variables in the super comoving coordinate system as follows. The first term in the above equation can be written as

$$\begin{aligned}\left.\frac{\partial(\rho \mathbf{u})}{\partial t}\right|_{\mathbf{r}} &= \rho \left.\frac{\partial \mathbf{u}}{\partial t}\right|_{\mathbf{r}} + \mathbf{u}\left.\frac{\partial \rho}{\partial t}\right|_{\mathbf{r}} = \rho \left.\frac{\partial \mathbf{u}}{\partial t}\right|_{\mathbf{r}} - \mathbf{u}\nabla \cdot (\rho \mathbf{u}) \\ &= \frac{\rho_c \Omega_m}{a^3}\tilde{\rho}\left(\left.\frac{\partial \mathbf{u}}{\partial t}\right|_{\tilde{\mathbf{r}}} - \frac{\mathcal{H}H_0}{a^2}\tilde{\mathbf{r}} \cdot \left.\tilde{\nabla}\mathbf{u}\right|_t\right) - \mathbf{u}\nabla \cdot (\rho \mathbf{u}) \\ &= \frac{\rho_c \Omega_m}{a^3}\tilde{\rho}\left\{\frac{\partial}{\partial t}\left[\frac{H_0 L}{a}\left(\tilde{\mathbf{v}} + \mathcal{H}\tilde{\mathbf{r}}\right)\right]_{\tilde{\mathbf{r}}} - K\right\} - \mathbf{u}\nabla \cdot (\rho \mathbf{u}) \\ &= \frac{\rho_c \Omega_m}{a^3}\tilde{\rho}\left(-\frac{H_0 L}{a^2}\dot{a}\tilde{\mathbf{v}} + \frac{H_0^2 L}{a^3}\frac{\partial \tilde{\mathbf{v}}}{\partial \tilde{t}} + L\ddot{a}\tilde{\mathbf{r}} - K\right) - \mathbf{u}\nabla \cdot (\rho \mathbf{u})\end{aligned}$$

where $K \equiv H\tilde{\mathbf{r}} \cdot \tilde{\nabla}\mathbf{u}$. The second part of the equation can be split into three terms as

$$\nabla \cdot (\rho \mathbf{u} \otimes \mathbf{u} + p\mathbf{I}) = \nabla p + \mathbf{u}\nabla \cdot (\rho \mathbf{u}) + \rho \mathbf{u} \cdot \nabla \mathbf{u},$$

where the last term in the above equation is

$$\begin{aligned}\rho\mathbf{u}\cdot\nabla\mathbf{u} &= \rho\left[\frac{H_0 L}{a}(\tilde{\mathbf{v}}+\mathcal{H}\tilde{\mathbf{r}})\cdot\frac{1}{aL}\tilde{\nabla}\mathbf{u}\right]\\ &= \frac{\rho_c\Omega_m}{a^3}\tilde{\rho}\left(\frac{H_0\tilde{\mathbf{v}}\cdot\tilde{\nabla}\mathbf{u}}{a^2}+\frac{H_0\mathcal{H}\tilde{\mathbf{r}}\cdot\tilde{\nabla}\mathbf{u}}{a^2}\right)\\ &= \frac{\rho_c\Omega_m}{a^3}\tilde{\rho}\left[\frac{H_0^2 L}{a^3}\tilde{\mathbf{v}}\cdot\tilde{\nabla}(\tilde{\mathbf{v}}+\mathcal{H}\tilde{\mathbf{r}})+K\right]\\ &= \frac{\rho_c\Omega_m}{a^3}\tilde{\rho}\left(\frac{H_0^2 L}{a^3}\tilde{\mathbf{v}}\cdot\tilde{\nabla}\tilde{\mathbf{v}}+\frac{H_0 L}{a^2}\dot{a}\tilde{\mathbf{v}}+K\right).\end{aligned}$$

Rewriting the left hand side of Equation A.4, we find

$$\begin{aligned}\text{LHS (Eq. A.4)} =& \frac{\rho_c\Omega_m}{a^3}\tilde{\rho}\left(\frac{H_0^2 L}{a^3}\frac{\partial\tilde{\mathbf{v}}}{\partial\tilde{t}}+\frac{H_0^2 L}{a^3}\tilde{\mathbf{v}}\cdot\tilde{\nabla}\tilde{\mathbf{v}}+L\ddot{a}\tilde{\mathbf{r}}\right)\\ &+\frac{\rho_c\Omega_m H_0^2 L}{a^6}\tilde{\nabla}\tilde{p},\end{aligned}$$

and thus

$$\begin{aligned}-\rho\nabla\Phi &= -\frac{\rho_c\Omega_m}{a^3}\tilde{\rho}\frac{1}{aL}\tilde{\nabla}\left(\frac{H_0^2 L^2}{a^2}\tilde{\phi}-\frac{1}{2}a\ddot{a}L^2\tilde{r}^2\right)\\ &= -\frac{\rho_c\Omega_m}{a^6}\tilde{\rho}H_0^2 L\tilde{\nabla}\tilde{\phi}+\frac{\rho_c\Omega_m}{a^3}\tilde{\rho}\,\ddot{a}L\tilde{\mathbf{r}}.\end{aligned}$$

Putting these into Equation A.4, we obtain

$$\tilde{\rho}\frac{H_0^2 L}{a^3}\frac{\partial\tilde{\mathbf{v}}}{\partial\tilde{t}}+\tilde{\rho}\frac{H_0^2 L}{a^3}\tilde{\mathbf{v}}\cdot\tilde{\nabla}\tilde{\mathbf{v}}+\frac{H_0^2 L}{a^3}\tilde{\nabla}\tilde{p}=-\tilde{\rho}\frac{H_0^2 L}{a^3}\tilde{\nabla}\tilde{\phi},$$

and

$$\boxed{\tilde{\rho}\frac{\partial\tilde{\mathbf{v}}}{\partial\tilde{t}}+\tilde{\rho}\tilde{\mathbf{v}}\cdot\tilde{\nabla}\tilde{\mathbf{v}}+\tilde{\nabla}\tilde{p}=-\tilde{\rho}\tilde{\nabla}\tilde{\phi}} \tag{A.5}$$

We recover the same form as Equation A.4.

### A.1.3 Energy equation

Let us write the thermal part of the energy equation.

$$\frac{\partial\varepsilon}{\partial t}+\mathbf{u}\cdot\nabla\varepsilon=-\frac{p}{\rho}\nabla\cdot\mathbf{u} \tag{A.6}$$

Rewriting each component in the super comoving coordinate system, we have

$$\begin{aligned}\left.\frac{\partial\varepsilon}{\partial t}\right|_{\mathbf{r}} &= \frac{H_0}{a^2}\left[\frac{\partial}{\partial\tilde{t}}\left(\frac{H_0^2L^2}{a^2}\tilde{\varepsilon}\right)\Big|_{\tilde{\mathbf{r}}} - \mathcal{H}\tilde{\mathbf{r}}\cdot\left(\tilde{\nabla}\tilde{\varepsilon}\right)\Big|_{\tilde{t}}\right] \\ &= \frac{H_0^3L^2}{a^4}\left(-2\mathcal{H}\tilde{\varepsilon} + \frac{\partial\tilde{\varepsilon}}{\partial\tilde{t}} - \mathcal{H}\tilde{\mathbf{r}}\cdot\tilde{\nabla}\tilde{\varepsilon}\right),\end{aligned}$$

$$\begin{aligned}\mathbf{u}\cdot\nabla\varepsilon &= \frac{H_0L}{a}\left(\tilde{\mathbf{v}}+\mathcal{H}\tilde{\mathbf{r}}\right)\cdot\frac{1}{aL}\tilde{\nabla}\left(\frac{H_0^2L^2}{a^2}\tilde{\varepsilon}\right)_{\tilde{t}} \\ &= \frac{H_0^3L^2}{a^4}\left(\tilde{\mathbf{v}}\cdot\tilde{\nabla}\tilde{\varepsilon} + \mathcal{H}\tilde{\mathbf{r}}\cdot\tilde{\nabla}\tilde{\varepsilon}\right),\end{aligned}$$

and

$$\begin{aligned}-\frac{p}{\rho}\nabla\cdot\mathbf{u} &= -\frac{\rho_c\Omega_m H_0^2L^2}{a^5}\tilde{p}\frac{a^3}{\rho_c\Omega_m\tilde{\rho}}\frac{1}{aL}\tilde{\nabla}\cdot\frac{H_0L}{a}\left(\tilde{\mathbf{v}}+\mathcal{H}\tilde{\mathbf{r}}\right) \\ &= -\frac{H_0^3L^2}{a^4}\frac{\tilde{p}}{\tilde{\rho}}\tilde{\nabla}\cdot\left(\tilde{\mathbf{v}}+\mathcal{H}\tilde{\mathbf{r}}\right).\end{aligned}$$

Putting these into Equation A.6, we obtain

$$-2\mathcal{H}\tilde{\varepsilon} + \frac{\partial\tilde{\varepsilon}}{\partial\tilde{t}} + \tilde{\mathbf{v}}\cdot\tilde{\nabla}\tilde{\varepsilon} = -\frac{\tilde{p}}{\tilde{\rho}}\tilde{\nabla}\cdot\left(\tilde{\mathbf{v}}+\mathcal{H}\tilde{\mathbf{r}}\right)$$

$$\boxed{\frac{\partial\tilde{\varepsilon}}{\partial\tilde{t}} + \tilde{\mathbf{v}}\cdot\tilde{\nabla}\tilde{\varepsilon} + (3\gamma-5)\mathcal{H}\tilde{\varepsilon} = -\frac{\tilde{p}}{\tilde{\rho}}\tilde{\nabla}\cdot\tilde{\mathbf{v}}} \tag{A.7}$$

Here we have used $\tilde{p} = (\gamma-1)\tilde{\rho}\tilde{\varepsilon}$.

Multiplying Equation A.5 to $\tilde{\mathbf{v}}$ and arranging the terms, we have

$$\tilde{\rho}\tilde{\mathbf{v}}\cdot\frac{\partial\tilde{\mathbf{v}}}{\partial\tilde{t}} + \tilde{\rho}\tilde{\mathbf{v}}\cdot\left(\tilde{\mathbf{v}}\cdot\tilde{\nabla}\tilde{\mathbf{v}}\right) = -\tilde{\rho}\tilde{\mathbf{v}}\cdot\tilde{\nabla}\tilde{\phi} - \tilde{\mathbf{v}}\cdot\tilde{\nabla}\tilde{p}$$

$$\begin{aligned}\frac{\partial}{\partial\tilde{t}}\left(\frac{1}{2}\tilde{\rho}\tilde{v}^2\right) - \frac{1}{2}\tilde{v}^2\frac{\partial\tilde{\rho}}{\partial\tilde{t}} + \frac{1}{2}\tilde{\nabla}\cdot\left(\rho\tilde{v}^2\tilde{\mathbf{v}}\right) - \frac{1}{2}\tilde{v}^2\tilde{\nabla}\cdot\left(\tilde{\rho}\tilde{\mathbf{v}}\right) \\ = -\tilde{\nabla}\cdot\left(\tilde{\rho}\tilde{\mathbf{v}}\tilde{\phi}\right) + \tilde{\phi}\tilde{\nabla}\cdot\left(\tilde{\rho}\tilde{\mathbf{v}}\right) - \tilde{\nabla}\cdot\left(\tilde{\rho}\tilde{\mathbf{v}}\right) + \tilde{p}\tilde{\nabla}\cdot\tilde{\mathbf{v}} \\ = \frac{\partial}{\partial\tilde{t}}\left(\frac{1}{2}\tilde{\rho}\tilde{v}^2\right) + \frac{1}{2}\tilde{\nabla}\cdot\left(\rho\tilde{v}^2\tilde{\mathbf{v}}\right)\end{aligned}$$

$$\begin{aligned}
\frac{\partial}{\partial\tilde{t}}\left(\frac{1}{2}\tilde{\rho}\tilde{v}^2\right) &= -\tilde{\nabla}\cdot\left(\tilde{\rho}\tilde{\mathbf{v}}\tilde{\phi}+\tilde{p}\tilde{\mathbf{v}}+\frac{1}{2}\tilde{\rho}\tilde{v}^2\tilde{\mathbf{v}}\right)-\tilde{\phi}\frac{\partial\tilde{\rho}}{\partial\tilde{t}}+\tilde{p}\tilde{\nabla}\cdot\tilde{\mathbf{v}}\\
&= -\tilde{\nabla}\cdot\left(\tilde{\rho}\tilde{\mathbf{v}}\tilde{\phi}+\tilde{p}\tilde{\mathbf{v}}+\frac{1}{2}\tilde{\rho}\tilde{v}^2\tilde{\mathbf{v}}\right)-\tilde{\phi}\frac{\partial\tilde{\rho}}{\partial\tilde{t}}-\tilde{\rho}\frac{\partial\tilde{\varepsilon}}{\partial\tilde{t}}-\tilde{\rho}\tilde{\mathbf{v}}\cdot\tilde{\nabla}\tilde{\varepsilon}-\tilde{\rho}\tilde{\varepsilon}\mathcal{H}(3\gamma-5)\\
&= -\tilde{\nabla}\cdot(\sim)-\tilde{\phi}\frac{\partial\tilde{\rho}}{\partial\tilde{t}}-\left(\frac{\partial(\tilde{\rho}\tilde{\varepsilon})}{\partial\tilde{t}}-\tilde{\varepsilon}\frac{\partial\tilde{\rho}}{\partial\tilde{t}}\right)-\left[\tilde{\nabla}\cdot(\tilde{\rho}\tilde{\varepsilon}\tilde{\mathbf{v}})-\tilde{\varepsilon}\tilde{\nabla}\cdot(\tilde{\rho}\tilde{\mathbf{v}})\right]-\tilde{\rho}\tilde{\varepsilon}\mathcal{H}(3\gamma-5)\\
&= -\tilde{\nabla}\cdot\left(\tilde{\rho}\tilde{\mathbf{v}}\tilde{\phi}+\tilde{p}\tilde{\mathbf{v}}+\frac{1}{2}\tilde{\rho}\tilde{v}^2\tilde{\mathbf{v}}+\tilde{\rho}\tilde{\varepsilon}\tilde{\mathbf{v}}\right)-\tilde{\phi}\frac{\partial\tilde{\rho}}{\partial\tilde{t}}-\frac{\partial\left(\tilde{\rho}\tilde{\varepsilon}\right)}{\partial\tilde{t}}-\tilde{\rho}\tilde{\varepsilon}\mathcal{H}(3\gamma-5)
\end{aligned}$$

Manipulating these terms finally yields

$$\begin{aligned}
\frac{\partial}{\partial\tilde{t}}\left(\tilde{\rho}\tilde{\varepsilon}+\frac{1}{2}\tilde{\rho}\tilde{v}^2\right)=\frac{\partial}{\partial\tilde{t}}\left(\tilde{\rho}\tilde{e}\right) &= -\tilde{\nabla}\cdot\left[\tilde{\rho}\tilde{\phi}\tilde{\mathbf{v}}+\left(\tilde{\rho}\tilde{e}+\tilde{p}\right)\tilde{\mathbf{v}}\right]-\tilde{\phi}\frac{\partial\tilde{\rho}}{\partial\tilde{t}}-\tilde{\rho}\tilde{\varepsilon}\mathcal{H}(3\gamma-5)\\
&= -\tilde{\nabla}\cdot\left[\tilde{\rho}\tilde{\phi}\tilde{\mathbf{v}}+\left(\tilde{\rho}\tilde{e}+\tilde{p}\right)\tilde{\mathbf{v}}\right]+\tilde{\phi}\tilde{\nabla}\cdot(\tilde{\rho}\tilde{\mathbf{v}})-\tilde{\rho}\tilde{\varepsilon}\mathcal{H}(3\gamma-5),
\end{aligned}$$

and thus

$$\boxed{\frac{\partial}{\partial\tilde{t}}\left(\tilde{\rho}\tilde{e}\right)+\tilde{\nabla}\cdot\left[\left(\tilde{\rho}\tilde{e}+\tilde{p}\right)\tilde{\mathbf{v}}\right]=-\tilde{\rho}\tilde{\mathbf{v}}\cdot\tilde{\nabla}\tilde{\phi}-\tilde{\rho}\tilde{\varepsilon}\mathcal{H}(3\gamma-5)} \tag{A.8}$$

### A.1.4 Poisson equation

To obtain the Poisson equation in the super comoving coordinate system, we consider the acceleration given by the Friedmann equation,

$$\begin{aligned}
\frac{\ddot{a}}{a} &= -\frac{4\pi G}{3}\left(\bar{\rho}_m+\frac{3p}{c^2}\right)+\frac{\Lambda c^2}{3}\\
&= -\frac{4\pi G}{3}\left(\bar{\rho}_m-\rho_\Lambda\right).
\end{aligned}$$

The dark energy should also be considered in the Poisson equation as

$$\nabla^2\phi = 4\pi G(\rho_m-\rho_\Lambda).$$

Using Equation A.1, this can be written as

$$\begin{aligned}
\nabla^2\phi &= \frac{1}{a^2L^2}\tilde{\nabla}^2\left(\frac{H_0^2L^2}{a^2}\tilde{\phi}-\frac{1}{2}a\ddot{a}L^2\tilde{r}^2\right)\\
&= \frac{H_0^2}{a^4}\tilde{\nabla}^2\tilde{\phi}-\frac{\ddot{a}}{2a}\tilde{\nabla}^2\tilde{r}^2\\
&= \frac{H_0^2}{a^4}\tilde{\nabla}^2\tilde{\phi}-3\frac{\ddot{a}}{a}\\
&= \frac{H_0^2}{a^4}\tilde{\nabla}^2\tilde{\phi}+4\pi G\left(\bar{\rho}_m-\rho_\Lambda\right),
\end{aligned}$$

and

$$4\pi G(\rho_m - \rho_\Lambda) = \frac{H_0^2}{a^4}\tilde{\nabla}^2\tilde{\phi} + 4\pi G\left(\bar{\rho}_m - \rho_\Lambda\right)$$
$$\tilde{\nabla}^2\tilde{\phi} = \frac{4\pi G a^4}{H_0^2}\left(\rho_m - \bar{\rho}_m\right) = \frac{3}{2}a\Omega_m\left(\tilde{\rho} - 1\right).$$

Thus,

$$\boxed{\tilde{\nabla}^2\tilde{\phi} = \frac{3}{2}a\Omega_m\left(\tilde{\rho} - 1\right)} \tag{A.9}$$

## A.2 Bulge-to-Disc decomposition

In Section 4, we provide the bulge-to-disc ratio ($B/D$) of the NutCOLR galaxy, which is obtained by fitting the $I$-band surface brightness profile of the galaxy. Specifically, we assume that the profile can be approximated by the combination of an exponential profile and a sérsic profile with an index $n_s$, as

$$\mu(r) = [\mu_d + 1.086\,(r/r_d)] + \{\mu_b + 1.086\,\beta_n\,[(r/r_b)^{1/n_s} - 1]\},$$

where $r_d$ is the disc scale length, $\mu_0$ is the central surface light intensity of the disc, $\mu_b$ is the central surface light of the bulge, and $r_b$ is the scale length of the bulge. $\beta_n$ is the shape-dependent parameter that can be obtained by solving $\Gamma(2n_s) = 2\gamma(2n_s, \beta_n)$, where $\Gamma$ is the gamma function and $\gamma$ is the incomplete gamma function, and it can be approximated as $\beta_n \approx 1.9992n_s - 0.3271$ (Capaccioli, 1989). The total luminosity of the exponential disc or the bulge is

$$L_{\rm disc} = 2\pi 10^{-\mu_d/2.5}\,r_d^2$$
$$L_{\rm bulge} = 2\pi 10^{-\mu_b/2.5}\,r_b^2\,n_s\Gamma(2n_s)/\beta_n^{2n_s}.$$

$(B/D)_I$ can be computed as $L_{\rm bulge}/L_{\rm disc}$. We present the bulge-to-disc decomposition for the NutCOLR galaxy at $z = 0$ in Fig. A.1.

Also included in the right panel is the bulge-to-disc decomposition on stellar surface density. In this case, the profile is assumed to be

$$\Sigma(r) = \Sigma_d\,\exp[-(r/r_d)] + \Sigma_b\,\exp[-(r/r_b)^{1/n_s}]$$

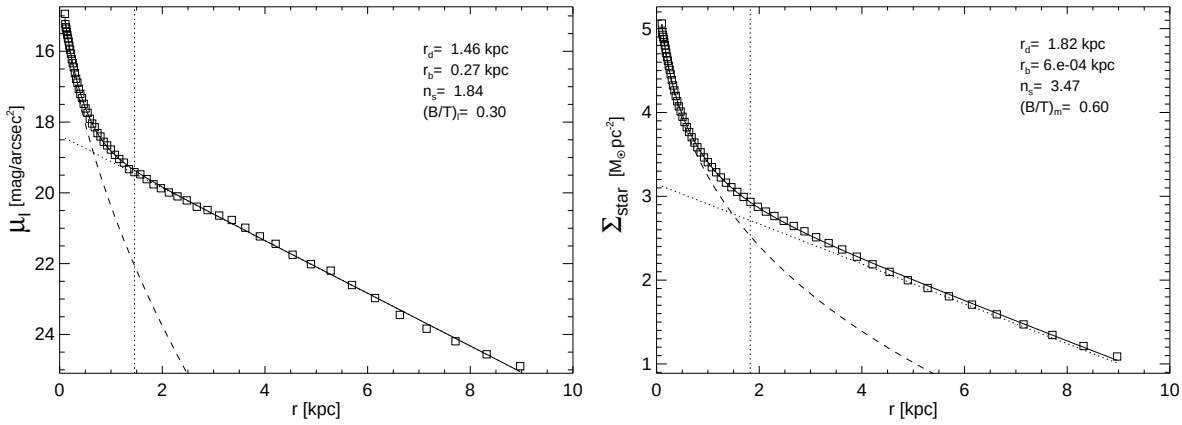


Figure A.1: *Left:* $I$-band bulge-to-disc decomposition of the NutCOLR galaxy at $z = 0$. The profile is computed for the face-on configuration. A vertical dotted line denotes the disc scale-length ($r_d$). Other derived quantities, the bulge scale-length ($r_b$), sérsic index ($n_s$), and the bulge-to-total ratio ($B/T$), are shown in the panel. No dust extinction is applied. *Right:* Bulge-to-disc decomposition on stellar surface density.

with

$$M_{\rm disc} = 2\pi\Sigma_d\, r_d^2$$

$$M_{\rm bulge} = 2\pi\Sigma_b\, r_b^2\, n_s\Gamma(2n_s).$$

## A.3 Mass accretion histories, and misalignment of the Nut galaxy

In the main body of the text, we show the time evolution of the specific angular momentum for the various components of a Milky Way-like DM halo (Figure 4.4). In particular, in Section 4.2, we argue that the difference in angular momentum between the central gas and the gas in the outer region of the halo arises because the mass of the central gas, which is composed of low angular momentum gas accreted at earlier times, is not negligible compared to the mass of accreting gas, and therefore reflects the history of gas accretion. To substantiate this claim, we include the mass assembly history of the various components in Figure A.2. As can be seen, the amount of gas in the central region ($M_{\rm gas} - M_{\rm gas}(r > 0.1r_{\rm vir})$) is comparable to the gas mass in the outer region ($r > 0.1r_{\rm vir}$) at all times. Thus, even if the newly accreted gas carries a larger amount of specific angular momentum, one expects that there will be a non-negligible time-delay for the entire central region to be spun to the same level. Note that by multiplying Figure A.2 with Figure 4.4, one can recover the total amount of angular momentum of each component.

Finally, bearing in mind its vector nature, we include the time evolution of the misalignment angle

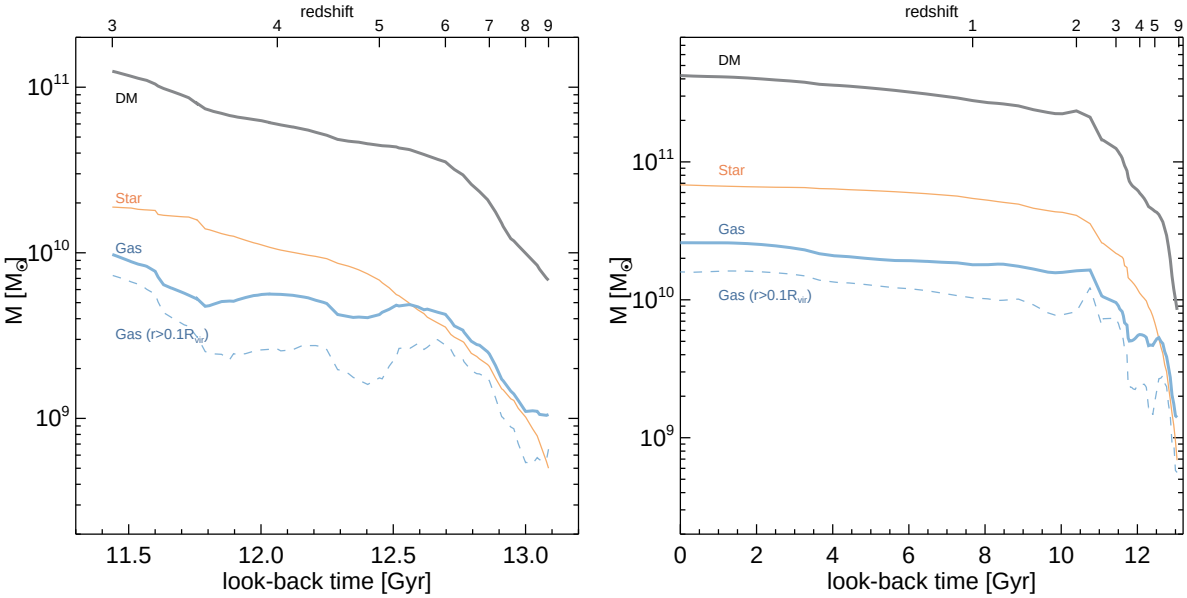


Figure A.2: Mass assembly histories of the various components in the NutFB run (left) and the NutCO run (right). Stars, dark matter, and gas in satellite galaxies are included in the measurement. Note that the amount of gas mass in the central region ($M_{\rm gas} - M_{\rm gas}(r > 0.1r_{\rm vir})$) is comparable (a factor 2-3 lower) to the gas mass in the outer region at all times.

between the total angular momentum of various components in Figure A.3. It can be seen that, at least at $z > 1$, baryons and dark matter are less aligned in the cooling run (solid and dotted blue curves) than in the adiabatic case (red solid line). Perhaps more importantly, the misalignment between the stellar angular momentum and the freshly accreted gas ($r > 0.1r_{\rm vir}$, dashed blue line) turns out to be even larger than these, implying that most of the gas angular momentum has to be redistributed in the vicinity of the galactic disc.

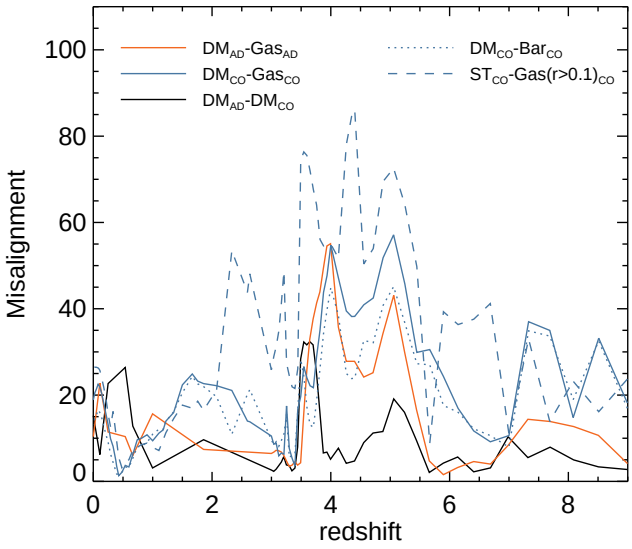


Figure A.3: Misalignment angle between angular momentum vectors of various components (DM: dark matter, Gas: gas; Bar: baryons; ST: star) from the the adiabatic run (AD) and the cooling run (CO). Note that the misalignment between stars ($r < 0.1r_{\rm vir}$) and outer gas ($r > 0.1r_{\rm vir}$) in the cooling run is more significant than that between gas and dark matter in the adiabatic run.

# References


Abadi M. G., Navarro J. F., Steinmetz M., Eke V. R., 2003, The Astrophysical Journal, 597, 21

Adams W. S., Burwell C. G., 1920, The Astrophysical Journal, 51, 121

Adams W. S., MacCormack E., 1935, The Astrophysical Journal, 81, 119

Adelberger K. L., Steidel C. C., Shapley A. E., Pettini M., 2003, The Astrophysical Journal, 584, 45

Agertz O., Moore B., Stadel J., Potter D., Miniati F., Read J., Mayer L., Gawryszczak A., Kravtsov A., Nordlund Å., Pearce F., Quilis V., Rudd D., Springel V., Stone J., Tasker E., Teyssier R., Wadsley J., Walder R., 2007, Monthly Notices of the Royal Astronomical Society, 380, 963

Agertz O., Teyssier R., Moore B., 2011, Monthly Notices of the Royal Astronomical Society, 410, 1391

Aguirre A., Hernquist L., Schaye J., Katz N., Weinberg D. H., Gardner J., 2001, The Astrophysical Journal, 561, 521

Anderson M. E., Bregman J. N., 2010, The Astrophysical Journal, 714, 320

Arnett D., 1996, Supernovae and Nucleosynthesis: An Investigation of the History of Matter, from the Big Bang to the Present , 1996. Princeton University Press

Arrigoni M., Trager S. C., Somerville R. S., Gibson B. K., 2010, Monthly Notices of the Royal Astronomical Society, 402, 173

Asplund M., Grevesse N., Sauval A. J., Scott P., 2009, Annual Review of Astronomy and Astrophysics, 47, 481

Aubert D., Pichon C., Colombi S., 2004, Monthly Notices of the Royal Astronomical Society, 352, 376

Avila-Reese V., Firmani C., Hernández X., 1998, The Astrophysical Journal, 505, 37

Bacon R. et al., 2006, in Society of Photo-Optical Instrumentation Engineers (SPIE) Conference Series, Vol. 6269, Society of Photo-Optical Instrumentation Engineers (SPIE) Conference Series

Barger A. J., Cowie L. L., Sanders D. B., Fulton E., Taniguchi Y., Sato Y., Kawara K., Okuda H., 1998, Nature, 394, 248

Barnes J., Hut P., 1986, Nature, 324, 446

Beals C. S., 1929, Monthly Notices of the Royal Astronomical Society, 90, 202

Becker R. H. et al., 2001, The Astronomical Journal, 122, 2850

Bell E. F., McIntosh D. H., Katz N., Weinberg M. D., 2003, The Astrophysical Journal Supplement Series, 149, 289

Benson A. J., Bower R. G., Frenk C. S., Lacey C. G., Baugh C. M., Cole S., 2003, The Astrophysical Journal, 599, 38

Benson A. J., Lacey C. G., Baugh C. M., Cole S., Frenk C. S., 2002, Monthly Notices of the Royal Astronomical Society, 333, 156

Bertschinger E., 2001, The Astrophysical Journal Supplement Series, 137, 1

Bett P., Eke V., Frenk C. S., Jenkins A., Helly J., Navarro J., 2007, Monthly Notices of the Royal Astronomical Society, 376, 215

Bigiel F., Leroy A., Walter F., Brinks E., de Blok W. J. G., Madore B., Thornley M. D., 2008, The Astronomical Journal, 136, 2846

Binney J., 1977, The Astrophysical Journal, 215, 483

Binney J., 2004, Monthly Notices of the Royal Astronomical Society, 347, 1093

Binney J., Tabor G., 1995, Monthly Notices of the Royal Astronomical Society, 276, 663

Birnboim Y., Dekel A., 2003, Monthly Notices of the Royal Astronomical Society, 345, 349

Bîrzan L., Rafferty D. A., McNamara B. R., Wise M. W., Nulsen P. E. J., 2004, The Astrophysical Journal, 607, 800

Blandford R. D., Begelman M. C., 1999, Monthly Notices of the Royal Astronomical Society, 303, L1

Blandford R. D., Znajek R. L., 1977, Monthly Notices of the Royal Astronomical Society, 179, 433

Bodenheimer P., Laughlin G. P., Rózyczka M., Yorke H. W., 2007, Numerical Methods in Astrophysics: An Introduction. Taylor & Francis, New York

Boehringer H., Voges W., Fabian A. C., Edge A. C., Neumann D. M., 1993, Monthly Notices of the Royal Astronomical Society, 264, L25

Bond J. R., Cole S., Efstathiou G., Kaiser N., 1991, The Astrophysical Journal, 379, 440

Bond J. R., Kofman L., Pogosyan D., 1996, Nature, 380, 603

Bondi H., Hoyle F., 1944, Monthly Notices of the Royal Astronomical Society, 104, 273

Book L. G., Brooks A., Peter A. H. G., Benson A. J., Governato F., 2011, Monthly Notices of the Royal Astronomical Society, 411, 1963

Booth C. M., Schaye J., 2009, Monthly Notices of the Royal Astronomical Society, 398, 53

Bower R. G., Benson A. J., Malbon R., Helly J. C., Frenk C. S., Baugh C. M., Cole S., Lacey C. G., 2006, Monthly Notices of the Royal Astronomical Society, 370, 645

Brammer G. B., van Dokkum P. G., Coppi P., 2008, The Astrophysical Journal, 686, 1503

Brook C. B., Governato F., Roškar R., Stinson G., Brooks A. M., Wadsley J., Quinn T., Gibson B. K., Snaith O., Pilkington K., House E., Pontzen A., 2011, Monthly Notices of the Royal Astronomical Society, 595

Brook C. B., Kawata D., Gibson B. K., Freeman K. C., 2004, The Astrophysical Journal, 612, 894

Brooks A. M., Governato F., Quinn T., Brook C. B., Wadsley J., 2009, The Astrophysical Journal, 694, 396

Brüggen M., Kaiser C. R., 2002, Nature, 418, 301

Bruzual G., Charlot S., 2003, Monthly Notices of the Royal Astronomical Society, 344, 1000

Bryan G. L., Norman M. L., 1997, in Astronomical Society of the Pacific Conference Series, Vol. 123, Computational Astrophysics; 12th Kingston Meeting on Theoretical Astrophysics, Clarke D. A., West M. J., eds., p. 363

Bryan G. L., Norman M. L., 1998, The Astrophysical Journal, 495, 80

Buat V., 1992, Astronomy and Astrophysics, 264, 444

Bullock J. S., Dekel A., Kolatt T. S., Kravtsov A. V., Klypin A. A., Porciani C., Primack J. R., 2001, The Astrophysical Journal, 555, 240

Bundy K., Ellis R. S., Conselice C. J., 2005, The Astrophysical Journal, 625, 621

Burkert A., Bodenheimer P., 1996, Monthly Notices of the Royal Astronomical Society, 280, 1190

Cantalupo S., 2010, Monthly Notices of the Royal Astronomical Society, 403, L16

Capaccioli M., 1989, in World of Galaxies (Le Monde des Galaxies), Corwin Jr. H. G., Bottinelli L., eds., pp. 208–227

Cappellari M. et al., 2012, Nature, 484, 485

Cardelli J. A., Clayton G. C., Mathis J. S., 1989, The Astrophysical Journal, 345, 245

Castor J. I., Abbott D. C., Klein R. I., 1975, The Astrophysical Journal, 195, 157

Cayrel R., Depagne E., Spite M., Hill V., Spite F., François P., Plez B., Beers T., Primas F., Andersen J., Barbuy B., Bonifacio P., Molaro P., Nordström B., 2004, Astronomy and Astrophysics, 416, 1117

Cen R., 1992, The Astrophysical Journal Supplement Series, 78, 341

Cen R., Ostriker J. P., 1999, The Astrophysical Journal, 514, 1

Cen R., Ostriker J. P., 2006, The Astrophysical Journal, 650, 560

Ceverino D., Dekel A., Mandelker N., Bournaud F., Burkert A., Genzel R., Primack J., 2012, Monthly Notices of the Royal Astronomical Society, 420, 3490

Ceverino D., Klypin A., 2009, The Astrophysical Journal, 695, 292

Chevalier R. A., 1974, The Astrophysical Journal, 188, 501

Choi E., Ostriker J. P., Naab T., Johansson P. H., 2012, ArXiv e-prints

Chung A., Yun M. S., Naraynan G., Heyer M., Erickson N. R., 2011, The Astrophysical Journal, 732, L15

Churazov E., Brüggen M., Kaiser C. R., Böhringer H., Forman W., 2001, The Astrophysical Journal, 554, 261

Ciotti L., Ostriker J. P., 1997, The Astrophysical Journal, 487, L105+

Ciotti L., Ostriker J. P., 2001, The Astrophysical Journal, 551, 131

Ciotti L., Ostriker J. P., 2007, The Astrophysical Journal, 665, 1038

Codis S., Pichon C., Devriendt J., Slyz A., Pogosyan D., Dubois Y., Sousbie T., 2012, astro-ph/1201.5794C

Cole S., Lacey C. G., Baugh C. M., Frenk C. S., 2000, Monthly Notices of the Royal Astronomical Society, 319, 168

Cole S. et al., 2001, Monthly Notices of the Royal Astronomical Society, 326, 255

Colella P., Woodward P. R., 1984, J. Comp. Phys., 54, 174

Commerçon B., Hennebelle P., Audit E., Chabrier G., Teyssier R., 2008, Astronomy and Astrophysics, 482, 371

Cowie L. L., Songaila A., Hu E. M., Cohen J. G., 1996, The Astronomical Journal, 112, 839

Crain R. A., Eke V. R., Frenk C. S., Jenkins A., McCarthy I. G., Navarro J. F., Pearce F. R., 2007, Monthly Notices of the Royal Astronomical Society, 377, 41

Creasey P., Theuns T., Bower R. G., Lacey C. G., 2011, Monthly Notices of the Royal Astronomical Society, 415, 3706

Croft R. A. C., Di Matteo T., Springel V., Hernquist L., 2009, Monthly Notices of the Royal Astronomical Society, 400, 43

Croton D. J., Springel V., White S. D. M., De Lucia G., Frenk C. S., Gao L., Jenkins A., Kauffmann G., Navarro J. F., Yoshida N., 2006, Monthly Notices of the Royal Astronomical Society, 365, 11

Crutcher R. M., Wandelt B., Heiles C., Falgarone E., Troland T. H., 2010, The Astrophysical Journal, 725, 466

Daddi E., Cimatti A., Renzini A., Fontana A., Mignoli M., Pozzetti L., Tozzi P., Zamorani G., 2004, The Astrophysical Journal, 617, 746

Daddi E., Dickinson M., Morrison G., Chary R., Cimatti A., Elbaz D., Frayer D., Renzini A., Pope A., Alexander D. M., Bauer F. E., Giavalisco M., Huynh M., Kurk J., Mignoli M., 2007, The Astrophysical Journal, 670, 156

Daddi E., Elbaz D., Walter F., Bournaud F., Salmi F., Carilli C., Dannerbauer H., Dickinson M., Monaco P., Riechers D., 2010, The Astrophysical Journal, 714, L118

Dalcanton J. J., Spergel D. N., Summers F. J., 1997, The Astrophysical Journal, 482, 659

Dalla Vecchia C., Bower R. G., Theuns T., Balogh M. L., Mazzotta P., Frenk C. S., 2004, Monthly Notices of the Royal Astronomical Society, 355, 995

Dalla Vecchia C., Schaye J., 2008, Monthly Notices of the Royal Astronomical Society, 387, 1431

Dalla Vecchia C., Schaye J., 2012, ArXiv e-prints

Davé R., Cen R., Ostriker J. P., Bryan G. L., Hernquist L., Katz N., Weinberg D. H., Norman M. L., O'Shea B., 2001, The Astrophysical Journal, 552, 473

Dekel A., Birnboim Y., 2006, Monthly Notices of the Royal Astronomical Society, 368, 2

Dekel A., Birnboim Y., Engel G., Freundlich J., Goerdt T., Mumcuoglu M., Neistein E., Pichon C., Teyssier R., Zinger E., 2009, Nature, 457, 451

Dekel A., Silk J., 1986, The Astrophysical Journal, 303, 39

Deutsch A. J., 1956, The Astrophysical Journal, 123, 210

Devriendt J., Rimes C., Pichon C., Teyssier R., Le Borgne D., Aubert D., Audit E., Colombi S., Courty S., Dubois Y., Prunet S., Rasera Y., Slyz A., Tweed D., 2010, Monthly Notices of the Royal Astronomical Society, 403, L84

Devriendt J. E. G., Guiderdoni B., Sadat R., 1999, Astronomy and Astrophysics, 350, 381

Di Matteo T., Colberg J., Springel V., Hernquist L., Sijacki D., 2008, The Astrophysical Journal, 676, 33

Di Matteo T., Springel V., Hernquist L., 2005, Nature, 433, 604

Doroshkevich A. G., 1970, Astrophysics, 6, 320

Doumler T., Knebe A., 2010, Monthly Notices of the Royal Astronomical Society, 403, 453

Drake S. A., 1986, in Lecture Notes in Physics, Berlin Springer Verlag, Vol. 254, Cool Stars, Stellar Systems and the Sun, Zeilik M., Gibson D. M., eds., p. 369

Dubois Y., Devriendt J., Slyz A., Teyssier R., 2010, Monthly Notices of the Royal Astronomical Society, 409, 985

Dubois Y., Devriendt J., Slyz A., Teyssier R., 2012a, Monthly Notices of the Royal Astronomical Society, 420, 2662

Dubois Y., Pichon C., Devriendt J., Silk J., Haehnelt M., Kimm T., Slyz A., 2012b, astro-ph/1206.5838

Dubois Y., Teyssier R., 2008, Astronomy and Astrophysics, 477, 79

Dubois Y., Teyssier R., 2010, Astronomy and Astrophysics, 523, A72

Dunkley J., Spergel D. N., Komatsu E., Hinshaw G., Larson D., Nolta M. R., Odegard N., Page L., Bennett C. L., Gold B., Hill R. S., Jarosik N., Weiland J. L., Halpern M., Kogut A., Limon M., Meyer S. S., Tucker G. S., Wollack E., Wright E. L., 2009, The Astrophysical Journal, 701, 1804

Durier F., Dalla Vecchia C., 2012, Monthly Notices of the Royal Astronomical Society, 419, 465

Dutton A. A., van den Bosch F. C., 2009, Monthly Notices of the Royal Astronomical Society, 396, 141

Efstathiou G., Jones B. J. T., 1979, Monthly Notices of the Royal Astronomical Society, 186, 133

Eggen O. J., Lynden-Bell D., Sandage A. R., 1962, The Astrophysical Journal, 136, 748

Eisenstein D. J., Hu W., 1998, The Astrophysical Journal, 496, 605

Eisenstein D. J., Hut P., 1998, The Astrophysical Journal, 498, 137

Elbaz D., Daddi E., Le Borgne D., Dickinson M., Alexander D. M., Chary R.-R., Starck J.-L., Brandt W. N., Kitzbichler M., MacDonald E., Nonino M., Popesso P., Stern D., Vanzella E., 2007, Astronomy and Astrophysics, 468, 33

Elmegreen D. M., Elmegreen B. G., Ravindranath S., Coe D. A., 2007, The Astrophysical Journal, 658, 763

Evans, II N. J., Dunham M. M., Jørgensen J. K., Enoch M. L., Merín B., van Dishoeck E. F., Alcalá J. M., Myers P. C., Stapelfeldt K. R., Huard T. L., Allen L. E., Harvey P. M., van Kempen T., Blake G. A., Koerner D. W., Mundy L. G., Padgett D. L., Sargent A. I., 2009, The Astrophysical Journal Supplement Series, 181, 321

Fabian A. C., 1994, Annual Review of Astronomy and Astrophysics, 32, 277

Fabian A. C., Sanders J. S., Taylor G. B., Allen S. W., Crawford C. S., Johnstone R. M., Iwasawa K., 2006, Monthly Notices of the Royal Astronomical Society, 366, 417

Fall S. M., Efstathiou G., 1980, Monthly Notices of the Royal Astronomical Society, 193, 189

Fan X., Carilli C. L., Keating B., 2006, Annual Review of Astronomy and Astrophysics, 44, 415

Fardal M. A., Katz N., Gardner J. P., Hernquist L., Weinberg D. H., Davé R., 2001, The Astrophysical Journal, 562, 605

Faucher-Giguere C., Keres D., Ma C., 2011, ArXiv e-prints

Faucher-Giguère C.-A., Kereš D., 2011, Monthly Notices of the Royal Astronomical Society, 412, L118

Faucher-Giguère C.-A., Kereš D., Dijkstra M., Hernquist L., Zaldarriaga M., 2010, The Astrophysical Journal, 725, 633

Ferrarese L., Merritt D., 2000, The Astrophysical Journal, 539, L9

Firmani C., Avila-Reese V., 2000, Monthly Notices of the Royal Astronomical Society, 315, 457

Firmani C., Avila-Reese V., 2009, Monthly Notices of the Royal Astronomical Society, 396, 1675

Fontanot F., De Lucia G., Monaco P., Somerville R. S., Santini P., 2009, Monthly Notices of the Royal Astronomical Society, 397, 1776

Forman W., Nulsen P., Heinz S., Owen F., Eilek J., Vikhlinin A., Markevitch M., Kraft R., Churazov E., Jones C., 2005, The Astrophysical Journal, 635, 894

Freeman K. C., 1970, The Astrophysical Journal, 160, 811

Fryxell B., Olson K., Ricker P., Timmes F. X., Zingale M., Lamb D. Q., MacNeice P., Rosner R., Truran J. W., Tufo H., 2000, The Astrophysical Journal Supplement Series, 131, 273

Fujita A., Martin C. L., Mac Low M.-M., New K. C. B., Weaver R., 2009, The Astrophysical Journal, 698, 693

Ganguly R., Brotherton M. S., 2008, The Astrophysical Journal, 672, 102

Gebhardt K., Bender R., Bower G., Dressler A., Faber S. M., Filippenko A. V., Green R., Grillmair C., Ho L. C., Kormendy J., Lauer T. R., Magorrian J., Pinkney J., Richstone D., Tremaine S., 2000, The Astrophysical Journal, 539, L13

Geen S., Slyz A., Devriendt J., 2012, astro-ph/1204.3327G

Genzel R. et al., 2011, The Astrophysical Journal, 733, 101

Genzel R. et al., 2010, Monthly Notices of the Royal Astronomical Society, 407, 2091

Giavalisco M., , et al., 2004, The Astrophysical Journal, 600, L93

Gillmon K., Shull J. M., Tumlinson J., Danforth C., 2006, The Astrophysical Journal, 636, 891

Girardi L., Bressan A., Bertelli G., Chiosi C., 2000, Astronomy and Astrophysics Supplement Series, 141, 371

Gnedin N. Y., Kravtsov A. V., Rudd D. H., 2011, The Astrophysical Journal Supplement Series, 194, 46

Godunov S. K., 1959, Mat. Sbornik, 47, 271, Translated as JPRS 7225 by U.S. Dept. of Commerce, 1960

Governato F., Brook C., Mayer L., Brooks A., Rhee G., Wadsley J., Jonsson P., Willman B., Stinson G., Quinn T., Madau P., 2010, Nature, 463, 203

Governato F., Brook C. B., Brooks A. M., Mayer L., Willman B., Jonsson P., Stilp A. M., Pope L., Christensen C., Wadsley J., Quinn T., 2009, Monthly Notices of the Royal Astronomical Society, 398, 312

Governato F., Mayer L., Wadsley J., Gardner J. P., Willman B., Hayashi E., Quinn T., Stadel J., Lake G., 2004, The Astrophysical Journal, 607, 688

Governato F., Willman B., Mayer L., Brooks A., Stinson G., Valenzuela O., Wadsley J., Quinn T., 2007, Monthly Notices of the Royal Astronomical Society, 374, 1479

Graham A. W., 2012, The Astrophysical Journal, 746, 113

Graham A. W., Worley C. C., 2008, Monthly Notices of the Royal Astronomical Society, 388, 1708

Greggio L., Renzini A., 1983, Astronomy and Astrophysics, 118, 217

Guedes J., Callegari S., Madau P., Mayer L., 2011, The Astrophysical Journal, 742, 76

Guiderdoni B., Rocca-Volmerange B., 1987, Astronomy and Astrophysics, 186, 1

Gültekin K., Richstone D. O., Gebhardt K., Lauer T. R., Tremaine S., Aller M. C., Bender R., Dressler A., Faber S. M., Filippenko A. V., Green R., Ho L. C., Kormendy J., Magorrian J., Pinkney J., Siopis C., 2009, The Astrophysical Journal, 698, 198

Gunn J. E., Peterson B. A., 1965, The Astrophysical Journal, 142, 1633

Haardt F., Madau P., 1996, The Astrophysical Journal, 461, 20

Haehnelt M. G., Madau P., Kudritzki R., Haardt F., 2001, The Astrophysical Journal, 549, L151

Hamann F., Barlow T. A., Junkkarinen V., Burbidge E. M., 1997, The Astrophysical Journal, 478, 80

Häring N., Rix H.-W., 2004, The Astrophysical Journal, 604, L89

Harten A., Lax P., van Leer B., 1983, SIAM, 25, 35

Hatton S., Devriendt J. E. G., Ninin S., Bouchet F. R., Guiderdoni B., Vibert D., 2003, Monthly Notices of the Royal Astronomical Society, 343, 75

Hillebrandt W., Niemeyer J. C., 2000, Annual Review of Astronomy and Astrophysics, 38, 191

Hinshaw G. et al., 2009, The Astrophysical Journal Supplement Series, 180, 225

Hjorth J. et al., 2003, Nature, 423, 847

Hockney R. W., Eastwood J. W., 1988, Computer simulation using particles. Bristol: Hilger

Hoffman Y., 1986, The Astrophysical Journal, 301, 65

Hopkins P. F., Cox T. J., Hernquist L., Narayanan D., Hayward C. C., Murray N., 2012a, ArXiv e-prints

Hopkins P. F., Quataert E., Murray N., 2011, Monthly Notices of the Royal Astronomical Society, 417, 950

Hopkins P. F., Quataert E., Murray N., 2012b, Monthly Notices of the Royal Astronomical Society, 421, 3522

Hopkins P. F., Quataert E., Murray N., 2012c, Monthly Notices of the Royal Astronomical Society, 421, 3488

Howarth I. D., Prinja R. K., 1989, The Astrophysical Journal Supplement Series, 69, 527

Hoyle F., Fowler W. A., 1960, The Astrophysical Journal, 132, 565

Hubble E., 1929, Proceedings of the National Academy of Science, 15, 168

Hummels C. B., Bryan G. L., 2012, The Astrophysical Journal, 749, 140

Humphreys R. M., Davidson K., 1994, Publications of the Astronomical Society of the Pacific, 106, 1025

Iben, Jr. I., Tutukov A. V., 1984, The Astrophysical Journal Supplement Series, 54, 335

Iwamoto K., Nakamura T., Nomoto K., Mazzali P. A., Danziger I. J., Garnavich P., Kirshner R., Jha S., Balam D., Thorstensen J., 2000, The Astrophysical Journal, 534, 660

Jenkins A., Frenk C. S., White S. D. M., Colberg J. M., Cole S., Evrard A. E., Couchman H. M. P., Yoshida N., 2001, Monthly Notices of the Royal Astronomical Society, 321, 372

Johansson P. H., Naab T., Ostriker J. P., 2012, astro-ph/1202.3441J

Joung M. R., Cen R., Bryan G. L., 2009, The Astrophysical Journal, 692, L1

Juneau S., Glazebrook K., Crampton D., McCarthy P. J., Savaglio S., Abraham R., Carlberg R. G., Chen H.-W., Le Borgne D., Marzke R. O., Roth K., Jørgensen I., Hook I., Murowinski R., 2005, The Astrophysical Journal, 619, L135

Kalirai J. S., Hansen B. M. S., Kelson D. D., Reitzel D. B., Rich R. M., Richer H. B., 2008, The Astrophysical Journal, 676, 594

Kassin S. A., de Jong R. S., Weiner B. J., 2006, The Astrophysical Journal, 643, 804

Kassin S. A., Devriendt J., Fall S. M., de Jong R. S., Allgood B., Primack J. R., 2012, astro-ph/1205.0253K

Katz N., 1992, The Astrophysical Journal, 391, 502

Katz N., Keres D., Dave R., Weinberg D. H., 2003, in Astrophysics and Space Science Library, Vol. 281, The IGM/Galaxy Connection. The Distribution of Baryons at z=0, J. L. Rosenberg & M. E. Putman, ed., pp. 185–+

Katz N., Weinberg D. H., Hernquist L., 1996, The Astrophysical Journal Supplement Series, 105, 19

Kauffmann G., Colberg J. M., Diaferio A., White S. D. M., 1999, Monthly Notices of the Royal Astronomical Society, 303, 188

Kauffmann G., Haehnelt M., 2000, Monthly Notices of the Royal Astronomical Society, 311, 576

Kauffmann G., White S. D. M., Guiderdoni B., 1993, Monthly Notices of the Royal Astronomical Society, 264, 201

Kaviraj S., Schawinski K., Silk J., Shabala S. S., 2011a, Monthly Notices of the Royal Astronomical Society, 415, 3798

Kaviraj S., Tan K.-M., Ellis R. S., Silk J., 2011b, Monthly Notices of the Royal Astronomical Society, 411, 2148

Kawata D., Gibson B. K., 2005, Monthly Notices of the Royal Astronomical Society, 358, L16

Kay S. T., Thomas P. A., Theuns T., 2003, Monthly Notices of the Royal Astronomical Society, 343, 608

Kenney J. D., Young J. S., 1988, The Astrophysical Journal, 326, 588

Kennicutt, Jr. R. C., 1989, The Astrophysical Journal, 344, 685

Kennicutt, Jr. R. C., 1998, The Astrophysical Journal, 498, 541

Kereš D., Katz N., Fardal M., Davé R., Weinberg D. H., 2009, Monthly Notices of the Royal Astronomical Society, 395, 160

Kereš D., Katz N., Weinberg D. H., Davé R., 2005, Monthly Notices of the Royal Astronomical Society, 363, 2

Khochfar S., Ostriker J. P., 2008, The Astrophysical Journal, 680, 54

Khochfar S., Silk J., 2011, Monthly Notices of the Royal Astronomical Society, 410, L42

Khochfar S., Silk J., Windhorst R. A., Ryan, Jr. R. E., 2007, The Astrophysical Journal, 668, L115

Khokhlov A. M., 1998, J. Comp. Phys., 143, 519

Kimm T., Kaviraj S., Devriendt J., Cohen S., Windhorst R., Dubois Y., Slyz A., Hathi N., Ryan, Jr R., O'Connell R., Dopita M., Silk J., 2012, astro-ph/1205.3801K

Kimm T., Slyz A., Devriendt J., Pichon C., 2011, Monthly Notices of the Royal Astronomical Society, 413, L51

Kimm T., Somerville R. S., Yi S. K., van den Bosch F. C., Salim S., Fontanot F., Monaco P., Mo H., Pasquali A., Rich R. M., Yang X., 2009, Monthly Notices of the Royal Astronomical Society, 394, 1131

King A., 2003, The Astrophysical Journal, 596, L27

Klypin A., Kravtsov A. V., Valenzuela O., Prada F., 1999, The Astrophysical Journal, 522, 82

Kobayashi C., Karakas A. I., Umeda H., 2011, Monthly Notices of the Royal Astronomical Society, 414, 3231

Kobayashi C., Nakasato N., 2011, The Astrophysical Journal, 729, 16

Kobayashi C., Umeda H., Nomoto K., Tominaga N., Ohkubo T., 2006, The Astrophysical Journal, 653, 1145

Konigl A., Kartje J. F., 1994, The Astrophysical Journal, 434, 446

Körding E. G., Jester S., Fender R., 2006, Monthly Notices of the Royal Astronomical Society, 372, 1366

Kormendy J., Richstone D., 1995, Annual Review of Astronomy and Astrophysics, 33, 581

Krumholz M. R., McKee C. F., 2005, The Astrophysical Journal, 630, 250

Krumholz M. R., Tan J. C., 2007, The Astrophysical Journal, 654, 304

Lacey C., Cole S., 1993, Monthly Notices of the Royal Astronomical Society, 262, 627

Larson R. B., 1974, Monthly Notices of the Royal Astronomical Society, 169, 229

Lee M.-Y., Stanimirović S., Douglas K. A., Knee L. B. G., Di Francesco J., Gibson S. J., Begum A., Grcevich J., Heiles C., Korpela E. J., Leroy A. K., Peek J. E. G., Pingel N. M., Putman M. E., Saul D., 2012, The Astrophysical Journal, 748, 75

Leitherer C., Ortiz Otálvaro P. A., Bresolin F., Kudritzki R.-P., Lo Faro B., Pauldrach A. W. A., Pettini M., Rix S. A., 2010, The Astrophysical Journal Supplement Series, 189, 309

Leitherer C., Robert C., Drissen L., 1992, The Astrophysical Journal, 401, 596

Leitherer C., Schaerer D., Goldader J. D., González Delgado R. M., Robert C., Kune D. F., de Mello D. F., Devost D., Heckman T. M., 1999, The Astrophysical Journal Supplement Series, 123, 3

Leitner S. N., Kravtsov A. V., 2011, The Astrophysical Journal, 734, 48

Lemaître G., 1927, Annales de la Societe Scietifique de Bruxelles, 47, 49

Lin Y.-T., Mohr J. J., Stanford S. A., 2003, The Astrophysical Journal, 591, 749

Mac Low M.-M., Ferrara A., 1999, The Astrophysical Journal, 513, 142

Macciò A. V., Kang X., Fontanot F., Somerville R. S., Koposov S., Monaco P., 2010, Monthly Notices of the Royal Astronomical Society, 402, 1995

Madau P., Pozzetti L., Dickinson M., 1998, The Astrophysical Journal, 498, 106

Maeder A., 1990, Astronomy and Astrophysics Supplement Series, 84, 139

Magorrian J., Tremaine S., Richstone D., Bender R., Bower G., Dressler A., Faber S. M., Gebhardt K., Green R., Grillmair C., Kormendy J., Lauer T., 1998, The Astronomical Journal, 115, 2285

Malesani D. et al., 2004, The Astrophysical Journal, 609, L5

Maller A. H., Dekel A., Somerville R., 2002, Monthly Notices of the Royal Astronomical Society, 329, 423

Mannucci F., Della Valle M., Panagia N., 2006, Monthly Notices of the Royal Astronomical Society, 370, 773

Maraston C., 2005, Monthly Notices of the Royal Astronomical Society, 362, 799

Marconi A., Hunt L. K., 2003, The Astrophysical Journal, 589, L21

Marri S., White S. D. M., 2003, Monthly Notices of the Royal Astronomical Society, 345, 561

Martel H., Shapiro P. R., 1998, Monthly Notices of the Royal Astronomical Society, 297, 467

Martin C. L., 1999, The Astrophysical Journal, 513, 156

Martin C. L., 2005, The Astrophysical Journal, 621, 227

Matteucci F., Greggio L., 1986, Astronomy and Astrophysics, 154, 279

Matteucci F., Recchi S., 2001, The Astrophysical Journal, 558, 351

Mazzali P. A., Iwamoto K., Nomoto K., 2000, The Astrophysical Journal, 545, 407

Mazzali P. A., Lucy L. B., 1993, Astronomy and Astrophysics, 279, 447

McGaugh S. S., 2005, The Astrophysical Journal, 632, 859

McGaugh S. S., Schombert J. M., de Blok W. J. G., Zagursky M. J., 2010, The Astrophysical Journal, 708, L14

McKee C. F., 1999, in NATO ASIC Proc. 540: The Origin of Stars and Planetary Systems, Lada C. J., Kylafis N. D., eds., p. 29

McKee C. F., Ostriker E. C., 2007, Annual Review of Astronomy and Astrophysics, 45, 565

McKee C. F., Ostriker J. P., 1977, The Astrophysical Journal, 218, 148

McKee C. F., Zweibel E. G., Goodman A. A., Heiles C., 1993, in Protostars and Planets III, Levy E. H., Lunine J. I., eds., p. 327

McLure R. J., Dunlop J. S., 2002, Monthly Notices of the Royal Astronomical Society, 331, 795

McLure R. J., Dunlop J. S., de Ravel L., Cirasuolo M., Ellis R. S., Schenker M., Robertson B. E., Koekemoer A. M., Stark D. P., Bowler R. A. A., 2011, Monthly Notices of the Royal Astronomical Society, 418, 2074

McMillan P. J., 2011, Monthly Notices of the Royal Astronomical Society, 414, 2446

McNamara B. R., Nulsen P. E. J., 2007, Annual Review of Astronomy and Astrophysics, 45, 117

McNamara B. R., Nulsen P. E. J., Wise M. W., Rafferty D. A., Carilli C., Sarazin C. L., Blanton E. L., 2005, Nature, 433, 45

Mihos J. C., Hernquist L., 1994, The Astrophysical Journal, 437, 611

Mitchell N. L., McCarthy I. G., Bower R. G., Theuns T., Crain R. A., 2009, Monthly Notices of the Royal Astronomical Society, 395, 180

Mo H., van den Bosch F. C., White S., 2010, Galaxy Formation and Evolution. Springer

Mo H. J., Mao S., White S. D. M., 1998, Monthly Notices of the Royal Astronomical Society, 295, 319

Monaco P., Fontanot F., Taffoni G., 2007, Monthly Notices of the Royal Astronomical Society, 375, 1189

Monaghan J. J., 1992, Annual Review of Astronomy and Astrophysics, 30, 543

Moore B., Ghigna S., Governato F., Lake G., Quinn T., Stadel J., Tozzi P., 1999, The Astrophysical Journal, 524, L19

Mori M., Yoshii Y., Tsujimoto T., Nomoto K., 1997, The Astrophysical Journal, 478, L21

Morton D. C., 1967, The Astrophysical Journal, 150, 535

Muñoz-Cuartas J. C., Macciò A. V., Gottlöber S., Dutton A. A., 2011, Monthly Notices of the Royal Astronomical Society, 411, 584

Murray N., Chiang J., Grossman S. A., Voit G. M., 1995, The Astrophysical Journal, 451, 498

Nakamura F., Li Z.-Y., 2008, The Astrophysical Journal, 687, 354

Nakamura T., Mazzali P. A., Nomoto K., Iwamoto K., 2001, The Astrophysical Journal, 550, 991

Narayan R., Yi I., 1994, The Astrophysical Journal, 428, L13

Narayan R., Yi I., 1995, The Astrophysical Journal, 444, 231

Navarro J. F., Benz W., 1991, The Astrophysical Journal, 380, 320

Navarro J. F., Frenk C. S., White S. D. M., 1997, The Astrophysical Journal, 490, 493

Navarro J. F., Steinmetz M., 2000, The Astrophysical Journal, 538, 477

Navarro J. F., White S. D. M., 1993, Monthly Notices of the Royal Astronomical Society, 265, 271

Nomoto K., Kondo Y., 1991, The Astrophysical Journal, 367, L19

Nomoto K., Thielemann F.-K., Yokoi K., 1984, The Astrophysical Journal, 286, 644

Nomoto K., Tominaga N., Umeda H., Kobayashi C., Maeda K., 2006, Nuclear Physics A, 777, 424

Nugent P., Baron E., Branch D., Fisher A., Hauschildt P. H., 1997, The Astrophysical Journal, 485, 812

Ocvirk P., Pichon C., Teyssier R., 2008, Monthly Notices of the Royal Astronomical Society, 390, 1326

Okamoto T., Eke V. R., Frenk C. S., Jenkins A., 2005, Monthly Notices of the Royal Astronomical Society, 363, 1299

Omma H., Binney J., Bryan G., Slyz A., 2004, Monthly Notices of the Royal Astronomical Society, 348, 1105

Oppenheimer B. D., Davé R., 2006, Monthly Notices of the Royal Astronomical Society, 373, 1265

Oser L., Naab T., Ostriker J. P., Johansson P. H., 2012, The Astrophysical Journal, 744, 63

O'Shea B. W., Bryan G., Bordner J., Norman M. L., Abel T., Harkness R., Kritsuk A., 2004, ArXiv Astrophysics e-prints

Ostriker E. C., Shetty R., 2011, The Astrophysical Journal, 731, 41

Padoan P., Nordlund Å., 2011, The Astrophysical Journal, 730, 40

Padovani P., Matteucci F., 1993, The Astrophysical Journal, 416, 26

Patat F. et al., 2001, The Astrophysical Journal, 555, 900

Peebles P. J. E., 1969, The Astrophysical Journal, 155, 393

Peebles P. J. E., 1971, Astronomy and Astrophysics, 11, 377

Peirani S., Jung I., Silk J., Pichon C., 2012, astro-ph/1205.4695P

Peirani S., Mohayaee R., de Freitas Pacheco J. A., 2004, Monthly Notices of the Royal Astronomical Society, 348, 921

Pérez-González P. G., Rieke G. H., Villar V., Barro G., Blaylock M., Egami E., Gallego J., Gil de Paz A., Pascual S., Zamorano J., Donley J. L., 2008, The Astrophysical Journal, 675, 234

Persic M., Salucci P., 1992, Monthly Notices of the Royal Astronomical Society, 258, 14P

Pettini M., Rix S. A., Steidel C. C., Adelberger K. L., Hunt M. P., Shapley A. E., 2002, The Astrophysical Journal, 569, 742

Pichon C., Pogosyan D., Kimm T., Slyz A., Devriendt J., Dubois Y., 2011, ArXiv e-prints

Piontek F., Steinmetz M., 2011, Monthly Notices of the Royal Astronomical Society, 410, 2625

Pipino A., Devriendt J. E. G., Thomas D., Silk J., Kaviraj S., 2009, Astronomy and Astrophysics, 505, 1075

Podsiadlowski P., Mazzali P. A., Nomoto K., Lazzati D., Cappellaro E., 2004, The Astrophysical Journal, 607, L17

Ponman T. J., Cannon D. B., Navarro J. F., 1999, Nature, 397, 135

Pounds K. A., Reeves J. N., King A. R., Page K. L., O'Brien P. T., Turner M. J. L., 2003, Monthly Notices of the Royal Astronomical Society, 345, 705

Powell L. C., Slyz A., Devriendt J., 2011, Monthly Notices of the Royal Astronomical Society, 414, 3671

Press W. H., Schechter P., 1974, The Astrophysical Journal, 187, 425

Press W. H., Teukolsky S. A., Vetterling W. T., Flannery B. P., 1992, Numerical recipes in FORTRAN. The art of scientific computing. Cambridge University Press

Prinja R. K., Barlow M. J., Howarth I. D., 1990, The Astrophysical Journal, 361, 607

Proga D., 2007, The Astrophysical Journal, 661, 693

Prunet S., Pichon C., Aubert D., Pogosyan D., Teyssier R., Gottloeber S., 2008, The Astrophysical Journal Supplement Series, 178, 179

Quilis V., Bower R. G., Balogh M. L., 2001, Monthly Notices of the Royal Astronomical Society, 328, 1091

Rasera Y., Teyssier R., 2006, Astronomy and Astrophysics, 445, 1

Rees M. J., Ostriker J. P., 1977, Monthly Notices of the Royal Astronomical Society, 179, 541

Reimers D., 1975, Memoires of the Societe Royale des Sciences de Liege, 8, 369

Robertson B., Yoshida N., Springel V., Hernquist L., 2004, The Astrophysical Journal, 606, 32

Rosdahl J., Blaizot J., 2012, Monthly Notices of the Royal Astronomical Society, 423, 344

Roth N., Kasen D., Hopkins P. F., Quataert E., 2012, astro-ph/1204.0063

Rupke D. S., Veilleux S., Sanders D. B., 2005, The Astrophysical Journal Supplement Series, 160, 115

Rutkowski M. J. et al., 2012, The Astrophysical Journal Supplement Series, 199, 4

Sales L. V., Navarro J. F., Schaye J., Vecchia C. D., Springel V., Booth C. M., 2010, Monthly Notices of the Royal Astronomical Society, 409, 1541

Salim S. et al., 2007, The Astrophysical Journal Supplement Series, 173, 267

Salpeter E. E., 1955, The Astrophysical Journal, 121, 161

Sanders D. B., Mirabel I. F., 1996, Annual Review of Astronomy and Astrophysics, 34, 749

Savage B. D., Bohlin R. C., Drake J. F., Budich W., 1977, The Astrophysical Journal, 216, 291

Scannapieco C., Tissera P. B., White S. D. M., Springel V., 2006, Monthly Notices of the Royal Astronomical Society, 371, 1125

Scannapieco C., White S. D. M., Springel V., Tissera P. B., 2009, Monthly Notices of the Royal Astronomical Society, 396, 696

Scannapieco E., Brüggen M., 2010, Monthly Notices of the Royal Astronomical Society, 405, 1634

Schmidt M., 1959, The Astrophysical Journal, 129, 243

Schuster K. F., Kramer C., Hitschfeld M., Garcia-Burillo S., Mookerjea B., 2007, Astronomy and Astrophysics, 461, 143

Searle L., Zinn R., 1978, The Astrophysical Journal, 225, 357

Shakura N. I., Sunyaev R. A., 1973, Astronomy and Astrophysics, 24, 337

Shapley A. E., Steidel C. C., Pettini M., Adelberger K. L., 2003, The Astrophysical Journal, 588, 65

Sharma S., Steinmetz M., 2005, The Astrophysical Journal, 628, 21

Shu F. H., 1992, Physics of Astrophysics, Vol. II. University Science Books

Sijacki D., Springel V., 2006, Monthly Notices of the Royal Astronomical Society, 366, 397

Sijacki D., Springel V., Di Matteo T., Hernquist L., 2007, Monthly Notices of the Royal Astronomical Society, 380, 877

Silk J., 1977, The Astrophysical Journal, 211, 638

Silk J., Rees M. J., 1998, Astronomy and Astrophysics, 331, L1

Simon J. D., Geha M., 2007, The Astrophysical Journal, 670, 313

Sirko E., 2005, The Astrophysical Journal, 634, 728

Slyz A. D., Devriendt J. E. G., Bryan G., Silk J., 2005, Monthly Notices of the Royal Astronomical Society, 356, 737

Sofue Y., Rubin V., 2001, Annual Review of Astronomy and Astrophysics, 39, 137

Somerville R. S., Hopkins P. F., Cox T. J., Robertson B. E., Hernquist L., 2008, Monthly Notices of the Royal Astronomical Society, 391, 481

Sommer-Larsen J., Götz M., Portinari L., 2003, The Astrophysical Journal, 596, 47

Spergel D. N., Verde L., Peiris H. V., Komatsu E., Nolta M. R., Bennett C. L., Halpern M., Hinshaw G., Jarosik N., Kogut A., Limon M., Meyer S. S., Page L., Tucker G. S., Weiland J. L., Wollack E., Wright E. L., 2003, The Astrophysical Journal Supplement Series, 148, 175

Springel V., 2005, Monthly Notices of the Royal Astronomical Society, 364, 1105

Springel V., Hernquist L., 2003, Monthly Notices of the Royal Astronomical Society, 339, 289

Springel V., White S. D. M., Jenkins A., Frenk C. S., Yoshida N., Gao L., Navarro J., Thacker R., Croton D., Helly J., Peacock J. A., Cole S., Thomas P., Couchman H., Evrard A., Colberg J., Pearce F., 2005, Nature, 435, 629

Stanek K. Z. et al., 2003, The Astrophysical Journal, 591, L17

Stark D. P., Ellis R. S., Bunker A., Bundy K., Targett T., Benson A., Lacy M., 2009, The Astrophysical Journal, 697, 1493

Steidel C. C., Erb D. K., Shapley A. E., Pettini M., Reddy N., Bogosavljević M., Rudie G. C., Rakic O., 2010, The Astrophysical Journal, 717, 289

Steidel C. C., Giavalisco M., Pettini M., Dickinson M., Adelberger K. L., 1996, The Astrophysical Journal, 462, L17

Stewart K. R., Kaufmann T., Bullock J. S., Barton E. J., Maller A. H., Diemand J., Wadsley J., 2011a, The Astrophysical Journal, 735, L1

Stewart K. R., Kaufmann T., Bullock J. S., Barton E. J., Maller A. H., Diemand J., Wadsley J., 2011b, The Astrophysical Journal, 738, 39

Stinson G., Seth A., Katz N., Wadsley J., Governato F., Quinn T., 2006, Monthly Notices of the Royal Astronomical Society, 373, 1074

Stone J. M., Norman M. L., 1992, The Astrophysical Journal Supplement Series, 80, 753

Strickland D. K., Heckman T. M., 2009, The Astrophysical Journal, 697, 2030

Stringer M. J., Benson A. J., 2007, Monthly Notices of the Royal Astronomical Society, 382, 641

Sutherland R. S., Dopita M. A., 1993, The Astrophysical Journal Supplement Series, 88, 253

Teyssier R., 2002, Astronomy and Astrophysics, 385, 337

Teyssier R., Chapon D., Bournaud F., 2010, The Astrophysical Journal, 720, L149

Thacker R. J., Couchman H. M. P., 2000, The Astrophysical Journal, 545, 728

Thacker R. J., Tittley E. R., Pearce F. R., Couchman H. M. P., Thomas P. A., 2000, Monthly Notices of the Royal Astronomical Society, 319, 619

Theuns T., Leonard A., Efstathiou G., Pearce F. R., Thomas P. A., 1998, Monthly Notices of the Royal Astronomical Society, 301, 478

Thomas D., 1999, Monthly Notices of the Royal Astronomical Society, 306, 655

Thomas D., Greggio L., Bender R., 1998, Monthly Notices of the Royal Astronomical Society, 296, 119

Thomas D., Greggio L., Bender R., 1999, Monthly Notices of the Royal Astronomical Society, 302, 537

Thomas D., Maraston C., Bender R., Mendes de Oliveira C., 2005, The Astrophysical Journal, 621, 673

Thomsen B., Hjorth J., Watson D., Gorosabel J., Fynbo J. P. U., Jensen B. L., Andersen M. I., Dall T. H., Rasmussen J. R., Bruntt H., Laurikainen E., Augusteijn T., Pursimo T., Germany L., Jakobsson P., Pedersen K., 2004, Astronomy and Astrophysics, 419, L21

Thornton K., Gaudlitz M., Janka H.-T., Steinmetz M., 1998, The Astrophysical Journal, 500, 95

Tominaga N., Umeda H., Nomoto K., 2007, The Astrophysical Journal, 660, 516

Toro E. F., Spruce M., Speares W., 1994, Shock Waves, 4, 25

Trager S. C., Faber S. M., Worthey G., González J. J., 2000, The Astronomical Journal, 119, 1645

Truelove J. K., Klein R. I., McKee C. F., Holliman, II J. H., Howell L. H., Greenough J. A., 1997, The Astrophysical Journal, 489, L179

Turnshek D. A., Grillmair C. J., Foltz C. B., Weymann R. J., 1988, The Astrophysical Journal, 325, 651

Tutukov A. V., Iungelson L. R., 1980in IAU Symposium, Vol. 88, Close Binary Stars: Observations and Interpretation, Plavec M. J.Popper D. M., Ulrich R. K., eds., Reidel, Dordrecht, pp. 15–22

Tweed D., Devriendt J., Blaizot J., Colombi S., Slyz A., 2009, Astronomy and Astrophysics, 506, 647

Umeda H., Nomoto K., 2002, The Astrophysical Journal, 565, 385

van de Voort F., Schaye J., Booth C. M., Haas M. R., Dalla Vecchia C., 2011, Monthly Notices of the Royal Astronomical Society, 414, 2458

van den Bosch F. C., 2002, Monthly Notices of the Royal Astronomical Society, 331, 98

van den Bosch F. C., Abel T., Croft R. A. C., Hernquist L., White S. D. M., 2002, The Astrophysical Journal, 576, 21

van Dokkum P. G., Conroy C., 2010, Nature, 468, 940

van Leer B., 1979, J. Comp. Phys., 32, 101

Vassiliadis E., Wood P. R., 1993, The Astrophysical Journal, 413, 641

Vitvitska M., Klypin A. A., Kravtsov A. V., Wechsler R. H., Primack J. R., Bullock J. S., 2002, The Astrophysical Journal, 581, 799

Wadepuhl M., Springel V., 2011, Monthly Notices of the Royal Astronomical Society, 410, 1975

Wadsley J. W., Stadel J., Quinn T., 2004, New Astronomy, 9, 137

Wechsler R. H., Bullock J. S., Primack J. R., Kravtsov A. V., Dekel A., 2002, The Astrophysical Journal, 568, 52

Weidemann V., 2000, Astronomy and Astrophysics, 363, 647

Weinberg D. H., Hernquist L., Katz N., 1997, The Astrophysical Journal, 477, 8

Weymann R., 1962, The Astrophysical Journal, 136, 844

White S. D. M., 1984, The Astrophysical Journal, 286, 38

White S. D. M., Rees M. J., 1978, Monthly Notices of the Royal Astronomical Society, 183, 341

Wiersma R. P. C., Schaye J., Smith B. D., 2009, Monthly Notices of the Royal Astronomical Society, 393, 99

Williams R. J., Quadri R. F., Franx M., van Dokkum P., Labbé I., 2009, The Astrophysical Journal, 691, 1879

Windhorst R. A. et al., 2011, The Astrophysical Journal Supplement Series, 193, 27

Wong T., Blitz L., 2002, The Astrophysical Journal, 569, 157

Woosley S. E., Weaver T. A., 1994, The Astrophysical Journal, 423, 371

Woosley S. E., Weaver T. A., 1995, The Astrophysical Journal Supplement Series, 101, 181

Xue Y.-J., Wu X.-P., 2000, The Astrophysical Journal, 538, 65

Zavala J., Okamoto T., Frenk C. S., 2008, Monthly Notices of the Royal Astronomical Society, 387, 364

Zel'dovich Y. B., 1970, Astronomy and Astrophysics, 5, 84

Zuckerman B., Evans, II N. J., 1974, The Astrophysical Journal, 192, L149